



Universität für Bodenkultur Wien



# Hybrid Adaptable Plasmonic Nanostructures for Biosensing

Submitted by

MSc. Nestor Gisbert Quilis

A thesis submitted for the degree of  
Doctor of Philosophy (PhD)

University of Natural Resources and Life Sciences, BOKU, Vienna  
Austrian Institute of Technology, AIT, Vienna

Supervisors:

Jakub Dostalek, PhD, BioSensor Technologies, AIT  
Prof. Dr. Wolfgang Knoll, Institute for Biophysics, BOKU

Co-Supervisors:

Prof. Dr. Ulrich Jonas, University of Siegen



I hereby declare that I am the sole author of this work; no assistance other than that permitted has been used and all quotes and concepts taken from unpublished sources, published literature or the internet in wording or in basic content have been identified by footnotes or with precise source citations.

A handwritten signature in blue ink that reads "Nestor". The signature is written in a cursive style with a horizontal line underneath the letters.

**Vienna, July 2020; Nestor Gisbert Quilis**



“Nothing in life is to be  
feared, it is only to be understood.  
Now is the time to understand more,  
so that we may fear less”

**Marie Curie**



## Acknowledgements

I would like to express my gratitude to Prof. Wolfgang Knoll for offering his help as supervisor at BOKU.

My sincere appreciation goes to Dr. Jakub Dostalek, for always knowing how to steer the boat in the right direction and bringing such nice group of people together. It was a pleasure to do science with you.

My deepest appreciation goes to the BST team that rapidly turned into a second family. To Priya, for being such a caring colleague and bring the Indian flavor to the group. Stefan has always been the helpful hand at the lab, always ready to discuss any single matter in the universe, my sincere gratitude. To Simone, for those extraordinary climbing & lab discussion sessions. To Daria, Biogel buddy, it has been a pleasure to share together the ITN experience, and all the polish evenings as well. To Hulan, for her amazing sense of humor. Imran and Nitya, thank you guys for taking the time to introduce the newcomers to the lab. Anil, thank you for bringing the rhythm and the dancing, keep it up. Vanessa, thank you for making my name famous and never make a day in the lab boring. Mark and Chiara, thank you guys for your contagious optimism. Also, to the rest of the BST group members and BIOGEL folks, they always contributed to create a fantastic atmosphere and made the journey more enjoyable.

Special thanks to my new MADx family, who patiently waited for me to finish this work and always supported me during the way, especially on Friday afternoons.

Amb especial afecte vull agrair el suport de la meva família, ells són els que realment han fet possible aquesta experiència. A la mare, per la seva estima infinita i per les abraçades a peu d'aeroport que escalfen el cor, i et fan sentir que ja ets a casa. Al pare, per la seva ajuda desinteressada amb integrals, derivades i tangents i el seu humor marca de la casa. Gràcies pares per tot el que ens heu donat. A Patri, germana bessona, companya de jocs, batalles, estudis i aventures, per a ella no hi ha prou paraules. És un regal poder comptar amb tu, dir que em sent afortunat i orgullós és quedar-me ben ben curt, mil gràcies per estar sempre, seguim compartint camí germaneta, amb tu, tot és més fàcil. Als avis, a l'avi Ramon i l'àvia Carmen per fer de segons pares al torn de matí/vesprada i per donar suport quan calia. A l'avi Pepito i l'àvia Maruja, per la seva ajuda incondicional amb tot allò que hem anat fent durant els anys. A Amanda, per ser una cosina excel·lent i omplir-nos de bons records, i a la

resta dels Fornilles que fan de cada retrobament tota una experiència. A Isabel, per ser el major exponent de la família que es tria, perquè des de que vas entrar a les nostres vides, t'has convertit amb la tercera bessona, gràcies per acompanyar-nos en aquest viatge. A Adrián i Matías, que sent pols totalment oposats i tots dos uns personatges d'emmarcar, són els millors confidents des de la distància.

A Raquel, porque hay muy pocos amigos capaces de enseñarte el baile de la medusa y esperar siempre a que vuelvas, que lo que unió Silo y Hannover dure para siempre. A Sofie, porque nos enseñó a todos a ser un poco más griegos y que la inocencia no es solo cosa de niños. A mi estratosférica familia Balkañera en Viena, por muchos más bailes juntos chicos, takatá, takapúm. Gracias Dovi por hacer la cuarentena invisible y de Don Julios un lugar increíble, mi casa su casa, nos vemos pronto hermano.

Grazie Greca per aver condiviso questi anni di tesi, per aver creato supereroi quando ce n'era bisogno, e spingere sempre avanti. Di cuore, buona fortuna per le tue prossime avventure Pinguila.







## Abstract

In the past decades, metallic nanostructures were pursued for specific functionalities in diverse areas including light harvesting, photo-catalysis, drug delivery and sensing. These applications take advantage of the highly confined and enhanced electromagnetic field intensity occurring at their surface upon the resonant excitation of surface plasmons. Precise nanoscale control of the probing of specific sub-areas of such nanostructures by the confined surface plasmon field is the key in order to unlock their potential and translate this research to new viable technologies.

This thesis focuses on the development and implementation of new methods for the facile preparation of well-defined hybrid plasmonic materials, which are composed of gold nanoparticle arrays and hydrogels formed by responsive polymer networks. Such systems are prepared over large surface areas to serve as a transducer that allows for sensitive surface plasmon-enabled or surface plasmon-enhanced optical readout of assays. They provide attractive properties such as tunability by externally applied stimulus to serve in novel sensing schemes in surface plasmon resonance (SPR), surface enhanced Raman spectroscopy (SERS) and plasmon enhanced fluorescence spectroscopy (SPFS).

Firstly, there was developed an approach for the preparation of well-ordered gold nanoparticle arrays on  $\text{cm}^2$  surface areas with highly tunable size and spacing. It relies on UV-laser interference lithography (UV-LIL) that is combined with dry etching and endows the patterning in a rapid and cost-efficient manner. The homogeneity of the prepared arrays as well as the performance of the metallic nanostructures to serve as substrates in SERS were investigated.

Secondly, a template stripping was pursued in order to embed gold nanoparticle arrays to a thin thermo-responsive hydrogel film. There were prepared tethered or free-standing hydrogel membranes carrying the gold nanoparticle arrays supporting lattice collective localized surface plasmons. The resonant excitation of these plasmonic modes display remarkably sharper resonances, lower losses and enhanced electromagnetic field intensity compared to regular localized surface plasmons. In addition, the plasmonic characteristics of this material can be reversibly actuated by temperature variations and solvent exchange.

Thirdly, there was achieved local attachment of functional hydrogel materials that can serve as a three-dimensional binding matrix at the surface of gold nanoparticles. The nanoscale precision to align the hydrogel-based biointerface with the nanoparticle arrays

was achieved by using photo-crosslinkable polymers and UV-LIL with a phase mask configuration that generates a high contrast UV-interference pattern.

Fourthly, an immunoassay with plasmon-enhanced fluorescence readout was performed using such material with thermo-responsive hydrogel binding matrix. The collapsing of the hydrogel after the capture of target analyte was explored for additional amplification based on the compacting of captured analytes at a narrow sub-area where electromagnetic field is confined and that is also referred as to the plasmonic hotspot. For the local decoration of plasmonic hotspot, an alternative approach based on plasmon-enhanced two-photon cross-linking was also investigated by using anthraquinone-based crosslinkers.

Moreover, this thesis comprises additional collaborative projects including the characterization of bicyclic RGD peptides with superior selectivity and specificity for  $\alpha v \beta 3$  and  $\alpha 5 \beta 1$  integrin, and SPR and SERS study of affinity binding of analytes in plasmonic nanohole arrays with flow-through configuration and actuated sensor response.

## Zusammenfassung

In den letzten Jahrzehnten wurden in vielfältigen Bereichen wie Light Harvesting, Photokatalyse, Drug Delivery und auch in der Sensorik metallische Nanostrukturen für spezifische Anwendungen entwickelt. Diese nutzen stark lokalisierte und verstärkte elektromagnetischen Felder, die bei der resonanten Anregung von Plasmonen an der Oberfläche auftreten. Präzise Kontrolle der Anregung auf der Nanoebene ist der Schlüssel, um das Potential dieser Forschung zu entfalten und in neue nutzbare Technologien umzuwandeln.

Diese Arbeit konzentriert sich auf die Entwicklung und Umsetzung neuer Methoden für die einfache Herstellung von plasmonischen Hybridmaterialien aus Goldnanopartikelarrays und Hydrogelen aus responsiven Polymernetzwerken. Solche Systeme, großflächig auf der Oberfläche aufgetragen, dienen als Transducer, um Assays plasmonisch verstärkt optisch auszulesen. Die Möglichkeit der Veränderung der Eigenschaften durch extern angelegte Stimuli machen es möglich, sie in neuartigen Sensorkonzepten für Oberflächenplasmonenresonanz (SPR), oberflächenverstärkter Raman-Spektroskopie (SERS) und plasmonenverstärkter Fluoreszenzspektroskopie einzusetzen (SPFS).

Zuerst wurde ein Protokoll für die Herstellung geordneter Goldnanopartikelarrays auf cm<sup>2</sup>-großen Oberflächen mit definierter Größe und Periode entwickelt. Dabei wurde UV-Laser-Interferenzlithographie (UV-LIL) mit einer Trockenätztechnik kombiniert und somit eine schnelle und kostengünstige Strukturierung der Oberfläche ermöglicht. Die Homogenität der hergestellten Arrays, sowie die Performance der metallischen Nanostrukturen als Substrate in SERS wurden untersucht.

Zweitens wurde Template-Stripping verwendet, um Goldnanopartikelarrays in einen dünnen thermo-responsiven Hydrogelfilm einzubetten. Es wurden an die Oberfläche gebundene oder freistehende Hydrogelmembranen mit Goldnanopartikelarrays entwickelt, die kollektiv lokalisierte Oberflächenplasmonen anregen. Die resonante Anregung dieser plasmonischen Modi ergibt im Vergleich zu regulären lokalisierten Oberflächenplasmonen viel schärfere Resonanzen, geringere Verluste und eine erhöhte elektromagnetische Feldstärke. Darüber hinaus können die plasmonischen Eigenschaften dieses Materials durch Temperaturänderungen und Lösungsmittelaustausch reversibel aktiviert werden.

Drittens wurden funktionelle Hydrogele lokal angebunden, um als dreidimensionale Bindungsmatrix an der Oberfläche von Goldnanopartikeln zu dienen. Die Ausrichtung auf der Nanoebene der hydrogelbasierten Fläche mit den Nanopartikelarrays wurde

durch die Verwendung von photovernetzbaeren Polymeren und UV-LIL mit einer Phasenmaskenkonfiguration erreicht, die ein kontrastreiches UV-Interferenzmuster erzeugt.

Viertens wurde ein Immunoassay mit plasmonverstärkter Fluoreszenz-Auslesung mit thermo-responsiver Hydrogelbindungsmatrix durchgeführt. Für das starke Amplifizieren des Signals wurde hierbei das Hydrogel nach dem Binden des Analyten thermisch kollabiert. Dadurch wurde der Analyt in einen Bereich transportiert, in dem das elektromagnetische Feld lokalisiert ist, auch als ‚plasmonischer Hotspot‘ bezeichnet. Weiters wurde für diese lokale Bindung an den plasmonischen Hotspot auch ein alternativer Ansatz untersucht, der plasmonenverstärkte Zwei-Photonen-Vernetzung mit einem Crosslinker auf Anthrachinon-Basis verwendet.

Darüber hinaus umfasst diese Arbeit weitere Kooperationsprojekte, wie die Charakterisierung von bicyclischen RGD-Peptiden mit hoher Selektivität und Spezifität für  $\alpha\beta3$  und  $\alpha5\beta1$  integrin sowie eine SPR- und SERS-Studie zur Affinitätsbindung von Analyten in plasmonischen Nanoholearrays mit Durchflusskonfiguration und angesteuerter Sensorantwort.

## Publications

This thesis is based on the following book chapter and scientific studies marked in bold [1-8]:

### Book chapter:

[1] **Gisbert Quilis, N.**; Sharma, N.; Fossati, S.; Knoll, W.; Dostalek, J., Responsive Polymer Networks and Brushes for Active Plasmonics. *Polymer and Biopolymer Brushes: for Materials Science and Biotechnology 2 Volume Set* **2017**, 687-707.

### Publications:

[2] **Gisbert Quilis, N.**; Lequeux, M.; Venugopalan, P.; Khan, I.; Knoll, W.; Boujday, S.; de La Chapelle, M. L.; Dostalek, J., Tunable laser interference lithography preparation of plasmonic nanoparticle arrays tailored for SERS. *Nanoscale* **2018**, 10 (21), 10268-10276.

Author contributions: NGQ developed the concept, performed the experiments and analyzed the data regarding the preparation and characterization of gold nanoparticle arrays. PV conducted the FDTD numerical simulations. ML acquired the SERS spectra. JD supervised the project. NGQ and JD wrote the manuscript. All authors commented and discussed the final manuscript.

[3] **Gisbert Quilis, N.**; van Dongen, M.; Venugopalan, P.; Kotlarek, D.; Petri, C.; Moreno Cencerrado, A.; Stanescu, S.; Toca Herrera, J. L.; Jonas, U.; Möller, M.; Mourran, A.; Dostalek, J., Actively Tunable Collective Localized Surface Plasmons by Responsive Hydrogel Membrane. *Advanced Optical Materials* **2019**, 7 (15), 1900342.

Author contributions: The design, preparation, characterization and implementation of the hybrid hydrogel membranes carrying gold nanoparticles was carried out by NGQ. MvD supported the preparation and stripping of free-standing membranes. DK supported the stripping process of the tethered membranes. PV conducted the FDTD numerical simulations. AMC performed the AFM experiments in water. CP synthesized the pNIPAAm-based hydrogel. JD supervised the project. NGQ and JD wrote the manuscript. All authors commented and discussed the final manuscript.

[4] **Gisbert Quilis, N.**; Hageneder, S.; Fossati, S.; Auer, S. K.; Venugopalan, P.; Bozdogan, A.; Petri, C.; Moreno-Cencerrado, A.; Toca-Herrera, J. L.; Jonas, U., UV-Laser Interference Lithography for Local Functionalization of Plasmonic Nanostructures

with Responsive Hydrogel. *The Journal of Physical Chemistry C* **2020**, 124 (5), 3297-3305.

Author contributions: The manuscript was written through contributions of all authors. The design, preparation and characterization of gold nanostructures exhibiting locally attached hydrogel polymeric networks was conducted by NGQ. SF built the optical set up for the fluorescent readout of assays. SH performed the SPFS-based assay and SA recorded the transmission spectra of the hybrid plasmonic system at varying temperatures. AMC performed the AFM experiments in water. JD supervised the project. NGQ and JD wrote the manuscript. All authors commented and discussed the final manuscript.

**[5] Gisbert Quilis, N.;** Vedaraman, S.; van Dongen, M.; Klees, S.; Weber, A.; Nishiguchi, A.; Toca-Herrera, J. L.; de Laporte, L.; Möller, M.; Murran, A.; Jonas, U.; Dostalek, J., Plasmon-enhanced two-photon crosslinking for local functionalization of metallic nanostructures. *In preparation*.

Author contributions: NGQ planned and conducted the experiments concerning the preparation and characterization of the nanostructures carrying the anthraquinone-based hydrogel. SV and AN supported the two-photon crosslinking experiments with the Nanoscribe. MvD supported the preparation and characterization of the samples. AW performed the AFM experiments and determined the Young's modulus. JD supervised the project. NGQ and JD wrote the manuscript.

**Other collaborative projects:**

**[6] Bernhagen, D.;** Jungbluth, V.; **Gisbert Quilis, N.;** Dostalek, J.; White, P. B.; Jalink, K.; Timmerman, P., Bicyclic RGD peptides with exquisite selectivity for the integrin  $\alpha\beta 3$  receptor using a “random design” approach. *ACS combinatorial science* **2019**, 21 (3), 198-206.

Author contributions: The manuscript was written through contributions of all authors. DB and PT conceived the concept and analyzed the data. DB performed peptide syntheses, competition and binding ELISA experiments, and in vitro integrin staining experiments. VJ, NGQ, and JD designed, performed, and analyzed the SPR experiments. PBW performed and analyzed the NMR experiments. DB, KJ and PT evaluated the confocal images. DB, PBW, and PT wrote the manuscript.

**[7] Bernhagen, D.;** Jungbluth, V.; **Gisbert Quilis, N.;** Dostalek, J.; White, P. B.; Jalink, K.; Timmerman, P., High-Affinity  $\alpha 5\beta 1$ -Integrin-Selective Bicyclic RGD Peptides Identified via Screening of Designed Random Libraries. *ACS combinatorial science* **2019**, 21 (8), 598-607.



Author contributions: The manuscript was written through contributions of all authors. DB and PT conceived the concept and analyzed the data. DB performed peptide syntheses, competition and binding ELISA experiments, and in vitro integrin staining experiments. VJ, NGQ, and JD designed, performed, and analyzed the SPR/SPFS experiments. PBW performed and analyzed the NMR experiments. DB, KJ, and PT analyzed the confocal images. DB, PBW, and PT wrote the manuscript.

[8] Kotlesek, D.; Fossati, S.; Venugopalan, P.; **Gisbert Quilis, N.**; Slabý, J.; Homola, J.; Lequeux, M.; Amiard, F.; de la Chapelle, M. L.; Jonas, U., Actuated plasmonic nanohole arrays for sensing and optical spectroscopy applications. *Nanoscale* 2020, 12 (17), 9756-9768.

Author contributions: DK conducted the experiments regarding the preparation and implementation of the nanohole arrays with hydrogel cushion. NGQ supported the development of the template stripping approach for the preparation of the plasmonic architecture. PV and SF performed the FDTD simulations. JS supported the acquisition of the reflectivity spectra. ML acquired the SERS spectra. DK and JD wrote the manuscript. All authors commented and discussed the final manuscript.

[9] Geiss, F.; Fossati, S.; Khan, I.; **Gisbert Quilis, N.**; Knoll, W.; Dostalek, J. In UV-SPR biosensor for biomolecular interaction studies, *Optical Sensors 2017*, International Society for Optics and Photonics: **2017**; p 1023107



---

## Contents

Acknowledgements	i
Abstract	v
Zusammenfassung	vii
Publications	ix
1 Introduction	5
1.1 Surface plasmon resonance	5
1.1.1 Propagating surface plasmons (PSPs)	6
1.1.2 Localized surface plasmons (LSPs)	8
1.2 Preparation of plasmonic nanostructures	10
1.3 Active / Adaptive Plasmonics	12
1.4 Plasmonic biosensors	14
1.4.1 Refractometric SPR-based biosensors	16
1.4.2 Plasmon-enhanced spectroscopy	19
1.5 Biointerfaces	22
1.5.1 Self-assembly monolayers (SAMs)	22
1.5.2 Polymer brushes (PB)	22
1.5.3 Hydrogel polymeric networks	24
1.5.4 Selective functionalization of plasmonic hotspots	26
2 Research aims	31
3 Results	34
3.1 Tunable laser interference lithography preparation of plasmonic nanoparticle arrays tailored for SERS	37
3.2 Actively tunable collective localized surface plasmons by responsive hydrogel membrane	51
3.3 UV-laser interference lithography for local functionalization of plasmonic nanostructures with responsive hydrogel	63

3.4	Plasmon-enhanced two-photon crosslinking for local functionalization of metallic nanostructures	77
3.5	Actuated plasmonic nanohole arrays for sensing and optical spectroscopy applications	87
3.6	Study of Integrin-selective bicyclic RGD-peptides	103
4	Summary and outlook	155
4.1	Summary	155
4.2	Future Outlook	156
	References	158
	List of Figures	167
	Abbreviations	169



# 1 Introduction







Light is behind many indispensable phenomena and plays a crucial role in our everyday life enabling us to produce, store and transfer energy, see the world and its colors, or take advantage of photosynthesis in plants, to name but a few examples. Light can be described in form of electromagnetic (EM) waves and optics is the research field that deals with its manipulation, generation, and detection. The work constituting this thesis relates to the research sub-field of optics that is referred to as plasmonics, which concerns the confinement and manipulation of light at the nanoscale by using metallic nanostructures. Such plasmonic materials allow to overcome the diffraction limit of conventional optics (e.g. dielectric lens) and capitalize on the surface plasmon resonance (SPR) phenomenon that originates from collective oscillations of charge density at metallic nanostructures. Development of plasmonic materials is rapidly progressing in several fields enabling tailored manipulation and control of EM radiation at deeply sub-wavelength scale<sup>1</sup> with capability to enhance weak spectroscopic signals<sup>2</sup>, track molecular interactions in real-time<sup>3</sup>, enhance yield in photocatalysis<sup>4</sup> and locally facilitate rapid heat generation<sup>5</sup>. These important key features offered by plasmonic nanostructures enabled the development of tighter miniaturized opto-electronic devices<sup>6</sup>,<sup>7</sup> and among others impact in important field of biomedical sciences<sup>8</sup>.

Current developments in the design of biomaterials and methods for their preparation and integration with plasmonic architectures have fostered new functionalities that find application in tissue engineering<sup>9</sup>, controlled drug delivery<sup>10, 11</sup>, sensing and coatings for medical devices<sup>12, 13</sup>. Physical and chemical properties of those materials can be engineered by carefully integrating functional groups and implemented with tailored surface chemistries<sup>14</sup>. Improved control of those interfaces is crucial in order to serve in biomedical applications where specific capture of target species and avoiding of non-specific interactions is of ultimate importance. Polymer networks forming hydrogels are important examples of biomaterials that can be modified with specific functional moieties that can also react to external stimuli such pH, temperature, light or electric current among others, which enables to trigger specific responses “on-demand” opening up a new range of possibilities for biomedical applications<sup>15</sup>.

## 1.1 Surface plasmon resonance

Surface plasmons (SPs) originate from the EM radiation coupled with collective density oscillations of conductive electrons at the interface between a dielectric and metal below its plasma frequency<sup>16</sup>. SPs can travel along the interface of flat or corrugated continuous metallic surfaces (propagating surface plasmons, PSPs) or be resonantly excited at

subwavelength-sized nanostructures (localized surface plasmons, LSPs) as shown in Figure 1.

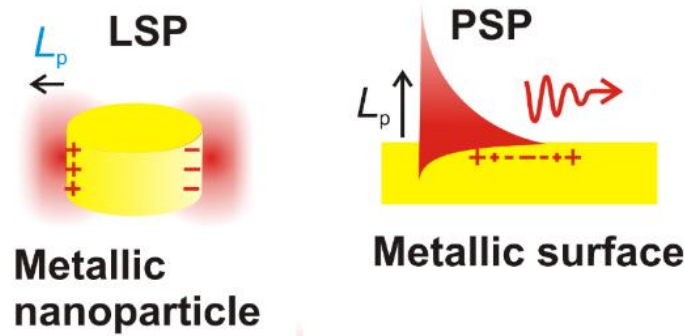


**Figure 1.** Schematic of localized and propagating surface plasmons with its typical penetration depth ( $L_p$ ). Image adapted from<sup>17</sup>.

### 1.1.1 Propagating surface plasmons (PSPs)

PSPs are evanescent waves with transverse magnetic (TM) polarization that travel along metallic surfaces and for a flat interface between semi-infinite metal and dielectric their complex propagation constant can be expressed as:

$$\beta = k_0 \sqrt{\frac{n_m^2 n_d^2}{n_m^2 + n_d^2}}, \quad (1.1)$$

Where  $n_m$  and  $n_d$  are the complex refractive indices of the metal and dielectric respectively, and  $k_0 = 2\pi/\lambda$  is the wave vector of light in vacuum. The evanescent field of PSPs exponentially decays perpendicular from the metal surface with a penetration depth  $L_p$ . It can be defined as a distance  $L_p = (\beta^2 - k_0^2 n_d^2)^{1/2}$ , to which the field amplitude drops by  $1/e$ . The probing depth of the SP field intensity is generally represented as the distance  $L_p/2$  and for example, for PSPs at a gold surface in contact with aqueous medium ( $n=1.33$ ), it is about 100 nm for the red part of spectrum ( $\lambda=633$  nm)<sup>18</sup>.

In order to transfer energy of EM radiation travelling in the far field to PSPs, their momentum and frequency needs to be matched. However, Figure 2 shows that this is not possible as such dependence of frequency on the momentum (referred as to dispersion relation) does not intersect with that of PSPs at a metal surface with the dielectric on its top. In order to fulfil this requirement, the momentum of EM radiation needs to be increased, which can be achieved by several schemes including using a high refractive index prism or by corrugating a metallic surface<sup>16</sup>.

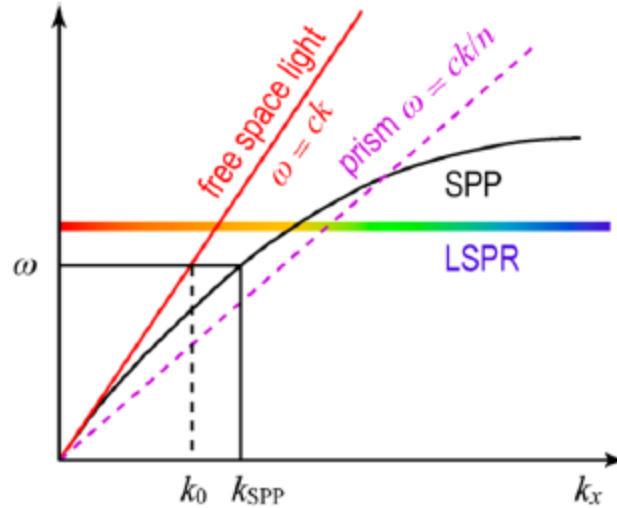


**Figure 2.** Dispersion relation of photons in free space (red), after coupling with a prism (violet) and that of PSPs (black). Image adapted from<sup>19</sup>.

Attenuated total internal reflection (ATR) can be employed to attain the additional momentum by using the prism. The Kretschmann configuration of the ATR is typically utilized so that a light beam is launched through a high refractive index prism ( $n_p$ ) with a thin metallic film at its base. An evanescent wave penetrating into the metallic film is generated when the angle of incidence ( $\theta$ ) is higher than the critical angle ( $\theta_c$ ) and thus the total internal reflection occurs. A fraction of the incident light is reflected back to the prism and the other part is coupled to PSPs at the outer interface with the lower refractive index dielectric ( $n_d$ ), as shown in Figure 3a. The SPR occurs when this coupling is strongest, which is observed when the parallel component of the propagation vector of the light beam matches the real part of the propagation constant of PSPs at the metal-dielectric interface<sup>20</sup>. As seen in Equation 1.2, either the incident angle with a fixed monochromatic light ( $\lambda$ ) or the wavelength of illumination at a fixed angle ( $\theta$ ) can be adjusted to excite PSPs:

$$Re\{\beta\} = \frac{2\pi}{\lambda} n_p \sin(\theta). \quad (1.2)$$

Another approach to excite PSPs is based on the employment of corrugated gratings with a given period ( $\Lambda$ ) as illustrated in Figure 3b. Optical waves incident with a given angle ( $\theta$ ) and perpendicular to the grating grooves can be phase-matched via diffraction under the conditions<sup>21</sup> expressed as follows:

$$\frac{2\pi}{\lambda} n_d \sin(\theta) \pm m \frac{\lambda}{\Lambda} = \pm Re\{\beta\}, \quad (1.3)$$

Where  $m$  is the integer diffraction order and  $Re\{\beta\}$  is the real part of the complex PSP propagation constant.

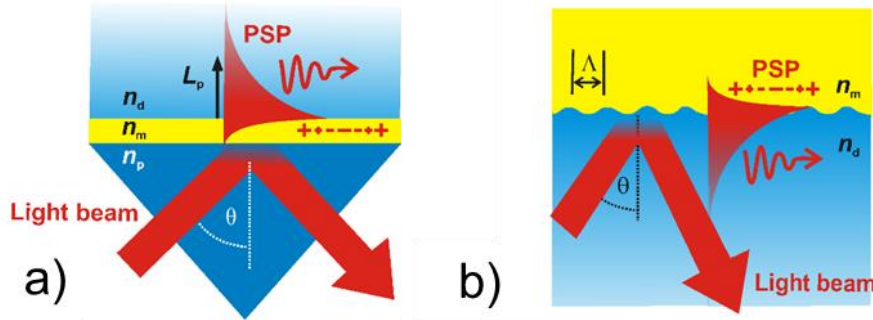


**Figure 3.** Schematics of the a) ATR and b) grating-coupled configuration supporting the excitation of PSPs. Image adapted from<sup>22</sup>.

The resonant excitation of PSPs at the dielectric interface is generally manifested as a dip in the reflectivity spectrum at a certain combination of wavelength and angle of incidence. Figure 4 shows how refractive index variations in the dielectric medium (with  $n_d$  at the interface with the metallic film) affect the resonant wavelength position of the PSPs according to the equations 1.2 and 1.3 for both configurations, employing gold as SPR-active material.

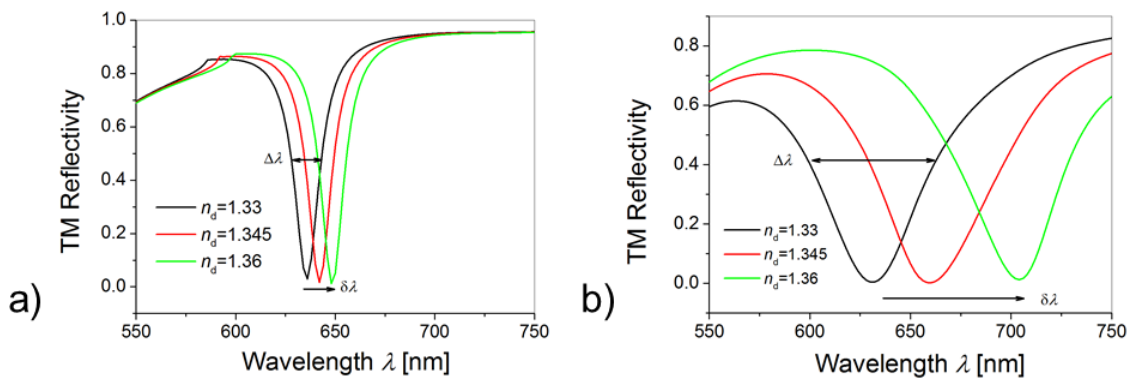


**Figure 4.** Refractive index sensitivity of PSPs with a) grating-coupled scheme ( $\Lambda=440$  nm, amplitude of 12.5 nm and  $\theta=0$  deg) and b) ATR configuration (50 nm thick gold layer,  $n_p=1.845$ ,  $\theta=51.7$  deg). Image adapted from<sup>22</sup>.

### 1.1.2 Localized surface plasmons (LSPs)

LSPs supported by metallic nanostructures can be directly excited with an incident light beam, which is manifested as an increase of the absorption and scattering at specific wavelengths. The localized surface plasmon resonance (LSPR) can be observed in metallic nanostructures with a characteristic size smaller than the incident wavelength employed for excitation. LSPs can be excited on individual metallic nanoparticles<sup>23</sup>,

dimers<sup>24</sup>, higher-order ensembles<sup>25</sup>, arrays<sup>26</sup>, structured surfaces such as nanoholes<sup>27</sup> or hierarchically-organized structures<sup>28</sup>. The LSPR is accompanied with tighter confinement of the EM field at the metallic nanoparticle surface<sup>29</sup> compared to the PSPs. The spectral position of the LSPR is highly dependent on the size, shape, spacing and material composition of the nanosized objects as well as the surrounding medium<sup>30, 31</sup>.

As shown in Figure 5a, similar to PSPs also LSPs are sensitive to refractive index variations of the dielectric  $n_d$  that surrounds the metallic nanoparticles. However, the spectral shift of the respective absorption band is about one order of magnitude lower compared to the variations in reflectivity dip associated with the excitation of PSPs counterparts<sup>32</sup>. Importantly, the probing depth  $L_p$  is considerably shorter than for the PSPs, typically in the range of ten of nanometers. Another approach that leads to strong variations in spectral position of the LSPR peak is to change the distance between closely arranged dimer particles or arrays (Figure 5b) that is ascribed to the near field-coupling at the junctions between particles<sup>33</sup>. In addition, other class of metallic nanostructures can also support both PSPs and LPs modes that are coupled. For instance, nanohole arrays displaying extraordinary optical transmission exhibit such phenomenon<sup>34</sup>.

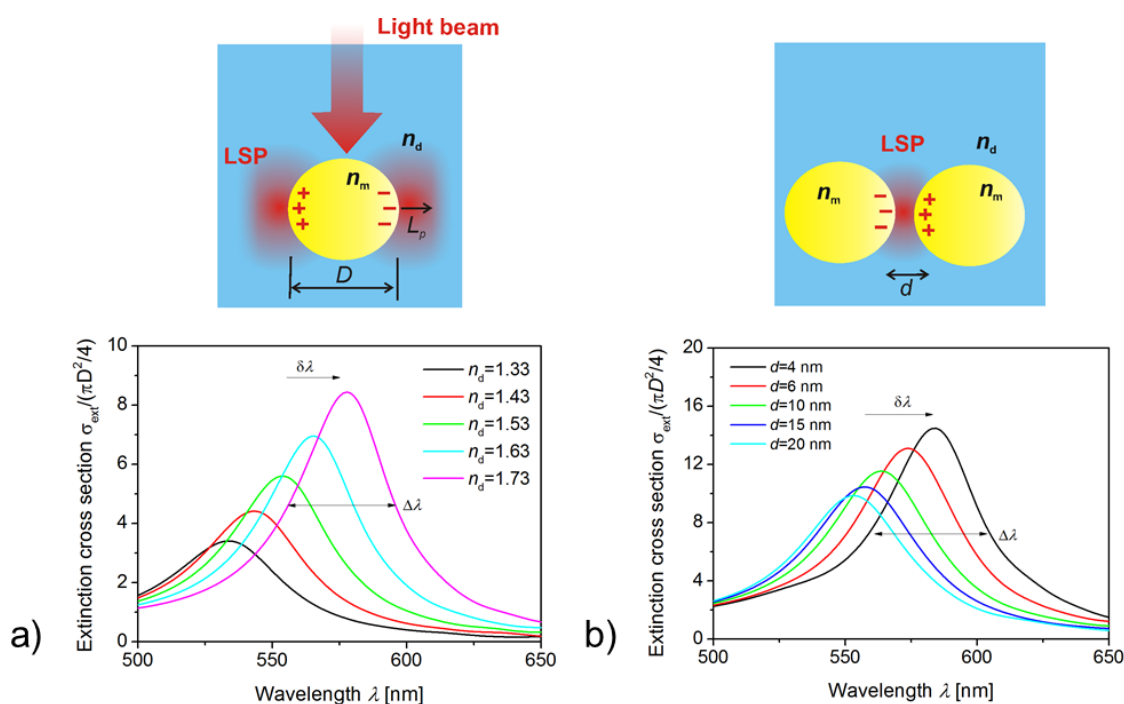


**Figure 5.** a) Shifts in the LSPR for individual spherical Au particles with diameter  $D=30$  nm by refractive index variations ( $n_d$ ) and b) spectral position variations due to gap distance changes between a closely arranged oblate nanoparticle dimer ( $D=40$  and  $30$  nm). Image adapted from<sup>22</sup>.

LSPR-based nanostructures can be prepared on solid surfaces with macroscopic areas by techniques that are evolving rapidly<sup>35, 36</sup>. The vast majority of reported structures use

gold or silver as plasmon-active material. However, nanostructures made of these materials suffer from strong non-radiative and radiative damping, exhibiting strong Ohmic losses at visible and near-infrared wavelengths, which inherently broadens the LSPR, limiting the performance of the engineered structures<sup>37</sup>. Aluminum can be used in the UV part of the spectrum as a plasmonic material with relatively low losses<sup>38, 39</sup>. Copper can also be a cheap alternative to gold, but it quickly oxidizes in air, which impedes its optical performance<sup>40</sup>. If properly designed, semiconductors (e.g. doped semiconductors) can also display a negative real part of permittivity in the near-infrared and infrared part of spectrum needed for the excitation PSPs and LSPs<sup>41</sup>. The broadening of the LSPR line-width can be greatly mitigated by employing periodically arranged particle arrays exhibiting a symmetric refractive index environment at the dielectric. This is accomplished by exploiting lattice collective localized plasmons (cLSPs) originating from diffraction coupling of LSPs on individual metallic nanoparticles<sup>42</sup>. The optical properties are changed when such lattice modes are excited, leading to spectrally sharper resonances associated with smaller optical losses<sup>43</sup>. These systems show similar characteristics as the architectures exploiting plasmonic Fano resonances, which are engineered to generate weakly damped plasmonic resonances by the use of constructive and destructive interference between discrete LSP modes with modes exhibiting a continuous dispersion<sup>44, 45</sup>.

## 1.2 Preparation of plasmonic nanostructures

The spectrum of nanofabrication techniques that can be used to prepare substrates with nanoscale features has expanded considerably in recent years<sup>46</sup>. A particular approach can be selected depending on the intended application, with some methods being more suitable for rapid and facile large-scale production and others more convenient to achieve precisely controlled configurations. Nanostructures can be grouped in several categories as outlined in Figure 6. 0D structures associated with systems like colloidal nanoparticles, 1D linked with architectures like nanoslits, 2D for geometries like nanohole or nanoparticle arrays bound to a substrate, quasi 3-D like nanopillar configurations and 3D structures as photonic crystals<sup>47</sup>.

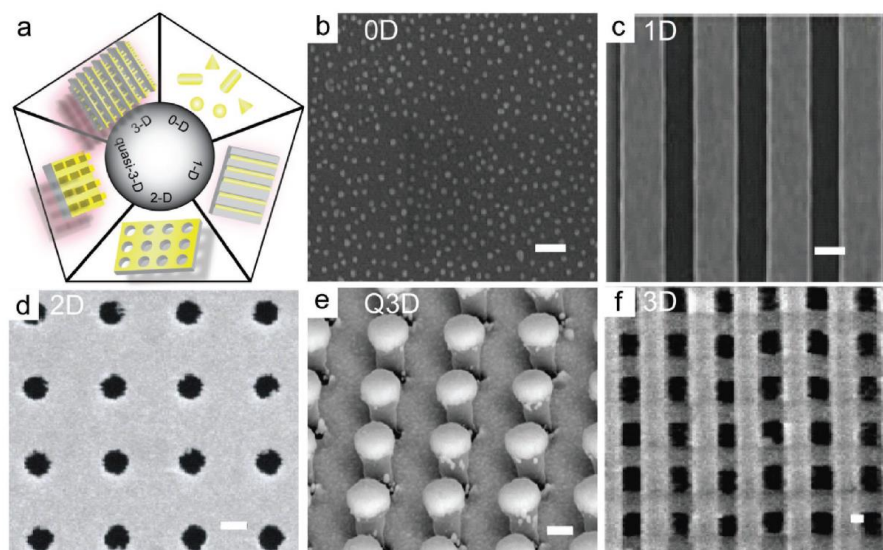


**Figure 6.** a) Schematic with different sorts of nanostructures classified with representative examples including scanning electron images of b) 0D systems, c) 1D systems, d) 2D architectures, e) Quasi 3D architectures and f) 3D architectures. Image adapted from<sup>47</sup>.

Methods for the wet synthesis of nanoparticles in solution have been extensively pursued and a plethora of protocols have been developed for the synthesis of nanoparticles with various shapes (e.g. stars, rods, cubes, and prisms)<sup>48-50</sup>. However, one of the main challenges of the chemical synthesis of such building blocks is the control over the process, often resulting in a random distribution of sizes. In addition, changes induced by pH and ionic strength may cause the precipitation of the nanoparticles. On the other hand, those methods are very cost-efficient and the prepared nanoparticles can be subsequently assembled in larger macroscopic structures via directed self-assembly<sup>51</sup>.

Physical nanofabrication methods such as electron-beam lithography (EBL) and focused ion beam lithography (FIB) are techniques able to create tailored plasmonic architectures with fine nanometric resolution<sup>52, 53</sup>. E-beam lithography relies on the deposition of an electron-sensitive material with subsequent scanning of an e-beam over the surface to write the intended structure. Depending whether a negative or positive tone resist is employed for the patterning, the exposed or the non-exposed regions with the e-beam remain or are washed away upon the developing step, respectively. The developed structures with well-defined geometries are employed either as a sacrificial layer or directly coated by evaporating a metallic layer. Focused ion beam can directly write the intended structure by directing a focused beam of ions onto the surface. Both approaches are not suitable for scaled up production due to high-cost and low patterning speed that limits their throughput.

Soft lithography techniques use often poly(dimethylsiloxane) (PDMS) stamps to repeatedly transfer the nanoscale features from a given surface to another one<sup>54</sup>. Nanoimprint lithography employs a curable material (UV-curable or thermoplastic) to generate the inverse motive pattern of the stamp<sup>55</sup>. The plasmonic architectures are attained by coating a thin metallic layer over the imprinted topology or use it as a mask for additional etching steps. The main drawback of such techniques is the requirement of a master for each engineered configuration, which is typically expensive.

Self-assembly to create templates at the nanoscale is a promising approach. Colloidal lithography or nanoscale lithography use monodisperse nanospheres that self-assemble forming a mask of closely arranged domains over a surface. Morphology, size and spacing can be adjusted by tuning chemical and physical parameters<sup>56</sup>. Wet etching or reactive ion etching can be then employed to transfer the pattern to the surface via the gaps between the spheres. The process is completed with the deposition of the chosen material, including multilayer-structures.

Block copolymer lithography takes advantage of the self-assembly of block copolymers over a surface forming nanostructured domains (typically from 10 to 100 nm)<sup>57</sup>. Such nanopattern acts as the template or mask for generating the metallic features. The morphology of the features can be tuned to a certain extend by changing the process parameters, such as the relative volume fraction of each polymer and its molecular weight or the degree of polymerization<sup>58</sup>.

In laser interference lithography (LIL), there is recorded an interference pattern generated by two or more coherent optical beams to a photosensitive photoresist layer followed by its development. This method allows for the rapid preparation of 2D and 3D metallic nanostructures over macroscopic areas by coating the recorded features with a metallic layer combined for instance with a lift off process or by using additional dry etching steps<sup>59, 60</sup>.

### **1.3 Active / Adaptive Plasmonics**

The advances in nanofabrication technologies we witnessed in the past decades have paved the way for the preparation of nanostructures with almost arbitrary shape and size, allowing for precise control of their plasmonic properties. For some applications, such materials with fixed properties fulfill their task exhibiting durable and constant optical response, while for other applications there are needed other materials that can be on demand reconfigured. Important examples include plasmonic switches or modulators, which are required for photonic circuits, or integrated optical polarizers and active color filters<sup>61, 62</sup>. In addition, optical biosensing platforms can also take advantage of adaptive



plasmonic materials with actuated characteristics<sup>63-67</sup>. This new field is called active plasmonics and relates to the reversible switching or tuning of the optical response of noble metallic nanostructures and thin films, arising from the plasmonic coupling effect.

Several approaches have been pursued for reversible modulation of the SPR in metallic nanostructures. These mostly rely on changes in refractive index of the dielectric medium that surrounds the metallic nanostructure, which detunes the resonant coupling to SPs as previously discussed in section 1.1. Besides systems with tuneable refractive index, also the modulation of charge density in SPR active material and variation in distance between near field coupled metallic nanoparticles have been engineered to actively control the optical response as depicted in Figure 7 and have been extensively reviewed by Jiang et al.<sup>19</sup>.

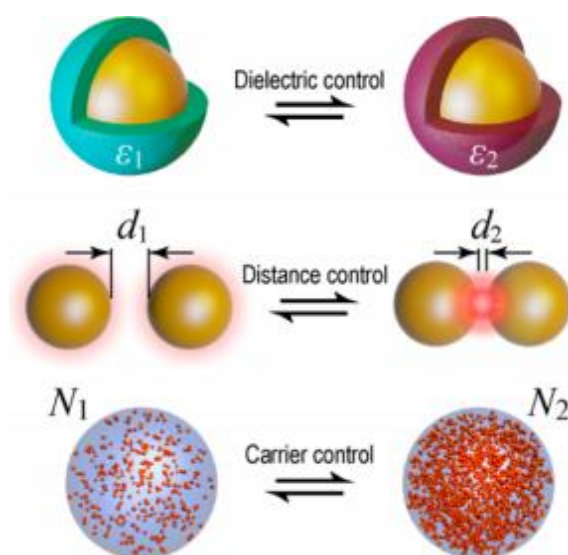


**Figure 7.** Three approaches to attain active plasmonic systems based on dielectric variations and tunable carriers or spacing. Image adapted from<sup>19</sup>.

In particular, the combination of plasmonic nanostructures with dielectric media exhibiting tuneable refractive index represents a facile approach due to the diversity and flexibility of such materials available and their ease of their preparation. The dielectric function of such adaptable plasmonic materials can be reversibly controlled by a broad range of external triggers (e.g. light, temperature, pH, shear stress and electric current)<sup>68</sup>. Organic photochromic molecules are promising candidates for all-optical control with fast switching speed under light irradiation<sup>69-70</sup>, but suffer from strong photo-bleaching and limited long-term stability. On the other hand, electrically controlled hybrid graphene-plasmonic nanostructures have shown to facilitate giant shifts in the NIR and MIR part of the spectrum<sup>71-72</sup>. Electrochemical switching by triggering reversible redox reactions with conductive polymers such polyaniline (PANI) and poly (3,4-ethylenedioxythiophene) (PEDOT) showed also remarkable switching performance. Such conductive polymers

are also responsive to pH variations offering the possibility to actuate the LSPR wavelength via the proton doping level with shifts of about 100 nm as shown in Figure 8<sup>73-75</sup>. An alternative approach to the mentioned materials is to replace them by their thermo-responsive counterparts. Stimuli-responsive polymer networks and brushes exhibit the unique capability to actuate the optical properties of plasmonic structures by inducing pronounced changes in the polymeric chains driven by e.g. temperature external stimuli.<sup>76-78</sup>

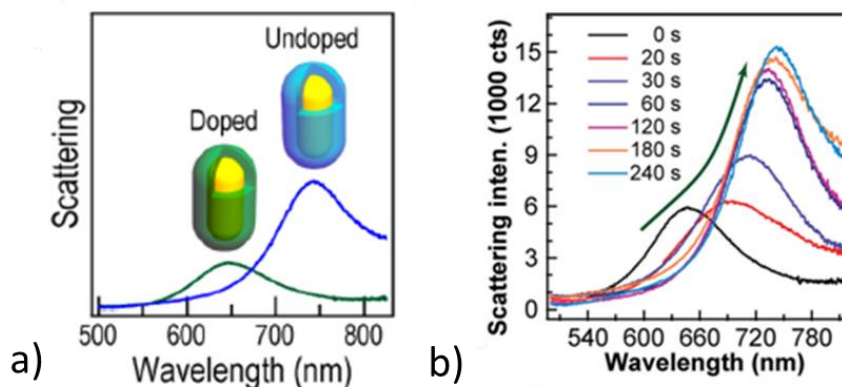


**Figure 8.** a) LSPR shift of Au nanorods capped with PANI polymer (thickness of 39 nm) between its doped and undoped state and b) its corresponding switching kinetics. Image adapted from<sup>75</sup>.

## 1.4 Plasmonic biosensors

Sensors accompany us in everyday life and we routinely use them in areas ranging from clinical diagnostic to industrial plants. Traditional methods for diagnosis based on detection species that serve as biomarkers or specific harmful cells include enzyme-linked immunoassays (ELISA) or cell cultures. However, these techniques can be operated only in specialized laboratories as they are often time consuming, require handling by highly trained personnel and rely on expensive equipment together with complex sample preparation before the test. In order to overcome these limitations biosensor technologies are pursued and we witness how they steadily revolutionize biomedical diagnostics with increasing market demand, which is expected to reach 27\$ billion by 2022 worldwide<sup>79, 80</sup>. The efforts are particularly devoted towards miniaturized sensing platforms that offer real-time, highly sensitive, specific, and multiplexed detection of chemical and biological species in a rapid and cost-effective manner. Point-of-care systems interfaced with mobile phone devices and wearable sensors are clear examples of technology that will impact personalized healthcare in the near future<sup>81, 82</sup>. Besides healthcare domain, other application fields include quality and safety control in the food industry, environmental monitoring, and homeland security<sup>83-85</sup>.

By definition, a biosensor is a device, which uses biorecognition elements attached to a physicochemical transduction system that translates the specific interaction with target analyte into a measurable signal, detecting the presence of a targeted chemical and biological entity. In general, a biosensor consists of three parts as depicted in Figure 9.

1. A biorecognition element (BRE) for specific interaction with a particular analyte. A broad spectrum of biorecognition elements is available to meet different specifications. Antibodies, peptides, aptamers, deoxyribonucleic acid (DNA) or ribonucleic acid (RNA), enzymes and cells are typically employed as capture elements in sensing platforms.
2. Physicochemical transducer, which converts the binding of target compounds into a thermometric, piezoelectric, electrochemical, magnetic or optical signal.
3. Signal output scheme that is responsible for the processing of the measured signal and generating the final sensor output.

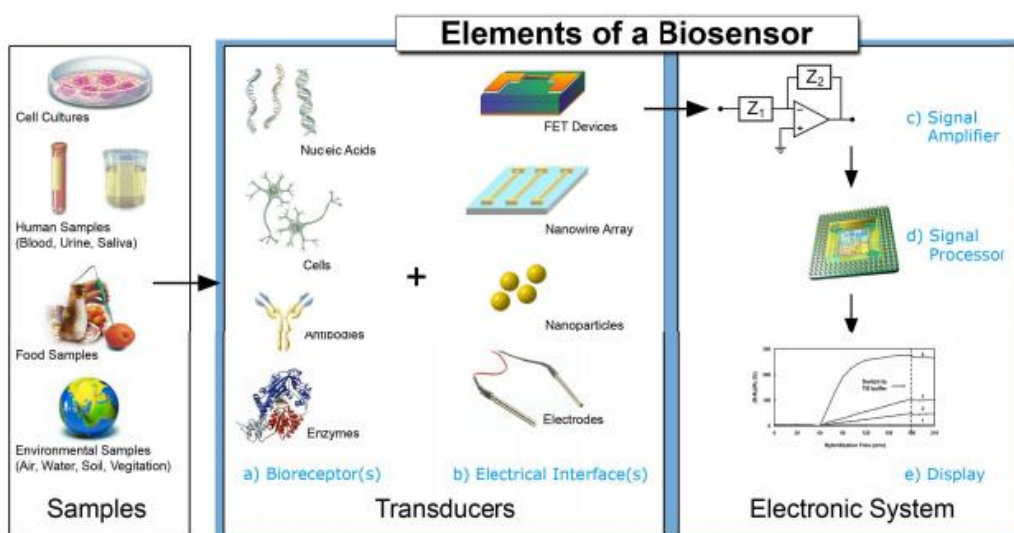


**Figure 9.** Components of a biosensor. Image adapted from<sup>86</sup>.

Depending of the intended application, a biosensor device should ideally provide a broad dynamic range with high sensitivity and selectivity for the particular compound of interest. Moreover, fast response, accuracy, reliability and long-term stability are key features together with the development of an easy-to-use device that is cost-efficient, robust and eventually miniaturized. Interferences originating from the matrix, where the species of interest are present, are often a major challenge in the implementation of biosensors. In order to minimize or avoid non-specific interaction with non-target analytes, surface chemistry strategies need to be implemented, which are dictated and tailored with respect to the specific sample to be analyzed. In this regard, anti-fouling polymer brushes and networks are emerging as excellent candidates<sup>87, 88</sup>. In addition, the development

of biosensors capable to perform early stage detection of biomarkers is of paramount importance in the field of medical diagnostics. Sensors with sufficient sensitivity can detect minute amounts of disease-related biomarkers, which allows for earlier treatment and therefore improved outcome for the patients suffering from illnesses such as cancer, especially before they present symptoms<sup>89</sup>. Therefore, great efforts are being made to engineer sensing technologies able to detect trace amounts of disease-specific molecular targets present in complex media (e.g. blood and saliva)<sup>90</sup>. Another milestone in sensing technologies is the continuous monitoring of arbitrary clinically relevant analytes and each application exhibits its own technical requirements<sup>91</sup>. Thus, advances in novel materials and sensing platforms highlight the opportunities to tackle these challenges related to the implementation of sensor systems in real clinical applications.

### 1.4.1 Refractometric SPR-based biosensors

Optical biosensors rely on the measurements of the properties of light that probe specific interactions of biorecognition elements with target analyte. Changes in spectral characteristics, interference, polarization, or decay time are exploited in common optical sensing platforms. The sensitivity of an optical biosensor is determined by the capability of the device to detect selected optical variations due to the interaction with target analyte. Label-free SPR-based sensors rely on the measurement of refractive index changes occurring at the sensor surface where specific capture of target analyte occurs. It can be monitored through the variations in the SPR spectral characteristics that is typically manifested as a reflectivity dip in wavelength or angular spectrum, see Figure 4 and 5. The refractive index increase on the sensor surface leads to a shift of this dip with a sensitivity defined as a ratio of the change in resonant wavelength ( $\lambda_{SPR}$ ) or coupling angle ( $\theta_{SPR}$ ), depending which one of the two modalities is utilized, and refractive index change ( $n_d$ ):

$$S_B = \frac{\delta\lambda_{SPR} \text{ (or } \delta\theta_{SPR})}{\Delta n_d} . \quad (1.4)$$

This enables the real-time detection of binding events from chemical and biological species when the surface is modified with specific BRE<sup>92</sup> such as antibodies, DNA, small peptides or aptamers. These biomolecules can be immobilized at the metallic sensor surface by using a plethora of established surface chemistries<sup>93, 94</sup> and SPR techniques have become an established technology for label-free studies of biomolecular interactions and rapid detection of chemical and biological species<sup>95, 96</sup>.

The accuracy with which the shift in SPR can be monitored is determined by the full width at half minimum / maximum (FWHM,  $\Delta\lambda$ ,  $\Delta\theta$ ) of the SPR dip / peak. Sharper resonances

with narrow linewidths allow for more precise resolving of the induced shifts and this is typically quantified by the figure of merit (FOM). It takes into account both sensitivity and FWHM and it is typically used to describe the performance of a given sensor.

$$FOM = \frac{S_B}{FWHM(\Delta\lambda, \Delta\theta)}. \quad (1.5)$$

The resolution of a refractometric biosensor is defined as the smallest RI change detectable from the baseline noise ( $\sigma$ ) and can be expressed as follows:

$$RI \text{ resolution} = \frac{\sigma}{S_B}. \quad (1.6)$$

The sensitivity of a plasmonic sensor to the capture of target analyte at their surface depends on several parameters, one of the most relevant being the probing depth  $L_p/2$ , which is linked to the type of SP mode used for the probing of the binding event. Higher bulk sensitivities (Equation 1.4) are typically attained with more delocalized modes such as PSPs. Typical  $S_B$  of SPR instruments based on PSPs are on the range of 1000-10000 nm/RIU and they allow for detection of surface coverage changes of captured biomolecules as small as 1 pg mm<sup>-2</sup><sup>97</sup>. In addition, a thin gold layer embedded between two dielectrics with symmetrical refractive index can support the excitation of long-range surface plasmons, which exhibit lower losses and higher penetration depths. Slavik et al. demonstrated a resolution of 57000 nm/RIU for such configuration<sup>98</sup>. Also, recently an hyperbolic metamaterial supporting plasmonic modes was developed yielding a sensitivity of 30000 nm/RIU<sup>99</sup>.

Bulk RI sensitivity for sensors exploiting LSPs on metallic nanostructures is lower than their PSP-based counterparts and typically reaches 100-600 nm/RIU in the visible and near-infrared part of the spectrum<sup>100, 101</sup>. It is worth of noting that higher RIU sensitivities are obtained for nanostructures resonant at longer wavelengths, independently of their shape<sup>102</sup>. For architectures that couple plasmonic modes via what is called plasmonic hybridization the bulk sensitivity can be significantly increased<sup>103</sup>. Veren et al. reported plasmonic architectures with a nanocross geometry supporting Fano resonances in the near-infrared part of the spectrum, displaying a bulk sensitivity larger than 1000 nm/RIU<sup>104</sup>. Shen et al. prepared gold mushrooms arrays displaying a sensitivity of 1010 nm/RIU with a limit of detection of 200 pM<sup>105</sup>.

However, for LSPR-based nanostructures, stronger localization of the LSP leads to shorter penetration depths  $L_p/2$  which compensates for the lower bulk refractive index sensitivity. In this case, the sensing performance can be rather evaluated in terms of surface sensitivity  $S_b$ , which offers a more accurate picture of the sensing capabilities than  $S_B$ . For plasmonic structures supporting coupled plasmonic modes a further

approach based on the second order surface sensitivity was recently proposed by Li et al. that evaluates the sensing performance more accurately<sup>106</sup>. As shown in Figure 10, the size of the biorecognition elements and target analyte can differ and for biomolecules with a size up to 10 nm LSPs typically offer suitable means for the probing with comparable penetration depth. For larger species such as lipid vesicles, viruses, or cells the probing with more delocalized PSPs may be more appropriate.

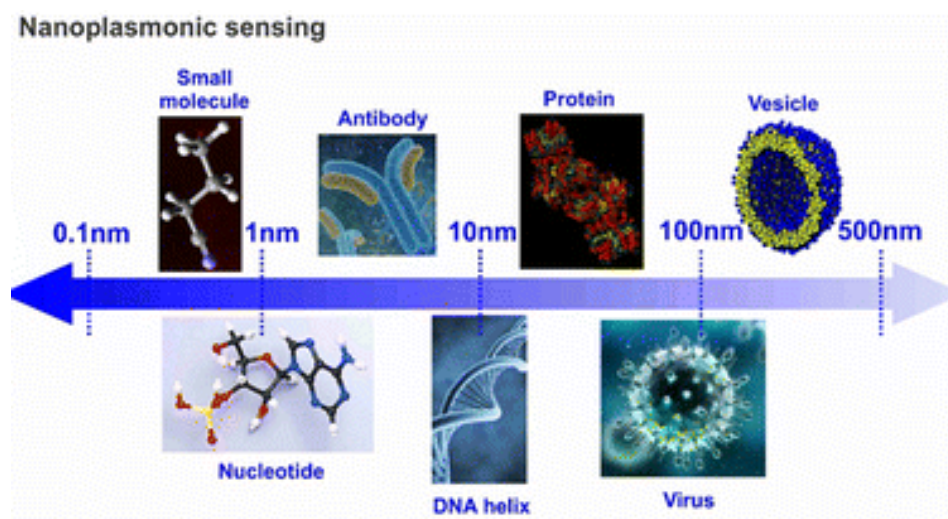


**Figure 10.** Size distribution of common ligand molecules and target analytes. Image adapted from<sup>107</sup>.

In addition, several strategies have been pursued in order to push the sensitivity of plasmonic biosensors with novel sensing schemes or advanced system configurations<sup>108</sup>. A straightforward approach to increase the limit of detection (LOD) is based on increasing the mass variations at the metallic surface by binding high molecular weight analytes in a multilayer system (e.g. sandwich assay). Detection of femtomolar analyte concentrations was attained by using, for instance, a sandwich immunoassays with a secondary antibody labeled with gold nanoparticles<sup>109</sup>. In order to enhance sensitivity on LSPR-based biosensors, the design of structures that display high EM field intensity is commonly pursued. This can be achieved, for instance, with nanoparticle dimers, with a strongly confined EM in the gap between particles<sup>110, 111</sup>. Other strategies involve the specific targeting of such areas where the EM is the strongest as the edges of nanostructures or gaps between closely arranged nanosized objects<sup>112</sup>. The latter approach is further discussed in detail in section 1.5.4 as it is one of the main focus of the presented work.

### 1.4.2 Plasmon-enhanced spectroscopy

Detection of low-molecular weight analytes present at minute concentration in analyzed samples remains a challenge for classical SPR-based biosensors due to small variations

of the refractive index changes occurring upon their capture at the metallic surface. In order to circumvent this limitation, other spectroscopic techniques taking advantage of the tight confinement and increased intensity of the EM field, provided by the resonant excitation SPs at the metallic surfaces, have been used. These mainly include surface-enhanced Raman spectroscopy (SERS), surface plasmon-enhanced fluorescence (SPFS) and surface-enhanced infrared spectroscopy (SEIRA)<sup>113, 114</sup>. In this work, mostly SERS and SPFS experiments have been conducted with plasmonic architectures and therefore these two methodologies are briefly described below.

#### 1.4.2.1 Surface plasmon-enhanced fluorescence spectroscopy (SPFS)

Fluorescence originates from spontaneous radiative emission of EM radiation in a quantum system that relaxes from its excited state to its ground state. Fluorescence is exploited in analytical technologies by using fluorophores and typical examples are quantum dots<sup>115, 116</sup> and organic dye molecules<sup>117</sup>. The excitation of such systems is attained by the irradiation with light at their absorption wavelength ( $\lambda_{\text{abs}}$ ) that is accompanied by the subsequent emission of light after relaxation, which occurs at longer wavelengths ( $\lambda_{\text{em}}$ ) due to the Stokes shift, see Figure 11.

Proteins, peptides or nucleic acids can be conjugated with fluorophores in order to use them as fluorescent labels for detection in assays, with a large number of coupling strategies available in order to suit the intended application<sup>118</sup>. A fluorophore with a reactive functional group is needed for the conjugation. Among the various options, fluorophores carrying a reactive N-Hydroxysuccinimide (NHS) group are commonly employed as it efficiently targets primary amines of the entity to be conjugated<sup>119</sup>. The labeled construct is utilized as detection probe in assays by excitation with light coincident at the wavelength of absorption of the fluorophore and measuring its emitted fluorescent signal. Direct or indirect schemes can be selected to fit the detection of the specific target analyte.

The coupling of such labeled proteins with the intense field of SPs provide means to greatly enhance the fluorescence intensity emitted from the vicinity of a metallic surface. There are several mechanisms that contribute to such surface plasmon-enhanced fluorescence phenomenon<sup>120, 121</sup>. The interaction of the fluorophores at their  $\lambda_{\text{abs}}$  and  $\lambda_{\text{em}}$  with the highly confined EM field at the SP modes modifies transitions between ground and excited states with additional paths as shown in Figure 11. By this means, enhancement of the excitation rate<sup>122, 123</sup>, modification of the quantum yield of the fluorophore, and faster radiative decay<sup>124, 125</sup> can occur and contribute to increased intensity of detected fluorescence light without enhancing the background. In addition,

fluorescence emission facilitated via SP modes allows for directional outcoupling from the metal surface at certain preferable angles, which offers means to collect it more efficiently compared to regular isotropic angular distribution<sup>126-128</sup>.

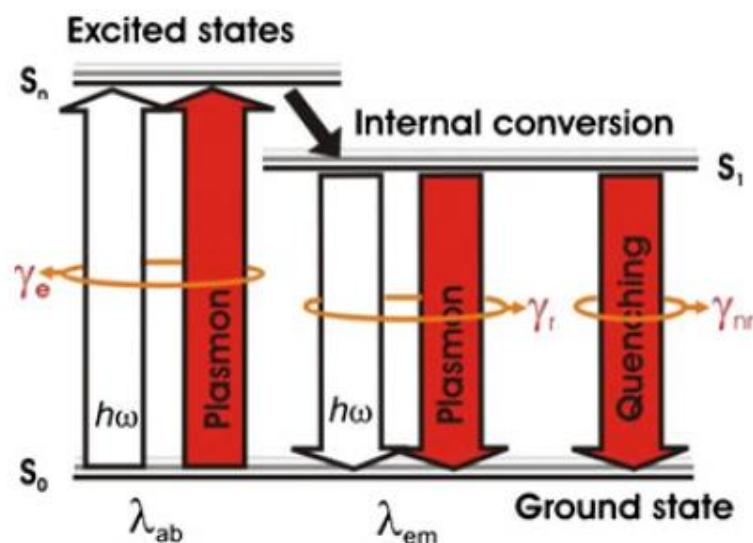


**Figure 11.** Schematic of the additional radiative paths for the excitation of fluorophores via surface plasmons. Image adapted from<sup>121</sup>.

Tabakman et al. reported a 100-fold fluorescence signal enhancement employing an antibody-labeled with a near infrared dye and a gold nanostructured film. In addition, the multiplexed capability was also assessed in a microarray format with LOD in the low femtomolar range<sup>129</sup>. Wang et al. also reported femtomolar sensitivity for fluorescence detection of free prostatespecific antigen (f-PSA) using a 3D high binding matrix exploiting the excitation of long-range surface plasmons modes<sup>130</sup>. An enhancement factor of 1000 was also demonstrated by Kinkhabwala et al. with closely arranged bowtie gold nanoantennas from an individual fluorophore with a low intrinsic quantum efficiency<sup>131</sup>. This technique can be also used to track and determine kinetic binding constants that are consistent with those measured with label-free SPR platforms as reported by Yu et al. for measuring DNA hybridization kinetics<sup>132</sup>.

#### 1.4.2.2 Surface-enhanced Raman spectroscopy (SERS)

Raman is the inelastic light scattering of photons due to excitation of molecular vibration modes with energy gain (anti-Stokes) or loss (Stokes) as given in Figure 12. The probability of the Raman process to occur is extremely low with an optical cross-section in the range of  $\sim 10^{-11}$ - $10^{-15}$  nm<sup>2</sup>, making the detection of Stokes-shifted Raman bands unpractical<sup>133</sup>. In combination with metallic surfaces exhibiting sub-wavelength features, this probability can be dramatically enhanced (reaching signal-enhancement values as large as  $10^{10}$ - $10^{15}$  in some cases) offering the possibility to detect analytes in trace



amounts down to the single molecule regime<sup>134, 135</sup>. This phenomenon is known as surface-enhanced Raman spectroscopy (SERS) originating fundamentally from two mechanisms, the strong near-field EM confinement at the metallic surface due to LSPs (main contribution  $\sim 10^{10-11}$ ), and a chemical contribution ( $\sim 10^3$ ) that originates from the capability of the molecules for transferring electrons to or from the metallic surface, typically generating a molecule-metal bond<sup>136</sup>.

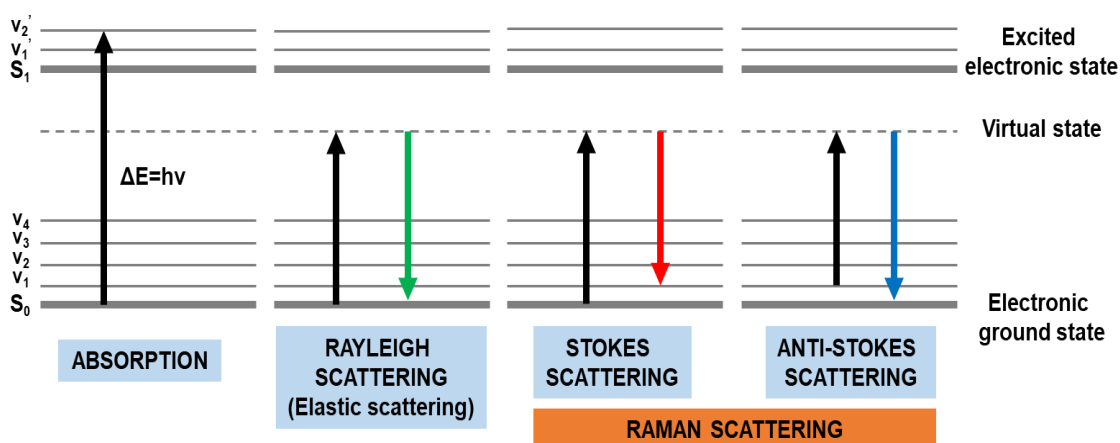


**Figure 12.** Schematic of the Raman scattering process with a Jablonski diagram.

Raman spectra contain the fingerprint of the analyte giving chemical structural information at molecular level, which has been for instance used to track DNA mutations<sup>137</sup>. In addition, SERS labels were developed for bioimaging in biomedical applications and specific coatings were applied to the nanostructures in order to use them for in vivo applications<sup>138</sup>. Moreover, SERS-immunoassays have also been developed for the detection of analytes with multiplexing capabilities<sup>139</sup>. Colloidal nanoparticles in solution synthesized by wet chemical methods<sup>140</sup>, 2D assemblies on solid supports<sup>141</sup> or 3D hierarchical structures have been extensively investigated as SERS tags as well<sup>142</sup>. Generation of hotspots with high EM field confinement is pursued with the design of nanostructures with sharp vertices and tips closely arranged in order to increase the confinement of the EM field and push down sensitivity<sup>143</sup>. Typically, the EM field intensity is the strongest as the gap distance decreases, in the range of a few nanometers. Matching the LSPR peak of the plasmonic architecture with the laser excitation wavelength plays also a crucial role to achieve strong SERS signal<sup>144</sup>.

## 1.5 Biointerfaces

Anchoring of BRE to the sensor surface requires robust linkage surface chemistries. Besides assuring sufficient surface density of the BREs tethered to the biosensor

surface, the used biointerface architecture should also preserve BRE biological activity and suppress non-specific adsorption of other non-targeted compounds that are present in the analyzed sample. To this end, mostly self-assembled monolayers (SAMs), polymer brushes (PB) and polymeric networks were adopted for the preparation of biointerfaces that (in part) fulfill the previous requirements. In addition, for LSP-based biosensors, the design of interfaces exploiting tailored surface chemistries that allow for selective attachment of BRE at specific locations (areas with strongly confined EM field) are particularly attractive to increase sensing performance and specific examples are described in section 1.5.4.

### 1.5.1 Self-assembly monolayers (SAMs)

SAMs spontaneously assemble onto a given surface (e.g. metals and oxides) forming a molecular ordered layer, which can be often deposited from a liquid or vapor phase and are composed of head (surface active) and tailored tail groups with alkyl chains as spacer between the two functional moieties<sup>145</sup>. SAMs offer a high degree of flexibility in their design and synthesis, representing an easy approach for the rapid functionalization of various surfaces with specific properties for a great number of technical applications such as coatings for biosensors and medical devices<sup>146</sup>. One representative example are organosilanes that form SAMs on hydroxylated surfaces (e.g. silicon oxide or glass) by formation of Si-O-Si bonds. Organosulfur materials such as n-alkyl sulfide and di-n-alkyl disulfides are very well known to form SAMs with metals like gold or silver, protecting the metal from oxidation<sup>147</sup>. Additionally, adsorption of fatty acids chains ( $C_nH_{2n+1}COOH$ ) to metal surfaces also occurs via the formation of a surface salt with the metal<sup>148</sup>. Schematic of the described SAMs is outlined in Figure 13.

Terminal functional moieties of the SAMs can be designed and introduced to obtain specific properties and enable post-modification with BRE. For biosensing purposes, mixed SAMs are commonly applied in order to prevent non-specific interactions at the surface and to control the surface density of immobilized BREs. Commonly, thiolates exhibiting poly (ethylene glycol) (PEG) or oligo(ethylene glycol) (OEG) as end groups are mixed with thiolates containing amino or carboxylate terminal moieties allowing for the post-modification with BRE via standard coupling strategies (typical ratios are 4:1 or 9:1)<sup>149, 150</sup>.

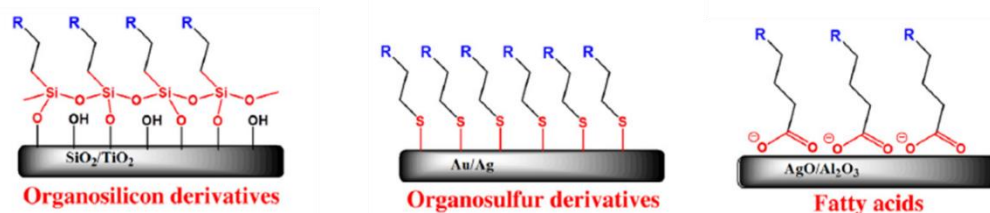


**Figure 13.** Schematic of common SAMs depicting material composition. Image adapted from<sup>151</sup>.

### 1.5.2 Polymer brushes (PB)

PB consist of polymer chains that are grafted onto a surface and can be covalently anchored to the surface by applying “grafting to” or grafting from” approaches. The first one relies on the direct attachment of polymer chains to the surface while the second method employs an initiator molecule enabling the subsequent growth of the polymer chain. The grafting density is an important parameter that represents the chain density per surface area. PB with low grafting density have a tendency to randomly coil (mushroom regime) while highly packed polymer chains are stretched perpendicular to the surface (brush regime), as illustrated in Figure 14, together with the chemical structure of commonly used polymer chains for the design of PB<sup>152</sup>.

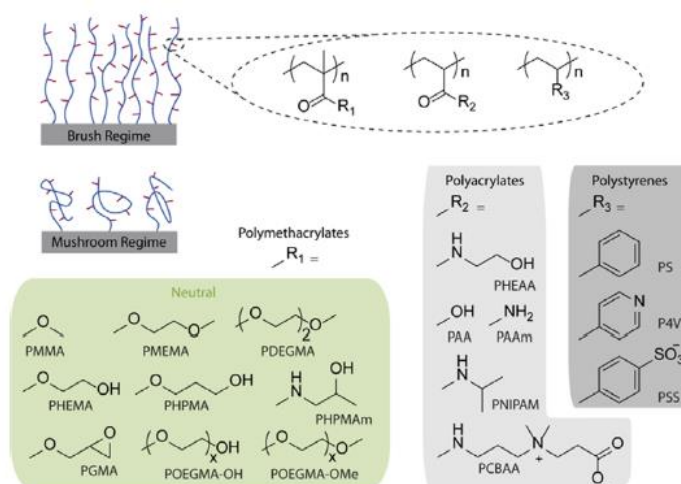


**Figure 14.** Schematic of PB regimes with chemical structures of typical polymer chain employed. Image adapted from<sup>152</sup>.

Protein fouling, especially from complex matrix such as blood, serum or milk can severely impair the performance of devices. Therefore, avoidance of non-specific adsorption of proteins at the functional surface plays a crucial role on practical applications and it is a major challenge for current systems. Non-fouling surfaces usually display high packing densities of polymer chains at the surface, which results in relative low binding capacity of BRE immobilized in such 2D biointerfaces. Huang et al. designed a hierarchical

structure composed of a first film with highly dense polymer brushes to avoid nonspecific interaction and a second layer with low surface packing density with high loading capacity. The architecture was produced by two different surface-initiated polymerization approaches as shown in Figure 15<sup>153</sup>.

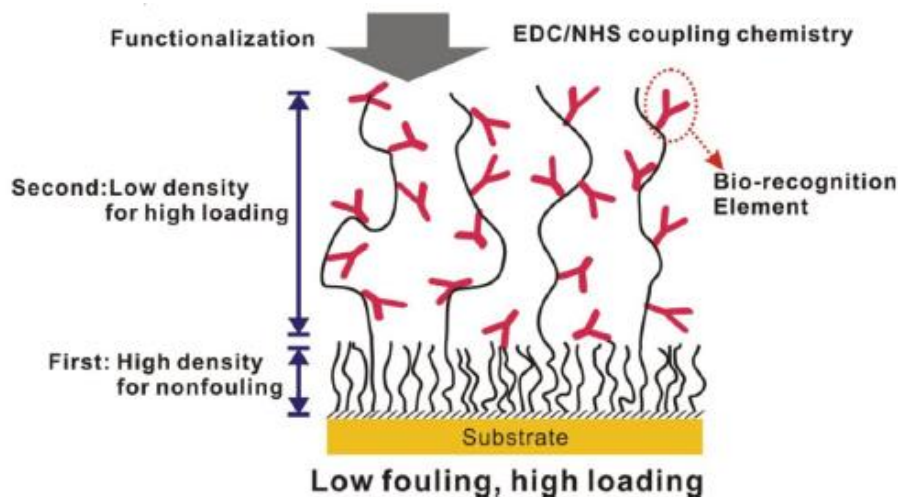


**Figure 15.** Schematic of the architecture combining both low and high density PB for attaining high loading capacity and nonfouling characteristics. Image adapted from<sup>153</sup>.

### 1.5.3 Hydrogel polymeric networks

Hydrogels are materials with a high content of water composed of an insoluble 3D network formed typically by natural or synthetic polymers. Such highly hydrophilic network mimics a biological environment offering high degree of compatibility with soft mechanical properties resembling that of living tissue, making hydrogels excellent biomaterials<sup>154</sup>. The crosslinking of polymer chains is generally attained via physical (e.g. hydrophobic, ionic interactions or hydrogen bonding) or chemical interactions between their specific segments (covalent bonding for instance by free radical polymerization)<sup>155</sup>. Properties of the hydrogel are strongly influenced by the crosslinking degree of the network. The swelling ratio of a cross-linked hydrogel system is defined as the change of thickness of the polymer upon immersion in a liquid compared to that in its collapsed or dry state. Structural parameters such as the polar groups inside the network or the cross-linking degree affect greatly the hydrophilicity of the film<sup>156</sup>. A highly cross-linked hydrogel networks results in a lower swelling degree and a higher number of ionic moieties largely increases the hydrophilicity<sup>157</sup>. The open 3D structure facilitates rapid diffusion of chemical and biological species and provides a higher loading capacity when modified with ligands compared to 2D configurations such as self-assembled monolayers.

In addition, hydrogel and PB can be designed to respond to stimulus when modified with appropriate functional moieties. These structures can be then actuated via pH, temperature, light or shear-stress among others, offering new functionalities in areas such as tissue engineering<sup>158</sup>, drug delivery<sup>159</sup> or biosensing<sup>160</sup>. Hydrogels can also be tethered to a surface in order to improve mechanical stability and handling for certain applications. The hydrogel polymer-backbone can be also modified with additional moieties that render the network non-fouling<sup>161</sup> or allow for the post-modification with biorecognition elements<sup>162</sup>.

### 1.5.3.1 Hydrogel optical waveguide spectroscopy

A hydrogel film anchored to a metallic surface can support additional waveguide modes when the thickness and refractive index of the film are adequately large. The propagation constant ( $\beta$ ) of the hydrogel waveguides (HW) can be obtained from the following dispersion relation:

$$\tan(kd_h) = \frac{\gamma_d n_h^2 / kn_d^2 + \gamma_m n_h^2 / kn_m^2}{1 - (\gamma_d n_h^2 / kn_d^2)(\gamma_m n_h^2 / kn_m^2)} \quad (1.7)$$

Where  $d_h$  is and  $n_h$  are the thickness and refractive index of the hydrogel, respectively and  $n_d$  is the refractive index of the dielectric (liquid) on the top of the hydrogel. Transverse propagation constants of the hydrogel, metal and dielectric can be expressed as ( $k^2 = k_0^2 n_h^2 - \beta^2$ ),  $\gamma_m^2 = \beta^2 - k_0^2 n_m^2$  and  $\gamma_d^2 = \beta^2 - k_0^2 n_d^2$ , respectively.

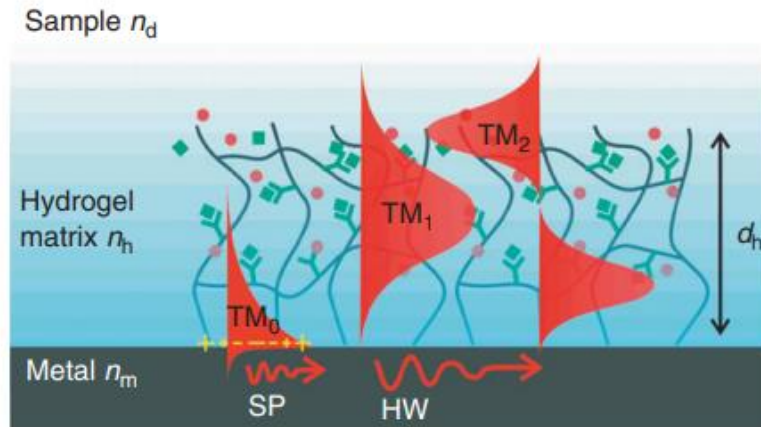


**Figure 16.** Schematic of SPs and higher HW modes inside a hydrogel film. Image adapted from<sup>18</sup>.

The excitation of SPs and hydrogel optical waveguide modes can be conducted by the phase matching approach using the Kretschmann configuration previously described (section 1.1). This resonant excitation with an incident monochromatic light is manifested as resonant dips in the reflectivity spectrum  $R(\theta)$  at certain angles. Both transverse magnetic (TM) and transverse electric (TE) modes can lead to the excitation of waveguide modes as shown in Figure 16. This technique enables the real-time tracking

of changes of the hydrogel such as density, thickness and refractive index variations. Those parameters can be determined by fitting the data with a transfer matrix-based model as previously reported<sup>162</sup>. This is an important tool because in contrast to the SPR technique, hydrogel optical waveguide spectroscopy (HOWS) can discriminate the changes in the thickness and refractive index of the hydrogel film independently in order to accurately determine both the parameters. An example is shown in Figure 17, where Toma et al. reported the swelling ratio and refractive index variations of pNIPAAm-based hydrogel films with temperature. The thickness and refractive index were calculated by fitting the measured spectra in Figure 17a and summarized in Figure 17b.<sup>163</sup> Zhang et al. also used the pNIPAAm based network as a biosensing platform for detecting 17 $\beta$ -estradiol using the same principle<sup>164</sup>.

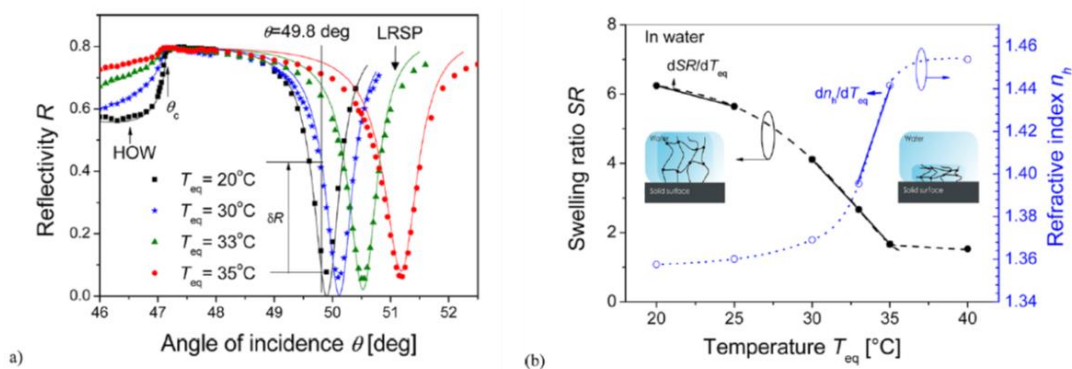


**Figure 17.** a) Reflectivity spectra obtained via SPR-HOWS measurements of a pNIPAAm thin film at different temperatures. b) Swelling ratio and refractive index as function of temperature. Image adapted from<sup>163</sup>.

#### 1.5.4 Selective functionalization of plasmonic hotspots

In the past years, several surface modification chemistry strategies have been developed to attain local functionalization of EM hotspots on metallic nanostructures supporting LSPs<sup>165</sup>. This approach capitalizes on the selective attachment of ligands only at the plasmonic hotspots, which are the areas where the EM field is the strongest (e.g. edges, sharp tips, or gaps between closely arranged objects) exhibiting therefore highest sensitivity for detecting molecular binding events. For instance, Feuz et al. demonstrated this concept by selectively functionalizing the inner wall of short-range ordered gold nano-hole arrays as depicted in Figure 18.  $\text{TiO}_2$  was deposited to cover exposed areas of the perforated film leaving the inner walls of the holes available for specific Au functionalization with thiol-based surface chemistry ( $\text{TiO}_2/\text{Au}/\text{TiO}_2$ ). An increased response kinetics due to the neutravidin binding to biotin was achieved, which was about 20 times higher compared to the samples with binding events happening across the

entire  $\text{TiO}_2/\text{Au}$  layer surface or only across the  $\text{TiO}_2$  active surface<sup>166</sup>. In addition, Zhang et al. directed the binding to the gap between two closely-arranged gold particles by depositing a 10 nm-thick Ti disk at the gap, achieving a 6 times higher shift of the LSPR position in the scattering spectra<sup>167</sup>. Recently, a method to attain partial passivation of gold nanocrescent nanostructures leaving only the tips exposed for further functionalization was also reported<sup>168</sup>. Another interesting approach reported by Beeram et al. relies on the thiol-exchange mediated chemistry at the edges of asymmetric crystalline gold nanoparticles resulting in 500 times increase detection of IgG antibodies to bound anti-IgG<sup>169</sup>. Light-triggered photochemical reactions represent another elegant strategy. The generation of hot electrons was reported to attain nano-localized chemistry<sup>170</sup>. Simoncelli et al. induced plasmon-induced desorption of thiols mediated by hot electrons that selectively cleave Au-S bonds at specific areas to control self-assembly at the nanoscale<sup>171</sup>. Two-photon cleavage and three-photon assisted delivery at the hotspot have also been introduced<sup>172</sup>.

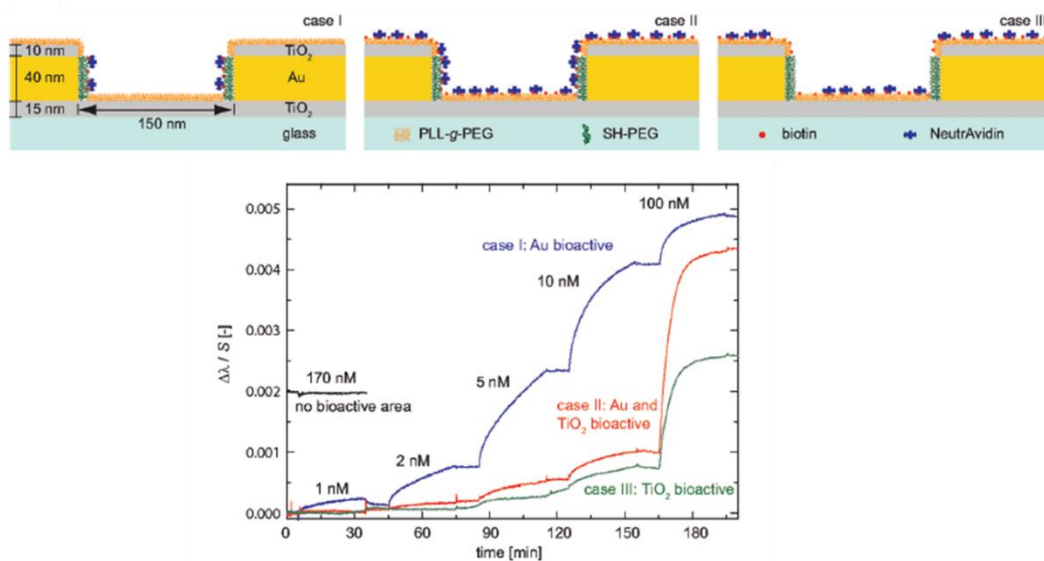


**Figure 18.** Schematic of the three studied surface chemistries and its associated binding kinetics for case I (Au targeted binding, blue), case II ( $\text{TiO}_2/\text{Au}$  active area, red) and case III ( $\text{TiO}_2$ -directed binding, green). Image adapted from<sup>166</sup>.

# 2 Research aims







Currently, we witness a lack of facile methods for the preparation of metallic nanostructured materials with precisely controlled morphology that can be actively on demand and adapted for a specific purpose. In addition, the interface of metallic nanostructures requires precise chemical modification, particularly for sensing applications, in order to selectively dock target species at narrow zones where the electromagnetic field coupled to localized surface plasmons is confined (referred as to plasmonic hotspots) and where they can be optically probed with maximum efficiency. Local functionalization of those narrow areas is challenging, and only a reduced number of approaches have been proposed and demonstrated to partially achieve this goal. Thus, the combination of facile, cost-efficient preparation of metallic nanostructures over large surface areas with the possibility to actively control their characteristics and tailor their surface modification with nanoscale precision would fully unleash the potential of plasmonic nanomaterials and boost up their applications in areas of analytical technologies based on optical spectroscopy. Among other approaches, the use of “smart” materials that are responsive to external stimuli represent an attractive approach to modulate optical response of plasmonic nanomaterials. This thesis concerns the utilization of responsive polymer networks for actuating of localized surface plasmon resonance on metallic nanostructures by refractive index changes and modulated near field coupling. In addition, optical methods for the spatially-controlled attachment of responsive polymers that form hydrogels and can serve as an efficient large binding capacity matrix are pursued. Developed materials are of particular interest for sensor schemes relying on SPR, PEF, and SERS for sensitive detection of biomolecules. The thesis is further organized in six chapters as follows:

In chapter 3.1, a method developed for the preparation of gold nanoparticle arrays with controlled morphology and spacing is presented. It relies on laser interference lithography combined with a dry etching approach. These structures constitute the building blocks for the following projects in the thesis, allowing for the preparation of hybrid plasmonic architectures and can also serve as SERS substrates.

In chapter 3.2, a new approach to actuate gold nanoparticle arrays by their embedding to tethered and free-standing thermo-responsive hydrogel membranes is discussed. They are prepared using a template stripping method and the excitation of collective localized plasmon modes with sharp resonances and low losses is presented. The reversible actuation of the LSPR is also demonstrated.

In chapter 3.3, a lithography approach based on the local attachment of responsive polymer networks in the vicinity of gold nanoparticles using a high contrast UV-

interference lithography is reported. The performance of the hybrid plasmonic substrate is evaluated with plasmon-enhanced fluorescence readout of immunoassays.

In chapter 3.4, a plasmon-enhanced two photon crosslinking mechanism is investigated in order to selectively attach and crosslink polymer networks at the edges of gold nanoparticles where the plasmonic hotspot is located. The mechanical and optical properties are studied in order to prove that the locally attached polymer network forms a hydrogel that can swell and collapse.

In chapter 3.5, a collaborative project based on a nanohole array hybrid architecture coupled with gold nanoparticles is reported. It utilizes a thermo-responsive hydrogel to reversibly and rapidly actuate the structure and its possible utilization to probe molecular binding events by SPR and SERS is demonstrated.

In chapter 3.6, another collaborative project focusing on the characterization of affinity binding constants of bicycle RGD peptides with  $\alpha\beta_3$  and  $\alpha_5\beta_1$  integrins is presented. The study of molecular interactions is carried out measuring the binding kinetics of these low molecular weight peptides by SPFS.



# 3 Results



# 3.1

Tunable laser interference lithography  
preparation of plasmonic nanoparticle arrays  
tailored for SERS





Cite this: *Nanoscale*, 2018, **10**, 10268

## Tunable laser interference lithography preparation of plasmonic nanoparticle arrays tailored for SERS†

Nestor Gisbert Quilis,<sup>a</sup> Médéric Lequeux,<sup>b,c</sup> Priyamvada Venugopalan,<sup>a</sup> Imran Khan,<sup>a,d</sup> Wolfgang Knoll,<sup>a</sup> Souhir Boujday,<sup>b,c</sup> Marc Lamy de la Chapelle<sup>b,e</sup> and Jakub Dostalek<sup>b,\*a</sup>

The facile preparation of arrays of plasmonic nanoparticles over a square centimeter surface area is reported. The developed method relies on tailored laser interference lithography (LIL) that is combined with dry etching and it offers means for the rapid fabrication of periodic arrays of metallic nanostructures with well controlled morphology. Adjusting the parameters of the LIL process allows for the preparation of arrays of nanoparticles with a diameter below hundred nanometers independently of their lattice spacing. Gold nanoparticle arrays were precisely engineered to support localized surface plasmon resonance (LSPR) with different damping at desired wavelengths in the visible and near infrared part of the spectrum. The applicability of these substrates for surface enhanced Raman scattering is demonstrated where cost-effective, uniform and reproducible substrates are of paramount importance. The role of deviations in the spectral position and the width of the LSPR band affected by slight variations of plasmonic nanostructures is discussed.

Received 29th November 2017,  
Accepted 21st March 2018

DOI: 10.1039/c7nr08905h

rsc.li/nanoscale

## Introduction

Metallic nanostructures exhibiting localized surface plasmon resonance (LSPR) are attracting increasing attention in numerous fields that can benefit from their extraordinary optical properties. These particularly include research in nanophotonics<sup>1,2</sup> and their applications for light management in thin film devices,<sup>3,4</sup> amplified optical spectroscopy, and analytical technologies.<sup>5,6</sup> These nanostructures possess the capability to couple light energy to localized surface plasmons (LSPs), which originate from collective oscillations of electron density and associated electromagnetic field. The excitation of these modes leads to enhanced absorption, scattering and sub-wavelength confinement of light energy at narrow spectral

windows. These phenomena are accompanied by strongly increased electromagnetic field intensity, which is attractive for amplifying weak spectroscopic signals such as Raman scattering, fluorescence, and infrared absorption spectroscopy. Enhancement factors up to several orders of magnitudes were reported to open the door for the ultrasensitive detection of chemical and biological species.<sup>7,8</sup>

In the past decades, nanotechnology research took advantage of rapidly advancing fabrication methods with gradually improved precision and control in the preparation of nanostructured materials. Electron beam lithography and focused ion beam milling<sup>9–11</sup> positioned themselves as irreplaceable tools in the nanophotonics research domain and are routinely used for the fabrication of plasmonic nanostructures with tailored morphology. However, these techniques do not allow fully harnessing the potential of such materials in practical applications. The reasons are that they are not suitable for scaled up production due to their limited throughput, costly instrumentation and are capable of patterning only small areas. In order to overcome these drawbacks, other methods for nanoscale patterning that are simpler and cost-effective have been pursued. These include nanoimprint lithography, which offers the means for repeated replicating of nanoscale features by using a working stamp casted from a pre-fabricated master.<sup>12–14</sup> Other techniques were developed based on the self-assembly of building blocks forming nanoscale periodic

<sup>a</sup>Biosensor Technologies, AIT-Austrian Institute of Technology GmbH, Konrad-Lorenz-Strasse 24, 3430 Tulln, Austria. E-mail: jakub.dostalek@ait.ac.at

<sup>b</sup>Université Paris 13, Sorbonne Paris Cité, Laboratoire CSPBAT, CNRS, UMR 7244, 74 rue Marcel Cachin, 93017 Bobigny, France

<sup>c</sup>Sorbonne Université, CNRS, UMR 7197, Laboratoire de Réactivité de Surface, LRS, F75252 Paris, France

<sup>d</sup>AIT-Austrian Institute of Technology, Center for Energy, Photovoltaic Systems, Giefinggasse 2, A-1210 Vienna, Austria

<sup>e</sup>Institut des Molécules et Matériaux du Mans (IMMM - UMR CNRS 6283), Avenue Olivier Messiaen, 72085 Le Mans cedex 9, France

† Electronic supplementary information (ESI) available. See DOI: 10.1039/c7nr08905h



features that can be employed as a lithographic mask.<sup>15–17</sup> This approach was utilized in nanosphere lithography or block copolymer lithography for large area structuring; however, it lacks long range order and suffers from edge defects and lower homogeneity.<sup>18</sup> Chemically synthesized metallic nanoparticles can be assembled into tailored plasmonic nanostructures by using atomic force microscopy<sup>19</sup> or, for instance, end-to-end coupling of metallic nanorods was reported for the preparation of dimers with the use of selective local modification of end tips.<sup>20</sup> Interestingly, chemically synthesized gold nanoparticles were infiltrated into a three-dimensional network of polymer fibers to increase their surface density compared to two-dimensional architectures and to take advantage of their hydrophobic properties.<sup>21</sup> In addition, natural materials carrying hierarchical micro-nano-structures (*e.g.* rose petal, taro leaf and lotus leaf) were coated with metal and demonstrated to serve as low-cost SERS-active substrates with superhydrophobic properties enabling efficient enrichment of chemical and biological species to specific areas probed with intense electromagnetic field intensity.<sup>22,23</sup>

Laser interference lithography (LIL) represents an alternative method that is suitable for the preparation of periodic nanoscale features with controlled size and shape.<sup>24–26</sup> LIL techniques offer the advantage of mass production-compatible preparation<sup>27,28</sup> and represent an attractive means for (arguably) the simple and fast patterning of large areas of up to hundreds of square centimeters. LIL utilizes the recording of an interference field pattern into a photosensitive resist material<sup>29,30</sup> and in combination with lift-off or ion etching steps, it can be used for the preparation of arrays of metallic nanoparticles. For the lift-off approach, metallic nanoparticles are made by depositing a metal inside cavities formed in a photosensitive resist, which is subsequently removed by a solvent.<sup>31</sup> In this variant of the LIL approach, the size of metallic nanoparticles is controlled by the cavity diameter that is typically proportional to the period length.<sup>32–34</sup> The employment of a sacrificial layer is frequently required in order to facilitate the lift-off as it is often limited by the steepness of the cavity sidewalls.<sup>35,36</sup> The ion etching modality employs a nano-patterned resist that serves as a mask on the top of a metallic layer. This mask is transferred to the metal by a dry etching step, which attacks areas that are not protected by the resist material.<sup>37–40</sup> In both approaches, the tuning of LSPR on prepared arrays of metallic nanoparticles has been mainly achieved by changing the angle  $\theta$  between the interfering beams upon the recording of the mask. Then both the period and diameter of metallic nanoparticles are varied and thus not all geometrical combinations are accessible. In addition, lift-off-based LIL implementations are typically not suitable for the preparation of features with size below hundred nanometers unless very small periods of the arrays are prepared or complex systems such as extreme ultraviolet LIL with a beam emitted from a synchrotron are employed.<sup>41,42</sup>

Plasmonic nanostructures need to be carefully engineered to couple light at specific wavelength bands<sup>42,43</sup> for specific applications. This requires highly tunable nanofabrication

methods as plasmonic properties of arrays of metallic nanoparticles strongly depend on multiple parameters including particle size, shape, and inter-particle distance.<sup>43,44</sup> This paper reports on the LIL implementation that enables the highly versatile preparation of arrays of cylindrical metallic nanoparticles with independent control of their diameter and period. In addition, diameters below hundred nanometers can be achieved. The importance of such versatility is illustrated in an experiment where gold nanoparticle arrays that are resonant in the red and infrared part of the spectrum are tailored to serve as SERS substrates.

## Results and discussion

### Preparation of gold nanoparticle arrays over a large area

The LIL set-up employed in the reported experiments utilized a Lloyd's mirror configuration that is depicted in Fig. 1(a). The period of rectangular arrays of metallic nanoparticles  $\Lambda$  was controlled by the angle of two collimated interfering beams  $\theta$  hitting a photoresist layer. In order to prepare 2D arrays of metallic nanoparticles, the exposure was performed twice with the substrate rotated by 90° along the axis perpendicular to its surface. The period  $\Lambda$  decreases when increasing the angle  $\theta$  according to the formula  $\Lambda = \lambda/2 \sin(\theta)$ , where  $\lambda = 325$  nm is the wavelength of herein used coherent interfering beams. It is worth noting that the structured illuminated area depends on the length of the mirror  $L_M$  and in the reported setup it was about 2 cm. (Alternatively, another LIL configuration where the beam is split into two equal parts that are recombined over the resist surface can be used. Such a set-up allows for recording over a larger area but the configuration is more sensitive to fluctuations and more complex to align.<sup>26</sup>) The two exposures of interfering collimated beams form the pattern that is simulated in Fig. 1(b). For the used positive photoresist, the area exposed to high recording light intensity can be etched upon the subsequent development step. By controlling the development time  $t_{dev}$ , the photoresist layer can be fully removed from the exposed area to yield a mask in the form of periodic arrays of resist features. Optimized dose and dilution of the developer enable fine control over the process to create a homogeneous mask with arrays of cylindrically shaped photoresist objects. Afterwards, directional ion milling with argon ions is utilized in order to transfer these features to the gold layer that was deposited underneath the photoresist film. The regions that are not protected by the photoresist are etched away forming gold nanoparticles. The remaining photoresist on top of the gold nanoparticles is then removed with a gentle oxygen plasma treatment of the surface, resulting in regular gold nanoparticle arrays covering macroscopic areas. The fabrication process is briefly illustrated in Fig. 1c and an example of the prepared glass substrate with arrays of metallic nanoparticles is shown in Fig. 1d. An atomic force microscopy study (included in the ESI†) confirms that the oxygen plasma reduces the height of nanostructures by about 20 nm because of the removal of the residual photoresist mask. The height of



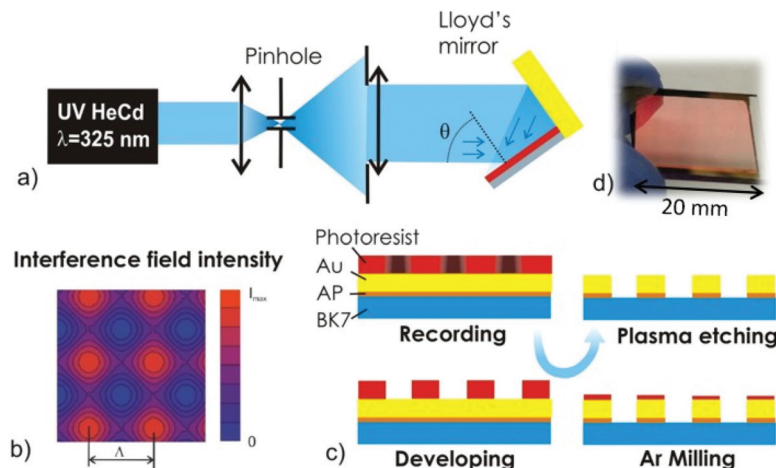


**Fig. 1** (a) Schematic of the Lloyd's mirror interferometer setup used for the LIL-based recording. (b) Simulations of the field intensity profile recorded for the photoresist. (c) Development of the photoresist and dry etching of Au NP arrays on a substrate with a thin adhesion promoter (AP). (d) Example of prepared gold nanoparticle arrays on a BK7 glass substrate with the size of  $20 \times 20 \text{ mm}^2$ .

metallic nanoparticles is 55–60 nm, which is slightly above the thickness of the deposited Au film due to the effect of weak etching into the glass substrate.

#### Tunability of the localized surface plasmon resonance

Gold nanoparticle arrays with a period between  $\lambda = 260 \text{ nm}$  and  $560 \text{ nm}$  were prepared by varying the interference angle  $\theta$  in the LIL recording step. In order to tune the diameter of nanoparticles  $D$ , the exposure dose was kept constant at  $6.75 \text{ mJ cm}^{-2}$  and the development time  $t_{\text{dev}}$  was varied. As illustrated in Fig. 2a, arrays of holes are prepared in the gold

film for the short development time  $t_{\text{dev}} = 95 \text{ s}$ . On increasing the development time to  $t_{\text{dev}} = 110 \text{ s}$ , arrays of rectangular-shaped, not connected nanoparticles are observed in Fig. 2b. Further prolonging the development time from  $t_{\text{dev}} = 165$  to  $220 \text{ s}$  yields arrays of cylindrical gold nanoparticles with diameters decreasing from  $D = 185$  to  $85 \text{ nm}$ , see Fig. 2c–e. The resonant coupling to LSPs supported by prepared gold nanoparticle arrays is manifested as a narrow dip in the transmission spectrum as shown in Fig. 2(f). The wavelength at which the minimum of the dip occurs ( $\lambda_{\text{LSPR}}$ ) shifts towards the near infrared (NIR) part of the spectrum when increasing

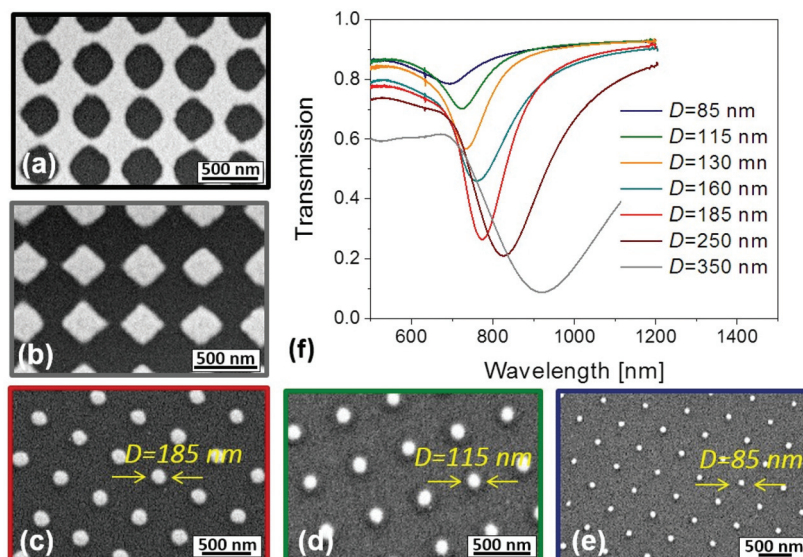


**Fig. 2** SEM images of metallic arrays with nanoscale features for varied development time  $t_{\text{dev}}$  and fixed period of  $\lambda = 460 \text{ nm}$ . (a) Nanohole arrays for  $t_{\text{dev}} = 95 \text{ s}$ ; (b) diamond-shaped nanoparticle arrays for  $t_{\text{dev}} = 110 \text{ s}$ , and arrays of cylindrical nanoparticles for (c)  $t_{\text{dev}} = 165 \text{ s}$ ,  $D = 185 \text{ nm}$ ; (d)  $t_{\text{dev}} = 195 \text{ s}$ ,  $D = 115 \text{ nm}$ ; (e)  $t_{\text{dev}} = 220 \text{ s}$ ,  $D = 85 \text{ nm}$ . (f) Transmission spectra measured for indicated gold disk diameters  $D$  and period  $\lambda = 460 \text{ nm}$  by collimated beam illuminating area of about  $0.5 \text{ mm}^2$ .



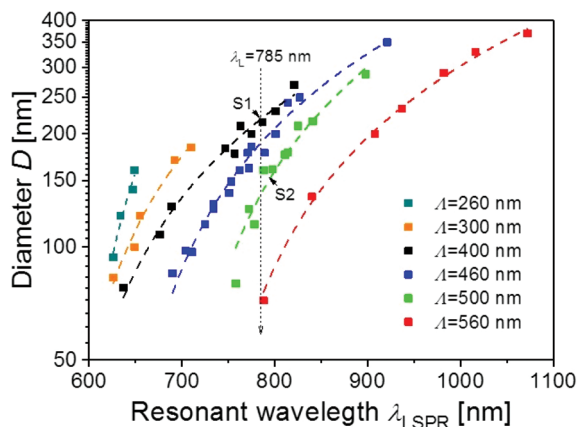


Fig. 3 Measured dependence of the resonant wavelength  $\lambda_{\text{LSPR}}$  on the diameter  $D$  and period between  $\Lambda$  of gold nanoparticle arrays in contact with air.

the diameter  $D$ . For example, LSPR can be tuned in the spectral window  $\lambda_{\text{LSPR}} = 700\text{--}900$  nm by changing the diameter from  $D = 85$  to  $350$  nm for the showed period of  $\Lambda = 460$  nm.

In general, the LSPR wavelength  $\lambda_{\text{LSPR}}$  on gold nanoparticle arrays is a function of both period  $\Lambda$  and diameter  $D$ . Its shift towards longer wavelengths by increasing the diameter  $D$  is more pronounced for longer periods  $\Lambda$ . This can be explained by diffraction coupling of LSPs for the interparticle distances that are in the wavelength range of the incident light.<sup>45</sup> The possibility of independent control of both period and diameter is demonstrated in Fig. 3. A series of samples with the period varied in the range of  $\Lambda = 260\text{--}560$  nm and diameter  $D = 70\text{--}350$  nm were prepared and transmission spectra were recorded. The analysis of these spectra confirms the tuning of the LSPR wavelength  $\lambda_{\text{LSPR}}$  between 620 and 1050 nm and reveals that identical  $\lambda_{\text{LSPR}}$  can occur for multiple combinations of  $\Lambda$  and  $D$ .

### Homogeneity of the prepared nanoparticle arrays

In order to characterize the spatial homogeneity of plasmonic properties of prepared nanostructures, we performed a mapping of the spectral position and width of LSPR bands on two substrates carrying gold nanoparticle arrays with  $\Lambda = 400$  nm and  $D = 215$  nm (S1) and  $\Lambda = 500$  nm and  $D = 165$  nm (S2). Fig. 4 shows an example of the LSPR transmission spectra acquired from a series of spots on the substrate S1 and from such a type of spectra, variations in the resonant wavelength  $\lambda_{\text{LSPR}}$  and the width of the full width in the half minimum  $\Delta\lambda_{\text{FWHM}}$  were determined.

Firstly, let us discuss the measurements performed by using a collimated beam that exhibits a diameter of about 1 mm and which was scanned over arrays of spots arranged on an area of  $1 \times 1$  cm<sup>2</sup>. The determined mean LSPR wavelength  $\lambda_{\text{LSPR}}$  and the width  $\Delta\lambda_{\text{FWHM}}$  are summarized in Table 1 for both substrates S1 and S2. The mean value and standard deviation of these parameters yield  $\lambda_{\text{LSPR}} = 782 \pm 4$  nm and

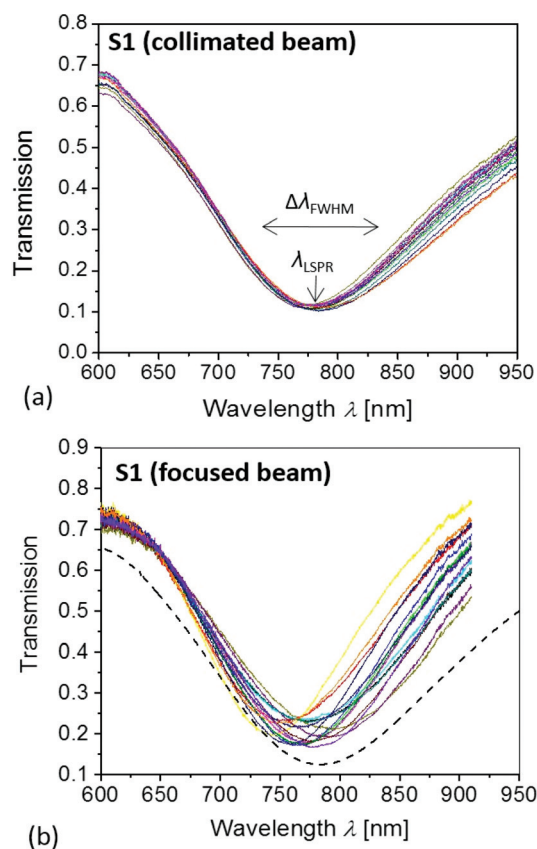


Fig. 4 Comparison of LSPR spectra measured on substrate S1 after functionalization with 4-mercaptobenzoic acid on (a) a series of spots with a large 1 mm diameter arranged over  $1 \times 1$  cm with collimated beam and (b) with focused beam diameter  $3 \mu\text{m}$  scanned over  $200 \times 200 \mu\text{m}$ . The dashed line in (b) shows the transmission spectrum measured with a large diameter beam on the same sample for comparison.

$\Delta\lambda_{\text{FWHM}} = 221 \pm 15$  nm for substrate S1. On the second substrate S2 with a longer period, an almost identical spectral position of  $\lambda_{\text{LSPR}} = 782 \pm 5$  nm and narrower resonance  $\Delta\lambda_{\text{FWHM}} = 106 \pm 2$  nm were observed (see the ESI†).

Afterwards, the transmission spectra were measured using a confocal microscope at a series of spots with a smaller diameter of about  $3 \mu\text{m}$ . Interestingly, for substrate S1 the spectral width of such LSPR spectra  $\Delta\lambda_{\text{FWHM}}$  was significantly lower and the variations in the spectral position  $\lambda_{\text{LSPR}}$  were more pronounced than for the data measured with a large diameter beam (compare examples presented in Fig. 4b and a). When probing this smaller area, the spectral position of  $\lambda_{\text{LSPR}} = 770 \pm 13$  nm and the resonance width of  $\lambda_{\text{FWHM}} = 172 \pm 12$  nm were determined. For substrate S2, similar variations in the spectral position of  $\lambda_{\text{LSPR}} = 787 \pm 7$  nm were measured; however, wider resonances  $\lambda_{\text{FWHM}} = 122 \pm 14$  were observed with a focused beam compared to a large diameter beam. This effect can be ascribed to the proximity of the diffraction edge, which is visible in the transmission spectra measured by a collimated large diameter beam and which becomes smeared by the



**Table 1** Specification of investigated substrates, values measured for a spot area of  $10 \mu\text{m}^2$  are stated and for  $1 \text{mm}^2$  are in the presented brackets

Substrate	$\lambda_{\text{LSPR}}$ [nm]	$\Delta\lambda_{\text{FWHM}}$ [nm]	$I(\Delta\lambda_{\text{R1}})$ [counts]	$I(\Delta\lambda_{\text{R2}})$ [counts]
S1, $\Lambda = 400 \text{ nm}$ , $D = 215 \pm 6 \text{ nm}$	$770 \pm 13$ ( $782 \pm 4$ )	$172 \pm 12$ ( $221 \pm 15$ )	$254 \pm 52$	$248 \pm 73$
S2, $\Lambda = 500 \text{ nm}$ , $D = 165 \pm 8 \text{ nm}$	$787 \pm 7$ ( $782 \pm 5$ )	$122 \pm 14$ ( $106 \pm 2$ )	$66 \pm 15$	$68 \pm 18$

varied angle when performing the measurement with a focused beam (see Fig. S2 in the ESI†).

In general, the variations in the LSPR spectra can be attributed to local deviations in the morphology of gold nanoparticles (particularly diameter  $D$ ) that are related to imperfections of the LIL fabrication process. The analysis of the AFM data (included in the ESI†) reveals that the diameter  $D$  varied with a standard deviation of  $\sigma(D) = 6 \text{ nm}$  on the S1 substrate and  $\sigma(D) = 8 \text{ nm}$  for the S2 substrate. From the slope in dependencies  $D(\lambda_{\text{LSPR}})$  presented in Fig. 3, it can be obtained that the LSPR wavelength changes with the diameter as  $\partial\lambda_{\text{LSPR}}/\partial D = 1$  and  $1.3$  for the prepared gold nanoparticle arrays with period  $\Lambda = 400$  (S1) and  $500 \text{ nm}$  (S2), respectively. Therefore, the measured variations in diameter  $D$  correspond to standard deviation in the LSPR wavelength of  $\sigma(\lambda_{\text{LSPR}}) = 6 \text{ nm}$  for S1 and  $\sigma(\lambda_{\text{LSPR}}) = 10 \text{ nm}$  for S2. Such values are lower than those experimentally observed when probing an area of about  $10 \mu\text{m}^2$  and this discrepancy can be ascribed to additional effects such as the polycrystalline nature of prepared gold nanoparticles and variations in roughness of the top nanoparticle surface and that of the glass substrate.

### Surface enhanced Raman spectroscopy on gold nanoparticle arrays

Arrays of gold nanoparticles can serve as an efficient substrate for the amplification of Raman scattering on a probe molecule when exposed to an intense LSP field. This effect occurs when the resonant wavelength  $\lambda_{\text{LSPR}}$  is located in the vicinity of the impinging (laser) light  $\lambda_{\text{L}}$  as well as that of Raman scattered light at specific spectral bands centered at wavelengths  $\lambda_{\text{R}}$ .<sup>46–48</sup> In order to demonstrate the applicability of the used LIL method for SERS, 4-mercaptobenzoic acid (4-MBA) was selected as a probe and the laser wavelength of  $\lambda_{\text{L}} = 785 \text{ nm}$  was used (see Fig. 5a). In addition, other molecules including 4-aminothiophenol and 1,2-di(4-pyridyl)ethylene were tested for the SERS measurement as seen in the ESI.†

It has been previously reported in several studies that the highest SERS enhancement factor on gold nanocylinders occurs with  $\lambda_{\text{LSPR}}$  located between the  $\lambda_{\text{L}}$  and (red shifted) Stokes vibrational band of the probe of interest, which has been validated for the visible part of the spectrum.<sup>49,50</sup> However, such a rule was found not to be valid for the gold nanoparticles that are resonant in the NIR part of the spectrum. Then the optimum  $\lambda_{\text{SPR}}$  was observed to be significantly blue shifted with respect to  $\lambda_{\text{L}}$ .<sup>51</sup> This can be partially attributed to the blue-shift of the maximum extinction (measured in far field) compared to the wavelength where the strongest enhancement in the near field occurs.<sup>52–54</sup> Another important factor is a decrease of the near field intensity for nanoparticles

with a larger diameter, supporting resonance in the NIR part of the spectrum compared to that for resonances in the visible,<sup>47</sup> and related more complex spectral dependence of the near field enhancement.<sup>55</sup>

Finite difference time domain (FDTD) simulations were carried out in order to elucidate the spectral dependence of Raman scattering efficiency on the prepared arrays of gold cylindrical nanoparticles. The plasmonically enhanced field intensity strength at laser wavelength  $\lambda_{\text{L}}$  and Raman band wavelengths  $\lambda_{\text{R}}$  were simulated in order to evaluate changes in the Raman scattering efficiency that is proportional to the term  $\sim |E(\lambda_{\text{L}})|^2 |E(\lambda_{\text{R}})|^2$ . As illustrated by the experimental data in Fig. 3, various combinations of period  $\Lambda$  and diameter  $D$  can be chosen to tune  $\lambda_{\text{LSPR}}$  on arrays of gold cylindrical nanoparticles close to the wavelength  $\lambda_{\text{L}}$ . Furthermore, a set of four pairs of period  $\Lambda$  and nanoparticle diameter  $D$  that define a geometry exhibiting  $\lambda_{\text{LSPR}}$  close to wavelength  $\lambda_{\text{L}} = 785 \text{ nm}$  were selected. The determined geometrical parameters that are specified in the inset of Fig. 6a agree well with those determined experimentally (see Fig. 3). The simulated transmission spectra presented in Fig. 6a show that when increasing the period  $\Lambda$  and decreasing the diameter  $D$ , the spectral width of the LSPR band decreases as the experimental data revealed. The spectral width of the resonant feature is a signature of LSP damping that directly affects the electromagnetic field enhancement. For the simulated geometries, the enhancement of electric field amplitude  $|E|/|E_0|$  was obtained from near-field plots (see an example in the inset of Fig. 6b) and it was averaged over the surface of a nanoparticle at  $2 \text{ nm}$  distance from its walls. At the wavelength  $\lambda_{\text{L}} = 785 \text{ nm}$ , the averaged electric field amplitude enhancement  $|E|/|E_0|$  rapidly increases with the period  $\Lambda$  while for the longer wavelengths  $\lambda_{\text{R}} = 850$  and  $900 \text{ nm}$ , the increase of  $|E|/|E_0|$  is slower, see Fig. 6. These simulations predict that the Raman scattering efficiency at these wavelengths  $\lambda_{\text{R}}$  (proportional to  $|E(\lambda_{\text{L}})|^2 |E(\lambda_{\text{R}})|^2$ ) is about 9 times higher for the period  $\Lambda = 500 \text{ nm}$  than for  $\Lambda = 400 \text{ nm}$ .

In following experiments, two substrates with the period  $\Lambda = 400 \text{ nm}$  (S1) and  $500 \text{ nm}$  (S2) were used for SERS measurements of 4-MBA. On these substrates, the diameter of the nanoparticle arrays was adjusted to  $D = 215 \text{ nm}$  and  $165 \text{ nm}$ , respectively, in order to set LSPR to the desired spectral region close to  $785 \text{ nm}$ . As can be seen in Fig. 5b and summarized in Table 1, the mean LSPR wavelength on both substrates is almost identical ( $\lambda_{\text{LSPR}} \sim 782 \text{ nm}$  as determined by transmission measurements with a collimated beam) but their resonance width substantially differs. The denser nanoparticle arrays with  $D = 215 \text{ nm}$  show a wider resonance with  $\Delta\lambda_{\text{FWHM}} = 172 \text{ nm}$ , while the sparser arrays support narrower LSPR with  $\Delta\lambda_{\text{FWHM}} = 122 \text{ nm}$ . In order to evaluate the strength and homo-



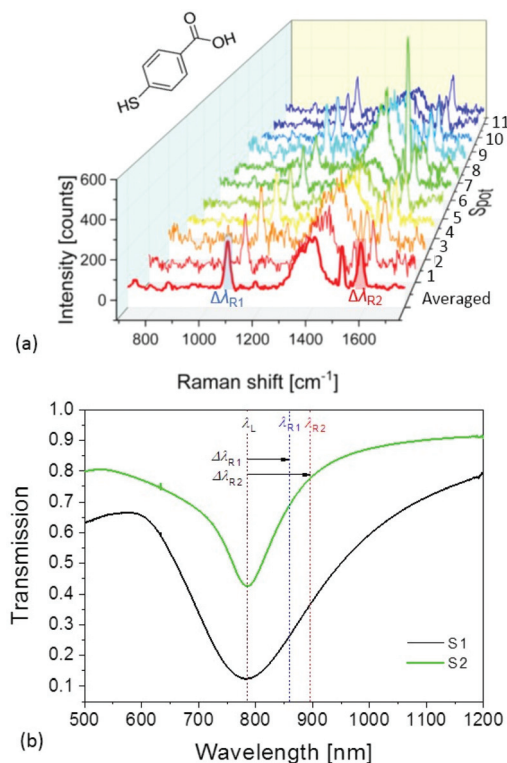


**Fig. 5** (a) Set of SERS spectra measured at different spots for 4-MBA attached to the S1 substrate (red curve represents the averaged spectrum). (b) LSPR spectra measured on substrates S1 and S2 with a large diameter beam.

generality of the SERS signal on the prepared LIL substrates, the focused laser beam at  $\lambda_L$  was scanned over their surface after 4-MBA was attached. A series of spots on a grid with  $50 \mu\text{m}$  spacing were evaluated on substrates S1 and S2. On every spot, the Raman spectrum was acquired when irradiating an area with a diameter of about  $1 \mu\text{m}$  (to which the beam at  $\lambda_L$  was focused) followed by the recording of the LSPR transmission spectrum at the same location (with a diameter of  $3 \mu\text{m}$  defined by the hole in the used confocal microscope). As can be seen in an example presented in Fig. 5a, the measured Stokes vibrational Raman spectra exhibit two strong bands attributed to the probe 4-MBA molecule located at wavelengths shifted by  $\Delta\lambda_{R1} = 1077 \text{ cm}^{-1}$  (corresponding to  $\lambda_{R1} = 857 \text{ nm}$ ) and by  $\Delta\lambda_{R2} = 1588 \text{ cm}^{-1}$  (corresponding to  $\lambda_{R2} = 896 \text{ nm}$ ).

The obtained SERS intensities are summarized in Table 1 and firstly, one can see that the average SERS peak intensity on S1 is about 3.7 fold higher than that on the S2 substrate. This observation is in stark contrast to performed FDTD simulations that predict that the longer period substrate S2 enhances the Raman scattering efficiency 9-times stronger than the S1 substrate. This discrepancy can be only partially explained by about a two-fold larger area of the cylindrical nanoparticles (normalized by the unit cell area) on the S1 substrate, which can thus accommodate more target analytes. In addition, weaker coupling strength and wider LSP resonance (see Fig. 5b) were experimentally observed on S2 (see Fig. 5b)

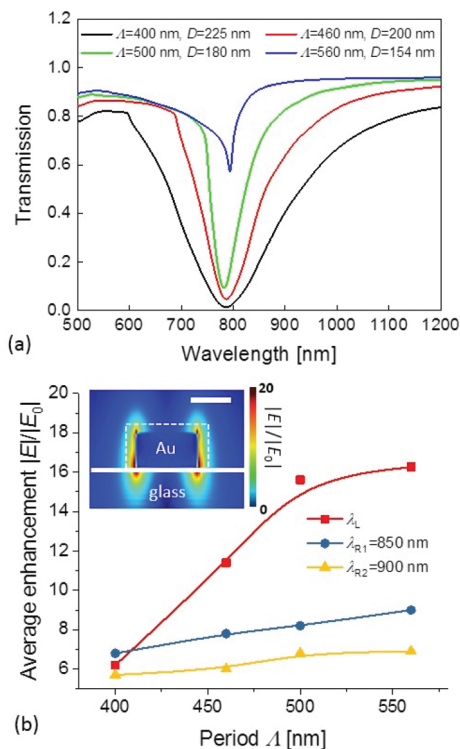


**Fig. 6** (a) Simulated LSPR transmission spectra for combinations of  $\Delta$  and  $D$  ensuring  $\lambda_{LSPR} \sim 800 \text{ nm}$ . (b) Dependence of the average electric field amplitude enhancement  $|E|/|E_0|$  on the nanostructure period  $\Delta$  for wavelength  $\lambda_L$  and  $\lambda_R = 850$  and  $900 \text{ nm}$ . The inset shows an example of simulated near field intensity for  $\Delta = 560 \text{ nm}$  with a dashed line representing the surface over which the field amplitude was averaged. All data were obtained for normally incident waves.

compared to the simulations (see Fig. 6a), which also decrease the SERS signal on this substrate. However, very probably also other parameters such as roughness, which was not taken into account in the model, play an important role.

Secondly, there can be seen that when scanning the laser beam over the surface of S1 and S2 substrates, a standard deviation of SERS peak intensity of 20–30% of the mean value occurs. These variations in SERS peak intensity can be mainly attributed to local changes in the LSPR wavelength  $\lambda_{LSPR}$ . It is worth noting that probing the area with a diameter of  $1 \mu\text{m}$  corresponds to the excitation of LSPs on  $\sim 3$  nanoparticles, which approaches the situation when individual nanoparticles are monitored.<sup>56</sup> Thus, even stronger variations in LSPR can be expected than those observed in transmission measurements on ensembles of about  $10^6$  nanoparticles carried on an area of  $1 \text{ mm}^2$  and of 30 nanoparticles carried on  $10 \mu\text{m}^2$  area (see Fig. 4 and Table 1).

## Experimental

### Materials

A S1805 G2 positive photoresist and AZ 303 developer were purchased from Micro Resist Technology (Germany).



Propylene glycol monomethyl ether acetate was obtained from Sigma-Aldrich (Germany). Mercaptobenzoic acid, 4-aminothiophenol and 1,2-di(4-pyridyl)ethylene were acquired from Sigma Aldrich (France).

### Preparation of gold nanoparticle arrays

A 2 nm thick chromium layer (adhesion layer) and a 50 nm thick gold layer were sequentially prepared on clean glass microscope slides ( $20 \times 20 \text{ mm}^2$ ). Both metals were deposited by thermal evaporation (HHV AUTO 306 from HHV Ltd) under a pressure better than  $2 \times 10^{-6}$  mbar. Glass substrates were spin-coated at 4500 rpm for 45 s using a Microposit S1805 G2 positive photoresist diluted (1 : 2) with propylene glycol monomethyl ether acetate, originating a 100 nm thick film. Afterwards, substrates were soft baked at 100 °C on a hot plate for 120 s. Prior to the exposure, a black tape was attached on the back side of the glass substrates in order to avoid back reflection of the recorded beam. Then, substrates were mounted to the Lloyd's mirror interferometer. Exposure was carried out utilizing a 4 mW HeCd laser (model IK 3031 R-C from Kimmon) at wavelength  $\lambda = 325 \text{ nm}$ . A spatial filter ( $\times 40$  microscope lens and pinhole with a diameter of 10  $\mu\text{m}$ ) was employed to expand the beam. An additional lens with a focal length of 1 m was used to collimate the beam to the interferometer. The distance between the spatial filter and the sample holder was around 1.8 m. The intensity of the laser beam at the sample holder was found to be  $30 \mu\text{W cm}^{-2}$ . The exposure dose was set to  $6.75 \text{ mJ cm}^{-2}$ . The periodicity of the particle arrays  $\Lambda_1 = 260 \text{ nm}$ ,  $\Lambda_2 = 300 \text{ nm}$ ,  $\Lambda_3 = 400 \text{ nm}$ ,  $\Lambda_4 = 460 \text{ nm}$ ,  $\Lambda_5 = 500 \text{ nm}$  and  $\Lambda_6 = 560 \text{ nm}$  was achieved by adjusting the angle of the interfering beams ( $\theta_1 = 38.68$ ,  $\theta_2 = 32.80$ ,  $\theta_3 = 23.97$ ,  $\theta_4 = 20.69$ ,  $\theta_5 = 18.97$ ,  $\theta_6 = 16.87$ ). After exposure, substrates were immersed in a diluted AZ 303 developer solution with distilled water at a ratio 1 : 15. Typical developing times were between 90–240 s. Directional dry etching with an argon milling system (Roth & Rau IonSys 500) was carried out to transfer the pattern into the underlying gold layer (etching time 450 seconds, 70 degrees). Finally, the remaining resist was removed using oxygen plasma for 5 minutes, 1 mbar and 40 W.

### Morphology measurements

Atomic force microscopy (PicoPlus from Molecular Imaging, Agilent Technologies) was used to investigate the morphology of nanoparticle arrays in the tapping mode. The average diameter was determined by analyzing the grain distribution of nanoparticle arrays using the free Gwyddion software. Additionally, scanning electron microscopy (Zeiss Supra 40 VP SEM) was employed to acquire complementary images.

### Attachment of SERS-active molecules

LIL-prepared arrays of gold nanoparticles were cleaned with ozone for two hours. Afterwards, the substrate with gold nanoparticles was rinsed with ethanol and immersed in 4-mercaptopbenzoic acid, 4-aminothiophenol or 1,2-di(4-pyridyl)ethylene dissolved in ethanol at a concentration of 1 mM for one day in

order to form a self-assembled monolayer *via* reaction by a thiol group or to physisorb on a gold surface. Finally, the substrate was rinsed with ethanol and dried.

### Optical measurements

Transmission spectra were obtained by using a Bruker Vertex 70 Fourier transform spectrometer (FTIR) with a diameter of the collimated polychromatic beam of  $0.5 \text{ mm}^2$ . In order to perform combined SERS and LSPR experiments with a focused beam, an Xplora Raman microspectrometer (Horiba Scientific, France) with a  $\times 100$  objective (numerical aperture of 0.9) was used. On each substrate, several spectra were acquired on a square area of  $200 \times 200 \mu\text{m}$  with a distance between neighboring spots of 50  $\mu\text{m}$ . In the case of LSPR measurements, the edge filter was removed and the transmission spectra were measured in the whole spectral range of 400–900 nm. Each spot was illuminated with a white lamp and the recorded spectra were normalized by that acquired on a reference area without the nanostructures. The transmitted light is collected from an area with a diameter of 3  $\mu\text{m}$  defined by the hole of the confocal microscope. The SERS measurements were performed in the backscattering configuration at room temperature with the same lens and a laser beam at  $\lambda_L = 785 \text{ nm}$  focused at a spot 1  $\mu\text{m}$  in diameter. The power of the laser beam at the spot was about 100  $\mu\text{W}$  and the Raman spectrum was accumulated by 20 s and artefacts corresponding to cosmic rays were removed. The transmission spectra were analyzed in order to determine the spectral position and the width of the LSPR band.

### Numerical simulations

In this work, FDTD calculations based on commercial software (FDTD solution, Lumerical Inc., Canada) are employed for simulating the electromagnetic fields around the arrays of gold nanoparticles arranged in a square lattice, taking into account the size of nanoparticles and the spacing between them. A single unit cell of the array, with a uniform mesh size of 2 nm ( $x$ ,  $y$  and  $z$  directions), was used to calculate the near field electric intensity and far field transmission spectra. Periodic boundary conditions are applied in the lateral directions while perfectly matched layers are placed above and below the structure in the perpendicular direction to absorb the transmitted and reflected electromagnetic waves. The optical constants of gold are taken from the literature.<sup>57</sup> The plane wave source covers a wavelength range of 400 to 950 nm. The structures are studied for the linearly polarized light under the condition of normal incidence.

## Conclusions

This paper reports on the not yet demonstrated tunability of laser interference lithography for the preparation of gold nanoparticle arrays with precisely controlled geometry enabling tailoring their LSPR characteristics over a broad spectral range. A series of substrates with arrays of cylindrical gold nano-



particles exhibiting an LSPR wavelength in the red and near infrared part of the spectrum were prepared by independently varying the diameter between 70 and 350 nm and period between 260 and 560 nm. Plasmonic substrates with identical LSPR wavelengths tuned to the vicinity of 785 nm and different spectral widths for SERS experiments were prepared. The importance of controlling both the LSPR wavelength and resonance width in order to enhance electromagnetic field intensity at both excitation and Raman scattered wavelength is demonstrated and sources of irregularities that affect the homogeneity of the SERS signal over the substrates are discussed. When probing an area of about millimeter diameter, deviations in the LSPR wavelength and spectral width of about several nanometers were typically observed. Interestingly, when such spectra were measured with a beam focused to a smaller area with a diameter of several microns, these standard deviations substantially increased. Such changes were ascribed to local variations in the morphology of disk-shaped nanoparticles (exhibited standard deviation in diameter of between 3 and 5%), which translate to the SERS signal exhibiting standard deviation between 20 and 30% when scanning over spots with an area of about  $1 \mu\text{m}^2$ . The presented methodology provides a tool for the preparation of highly tunable geometries over a large area, opening the door for further development of more complex and efficient plasmonic architectures using the gold nanoparticle arrays as building blocks. In future, this may include engineering of quasi-3D crystals<sup>58</sup> where surface plasmons on nanoparticle and nanohole arrays interplay<sup>59,60</sup> and support narrow multi-resonant features that potentially overlap with excitation wavelength and Raman scattered wavelength bands.

## Conflicts of interest

There are no conflicts to declare.

## Acknowledgements

NGQ acknowledges funding from the European Union's Horizon 2020 research and innovation programme under grant agreement No 642787, Marie Skłodowska-Curie Innovative Training Network BIOGEL, ML and PV from the project jointly funded by Agence Nationale de la Recherche (ANR) and Austrian Science Fund (FWF) under the grant agreements ANR-15-CE29-0026 and I 2647, respectively. IK is grateful for the support from the FWF through the project TRP 304-N20.

## Notes and references

- M. L. Brongersma, N. J. Halas and P. Nordlander, *Nat. Nanotechnol.*, 2015, **10**, 25–34.
- O. M. Maragò, P. H. Jones, P. G. Gucciardi, G. Volpe and A. C. Ferrari, *Nat. Nanotechnol.*, 2013, **8**, 807–819.
- C. F. Guo, T. Sun, F. Cao, Q. Liu and Z. Ren, *Nat. Nanotechnol.*, 2014, **3**, e161.
- H. A. Atwater and A. Polman, *Nat. Mater.*, 2010, **9**, 205–213.
- C. Valsecchi and A. G. Brolo, *Langmuir*, 2013, **29**, 5638–5649.
- M. E. Stewart, C. R. Anderton, L. B. Thompson, J. Maria, S. K. Gray, J. A. Rogers and R. G. Nuzzo, *Chem. Rev.*, 2008, **108**, 494–521.
- M. Bauch, K. Toma, M. Toma, Q. Zhang and J. Dostalek, *Plasmonics*, 2014, **9**, 781–799.
- A. Indrasekara, S. Meyers, S. Shubeita, L. C. Feldman, T. Gustafsson and L. Fabris, *Nanoscale*, 2014, **6**, 8891–8899.
- K. Ueno and H. Misawa, *Phys. Chem. Chem. Phys.*, 2013, **15**, 4093–4099.
- M. Chirumamilla, A. Gopalakrishnan, A. Toma, R. P. Zaccaria and R. Krahn, *Nanotechnology*, 2014, **25**, 235303.
- P. Mühlischlegel, H.-J. Eisler, O. Martin, B. Hecht and D. Pohl, *Science*, 2005, **308**, 1607–1609.
- B. D. Lucas, J. S. Kim, C. Chin and L. J. Guo, *Adv. Mater.*, 2008, **20**, 1129–1134.
- L. J. Guo, *Adv. Mater.*, 2007, **19**, 495–513.
- S.-W. Lee, K.-S. Lee, J. Ahn, J.-J. Lee, M.-G. Kim and Y.-B. Shin, *ACS Nano*, 2011, **5**, 897–904.
- D. O. Shin, J.-R. Jeong, T. H. Han, C. M. Koo, H.-J. Park, Y. T. Lim and S. O. Kim, *J. Mater. Chem.*, 2010, **20**, 7241–7247.
- S. Krishnamoorthy, C. Hinderling and H. Heinzelmann, *Mater. Today*, 2006, **9**, 40–47.
- C. Stelling, C. R. Singh, M. Karg, T. A. F. König, M. Thelakkat and M. Retsch, *Sci. Rep.*, 2017, **7**, 13.
- C. L. Haynes and R. P. Van Duyne, *J. Phys. Chem. B*, 2001, **105**, 5599–5611.
- P. Moutet, N. M. Sangeetha, L. Ressler, N. Vilar-Vidal, M. Comesana-Hermo, S. Ravaine, R. A. L. Vallee, A. M. Gabudean, S. Astilean and C. Farcau, *Nanoscale*, 2015, **7**, 2009–2022.
- I. Haidar, G. Levi, L. Mouton, J. Aubard, J. Grand, S. Lau-Truong, D. R. Neuville, N. Felidj and L. Boubekeur-Lecaque, *Phys. Chem. Chem. Phys.*, 2016, **18**, 32272–32280.
- J. D. Shao, L. P. Tong, S. Y. Tang, Z. N. Guo, H. Zhang, P. H. Li, H. Y. Wang, C. Du and X. F. Yu, *ACS Appl. Mater. Interfaces*, 2015, **7**, 5391–5399.
- S.-Y. Chou, C.-C. Yu, Y.-T. Yen, K.-T. Lin, H.-L. Chen and W.-F. Su, *Anal. Chem.*, 2015, **87**, 6017–6024.
- J.-A. Huang, Y.-L. Zhang, Y. Zhao, X.-L. Zhang, M.-L. Sun and W. Zhang, *Nanoscale*, 2016, **8**, 11487–11493.
- I. Wathuthanthri, Y. Liu, K. Du, W. Xu and C. H. Choi, *Adv. Funct. Mater.*, 2013, **23**, 608–618.
- J.-H. Seo, J. H. Park, S.-I. Kim, B. J. Park, Z. Ma, J. Choi and B.-K. Ju, *J. Nanosci. Nanotechnol.*, 2014, **14**, 1521–1532.
- C. Lu and R. Lipson, *Laser Photonics Rev.*, 2010, **4**, 568–580.
- A. Rodriguez, M. Echeverría, M. Ellman, N. Perez, Y. K. Verevkin, C. S. Peng, T. Berthou, Z. Wang, I. Ayerdi, J. Savall and S. M. Olaizola, *Microelectron. Eng.*, 2009, **86**, 937–940.





- 28 D. Xia, Z. Ku, S. Lee and S. Brueck, *Adv. Mater.*, 2011, **23**, 147–179.
- 29 A. J. Wolf, H. Hauser, V. Kübler, C. Walk, O. Höhn and B. Bläsi, *Microelectron. Eng.*, 2012, **98**, 293–296.
- 30 B. Bläsi, N. Tucher, O. Höhn, V. Kübler, T. Kroyer, C. Wellens and H. Hauser, *Proc. SPIE*, 2016, **9888**, 98880H.
- 31 S.-K. Meisenheimer, S. Jüchter, O. Höhn, H. Hauser, C. Wellens, V. Kübler, E. von Hauff and B. Bläsi, *Opt. Mater. Express*, 2014, **4**, 944.
- 32 J.-H. Seo, J. Park, D. Zhao, H. Yang, W. Zhou, B.-K. Ju and Z. Ma, *IEEE Photonics J.*, 2013, **5**, 2200106–2200106.
- 33 Y. Oh, J. W. Lim, J. G. Kim, H. Wang, B. H. Kang, Y. W. Park, H. Kim, Y. J. Jang, J. Kim, D. H. Kim and B. K. Ju, *ACS Nano*, 2016, **10**, 10143–10151.
- 34 M. Schade, B. Fuhrmann, C. Bohley, S. Schlenker, N. Sardana, J. Schilling and H. S. Leipner, *J. Appl. Phys.*, 2014, **115**, 084309.
- 35 C. Liu, M. Hong, H. Cheung, F. Zhang, Z. Huang, L. Tan and T. Hor, *Opt. Express*, 2008, **16**, 10701–10709.
- 36 M. Vala and J. Homola, *Opt. Express*, 2014, **22**, 18778–18789.
- 37 C. Liu, M. Hong, M. Lum, H. Flotow, F. Ghadessy and J. Zhang, *Appl. Phys. A*, 2010, **101**, 237–241.
- 38 H.-J. Ahn, P. Thiyagarajan, L. Jia, S.-I. Kim, J.-C. Yoon, E. L. Thomas and J.-H. Jang, *Nanoscale*, 2013, **5**, 1836–1842.
- 39 S. Bagheri, H. Giessen and F. Neubrech, *Adv. Opt. Mater.*, 2014, **2**, 1050–1056.
- 40 A. Tsargorodska, O. El Zubir, B. Darroch, M. L. Cartron, T. Basova, C. N. Hunter, A. V. Nabok and G. J. Leggett, *ACS Nano*, 2014, **8**, 7858–7869.
- 41 W. Karim, S. A. Tschupp, M. Oezaslan, T. J. Schmidt, J. Gobrecht, J. A. van Bokhoven and Y. Ekinici, *Nanoscale*, 2015, **7**, 7386–7393.
- 42 J. Huang, D. Fan, Y. Ekinici and C. Padeste, *Microelectron. Eng.*, 2015, **141**, 32–36.
- 43 C. L. Nehl and J. H. Hafner, *J. Mater. Chem.*, 2008, **18**, 2415–2419.
- 44 E. Petryayeva and U. J. Krull, *Anal. Chim. Acta*, 2011, **706**, 8–24.
- 45 B. Lamprecht, G. Schider, R. Lechner, H. Ditlbacher, J. Krenn, A. Leitner and F. Aussenegg, *Phys. Rev. Lett.*, 2000, **84**, 4721.
- 46 N. Félidj, J. Aubard, G. Lévi, J. R. Krenn, A. Hohenau, G. Schider, A. Leitner and F. R. Aussenegg, *Appl. Phys. Lett.*, 2003, **82**, 3095.
- 47 W. Lee, S. Y. Lee, R. M. Briber and O. Rabin, *Adv. Funct. Mater.*, 2011, **21**, 3424–3429.
- 48 N. Guillot and M. L. de la Chapelle, *J. Quant. Spectrosc. Radiat. Transfer*, 2012, **113**, 2321–2333.
- 49 I. Sow, J. Grand, G. Lévi, J. Aubard, N. Félidj, J.-C. Tinguely, A. Hohenau and J. Krenn, *J. Phys. Chem. C*, 2013, **117**, 25650–25658.
- 50 L. Billot, M. L. de La Chapelle, A.-S. Grimault, A. Vial, D. Barchiesi, J.-L. Bijeon, P.-M. Adam and P. Royer, *Chem. Phys. Lett.*, 2006, **422**, 303–307.
- 51 N. Guillot, H. Shen, B. Frémaux, O. Peron, E. Rinnert, T. Toury and M. Lamy de la Chapelle, *Appl. Phys. Lett.*, 2010, **97**, 023113.
- 52 B. M. Ross and L. P. Lee, *Opt. Lett.*, 2009, **34**, 896–898.
- 53 P. Alonso-González, P. Albella, F. Neubrech, C. Huck, J. Chen, F. Golmar, F. Casanova, L. Hueso, A. Pucci and J. Aizpurua, *Phys. Rev. Lett.*, 2013, **110**, 203902.
- 54 J. Zuloaga and P. Nordlander, *Nano Lett.*, 2011, **11**, 1280–1283.
- 55 F. J. Colas, M. Cottat, R. Gillibert, N. Guillot, N. Djaker, N. Lidgi-Guigui, T. Toury, D. Barchiesi, A. Toma, E. Di Fabrizio, P. Giuseppe Gucciardi and M. Lamy de la Chapelle, *J. Phys. Chem. C*, 2016, **120**, 13675–13683.
- 56 M. A. Beuwer, M. W. J. Prins and P. Zijlstra, *Nano Lett.*, 2015, **15**, 3507–3511.
- 57 P. B. Johnson and R. W. Christy, *Phys. Rev. Lett. B*, 1972, **12**, 4370–4379.
- 58 M. E. Stewart, N. H. Mack, V. Malyarchuk, J. Soares, T. W. Lee, S. K. Gray, R. G. Nuzzo and J. A. Rogers, *Proc. Natl. Acad. Sci. U. S. A.*, 2006, **103**, 17143–17148.
- 59 Q. M. Yu, P. Guan, D. Qin, G. Golden and P. M. Wallace, *Nano Lett.*, 2008, **8**, 1923–1928.
- 60 A. Artar, A. A. Yanik and H. Altug, *Appl. Phys. Lett.*, 2009, **95**, 051105.



## Supporting Information to: Tunable laser interference lithography preparation of plasmonic nanoparticle arrays tailored for SERS

Nestor Gisbert Quilis<sup>a</sup>, Médéric Lequeux<sup>b,c</sup>, Priyamvada Venugopalan<sup>a</sup>, Imran Khan<sup>a,d</sup>, Wolfgang Knoll<sup>a</sup>, Souhir Boujday<sup>c</sup>, Marc Lamy de la Chapelle<sup>b,e</sup> and Jakub Dostalek<sup>a</sup>

<sup>a</sup> Biosensor Technologies, AIT-Austrian Institute of Technology GmbH, Muthgasse11, 1190 Vienna, Austria. E-mail: Jakub.dostalek@ait.ac.at

<sup>b</sup> Université Paris 13, Sorbonne Paris Cité, Laboratoire CSPBAT, CNRS, (UMR 7244), 74 rue Marcel Cachin, 93017 Bobigny, France.

<sup>c</sup> Sorbonne Universités, UPMC Univ Paris 6, CNRS, UMR 7197, Laboratoire de Réactivité de Surface, F75005 Paris, France.

<sup>d</sup> AIT- Austrian Institute of Technology, Center for Energy, Photovoltaic Systems, Giefinggasse 2, A-1210 Vienna, Austria

<sup>e</sup> Institut des Molécules et Matériaux du Mans (IMMM - UMR CNRS 6283), Le Mans Université, Avenue Olivier Messiaen, 72085 Le Mans cedex 9, France

After the LIL recording step, periodic particle arrays with sub-wavelength size are generated upon development of the positive photoresist, with the height of the features around 100 nm. The dry etching treatment with argon ion beams removes the gold from the areas non-protected with the resist pattern, reducing the height approximately 20 nm. Finally, an oxygen plasma treatment is applied in order to remove the residual of photoresist on top of the prepared metallic nanoparticle arrays. This last step, as can be seen from a cross-section obtained by atomic force microscopy (AFM) in Figure S1, effectively removes the organic resist yielding a final height about 55-60 nm. The time and the power of the oxygen plasma treatment are optimized to ensure removal of the resist while preventing the melting of the gold nanoparticles.

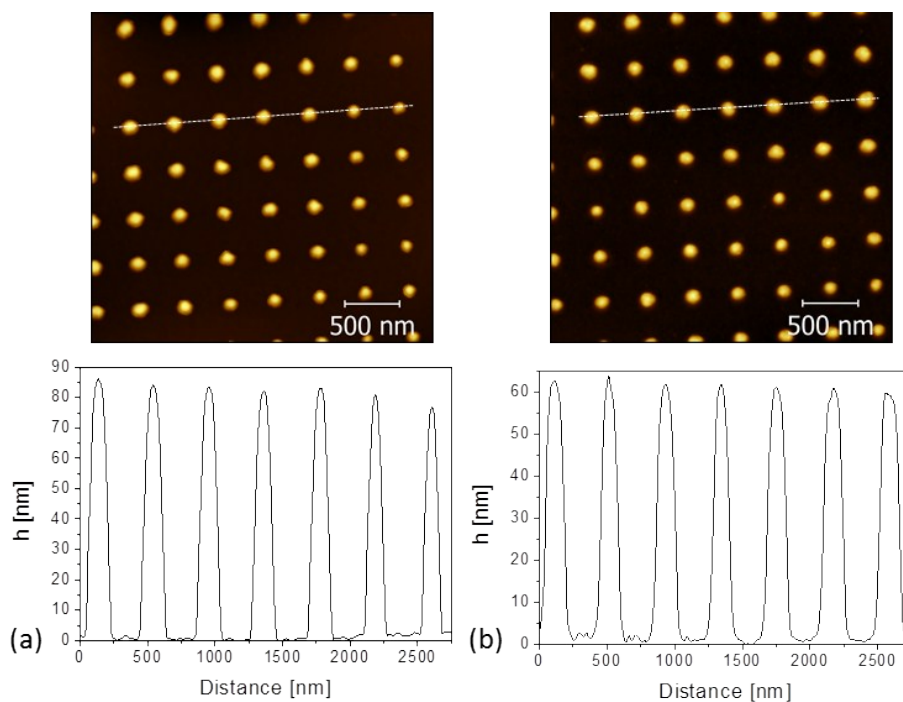


Figure S1. AFM image and modulation depth of the gold nanoparticles arrays after argon milling (a) and oxygen plasma (b) with  $\lambda=460$  nm and  $D=120$  nm.

The substrates S1 ( $\lambda=400$  nm and  $D=215$  nm) and S2 ( $\lambda=500$  nm and  $D=165$  nm) are tailored to exhibit a localized surface resonance in the vicinity of the laser line at 785 nm. Spectral changes in the transmission spectra for the sample S2 over the plasmonic substrate are measured with both a focused and collimated beam and given in the Figure S2. The study of the morphology performed by AFM for both substrates is outlined in Figure S3.

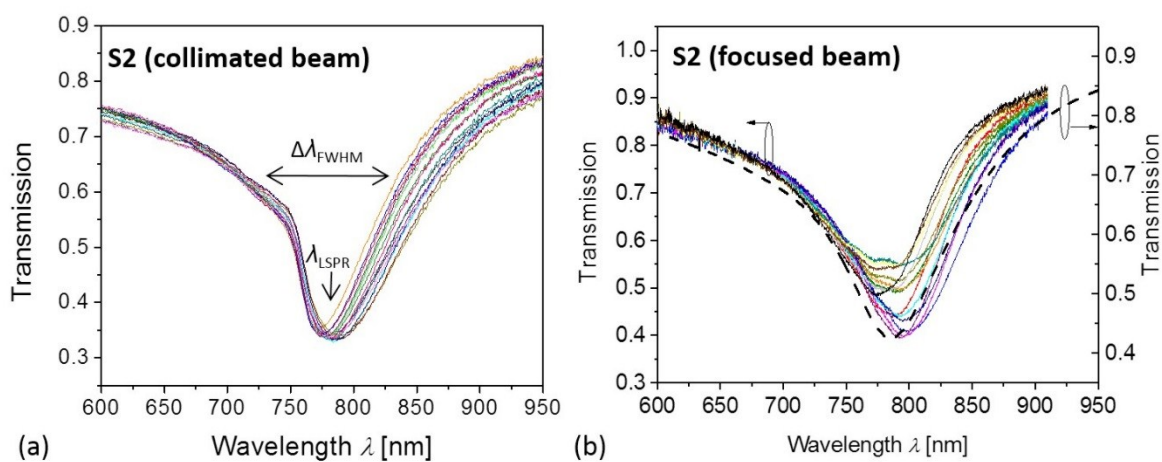


Figure S2. Comparison of the LSPR spectra measured on the substrate S1 on a) series of spots with a large 1 mm diameter arranged over  $1 \times 1$  cm with collimated beam and b) on with focused beam diameter  $3 \mu\text{m}$  scanned over  $200 \times 200 \mu\text{m}$ . Dashed line in b) shows transmission spectrum measured with large diameter beam on the same sample for comparison.

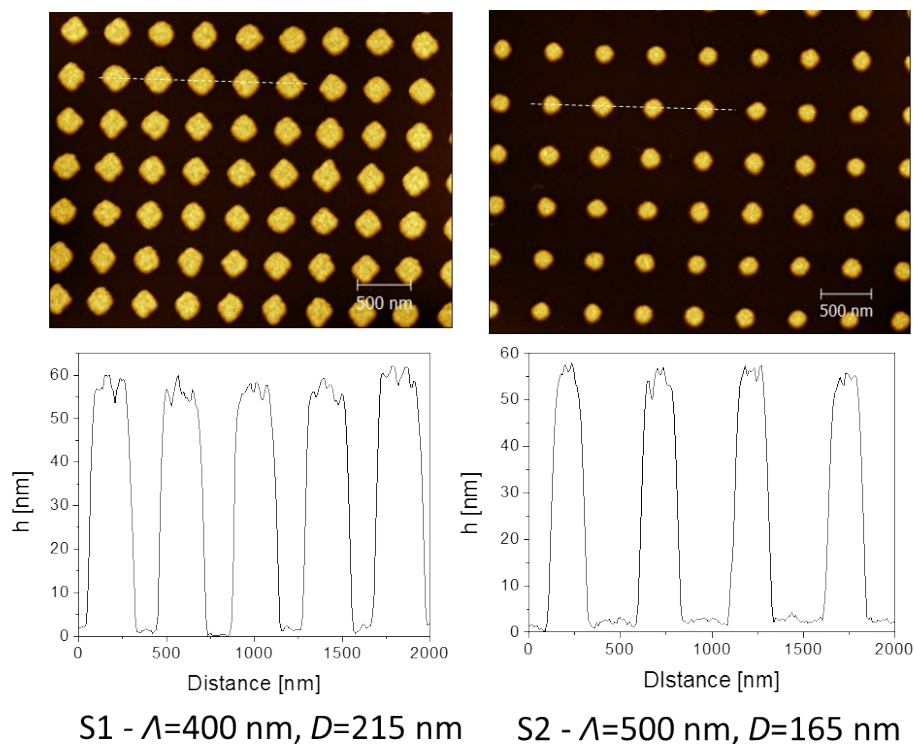
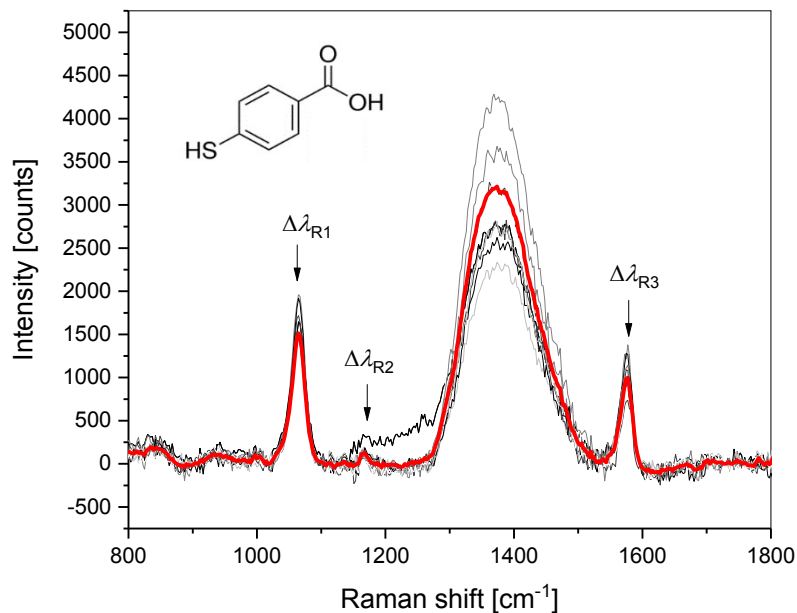


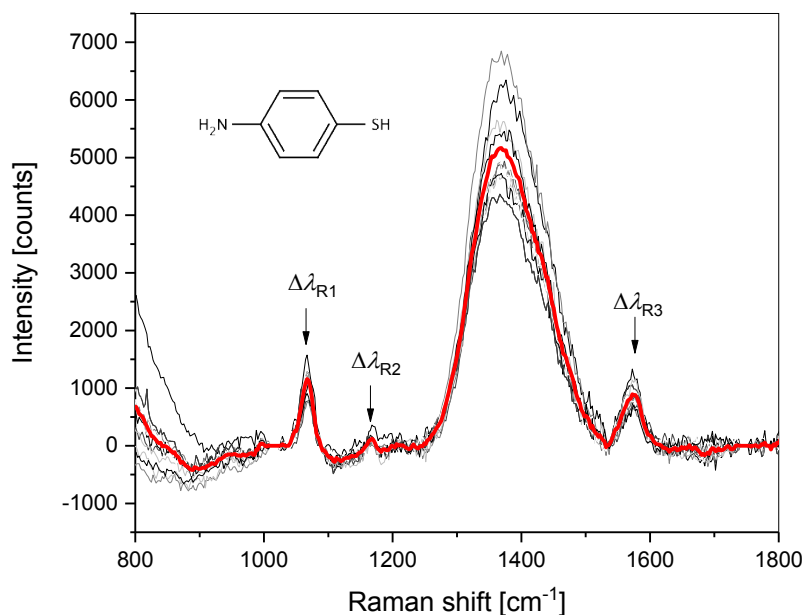
Figure S3. AFM observation of arrays of metallic nanoparticles carried by substrates S1 and S2.

SERS spectra were measured for 4-mercaptobenzoic acid, 4-aminothiophenol and 1,2-di(4-pyridyl)ethylene attached to a substrate with arrays of gold nanoparticles with  $\Lambda=500$  nm and  $D=165$  nm. These SERS measurements were performed in backscattering configuration at room temperature with  $\times 100$  lens and a laser beam at  $\lambda_L=785$  nm focused at a spot of  $1 \mu\text{m}$  in

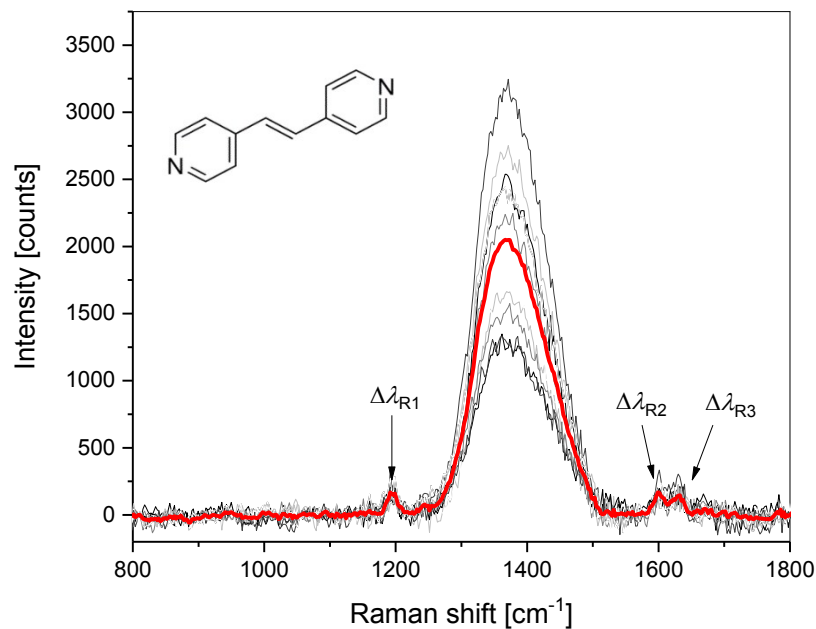
diameter. The power of the laser beam at the spot was about 2.5  $\mu\text{W}$  and Raman spectrum was accumulated by 30 s. Artefacts corresponding to cosmic rays were removed and raw spectra were compensated for the background. As Figure S4 shows, all measured spectra show broad bands at around 1400  $\text{cm}^{-1}$  and 1900  $\text{cm}^{-1}$ , which are attributed to the glass substrate. 4-mercaptobenzoic acid shows three peaks at  $\Delta\lambda_{R1}=1065 \text{ cm}^{-1}$ ,  $\Delta\lambda_{R2}=1166 \text{ cm}^{-1}$  and  $\Delta\lambda_{R3}=1576 \text{ cm}^{-1}$  with the intensity of 1166, 127 and 886 counts, respectively. Structurally similar 4-aminothiophenol shows three peaks at  $\Delta\lambda_{R1}=1072 \text{ cm}^{-1}$ ,  $\Delta\lambda_{R1}=1164 \text{ cm}^{-1}$  and  $\Delta\lambda_{R2}=1573 \text{ cm}^{-1}$  with the intensity 1523, 185 and 1016 counts, respectively. 1,2-Di(4-pyridyl)ethylene shows three weaker peaks at  $\Delta\lambda_{R1}=1095 \text{ cm}^{-1}$ ,  $\Delta\lambda_{R2}=1600 \text{ cm}^{-1}$  and  $\Delta\lambda_{R2}=1632 \text{ cm}^{-1}$  with the intensity of 162, 169, and 137 counts, respectively. These observations agree with SERS spectra reported before for other plasmonic nanostructures.<sup>1-3</sup>



a)



b)



c)

Figure S4. SERS spectra of a) 4-Mercaptobenzoic acid, b) 4-Aminothiophenol and c) 1,2-Di(4-pyridyl)ethylene measured on 10 spots arranged on a substrate with  $\Lambda=500$  nm and  $D=165$  nm (solid red line represents averaged signal).

#### References:

1. Yang, W. H.; Hulteen, J.; Schatz, G. C.; VanDuyne, R. P., A surface-enhanced hyper-Raman and surface-enhanced Raman scattering study of trans-1,2-bis(4-pyridyl)ethylene adsorbed onto silver film over nanosphere electrodes. Vibrational assignments: Experiment and theory. *J. Chem. Phys.* **1996**, *104* (11), 4313-4323.
2. Michota, A.; Bukowska, J., Surface-enhanced Raman scattering (SERS) of 4-mercaptobenzoic acid on silver and gold substrates. *J. Raman Spectrosc.* **2003**, *34* (1), 21-25.
3. Hu, X. G.; Wang, T.; Wang, L.; Dong, S. J., Surface-enhanced Raman scattering of 4-aminothiophenol self-assembled monolayers in sandwich structure with nanoparticle shape dependence: Off-surface plasmon resonance condition. *J. Phys. Chem. C* **2007**, *111* (19), 6962-6969.

# 3.2

Actively tunable collective localized surface plasmons by responsive hydrogel membrane



# Actively Tunable Collective Localized Surface Plasmons by Responsive Hydrogel Membrane

Nestor Gisbert Quilis, Marcel van Dongen, Priyamvada Venugopalan, Daria Kotlarek, Christian Petri, Alberto Moreno Cencerrado, Sorin Stanescu, Jose Luis Toca Herrera, Ulrich Jonas, Martin Möller, Ahmed Mourran, and Jakub Dostalek\*

Collective (lattice) localized surface plasmons (cLSP) with actively tunable and extremely narrow spectral characteristics are reported. They are supported by periodic arrays of gold nanoparticles attached to a stimuli-responsive hydrogel membrane, which can on demand swell and collapse to reversibly modulate arrays period and surrounding refractive index. In addition, it features a refractive index-symmetrical geometry that promotes the generation of cLSPs and leads to strong suppression of radiative losses, narrowing the spectral width of the resonance, and increasing of the electromagnetic field intensity. Narrowing of the cLSP spectral band down to 13 nm and its reversible shifting by up to 151 nm is observed in the near infrared part of the spectrum by varying temperature and by solvent exchange for systems with a poly(*N*-isopropylacrylamide)-based hydrogel membrane that is allowed to reversibly swell and collapse in either one or in three dimensions. The reported structures with embedded periodic gold nanoparticle arrays are particularly attractive for biosensing applications as the open hydrogel structure can be efficiently post-modified with functional moieties, such as specific ligands, and since biomolecules can rapidly diffuse through swollen polymer networks.

localized surface plasmons (LSPs) originating from collective electron density oscillations coupled with the associated electromagnetic field. The plasmonic materials rapidly find their applications in thin film optical devices for light harvesting,<sup>[3]</sup> in photocatalysis,<sup>[4]</sup> nanophotonic circuits,<sup>[5]</sup> amplified optical spectroscopy,<sup>[6]</sup> and sensors of chemical and biological species.<sup>[7]</sup> Recent advances in nanofabrication technologies allowed for the development of facile tools for the preparation of metallic nanostructures with precisely tailored plasmonic characteristics.<sup>[8]</sup> However, such properties are typically fixed as, after their preparation, the metallic nanostructures cannot be reconfigured. In order to overcome this limitation, there is pursued a new class of plasmonic materials that can be on-demand actuated and thus opens the door for actively controlled nanoscale manipulation with light.<sup>[9]</sup> These materials are

## 1. Introduction

Plasmonics provides an efficient means for nanoscale manipulation of light<sup>[1]</sup> in order to push forward the miniaturization and performance characteristics of a variety of optoelectronic technologies.<sup>[2]</sup> It utilizes metallic nanostructures that support

particularly important for integrated optics components such as modulators,<sup>[10]</sup> switches,<sup>[11]</sup> and polarizers<sup>[12]</sup> as well as in plasmonic high resolution displays,<sup>[13]</sup> and advanced sensing platforms.<sup>[14]</sup>

Several strategies have been explored for the reversible actuating of LSPs supported by metallic nanostructures.<sup>[15]</sup>

N. Gisbert Quilis, Dr. P. Venugopalan, D. Kotlarek, Dr. J. Dostalek  
BioSensor Technologies  
AIT-Austrian Institute of Technology GmbH  
Konrad-Lorenz-Strasse 24, 3430 Tulln, Austria  
E-mail: jakub.dostalek@ait.ac.at

M. van Dongen, Prof. M. Möller, Dr. A. Mourran  
DWI – Leibniz Institute for Interactive Materials  
Forckenbeckstrasse 50, 52056 Aachen, Germany

The ORCID identification number(s) for the author(s) of this article can be found under <https://doi.org/10.1002/adom.201900342>.

© 2019 Austrian Institute of Technology. Published by WILEY-VCH Verlag GmbH & Co. KGaA, Weinheim. This is an open access article under the terms of the Creative Commons Attribution License, which permits use, distribution and reproduction in any medium, provided the original work is properly cited.

The copyright line for this article was changed on 28 February 2020 after original online publication.

DOI: 10.1002/adom.201900342

Dr. P. Venugopalan  
CEST Kompetenzzentrum für elektrochemische  
Oberflächentechnologie GmbH  
TFZ, Wiener Neustadt  
Viktor-Kaplan-Strasse 2, 2700 Wiener Neustadt, Austria

Dr. C. Petri, Prof. U. Jonas  
Macromolecular Chemistry  
Department Chemistry-Biology  
University of Siegen  
Adolf Reichwein-Strasse 2, Siegen 57076, Germany

Dr. A. Moreno Cencerrado, Prof. J. L. Toca Herrera  
Institute for Biophysics  
Department of Nanobiotechnology  
University of Natural Resources and Life Sciences Vienna (BOKU)  
Muthgasse 11, Vienna 1190, Austria

Dr. S. Stanescu  
LIG Nanowise Ltd  
Williams House  
Manchester Science Park  
Manchester M15 6SE, UK

In particular, materials capping metallic nanostructures and exhibiting a tunable real part of the refractive index (by an external stimulus such as light,<sup>[16]</sup> temperature,<sup>[17]</sup> pH,<sup>[18]</sup> and electric current<sup>[19]</sup>) were pursued capitalizing on the sensitivity of LSPs to the optical density of surrounding medium. In addition, simultaneously modulating both the real and the imaginary part of the refractive index was demonstrated to strongly and reversibly shift the LSP excitation wavelength via electrochemical switching.<sup>[20]</sup> Another approach to actuate LSPs was explored based on the near field coupling between metallic nanoparticles with modulated gap distance<sup>[21,22]</sup> and by dynamically controlled far-field coupling to LSPs on periodic arrays of aluminum nanoparticles.<sup>[23]</sup> Chemically synthesized plasmonic nanoparticles were actuated by the pH-responsive polymer brushes<sup>[22]</sup> and the lithographically prepared aluminum nanoparticles were attached to polydimethylsiloxane elastomer<sup>[23]</sup> and mechanically stretched to reversibly vary the arrays period enabling tuning the excitation of LSP over the whole visible part of the spectrum. Besides controlling the surrounding environment of plasmonic nanoparticles, also the SPR-active material itself can be actuated as was showed by modulating the concentration of charge carriers in graphene nanostructures leading to strong spectral shifts of the plasmonic resonances in the near and mid infrared part of the spectrum.<sup>[24]</sup>

The vast majority of the reported actuated plasmonic nanostructures exhibit shifts in the LSPR wavelength that are smaller than the actual spectral width of the resonance, mostly because of employing absorbing materials.<sup>[25]</sup> Therefore complete switching “off” and “on” of the resonances is not possible, which limits the utilization of active plasmonic materials in the envisaged applications. To decrease the damping of LSPs, periodic arrays of metallic nanoparticles can be embedded in refractive index-symmetric geometry and thus exploit the diffraction coupling between neighboring nanoparticles.<sup>[26]</sup> Such structures can be designed to support collective (lattice) localized plasmon (cLSPs) with decreased radiative losses, which is manifested as

spectrally sharp plasmonic features<sup>[27]</sup> and is associated with stronger field intensity enhancement<sup>[28]</sup> compared to regular LSPs. These characteristics make plasmonic nanostructures supporting cLSPs attractive candidates for sensing of molecular species,<sup>[29]</sup> enhanced optical spectroscopy,<sup>[30]</sup> light harvesting,<sup>[31]</sup> and lasing.<sup>[32]</sup> As refractive index symmetry is required, typically immersion oils are employed to match the refractive index above and below the particle arrays in order to observe the cLSPs on glass or silicon substrates.<sup>[33]</sup> Only recently the using of low refractive index fluoropolymer layers enabled the excitation of cLSPs in aqueous environments<sup>[34]</sup> and self-assembled metallic nanoparticle arrays embedded to tethered responsive hydrogel layer and swollen in water were reported for switching of cLSP resonances.<sup>[35]</sup> The present paper reports on the implementation and strong actuating of cLSPs by using structures that rely on responsive hydrogel materials. A new approach to prepare periodic arrays of gold nanoparticles supported by either free-standing or surface-attached thermo-responsive poly(*N*-isopropylacrylamide)-based (pNIPAAm) hydrogel membrane was developed by using laser interference lithography combined with template stripping. The specific design of the geometry enables active tuning of the cLSP excitation by reversibly changing the refractive index symmetry as well as the lattice periodicity. In addition, the hydrogel materials swollen in aqueous environment provide the refractive index symmetry suitable for plasmonic biosensing applications and superior performance characteristics in refractometric-based surface plasmon resonance biosensors are demonstrated.

## 2. Results and Discussion

Two types of structures with actuated plasmonic properties were prepared. As **Figure 1** illustrates, these structures comprise gold nanoparticle arrays embedded on the top of surface-attached (A) or free-standing (B) responsive hydrogel membrane. The arrays

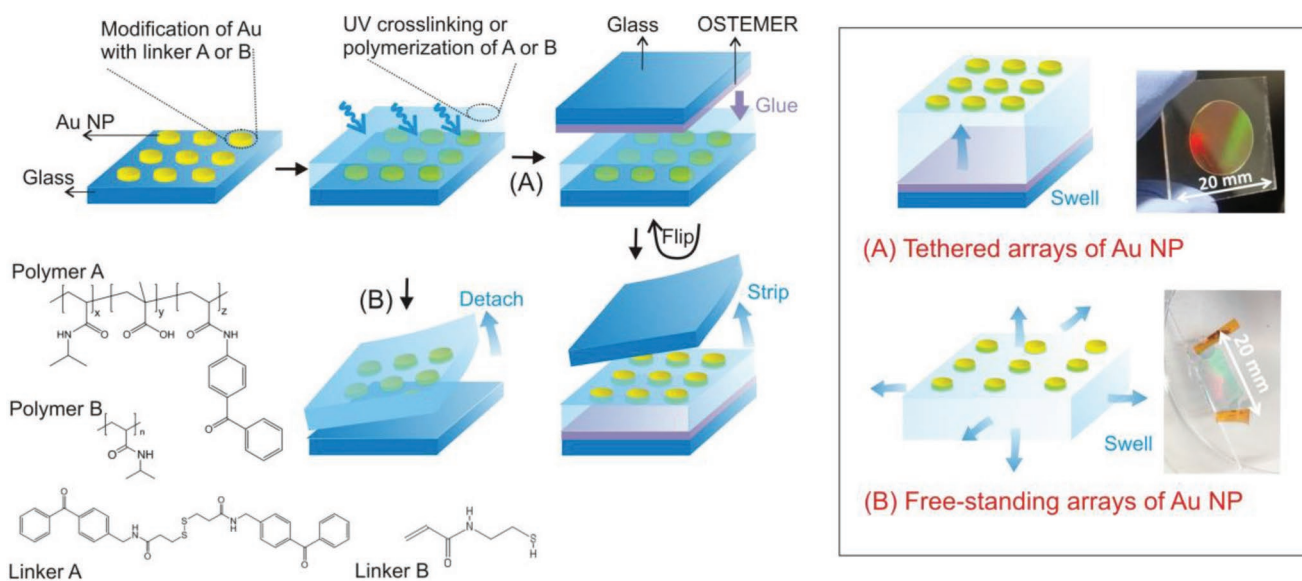


**Figure 1.** Schematic of the route for the preparation of gold nanoparticles arrays carried by A) tethered and B) free-standing pNIPAAm hydrogel film. The swelling of the structures in one and three dimensions is sketched in the right part together with examples of prepared materials.



of gold nanoparticles were fabricated by the UV laser interference lithography (UV-LIL) on a glass substrate that was modified with an anti-sticking layer. For the preparation of the surface-attached structure (A), the gold nanoparticles were decorated with photoactive benzophenone moieties (linker A). Then, pNIPAAm-based terpolymer with benzophenone groups attached to its chain (polymer A) was deposited on their top with a layer thickness of  $d_h = 0.28 \mu\text{m}$  followed by its simultaneous crosslinking and attaching to gold by irradiation with UV light. Finally, the structure was contacted and bonded to another glass substrate with a thin elastic Ostemer layer carrying epoxy groups. After the curing, the structure was stripped yielding the gold nanoparticles arrays supported by a surface-attached pNIPAAm-based terpolymer cushion. The second structure with a free-standing hydrogel membrane (B) utilized arrays of gold nanoparticles that were reacted with *N,N'*-bis(acryloyl)cystamine (linker B). On their top, a pNIPAAm layer (polymer B) with a thickness of  $d_h = 40 \mu\text{m}$  was in situ synthesized upon UV light irradiation. Contrary to the previous structure, the thicker crosslinked polymer layer with embedded periodic arrays of gold nanoparticles was detached by its swelling in ethanol in order to form a free-standing membrane.

## 2.1. Morphology of cLSP Arrays

The period  $\Lambda$  and diameter  $D$  of the arrays of gold nanoparticles was controlled in the range  $\Lambda = 360\text{--}560 \text{ nm}$  and  $D = 110\text{--}200 \text{ nm}$ , respectively, by adjusting the UV-LIL parameters.<sup>[36]</sup> Figure 2a shows an example of the topology of gold nanoparticle arrays prepared on glass substrate prior to the attachment of

pNIPAAm-based polymer. The topology was observed by atomic force microscopy (AFM) and it reveals cylindrically shaped gold nanoparticles with a height of about  $h = 50 \text{ nm}$ . As seen in Figure 2b, the height of the structure decreases after the embedding of gold nanoparticles to a pNIPAAm polymer layer in a surface-attached geometry (A). The pNIPAAm polymer networks in such structure swell when brought in contact with water (kept below the local solution critical temperature–LCST), which lifts up the nanoparticle arrays by the formed soft hydrogel cushion exhibiting low Young modulus.<sup>[37]</sup> Then, the in situ AFM does not capture the presence of gold nanoparticles as indicated by Figure 2c. The measured topology of the surface shows irregular features that can be attributed to the lateral stress-induced buckling of a thin hydrogel film that, due to surface attachment, is allowed to swell only in the direction perpendicular to the surface. Interestingly, the periodic pattern of gold nanoparticles suspended in swollen hydrogel retains its periodic arrangement as observed by the complementary optical measurements of structure B with a high numerical aperture lens, see the inset of Figure 2c. When increasing the temperature above pNIPAAm LCST of  $T_{\text{LCST}} = 32 \text{ }^\circ\text{C}$ , the hydrogel polymer network collapses, and the AFM performed in water again reveals the periodic arrays of gold nanoparticles as documented by Figure 2d. In this figure, small protrusions with characteristic size of about hundred nanometers can be seen as dark spots in the structure topology. Such domains were observed after the swelling and subsequent drying of similar hydrogel films (without embedded gold nanoparticle arrays) and they were attributed to the effect of “skin barrier” that was reduced by the incorporation of polar methacrylic acid to the polymer backbone (polymer A).<sup>[36]</sup>

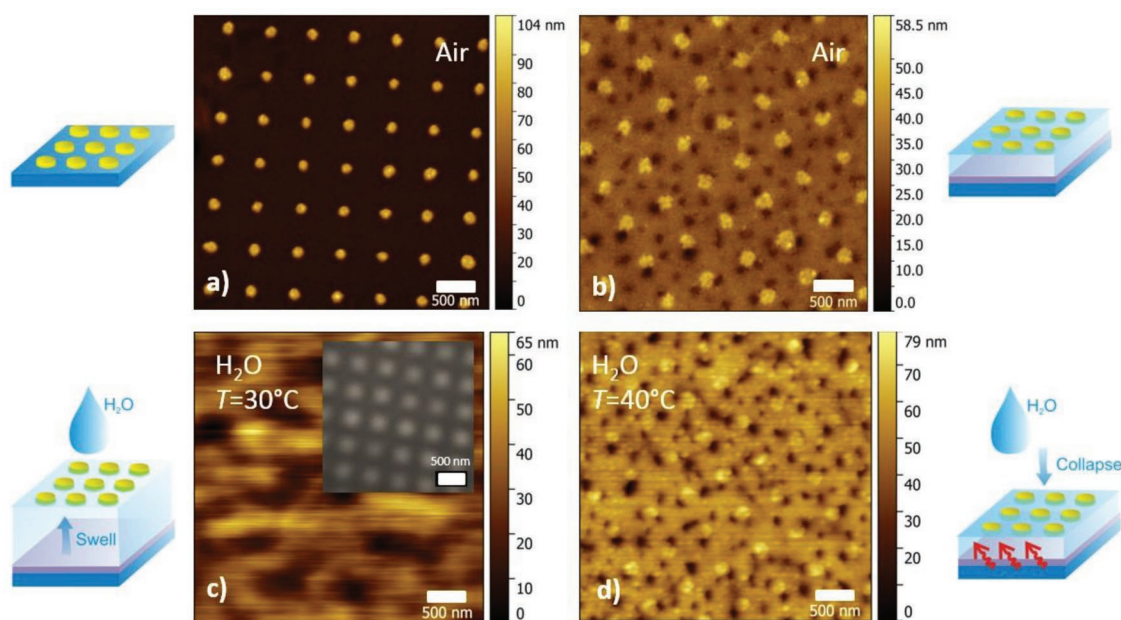


**Figure 2.** AFM observation of gold particle arrays on a) glass substrate after the UV-LIL fabrication (prepared with  $\Lambda = 560 \text{ nm}$ ,  $D = 150 \text{ nm}$ ), b) after their embedding to pNIPAAm-based polymer in a structure A followed by the rinsing with water and drying at a temperature above the pNIPAAm LCST (both images were taken in air). Observation of the tethered structure A in contact with water c) at  $T = 30 \text{ }^\circ\text{C}$  in swollen state and d) at  $T = 40 \text{ }^\circ\text{C}$  in the collapsed state. The inset in figure (c) represents an optical microscopy image of the swollen free-standing hydrogel film (structure B prepared with  $\Lambda = 360 \text{ nm}$ ,  $D = 140 \text{ nm}$ ) in water at room temperature.

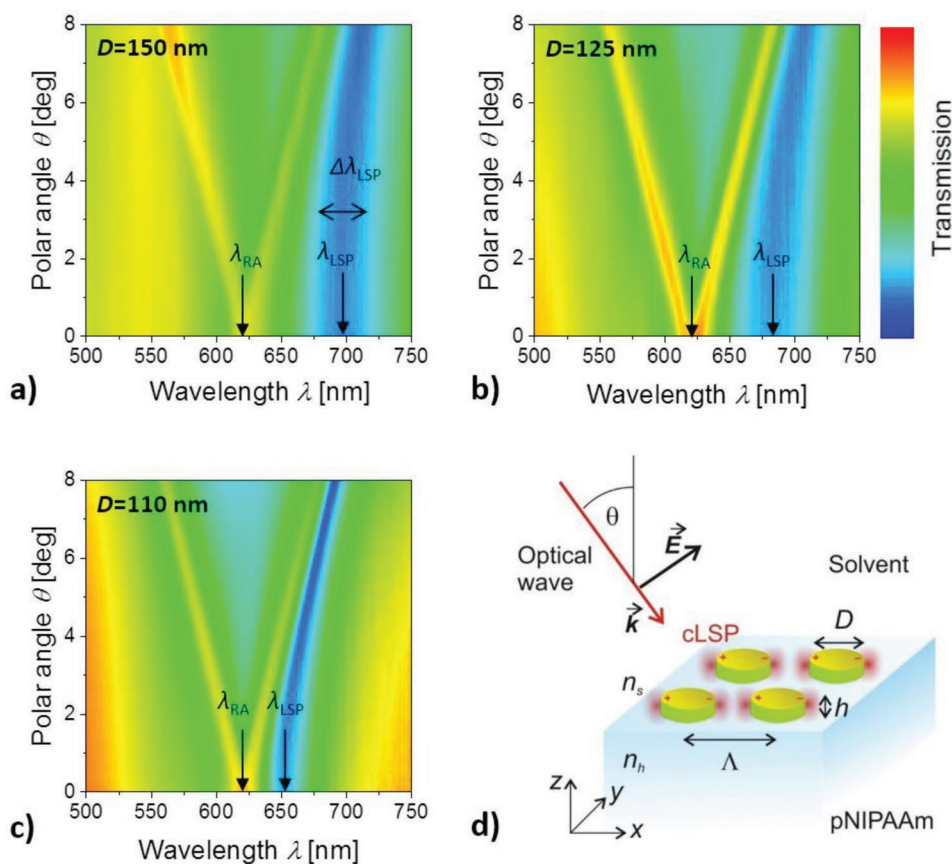


**Figure 3.** Angular–wavelength transmission spectra measured for the tethered structure A in contact with water at  $T = 22$  °C. The spectra were measured with TE polarization and the diameter of gold nanoparticles was varied as a)  $D = 150$  nm, b)  $D = 125$  nm, and c)  $D = 110$  nm while the period was set to  $\Lambda = 460$  nm. d) Schematics of the used geometry with arrays of gold nanoparticles that are probed by an incident optical wave.

## 2.2. Optical Characteristics of cLSP Structures

The changing of temperature below or above  $T_{LCST}$  of used thermo-responsive pNIPAAm polymer networks is accompanied by abrupt volume changes. These changes are associated with the polymer density variations, which translate to the modulating of hydrogel refractive index  $n_h$ . The surface-attached pNIPAAm layer in its hydrated swollen state ( $T < T_{LCST}$ ) exhibits a low refractive index of  $n_h = 1.36$  while in its collapsed state ( $T > T_{LCST}$ ) the refractive index increases to  $n_h = 1.46$ . These parameters were measured by optical waveguide spectroscopy combined with surface plasmon resonance<sup>[38]</sup> for the layer used in the geometry A. The measurements revealed that the swelling of the film perpendicular to its surface leads to the increase in its thickness from  $d_h = 275$  nm to about  $1 \mu\text{m}$  (data not shown). In its swollen state, the prepared pNIPAAm hydrogel exhibits a refractive index  $n_h$  that is close to that of water  $n_s = 1.33$ , which generates nearly symmetrical geometry around the arrays of gold nanoparticles. Such configuration promotes the diffraction coupling of LSPs supported by individual gold nanoparticles and it leads to the establishment of collective (lattice) modes–cLSPs. As investigated before, such modes occur when the spectral position of diffraction Rayleigh anomaly  $\lambda_{RA}$  is in the vicinity to LSP wavelength  $\lambda_{LSP}$ .<sup>[39]</sup> In order to tune the spectral distance between  $\lambda_{LSP}$  and  $\lambda_{RA}$ , the diameter  $D$  of gold nanoparticle arrays was adjusted for a

period fixed at  $\Lambda = 460$  nm. As reported before, varying diameter of arrays of gold nanoparticles from  $D = 150$  to  $110$  nm leads to a shift of the  $\lambda_{LSP}$  by  $50$  nm.<sup>[36]</sup> Therefore, decreasing the diameter  $D$  was utilized to push  $\lambda_{LSP}$  closer to the Rayleigh anomaly and thus to generate the cLSP mode. Such behavior is observed in the measured angular–wavelength transmission spectra presented in **Figure 3**. In these data, one can see a characteristic V-shaped feature centered at  $\lambda_{RA} = \Lambda n_h \approx 620$  nm, which corresponds to the splitting of  $\lambda_{RA}$  when deviating the incident angle  $\theta$ . At longer wavelengths, there can be seen a dip associated to the resonant excitation of LSPs that is shifting from  $700$  to  $650$  nm when decreasing the diameter  $D$ . Importantly, the LSP resonance wavelength  $\lambda_{LSP}$  become angular dispersive and its spectral width  $\Delta\lambda_{LSP}$  decreases when decreasing  $D$ , which can be attributed to its gradual shifting to the vicinity to  $\lambda_{RA}$  and diffraction coupling of cLSPs. The dispersive cLSPs band is observed for the transversally electric polarization of the incident beam (TE, with the electric field intensity vector parallel to the surface) as illustrated in Figure 3d showing the schematics of the geometry.

## 2.3. Actuating of cLSPs Arrays

The spectrally narrow resonances associated with the excitation of cLSPs can be actuated by breaking the refractive index

symmetry or by varying the arrays period  $\Lambda$ . The surface-attached structure A is allowed to swell and collapse only in perpendicular direction and thus only changing the refractive index symmetry is possible. The free-standing structure B is allowed to swell and collapse also in the lateral direction and therefore one can take advantage of the combined effect of modulating the arrays period  $\Lambda$  and refractive index  $n_h$ . The first approach was tested for the architecture A with  $\Lambda = 460$  nm and  $D = 110$  nm. As can be seen in **Figure 4a**, the temperature-triggered variations in the refractive index  $\Delta n_h \approx 0.10$  induced a reversible shift in the spectral position of cLSP resonance  $\lambda_{LSP}$ . The shift of  $\delta\lambda_{LSP} = 18.5$  nm was measured in the transmission spectrum for the normally incident optical beam  $\theta = 0^\circ$ . In addition, it illustrates that the perturbation of refractive index symmetry by the increasing of temperature leads to an increase in the spectral width of the resonance from  $\Delta\lambda_{LSP} = 38$  nm in swollen state (cLSPs are excited) to  $\Delta\lambda_{LSP} = 73$  nm when the hydrogel is collapsed (regular LSPs are excited). Similar experiment was carried out for the structure B carrying arrays of gold nanoparticles with  $\Lambda = 360$  nm and  $D = 140$  nm on the top of free-standing hydrogel membrane. When swollen in water at a temperature below  $T_{LCST}$ , the structure expands in lateral direction and the period of arrays increases to about  $\Lambda = 525$  nm, which is manifested as a shift of the first diffraction order Rayleigh anomaly to  $\lambda_{RA} = 700$  nm. As **Figure 4b** shows, the spectral position of the cLSPs is then located at a longer wavelength of  $\lambda_{LSP} = 747$  nm and exhibits the spectral width  $\Delta\lambda_{LSP} = 66$  nm. This width is wider compared to that for the surface-attached structure (A), which can be attributed to the larger diameter  $D$  of used nanoparticles. When increasing the temperature above the NIPAAm  $T_{LCST}$ , the spectral position  $\lambda_{LSP}$  shifts opposite compared to the structure A toward shorter wavelength of  $\lambda_{LSP} = 686$  nm and the spectral width increases to  $\Delta\lambda_{LSP} = 120$  nm. The reason for the blueshift of the resonance is the decreasing of the period  $\Lambda$  below 380 nm due to the shrinking of the structure, which stronger impacts the resonance compared to the increase of refractive index  $n_h$  (that redshifts the resonance position). It is important to note that the observed temperature actuating of responsive hydrogel membrane is accompanied with more than one order of magnitude stronger refractive index changes  $\Delta n_h$  compared to that occurring for water in the used temperature range.<sup>[33]</sup> Interestingly, when incubating the structure in ethanol, both  $\lambda_{RA}$  and  $\lambda_{LSP}$  are redshifted to 820 and 838 nm, respectively, and the spectral width of LSP resonance decreases to  $\lambda_{LSP} = 22$  nm. This observation can be explained by the fact that ethanol acts as a better solvent than water. Therefore, the period is prolonged to about  $\Lambda = 600$  nm and refractive index of more swollen hydrogel  $n_h$  is closer to that of the solvent  $n_s$ . In addition, the refractive index of ethanol  $n_s$  is higher than that of water, which further contributes to the red spectral shift. The performed measurements reveal that reproducible reversible shifts of  $\delta\lambda_{LSP} = 61$  nm were obtained by the repeated switching between the collapsed and the swollen state in water through modulating temperature  $T$ . Even stronger shifts of  $\delta\lambda_{LSP} = 151$  nm were observed for the changing of solvent between ethanol and water at a temperature above  $T_{LCST}$ . It is worth of mentioning that the pNIPAAm-based hydrogel film does not exhibit thermo-responsive behavior in ethanol<sup>[40]</sup> and

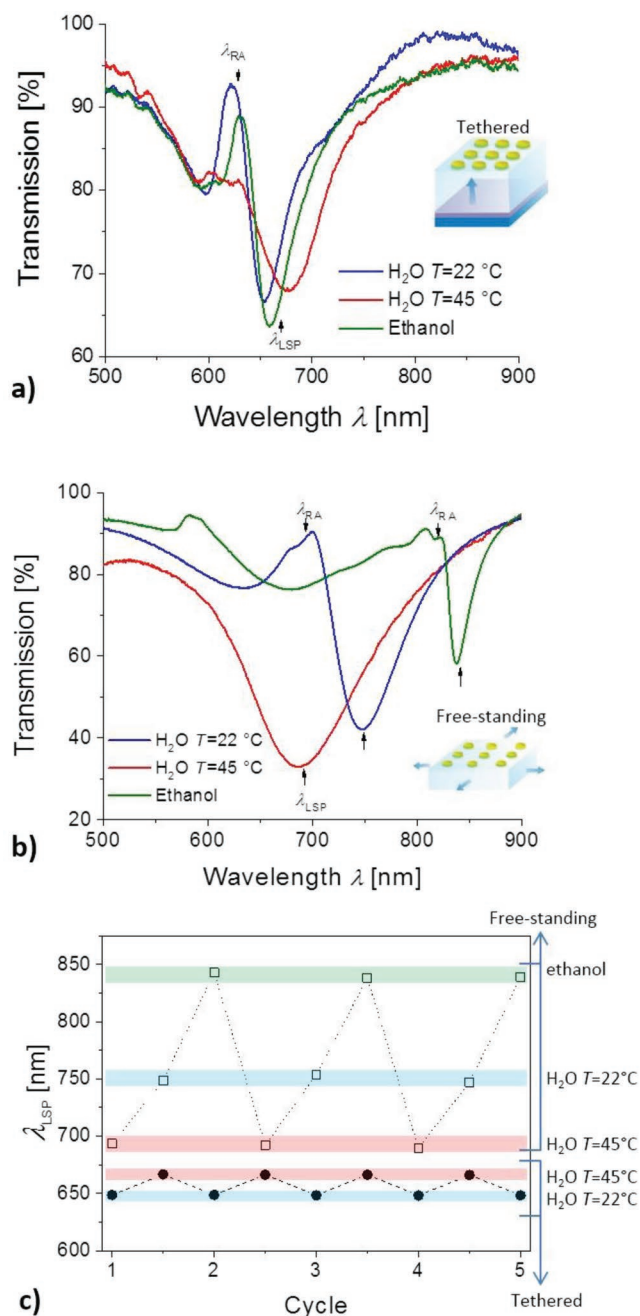


**Figure 4.** Transmission spectra measured for a) tethered structure (A, prepared with  $\Lambda = 460$  nm,  $D = 110$  nm) and b) free-standing structure (B, prepared with  $\Lambda = 360$  nm,  $D = 140$  nm) in contact with water at  $T = 22^\circ\text{C}$  (blue curve),  $T = 45^\circ\text{C}$  (red curve), and in contact with ethanol (green curve) at room temperature for the normally incident beam  $\theta = 0^\circ$ . c) Measured changes in the wavelength  $\lambda_{LSP}$  upon series of five cycles of swelling and collapsing in H<sub>2</sub>O and in ethanol for tethered (bottom) and free-standing (top).

thus changing temperature  $T$  does significantly affect the cLSP resonance in this solvent. The variations in  $\lambda_{LSP}$  are fully reversible and no changes were observed after more than five cycles of swelling in different solvents and modulated temperature, see **Figure 4d**.

## 2.4. Numerical Simulations

Based on the FDTD method, series of transmission spectra and distribution of near field intensity were simulated for the structure B that resembles arrays of gold nanoparticles on the top of the actuated free-standing hydrogel membrane (see Figure 4b). The simulated transmission spectra are presented in Figure 5 and they were obtained for the geometry describing the collapsed structure in water (I), swollen structure in water (II), and swollen structure in ethanol (III). These data show that the spectral positions of transmission dips  $\lambda_{\text{LSP}}$  associated with the resonant coupling to LSPs closely match the experimental values while the spectral widths  $[\Delta\lambda_{\text{LSP}} = 115 \text{ nm (I)}; \Delta\lambda_{\text{LSP}} = 34 \text{ nm (II)}; \Delta\lambda_{\text{LSP}} = 13 \text{ nm (III)}]$  are narrower compared to experimental values  $[\Delta\lambda_{\text{LSP}} = 120 \text{ nm}; \Delta\lambda_{\text{LSP}} = 66 \text{ nm}; \Delta\lambda_{\text{LSP}} = 22 \text{ nm, respectively}]$ . These discrepancies can be attributed to slight variations in the morphology of the prepared gold nanoparticle arrays over the measured surface area.<sup>[36]</sup> The near field simulations were

carried out for the wavelengths  $\lambda_{\text{LSP}}$  corresponding to the resonant excitation of LSPs. For the nonsymmetrical configuration I (when regular LSPs are excited) the field intensity enhancement peaks at the gold nanoparticle wall and decays when increasing the distance from the wall of gold nanoparticle. When normalized with the electric intensity of the incident beam, the field intensity enhancement at the nanoparticle walls yields  $|E/E_0|^2 = 100$ . For the geometry resembling the nanoparticle arrays on hydrogel cushion swollen in water II, the establishing of cLSPs leads to stronger maximum field intensity enhancement of  $|E/E_0|^2 = 375$ . Moreover, the increasing of the period  $\Lambda$  by swelling in ethanol (III) shifts the resonance closer to the Rayleigh anomaly  $\lambda_{\text{RA}}$  and the field intensity enhancement reaches a value as high as  $|E/E_0|^2 = 814$ . The confined LSP field intensity probes to the distance of  $d = 14 \text{ nm}$  (field intensity drops to half) for the geometry I and the mode supported at longer wavelengths on the structure III exhibits more delocalized field intensity profile probing up to the distance of 17 nm, see Figure 5c.

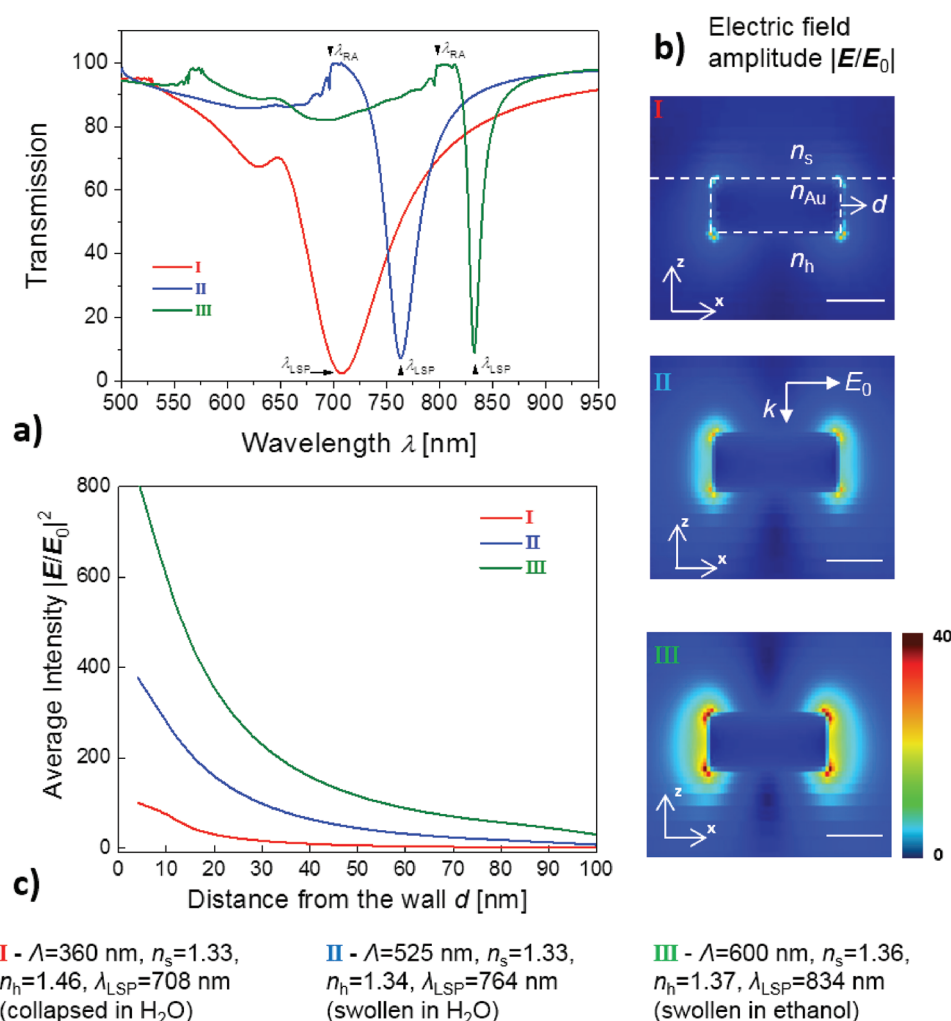


**Figure 5.** a) Simulated transmission spectra, b) spatial distribution electric field amplitude, and c) cross-section of the electric field intensity averaged over walls of gold nanoparticle arrays (with  $D = 140 \text{ nm}$ ) for the geometry experimentally determined for the free-standing structure B observed in Figure 4. The parameters used to represent the collapsed state in water (I, red), swollen state in water (II, blue), and swollen state ethanol (III, green) are stated at the bottom of the figure.

## 2.5. Refractometric Sensing Measurements

The examined surface-attached structure A was prepared by using a pNIPAAm-based terpolymer with incorporated methacrylic acid that can be post-modified with biomolecules in order to serve as a large capacity binding matrix in affinity biosensors. This functionality was already demonstrated in a variety of assays based on refractometric surface plasmon resonance<sup>[38,41]</sup> and surface plasmon-enhanced fluorescence<sup>[42]</sup> with amine coupling of ligand biomolecules<sup>[43]</sup> that are specific to target analyte. The probing of target analyte biomolecules that diffuse through hydrogel open polymer networks and become affinity captured can be performed by the enhanced intensity of cLSP field. This approach holds potential for improved sensitivity compared to classical LSP resonance sensors due to the narrower resonance of cLSPs resonances and thus improved figure of merit. The figure of merit (FOM) can be defined as a ratio of refractive index sensitivity of LSP resonant wavelength  $\delta\lambda_{\text{LSP}}/\delta n_s$  and the width of the resonance  $\Delta\lambda_{\text{LSP}}$ .

First, we investigated the dependence of the width of the spectral band  $\Delta\lambda_{\text{LSP}}$ , on the angle of incidence  $\theta$  for the structure A with  $\Lambda = 460$ ,  $D = 110$  nm, and swollen hydrogel cushion. As seen in Figure 3, the overlapping of the Rayleigh anomaly  $\lambda_{\text{RA}}$  with  $\lambda_{\text{LSP}}$  can be adjusted by varying  $\theta$ , which thus provides an additional facile handle to control the cLSPs damping. The measured transmission spectra presented in Figure 6a show that increasing  $\theta$  leads to the splitting of the cLSP resonance and its long wavelength branch is redshifted and its spectral width  $\Delta\lambda_{\text{LSP}}$  is gradually decreased due to the approaching of  $\lambda_{\text{RA}}$  to  $\lambda_{\text{LSP}}$ . These observations are summarized in Figure 6b and show that the increase of the angle of incidence  $\theta$  from  $0^\circ$  to  $8^\circ$  shifts  $\lambda_{\text{LSP}}$  from 655 to 695 nm and is accompanied with a decrease of the full width in the half minimum of the resonance  $\Delta\lambda_{\text{LSP}}$  from 38 to 13 nm.

Second, we observed the refractive index sensitivity of prepared structure  $\delta\lambda_{\text{LSP}}/\delta n_s$  for the same structure. Aqueous solutions spiked with sucrose were prepared to control the refractive index  $n_s$  between 1.330 and 1.339 refractive index units (RIU). These solutions were sequentially flowed over the plasmonic structure surface and transmission spectra were measured for the angle of incidence  $\theta = 8^\circ$ . As can be seen in Figure 7a, increasing of the refractive index  $n_s$  is accompanied with a redshift of the cLSP wavelength  $\lambda_{\text{LSP}}$  and the refractive index sensitivity of  $\delta\lambda_{\text{LSP}}/\delta n_s = 372$  nm/RIU was measured. As summarized in Table 1 for other investigated geometries, this sensitivity is higher compared to that measured for the collapsed hydrogel cushion as the swollen polymer networks supporting the nanoparticle arrays enables accessing of the whole volume probed by cLSPs for sensing. In a nutshell, the using of hydrogel membrane carrying arrays of gold nanoparticle allows tightly overlapping the  $\lambda_{\text{LSP}}$  and  $\lambda_{\text{RA}}$  leading to a figure of merit reaching values as high as FOM = 29 in aqueous environment. In addition, the hydrophilic hydrogel networks can be post modified with capture proteins as was demonstrated for covalent attaching of IgG antibodies, which has been manifested as a shift of 6 nm in the data presented in Figure 7b.

The developed material provides FOM above the values reported before for other plasmonic nanoparticle arrays supporting cLSPs on quartz substrate with refractive index

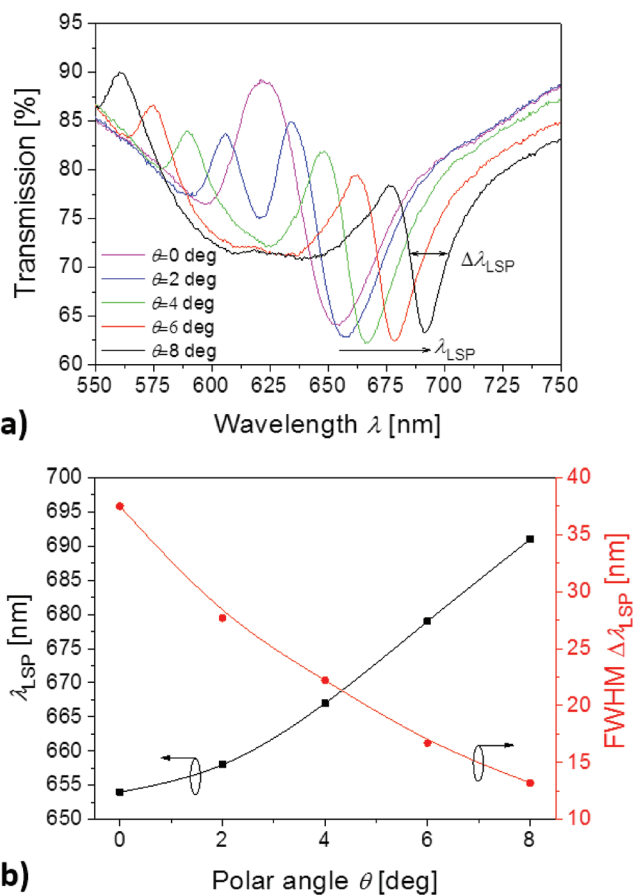


**Figure 6.** a) Wavelength transmission spectra measured for a tethered structure A as a function of the angle of incidence  $\theta$ . The measurement was done in TE polarization at  $T = 22^\circ\text{C}$  (swollen state) for a structure with  $\Lambda = 460$  nm and  $D = 110$  nm. b) Dependence of LSP wavelength position  $\lambda_{\text{LSP}}$  and the spectral width (FWHM)  $\Delta\lambda_{\text{LSP}}$  on the angle of incidence  $\theta$ .

symmetrical geometry generated by using high refractive index oils,<sup>[32]</sup> which makes the structure not suitable for biosensing applications. The response to the IgG antibody coupling is about three times larger than the variations recorded (1–2 nm) for a similar plasmonic architecture supporting cLSPs in water, composed of Au nanodisks arrays prepared on top of a low refractive index fluoropolymer (Cytop, refractive index of 1.34).<sup>[44]</sup> This can be explained by the larger probing volume and higher binding capacity conferred by the 3D hydrogel polymer networks compared to that of this architecture relying on a 2D self-assembled monolayers capping the Au nanoparticles. Moreover, it is important to note that fluoropolymers (contrary to the used hydrogel) are not suitable for chemical modification and are prone to unspecific sorption from complex samples, which complicates their utilization in biosensing.

## 3. Conclusion

New responsive architectures enabling remarkably strong modulation of extremely spectrally narrow localized surface plasmon resonances are reported. These structures are made

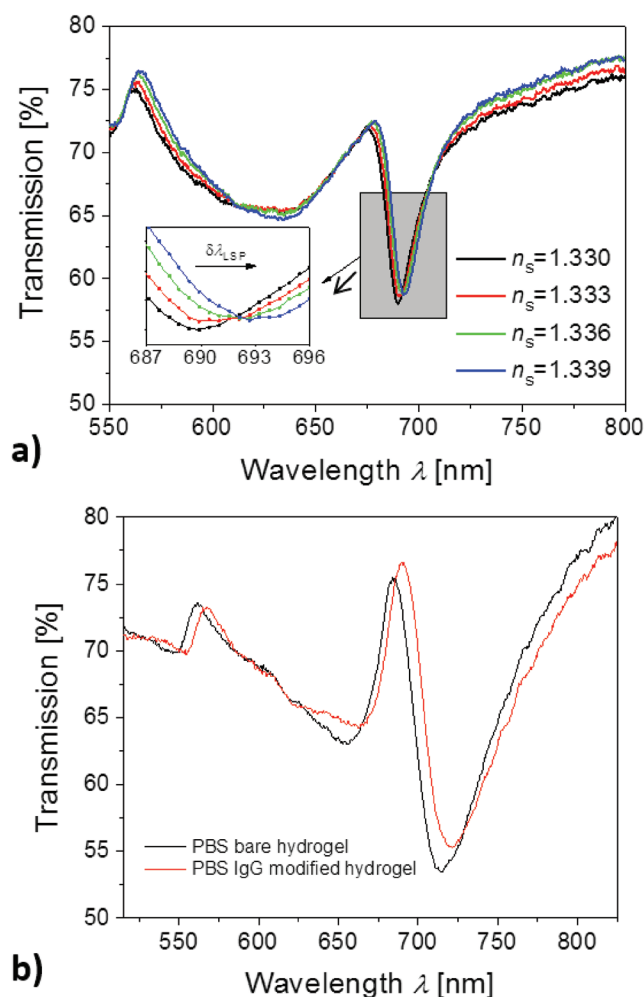


**Figure 7.** Measured dependence of LSP transmission spectra for tethered structure A on a) refractive index of a liquid brought in contact with the arrays of gold nanoparticles (prepared with  $\Lambda = 460$  nm and  $D = 110$  nm) and b) measured transmission changes due to the post-modification of the pNIPAAm-based polymer network with IgG biomolecules (structure prepared with  $\Lambda = 460$  nm and  $D = 150$  nm). Measurements were performed at the angle of incidence  $\theta = 8^\circ$ .

by a technique based on template stripping combined with UV laser interference lithography. It allows for the preparation of hybrid structures with arrays of plasmonic nanoparticles attached to a thermo-responsive hydrogel membrane with tunable period and surrounding refractive index. Compared to other approaches that combine self-assembly of synthetically-made spherical metallic nanoparticles and thermo-responsive polymer for actuating of hexagonal arrays with domain size  $< \mu\text{m}$ ,<sup>[45]</sup> the reported approach offers more versatile preparation means with controlled shape of nanoparticles and lattice configurations over larger areas with characteristic size  $> \mu\text{m}$ , and it enables actuating of the arrays period for free-standing membrane configuration. We demonstrate that the temperature modulation or exchanging the solvent allows for reversible shifting of plasmonic resonances in the near infrared part of the spectrum by up to 150 nm, which exceeds the spectral width of the resonance as low as 13 nm and allows its complete

switching “on” and “off.” The potential capabilities for bio-sensing with the tethered configuration employing a hydrogel that can be post-modified with protein ligands are assessed for the refractometric localized surface plasmon resonance biosensors, where a figure of merit as high as 29 was observed. The plasmonic architectures with on-demand tunable optical properties also hold potential to be employed as active plasmonic substrates in other biosensor modalities taking advantage of plasmonically amplified optical spectroscopy<sup>[17,46]</sup> and in miniature machines.<sup>[47]</sup> For instance, the tunable plasmonic wavelength may find its applications in multiplexed plasmon-enhanced fluorescence sensing or for the fine-tuning of surface-enhanced Raman spectroscopy enhancement for specific vibration bands.

#### 4. Experimental Section

**Materials:** Trichloro(1H,1H,2H,2H-perfluorooctyl)silane (perfluoro-silane) was obtained from Sigma-Aldrich (Germany). S1805 and A-Z303 from Microresist Technology (Germany) were employed as positive photoresist and its developer, respectively. Ostemer 322 Crystal Clear was purchased from Mercene Labs AB (Sweden). Polydimethylsiloxane Sylgard 184 was obtained from Dow Corning (USA). Dimethyl sulfoxide (DMSO), *N*-hydroxysuccinimide (NHS), *N*-(3-dimethylaminopropyl)-*N*'-ethylcarbodiimide hydrochloride (EDC), and immunoglobulin G (IgG) antibody from mouse serum were purchased from Sigma-Aldrich (Germany). Bis(acryloyl)cystamide (BAC, 98%) was from Alfa Aesar (Germany). *N,N'*-Methylenbis(acrylamide) (99%), 2-hydroxy-4'-(2-hydroxyethoxy)-2-methylpropiophenone (98%), and tris(2-carboxyethyl)-phosphine hydrochloride (TCEP,  $\geq 98\%$ ) were acquired from Sigma-Aldrich (Germany). *N*-Isopropylacrylamide (97%) from Sigma-Aldrich (Germany) was recrystallized from hexane and stored under nitrogen in the fridge until needed. In addition, a pNIPAAm-based terpolymer (composed of *N*-isopropylacrylamide, methacrylic acid, and *N*-(4-benzoylphenyl)prop-2-enamide at a ratio of 94:5:1) together with benzophenone-disulfide was synthesized as reported elsewhere.<sup>[48]</sup>

**Preparation of Gold Particle Arrays:** Perfluoro-silane was vapor deposited onto the surface of BK7 glass substrates. Briefly, the substrate was placed into an evacuated desiccator with the volume of 5.8 L and together with 13  $\mu\text{L}$  of perfluorosilane heated to  $T = 250^\circ\text{C}$  for 20 min. Then, the substrate was removed and coated by a 50 nm thick gold film by vacuum evaporation (HHV AUTO 306 from HHV LTD) in vacuum better than  $2 \times 10^{-6}$  mbar. Afterward, the gold layer was structured in order to yield periodic arrays of plasmonic nanoparticles. First, 100 nm thick S1805 resist layer was spun on top of the gold surface, followed by the recording of a periodic pattern by UV laser interference lithography according to protocol reported before.<sup>[36]</sup> Coherent beam was emitted at a wavelength of 325 nm from a HeCd laser (IK 3031 R-C from Kimmon, Japan) and exposure time was adjusted for the recording to yield an irradiation dose of 6.75  $\text{mJ cm}^{-2}$ . The beam was split to two interfering collimated waves with the angle between them set to 26.83°, 20.69°, and 16.87°, which translates to periodicities  $\Lambda$  of 360, 460, and 560 nm respectively. The pattern recorded in the photoresist layer was developed by AZ-303 developer forming periodic arrays of photoresist cylindrical features. The diameter of the photoresist features was adjusted by varying the development time between 150–240 s. Finally, the relief photoresist structure was transferred to the underneath gold layer by ion etching (450 s, 70°) with the IonSys 500 instrument from Roth & Rau (Germany). The remaining photoresist on top of the prepared gold nanoparticles was removed by an oxygen plasma treatment (5 min, 1 mbar and 40 W).

**Attachment of the Gold Nanoparticles to a Tethered Hydrogel Cushion:** First, the perfluoro-silane was deposited again in between the gold nanostructures on BK7 glass substrate, as described above. Afterward,

**Table 1.** Overview of actuating of LSP wavelength for tethered and free-standing structures and comparison of refractive index sensitivity to variations in the bulk refractive index  $n_s$ .

Geometrical parameters	$\delta\lambda_{LSP}$ [nm]	$\Delta\lambda_{LSP}$ [nm]	$\delta\lambda_{LSP}/\delta n_s$ [nm/RIU]	$\Delta\lambda_{LSP}$ [nm]	$\delta\lambda_{LSP}/\delta n_s$ [nm/RIU]
	$T = 22\text{--}45\text{ }^\circ\text{C}$	Swollen $T = 22\text{ }^\circ\text{C}$	Swollen $T = 22\text{ }^\circ\text{C}$	Collapsed $T = 45\text{ }^\circ\text{C}$	Collapsed $T = 45\text{ }^\circ\text{C}$
<b>A) Tethered hydrogel structure</b>					
$\Lambda = 460\text{ nm}$ $D = 110\text{ nm}$	18.5	38 ( $\theta = 0^\circ$ ) 13 ( $\theta = 8^\circ$ )	373	73 ( $\theta = 0^\circ$ )	190
$\Lambda = 460\text{ nm}$ $D = 150\text{ nm}$	28.6	88 ( $\theta = 0^\circ$ ) 45 ( $\theta = 8^\circ$ )	327	75 ( $\theta = 0^\circ$ )	134
$\Lambda = 560\text{ nm}$ $D = 150\text{ nm}$	29.5	56 ( $\theta = 0^\circ$ ) 35 ( $\theta = 8^\circ$ )	475	98 ( $\theta = 0^\circ$ )	329
$\Lambda = 560\text{ nm}$ $D = 200\text{ nm}$	28.2	135 ( $\theta = 0^\circ$ ) 102 ( $\theta = 8^\circ$ )	463	96 ( $\theta = 0^\circ$ )	246
<b>B) Free standing hydrogel structure</b>					
$\Lambda = 360\text{ nm}$ $D = 140\text{ nm}$	61 ( $\text{H}_2\text{O}$ ) 151 (EtOH)	66 ( $\text{H}_2\text{O}$ ) 22 (EtOH)	–	120	–

the substrate was incubated overnight in a  $1 \times 10^{-3}\text{ M}$  solution of benzophenone-disulfide dissolved in DMSO in order to form a self-assembled monolayer on the gold nanoparticles. Then a 3 wt% ethanolic solution of the pNIPAAm-based terpolymer was spun at 2000 rpm for 60 s on the substrate, and dried overnight at  $T = 50\text{ }^\circ\text{C}$  in a vacuum oven. The resulting film with a thickness of about 275 nm was crosslinked via the benzophenone moieties attached to the polymer chains by the irradiation with UV-lamp at a wavelength of 365 nm (irradiation dose of  $10\text{ J cm}^{-2}$ ). Subsequently, a drop of Ostemer resin was deposited onto the surface of another clean BK7 glass substrate and spread by pressing a flat block of PDMS on top of the droplet to form a thin layer. The Ostemer was pre-cured by irradiation with UV light at a wavelength of 365 nm (irradiation dose of  $2\text{ J cm}^{-2}$ ) through the PDMS block. Then the PDMS block was peeled-off and the substrate with the pre-cured Ostemer surface was pressed against the previously prepared gold nanoparticle arrays covered with the crosslinked pNIPAAm-based film. The elastic pre-cured Ostemer was overnight allowed to bind to the pNIPAAm-based surface via its epoxy groups at  $T = 50\text{ }^\circ\text{C}$ . Finally, the hydrogel film with attached gold nanoparticle arrays was separated from the perfluoro-silane modified BK7 substrate, see Figure 1.

**Attaching Gold Nanoparticles to Free-Standing Hydrogel Cushion:** The functionalization of gold nanoparticles with a thiol-acrylates was done by the in situ generation of *N*-(2-mercaptoethyl)acrylamide through the reduction of BAC with TCEP. In a typical experiment 10.42 mg ( $2 \times 10^{-3}\text{ M}$ ) of BAC and 11.47 mg ( $2 \times 10^{-3}\text{ M}$ ) TCEP were added to 20 mL of ethanol, and the mixture was heated to help dissolving the solids. The gold nanoparticles arrays were incubated in the freshly prepared solution for 1 h, followed by washing with ethanol and drying with a stream of dry nitrogen. Afterward, pNIPAAm film was polymerized on the top of this surface by using 1 g *N*-isopropylacrylamide monomer, 13.6 mg *N,N'*-methylenebis(acrylamide) as a crosslinker and 19.8 mg 2-hydroxy-4'-(2-hydroxyethoxy)-2-methylpropiophenone as a photoinitiator dissolved in DMSO. The polymerization was made in a home-built cell with a height of about 40  $\mu\text{m}$  under UV-irradiation in nitrogen environment ( $\text{O}_2 < 0.5\%$ ). The final structures were obtained by releasing the hydrogels by overnight incubation in ethanol yielding free-standing polymer networks with the gold particles upon drying.

**Morphological Characterization:** Atomic force microscopy in tapping mode was employed to study the topography of the tethered hydrogel film with arrays of gold nanoparticles. The measurements in air were performed by PicoPlus (Molecular Imaging, Agilent Technologies, USA), while the measurements in water were carried out by Nanowizard III (JPK Instruments, Germany) with temperature control by a Peltier element in the flow cell. The surfaces were probed by silicon nitride cantilevers DNP-S10 (Bruker, USA) with a nominal spring constant of  $0.24\text{ N m}^{-1}$ . Optical microscopy observation of nanoparticle arrays was

performed with a Nanopsis M instrument (Nanopsis Ltd., UK) utilizing super-resolution microscope amplifying lens with a focal length of 1–2  $\mu\text{m}$  (using a 20  $\mu\text{m}$  diameter barium titanate microsphere attached to the amplifying lens).

**Optical Spectroscopy of cLSPs:** Transmission spectroscopy measurements were carried out using an in-house developed optical system that was described in detail before.<sup>[36,49]</sup> Briefly, a sample with arrays of gold nanoparticles was mounted on a rotation stage driven by a stepper motor from Huber GmbH (Germany), in order to control the polar angle of collimated polychromatic light beam  $\theta$  impinging at its surface. The sample was interfaced with a flow-cell consisting of a thin PDMS gasket and transparent quartz substrate. The flow-cell with a volume of about 10  $\mu\text{L}$  was temperature controlled by using a Peltier device<sup>[17]</sup> that was connected to a driver LFI3751 from Wavelength Electronics (USA). The spectrum of light that passed through the sample was recorded by the spectrometer HR4000 from Ocean Optics (USA) or Shamrock SR-3031-B from Andor Technology (Ireland). The data were acquired and analyzed by a home-developed software in Labview from National Instruments (USA) or the software Solis from Andor Technology (UK). The acquired transmission spectra were normalized with the reference spectrum measured without the sample and corrected for the dark signal. Transporting of liquid samples through the flow-cell was conducted via fluidic tubing Tygon and a peristaltic pump from Ismatec (Switzerland) at a flow rate of  $50\text{ }\mu\text{L min}^{-1}$ . In refractometric experiments, a series of water samples were spiked with sucrose at a concentration between 2% and 6% (sucrose increases the refractive index by  $1.5 \times 10^{-3}$  refractive index units per %). The in situ post-modification of tethered pNIPAAm-based hydrogel was carried out incorporating IgG antibodies. The carboxylic groups carried by the crosslinked terpolymer were reacted with a mixture of EDC ( $75\text{ mg mL}^{-1}$ ) and NHS ( $21\text{ mg mL}^{-1}$ ) in water for 30 min. After rinsing with phosphate buffered saline (PBS), IgG protein dissolved ( $50\text{ }\mu\text{g mL}^{-1}$ ) in acetate buffer ( $\text{pH} = 4$ ) was flowed over the hydrogel surface for 60 min and finally rinsed with PBS.

**Numerical Simulations:** The finite difference time domain (FDTD) method that was implemented in a commercial software from Lumerical Inc. (Canada) was employed. The geometry of nanoparticle arrays was described by using Cartesian coordinates with the  $x$  and  $y$  axis in the plane and with  $z$  axis perpendicular to the plane of the arrays. A single unit cell with a uniform mesh size of 2 nm in all three directions was used to calculate the near field electric intensity and the far-field transmission spectra. Convergence checks lead to the conclusion that this mesh size was sufficient for accurate results. A transmission monitor was placed 0.4  $\mu\text{m}$  below the nanoparticle arrays and a 2D monitor in the  $xz$ -plane was employed for simulating near field distribution of the electric field intensity. The perfectly matched layers (PML) above and below the

structure and periodic Bloch boundary conditions in  $x$ - and  $y$ -direction were employed. Optical constants of gold were taken from literature.<sup>[50]</sup> Refractive index of a collapsed hydrogel membrane was estimated as  $n_h = 1.46$ , that of the membrane swollen in water as  $n_h = 1.34$  (refractive index of solvent  $n_s = 1.331$  at 700 nm and  $T = 25$  °C), and after swelling in ethanol as  $n_h = 1.36$  (refractive index of water  $n_s = 1.359$  at 700 nm and  $T = 20$  °C). These values were obtained assuming the volumetric swelling ratio in water of 8 (same material showed swelling in each direction of about 2 as observed for micro-disks<sup>[17,46]</sup>) and by relating this swelling ratio to data measured for similar thin hydrogel films with same volume swelling ratio.<sup>[17]</sup>

## Acknowledgements

N.G.Q., M.v.D., and D.K. acknowledge funding from the European Union's Horizon 2020 research and innovation programme under grant agreement No 642787, Marie Skłodowska-Curie Innovative Training Network BIOGEL, P.V. from the project jointly funded by Agence Nationale de la Recherche (ANR) and Austrian Science Fund (FWF) under the grant agreements ANR-15-CE29-0026 and I 2647, respectively. C.P. received support from the European Union's Horizon 2020 research and the innovation program under Grant Agreement No. 633937, project ULTRAPLACAD.

## Conflict of Interest

The authors declare no conflict of interest.

## Keywords

active plasmonics, biosensing, lattice resonance, metallic nanoparticles, responsive hydrogels

Received: February 26, 2019

Revised: April 19, 2019

Published online: May 20, 2019

- [1] D. K. Gramotnev, S. I. Bozhevolnyi, *Nat. Photonics* **2010**, *4*, 83.
- [2] a) J. A. Schuller, E. S. Barnard, W. Cai, Y. C. Jun, J. S. White, M. L. Brongersma, *Nat. Mater.* **2010**, *9*, 193; b) E. Ozbay, *Science* **2006**, *311*, 189.
- [3] a) H. A. Atwater, A. Polman, *Nat. Mater.* **2010**, *9*, 205; b) A. Aubry, D. Y. Lei, A. I. Fernández-Domínguez, Y. Sonnefraud, S. A. Maier, J. B. Pendry, *Nano Lett.* **2010**, *10*, 2574.
- [4] a) P. Wang, B. Huang, Y. Dai, M.-H. Whangbo, *Phys. Chem. Chem. Phys.* **2012**, *14*, 9813; b) I. Thomann, B. A. Pinaud, Z. Chen, B. M. Clemens, T. F. Jaramillo, M. L. Brongersma, *Nano Lett.* **2011**, *11*, 3440.
- [5] a) H. Wei, H. Xu, *Nanophotonics* **2012**, *1*, 155; b) Y. Fang, M. Sun, *Light: Sci. Appl.* **2015**, *4*, e294.
- [6] A. J. Haes, C. L. Haynes, A. D. McFarland, G. C. Schatz, R. P. Van Duyne, S. Zou, *MRS Bull.* **2005**, *30*, 368.
- [7] a) B. Špačková, P. Wrobel, M. Bocková, J. Homola, *Proc. IEEE* **2016**, *104*, 2380; b) M. E. Stewart, C. R. Anderton, L. B. Thompson, J. Maria, S. K. Gray, J. A. Rogers, R. G. Nuzzo, *Chem. Rev.* **2008**, *108*, 494.
- [8] S. Lal, N. K. Grady, J. Kundu, C. S. Levin, J. B. Lassiter, N. J. Halas, *Chem. Soc. Rev.* **2008**, *37*, 898.
- [9] a) K. F. MacDonald, Z. L. Sámson, M. I. Stockman, N. I. Zheludev, *Nat. Photonics* **2009**, *3*, 55; b) L. Cao, M. L. Brongersma, *Nat. Photonics* **2009**, *3*, 12; c) K. F. MacDonald, N. I. Zheludev, *Laser Photonics Rev.* **2010**, *4*, 562; d) B. Gjonaj, J. Aulbach, P. M. Johnson, A. P. Mosk, L. Kuipers, A. Lagendijk, *Nat. Photonics* **2011**, *5*, 360.
- [10] a) A. Emboras, C. Hoessbacher, C. Haffner, W. Heni, U. Koch, P. Ma, Y. Fedoryshyn, J. Niegemann, C. Hafner, J. Leuthold, *IEEE J. Sel. Top. Quantum Electron.* **2015**, *21*, 276; b) W. Cai, J. S. White, M. L. Brongersma, *Nano Lett.* **2009**, *9*, 4403.
- [11] a) V. K. Hsiao, Y. B. Zheng, B. K. Juluri, T. J. Huang, *Adv. Mater.* **2008**, *20*, 3528; b) T. Ming, L. Zhao, M. Xiao, J. Wang, *Small* **2010**, *6*, 2514.
- [12] a) T. Ellenbogen, K. Seo, K. B. Crozier, *Nano Lett.* **2012**, *12*, 1026; b) L. Wang, T. Li, R. Guo, W. Xia, X. Xu, S. Zhu, *Sci. Rep.* **2013**, *2603*, 3.
- [13] a) N. Dean, *Nat. Nanotechnol.* **2015**, *10*, 15; b) Z. Li, A. W. Clark, J. M. Cooper, *ACS Nano* **2016**, *10*, 498; c) K. Xiong, D. Tordera, G. Emilsson, O. Olsson, U. Linderhed, M. P. Jonsson, A. B. Dahlin, *Nano Lett.* **2017**, *17*, 7033.
- [14] a) M. G. Manera, E. Ferreira-Vila, J. M. Garcia-Martin, A. Garcia-Martin, R. Rella, *Biosens. Bioelectron.* **2014**, *58*, 114; b) Y. B. Zheng, Y.-W. Yang, L. Jensen, L. Fang, B. K. Juluri, A. H. Flood, P. S. Weiss, J. F. Stoddart, T. J. Huang, *Nano Lett.* **2009**, *9*, 819; c) D. Yoo, T. W. Johnson, S. Cherukulappurath, D. J. Norris, S.-H. Oh, *ACS Nano* **2015**, *9*, 10647.
- [15] N. Jiang, X. Zhuo, J. Wang, *Chem. Rev.* **2018**, *118*, 3054.
- [16] a) G. K. Joshi, K. N. Blodgett, B. B. Muhoherac, M. A. Johnson, K. A. Smith, R. Sardar, *Nano Lett.* **2014**, *14*, 532; b) J. Dintinger, I. Robel, P. V. Kamat, C. Genet, T. W. Ebbesen, *Adv. Mater.* **2006**, *18*, 1645.
- [17] M. Toma, U. Jonas, A. Mateescu, W. Knoll, J. Dostalek, *J. Phys. Chem. C* **2013**, *117*, 11705.
- [18] J.-W. Jeon, J. Zhou, J. A. Geldmeier, J. F. Ponder Jr., M. A. Mahmoud, M. El-Sayed, J. R. Reynolds, V. V. Tsukruk, *Chem. Mater.* **2016**, *28*, 7551.
- [19] V. Stockhausen, P. Martin, J. Ghilane, Y. Leroux, H. Randriamahazaka, J. Grand, N. Felidj, J. C. Lacroix, *J. Am. Chem. Soc.* **2010**, *132*, 10224.
- [20] a) W. Lu, N. Jiang, J. Wang, *Adv. Mater.* **2017**, *29*, 1604862; b) N. Jiang, L. Shao, J. Wang, *Adv. Mater.* **2014**, *26*, 3282.
- [21] Z. Sun, W. Ni, Z. Yang, X. Kou, L. Li, J. Wang, *Small* **2008**, *4*, 1287.
- [22] I. Tokareva, S. Minko, J. H. Fendler, E. Hutter, *J. Am. Chem. Soc.* **2004**, *126*, 15950.
- [23] M. L. Tseng, J. Yang, M. Semmlinger, C. Zhang, P. Nordlander, N. J. Halas, *Nano Lett.* **2017**, *17*, 6034.
- [24] a) Y. Yao, M. A. Kats, P. Genevet, N. Yu, Y. Song, J. Kong, F. Capasso, *Nano Lett.* **2013**, *13*, 1257; b) Y. Yao, M. A. Kats, R. Shankar, Y. Song, J. Kong, M. Loncar, F. Capasso, *Nano Lett.* **2014**, *14*, 214.
- [25] G. Lilley, M. Messner, K. Unterrainer, *Opt. Mater. Express* **2015**, *5*, 2112.
- [26] Y. Chu, E. Schonbrun, T. Yang, K. B. Crozier, *Appl. Phys. Lett.* **2008**, *93*, 181108.
- [27] S. R. K. Rodriguez, A. Abass, B. Maes, O. T. Janssen, G. Vecchi, J. G. Rivas, *Phys. Rev. X* **2011**, *1*, 021019.
- [28] M. Bauch, J. Dostalek, *Opt. Express* **2013**, *21*, 20470.
- [29] a) B. Ng, S. Hanham, V. Giannini, Z. Chen, M. Tang, Y. Liew, N. Klein, M. Hong, S. Maier, *Opt. Express* **2011**, *19*, 14653; b) P. Offermans, M. C. Schaafsma, S. R. Rodriguez, Y. Zhang, M. Crego-Calama, S. H. Brongersma, J. Gómez Rivas, *ACS Nano* **2011**, *5*, 5151.
- [30] a) K. Carron, W. Fluhr, M. Meier, A. Wokaun, H. Lehmann, *J. Opt. Soc. Am. B* **1986**, *3*, 430; b) G. Vecchi, V. Giannini, J. G. Rivas, *Phys. Rev. Lett.* **2009**, *102*, 146807.
- [31] Z. Li, S. Butun, K. Aydin, *ACS Nano* **2014**, *8*, 8242.
- [32] W. Zhou, M. Dridi, J. Y. Suh, C. H. Kim, M. R. Wasielewski, G. C. Schatz, T. W. Odom, *Nat. Nanotechnol.* **2013**, *8*, 506.
- [33] a) B. Auguie, W. L. Barnes, *Phys. Rev. Lett.* **2008**, *101*, 143902; b) A. D. Humphrey, W. L. Barnes, *Phys. Rev. B* **2014**, *90*, 075404.



- [34] J. Q. Li, J. Ye, C. Chen, L. Hermans, N. Verellen, J. Ryken, H. Jans, W. Van Roy, V. V. Moshchalkov, L. Lagae, P. Van Dorpe, *Adv. Opt. Mater.* **2015**, *3*, 176.
- [35] K. Volk, J. P. Fitzgerald, P. Ruckdeschel, M. Retsch, T. A. König, M. Karg, *Adv. Opt. Mater.* **2017**, *5*, 1600971.
- [36] N. G. Quilis, M. Lequeux, P. Venugopalan, I. Khan, W. Knoll, S. Boujday, M. L. de la Chapelle, J. Dostalek, *Nanoscale* **2018**, *10*, 10268.
- [37] M. J. Junk, R. d. Berger, U. Jonas, *Langmuir* **2010**, *26*, 7262.
- [38] Y. Wang, C.-J. Huang, U. Jonas, T. Wei, J. Dostalek, W. Knoll, *Biosens. Bioelectron.* **2010**, *25*, 1663.
- [39] B. Špačková, J. Homola, *Opt. Express* **2013**, *21*, 27490.
- [40] I. Anac, A. Aulasevich, M. J. N. Junk, P. Jakubowicz, R. F. Roskamp, B. Menges, U. Jonas, W. Knoll, *Macromol. Chem. Phys.* **2010**, *211*, 1018.
- [41] Q. Zhang, Y. Wang, A. Mateescu, K. Sergelen, A. Kibrom, U. Jonas, T. Wei, J. Dostalek, *Talanta* **2013**, *104*, 149.
- [42] C. J. Huang, J. Dostalek, W. Knoll, *Biosens. Bioelectron.* **2010**, *26*, 1425.
- [43] A. Aulasevich, R. F. Roskamp, U. Jonas, B. Menges, J. Dostalek, W. Knoll, *Macromol. Rapid Commun.* **2009**, *30*, 872.
- [44] J. Li, J. Ye, C. Chen, L. Hermans, N. Verellen, J. Ryken, H. Jans, W. Van Roy, V. V. Moshchalkov, L. Lagae, *Adv. Opt. Mater.* **2015**, *3*, 176.
- [45] a) K. Volk, J. P. S. Fitzgerald, P. Ruckdeschel, M. Retsch, T. A. F. König, M. Karg, *Adv. Opt. Mater.* **2017**, *5*, 1600971; b) K. Volk, J. P. S. Fitzgerald, M. Retsch, M. Karg, *Adv. Mater.* **2015**, *27*, 7332.
- [46] M. Nguyen, I. Kherbouche, M. Braik, A. Belkhir, L. Boubekeur-Lecaque, J. Aubard, C. Mangeney, N. Felidj, *ACS Omega* **2019**, *4*, 1144.
- [47] A. Mourran, H. Zhang, R. Vinokur, M. Moller, *Adv. Mater.* **2017**, *29*, 1604825.
- [48] K. Sergelen, C. Petri, U. Jonas, J. Dostalek, *Biointerphases* **2017**, *12*, 051002.
- [49] I. Khan, H. Keshmiri, F. Kolb, T. Dimopoulos, E. J. List-Kratochvil, J. Dostalek, *Adv. Opt. Mater.* **2016**, *4*, 435.
- [50] P. B. Johnson, R.-W. Christy, *Phys. Rev. B* **1972**, *6*, 4370.

# 3.3

UV-Laser interference lithography for local  
functionalization of plasmonic nanostructures  
with responsive hydrogel

# UV-Laser Interference Lithography for Local Functionalization of Plasmonic Nanostructures with Responsive Hydrogel

Nestor Gisbert Quilis, Simone Hageneder, Stefan Fossati, Simone K. Auer, Priyamvada Venugopalan, Anil Bozdogan, Christian Petri, Alberto Moreno-Cencerrado, Jose Luis Toca-Herrera, Ulrich Jonas, and Jakub Dostalek\*

Cite This: *J. Phys. Chem. C* 2020, 124, 3297–3305

Read Online

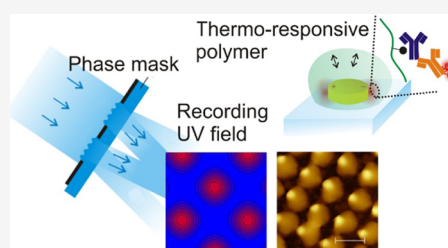
ACCESS |

Metrics & More

Article Recommendations

Supporting Information

**ABSTRACT:** A novel approach to local functionalization of plasmonic hotspots at gold nanoparticles with biofunctional moieties is reported. It relies on photocrosslinking and attachment of a responsive hydrogel binding matrix by the use of a UV interference field. A thermoresponsive poly(*N*-isopropylacrylamide)-based (pNIPAAm) hydrogel with photocrosslinkable benzophenone groups and carboxylic groups for its postmodification was employed. UV-laser interference lithography with a phase mask configuration allowed for the generation of a high-contrast interference field that was used for the recording of periodic arrays of pNIPAAm-based hydrogel features with the size as small as 170 nm. These hydrogel arrays were overlaid and attached on the top of periodic arrays of gold nanoparticles, exhibiting a diameter of 130 nm and employed as a three-dimensional binding matrix in a plasmonic biosensor. Such a hybrid material was postmodified with ligand biomolecules and utilized for plasmon-enhanced fluorescence readout of an immunoassay. Additional enhancement of the fluorescence sensor signal by the collapse of the responsive hydrogel binding matrix that compacts the target analyte at the plasmonic hotspot is demonstrated.



## INTRODUCTION

A variety of naturally occurring or synthetic biopolymers has been tailored for specific biomedical<sup>1</sup> and analytical<sup>2</sup> applications, and among these, stimuli-responsive polymers represent particularly attractive “smart” materials capitalizing on their ability to undergo physical or chemical changes triggered by an external stimulus.<sup>3–5</sup> Such materials can be incorporated into architectures that are on-demand actuated by stimuli, including temperature, pH, or electric current.<sup>6–8</sup> A prominent example of a responsive polymer is the poly(*N*-isopropylacrylamide) (pNIPAAm), which is well-known for its thermoresponsive behavior. pNIPAAm exhibits a lower critical solution temperature (LCST) with pronounced and fully reversible hydrophobic-to-hydrophilic transition close to the body temperature.<sup>9</sup> pNIPAAm has been utilized in drug delivery micro/nanogels,<sup>10</sup> for modulating cellular interactions,<sup>5,11</sup> biosensors,<sup>12</sup> and in opto-responsive coatings.<sup>13</sup>

The nanoscale patterning of responsive polymer materials is important to let them serve in diverse areas ranging from sensing,<sup>14</sup> optical components,<sup>15</sup> and catalysis<sup>16</sup> to tissue engineering<sup>17</sup> and cell biology.<sup>18</sup> Self-assembly represents a widely used method for the preparation of nano- and microstructures based on, for instance, block-copolymer that combines hydrophobic and hydrophilic segments.<sup>19,20</sup> In addition, casting of microstructures by polymerization in template cavities has been utilized for the fabrication of miniature responsive polymer objects actuated in aqueous solution.<sup>21</sup> To prepare structures that are attached to a solid

surface, photolithography has been extensively used for various types of responsive polymer structures.<sup>22</sup> Shadow mask photolithography-based methods typically enable facile means for the patterning of microstructures over macroscopic areas. To gain finer nanoscale control of the morphology of responsive polymer structures, electron beam lithography was employed for the structuring on a small footprint.<sup>23,24</sup> In addition, UV nanoimprint lithography has been introduced to harness both nanoscale precision and compatibility with scaled-up production.<sup>25</sup> This method is based on a transfer of a target motif carried by a stamp to a polymer layer by the subsequent polymerization<sup>26</sup> or photocrosslinking.<sup>27</sup>

Metallic nanostructures can be incorporated into responsive polymer architectures to provide means for their optical actuating<sup>28,29</sup> or to be employed for the optical readout in bioanalytical applications.<sup>30</sup> Metallic nanostructures support localized surface plasmons (LSPs) that tightly confine the electromagnetic field in their vicinity through its coupling with collective charge density oscillations. The resonant excitation of LSPs is accompanied by a strongly enhanced electromagnetic field intensity,<sup>31</sup> locally increased temperature<sup>32</sup> or, for instance, an emission of hot electrons.<sup>33</sup> In bioanalytical

Received: November 26, 2019

Revised: January 9, 2020

Published: January 10, 2020

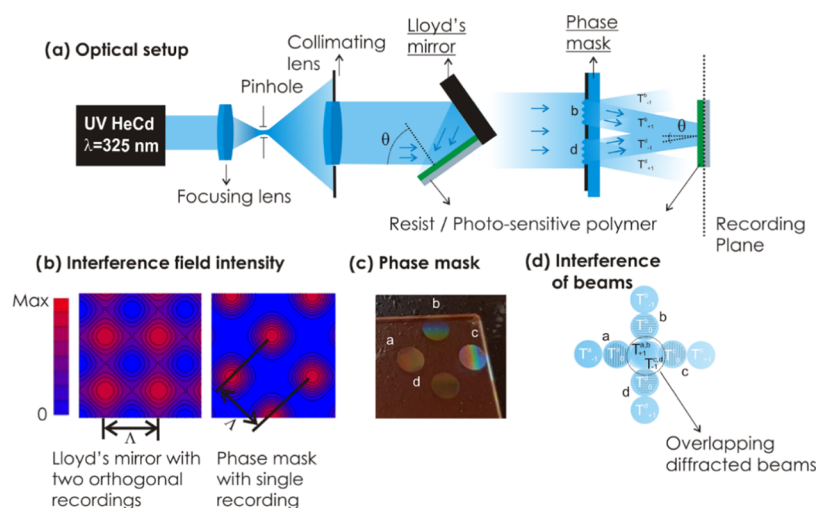


**Figure 1.** (a) Optical configuration of the UV-laser interference lithography with Lloyd's mirror configuration (left) and the phase mask configuration (right). (b) Simulations of the interference field generated by Lloyd's mirror configuration (left) and developed phase mask (right). (c) Schematics of the phase mask carrying four circular transmission gratings marked as a, b, c, and d. (d) Schematics of the overlapping of collimated waves at the recording plane with zero-order  $T_0$  and first-order diffracted  $T_{+/-1}$  beams.

sensing applications, the LSPs are utilized for the probing of target molecules that are brought in contact with the metallic nanoparticles. In affinity-based plasmonic biosensors, mostly thiol self-assembled monolayers are deployed at the two-dimensional (2D) surface of plasmonic nanoparticles for attaching of ligand molecules that specifically capture target molecules from the analyzed liquid sample.<sup>34</sup> In general, the sensitivity of LSP-based biosensors can be advanced by strategies that allow for selective capture of target analytes only at the regions where the electromagnetic field is confined (e.g., edges and walls of cylindrical gold nanoparticles), commonly referred as to “plasmonic hotspots”. To deploy ligand molecules that specifically capture target species at the plasmonic hotspot, 2D surface architectures were combined with lithography-based strategies generating masks.<sup>35,36</sup> In addition, other strategies, including material-orthogonal chemistries,<sup>37</sup> surface plasmon-triggered polymerization,<sup>38</sup> and surface plasmon-enhanced two-photon cleavage of photosensitive organic moieties,<sup>39</sup> have been reported to attain local functionalization of metallic nanostructures.

The LSPs typically probe rather small subareas of the metallic nanoparticles, and their field reaches only a short distance of several tens of nanometers away from their surface.<sup>40</sup> Therefore, the performance of various LSP-based biosensor modalities is hindered by the reduced probability of analyte capture in these narrow spatial zones, where the electromagnetic field is confined. The use of biointerfaces composed of 3D polymer brushes or networks provides means to increase the surface area and respective binding capacity,<sup>41,42</sup> offering higher capture probability of the target analyte in the hotspot zones probed by LSPs. The present paper reports on the local attachment of a 3D hydrogel binding matrix in the vicinity of well-ordered gold nanoparticles, which can be postmodified for specific affinity capture of target analytes and actuated for their compacting at the plasmonic hotspot.

## METHODS

**Materials.** OrmoPrime08, S1805 and SU-8 photoresist, SU-8 2000 thinner, and an AZ303 developer were purchased

from Micro Resist Technology (Germany). Dimethyl sulfoxide (DMSO), acetic acid, propylene glycol monomethyl ether acetate, and 1-ethyl-3-(3-dimethylaminopropyl)carbodiimide (EDC) were obtained from Sigma Aldrich (Germany). pNIPAAm-based terpolymer composed of *N*-isopropylacrylamide, methacrylic acid, and 4-methacryloyloxybenzophenone (in a ratio of 94:5:1), benzophenone disulfide, and 4-sulfotetrafluorophenol (TFPS) were synthesized in our laboratory as previously reported.<sup>43–45</sup>

IgG from mouse serum (mIgG, I 5381), Tween 20 (P9416), and bovine serum albumin (A2153) were purchased from Sigma Aldrich (Austria). Phosphate-buffered saline (PBS) and sodium acetate were obtained from VWR Chemicals (Austria). Alexa Fluor 790 goat anti-mouse IgG (a-mIgG, A11375) was acquired from Life Technologies (Eugene, OR).

**Optical Configuration of Laser Interference Lithography.** A He-Cd laser (IK 3031 R-C) from Kimmon (Japan) emitting at  $\lambda = 325$  nm with 4 mW was employed. The coherent beam was expanded with a spatial filter consisting of a pinhole (10  $\mu\text{m}$ ) and  $\times 40$  microscope lens. For Lloyd's mirror configuration, the expanded beam was collimated and impinged at a substrate carrying a photosensitive polymer and a UV-reflecting mirror with the area of several  $\text{cm}^2$ . The measured intensity of the beam in the recording plane was around 30  $\mu\text{W cm}^{-2}$ . For recording with the phase mask configuration, the power of the recording field in the recording plane was increased to 400  $\mu\text{W cm}^{-2}$ .

**Preparation of a Phase Mask.** OrmoPrime08 was employed as an adhesion promoter to prevent delamination of the resist. A Quartz substrate (20  $\times$  20  $\times$  1 mm) was dehydrated on a hot plate for 5 min at 200  $^\circ\text{C}$ , and the OrmoPrime solution composed of organofunctional silanes was subsequently spun on the top at 4000 rpm for 60 s. Then, the substrate was placed on the hot plate for 5 min at 150  $^\circ\text{C}$ . Afterward, undiluted S1805 positive photoresist was deposited at a spin rate of 4500 rpm applied for 45 s followed by a hard-bake treatment at 100  $^\circ\text{C}$  for 2 min. The substrate with a photoresist was placed in Lloyd's mirror setup for recording by laser interference lithography as previously reported.<sup>46</sup> An interference pattern, originating from two interfering beams,

was recorded in the photoresist layer, and a stencil mask with two symmetric circular apertures was utilized to define the area to be exposed. Custom-made stainless stencil masks were fabricated from PIU-PRINTEX (Austria) and carefully placed on top of the photoresist-coated glass substrates. The irradiation dose of  $18 \text{ mJ cm}^{-2}$  was used for the recording of two circular gratings, and subsequently, the substrate was rotated  $90^\circ$  and exposed once more to the same interference field with the same dose. Finally, the phase mask carrying 4 transmission gratings with two perpendicular orientations was obtained by immersing the substrate in the AZ303 developer solution diluted with deionized water (1:15 ratio) for 40 s. The angle of the collimated interfering beams was set to  $\theta = 13.6^\circ$ , yielding a period of the four gratings of  $\Lambda_{\text{PM}} = 690 \text{ nm}$ . The circular patterned area of each of the four gratings exhibited a diameter of 4 mm (see Figure 1). The measured depth of the resist gratings was about 250 nm (see Figure S1). This depth was achieved by optimizing the developing time after the recording step, and it corresponds to that providing the maximum efficiency of the first-order diffraction in transmission mode (of about 30%, data not shown).

**Preparation of Gold Nanoparticles.** Gold nanoparticle arrays were prepared as previously reported by the use of two-beam laser interference lithography with Lloyd's configuration.<sup>46</sup> Briefly, 2 nm Cr and 50 nm Au were evaporated (HHV AUTO 306 from HHV Ltd) on top of BK7 glass slides with the size of  $20 \times 20 \text{ mm}$ . Subsequently, a 100 nm thick layer of S1805 positive photoresist (diluted 1:2 with propylene glycol monomethyl ether acetate) was deposited at a spin rate of 4500 rpm applied for 45 s. Hard-baking of the resist was conducted at  $100^\circ \text{C}$  for 2 min. The angle between the interfering beams was set to  $\theta = 20.69^\circ$  yielding a period of  $\Lambda_{\text{G}} = 460 \text{ nm}$ , and the dose was set to  $6.75 \text{ mJ cm}^{-2}$ . The parameters were adjusted to obtain arrays of cylindrical resist features with a diameter of  $D = 132 \pm 5 \text{ nm}$  after the development step using the AZ303 developer (1:15 ratio deionized water). The arrays of resist features were transferred to the underlying gold layer using a dry etching process consisting of the bombardment of the surface with argon ions (Roth & Rau IonSys 500). Resist-free gold nanoparticles were finally obtained by exposing the substrate to an oxygen plasma process.

**Preparation of Hydrogel Nanostructures.** Covalent attachment of the pNIPAAm-based polymer to a BK7 glass substrate was achieved using a thin SU-8 linker layer. SU-8 was dissolved with its thinner (2% solution) and spun onto the surface of the BK7 glass substrate at the spin rate of 5000 rpm for 60 s. Afterward, the coated substrate was thermally cured in an oven at  $50^\circ \text{C}$  for 2 h. To attach the pNIPAAm-based polymer to gold nanoparticles, their gold surface was modified with UV-reactive benzophenone moieties by reacting overnight with 1 mM benzophenone disulfide dissolved in DMSO. Subsequently, a 2% pNIPAAm-based polymer dissolved in ethanol was spun (2000 rpm for 2 min) over the flat substrate (with SU-8 or with gold nanoparticle arrays carrying benzophenone disulfide), followed by its overnight drying in a vacuum oven ( $T = 50^\circ \text{C}$ ). The pNIPAAm-coated substrate was placed in the laser interference lithography setup. The 4-beam phase mask with  $\Lambda_{\text{PM}} = 690 \text{ nm}$  and the pNIPAAm-based polymer-coated substrate were made parallel to each other and separated by a distance of 5.6 mm by in-house made dedicated holders. The recording was carried out by four interfering beams transmitted through the phase mask ( $T_{-1}$

and  $T_{+1}$  transmission diffraction orders) with the middle part blocked to prevent the interference with a normally propagating beam ( $T_0$ ). The irradiation dose was set between 84 and  $240 \text{ mJ cm}^{-2}$  for the SU-8 substrates by adjusting the irradiation time and by keeping the intensity of the UV beam fixed ( $400 \mu\text{W cm}^{-2}$ ). Local crosslinking of the pNIPAAm-based polymer on top of gold nanoparticle arrays was attained by exposure to the UV interference field with a dose of  $108 \text{ mJ cm}^{-2}$  and the same UV beam intensity ( $400 \mu\text{W cm}^{-2}$ ). The irradiation dose was obtained as a product of the power of the collimated UV beam and the irradiation time that was set between 210 and 600 s. The pNIPAAm-based polymer in the nonexposed regions was washed away with deionized water, and the obtained structure was dried on the hot plate at a temperature above the LCST of pNIPAAm. For the control experiment, a 30 nm thick pNIPAAm hydrogel layer was attached and crosslinked on a flat 100 nm Au film that was reacted with benzophenone disulfide using a UV lamp (365 nm) and an irradiation dose of  $2 \text{ J cm}^{-2}$ .

**Morphological Characterization.** Atomic force microscopy (AFM) measurements of the patterned structures in contact with air were performed in tapping mode with the PicoPlus instrument (Molecular Imaging, Agilent Technologies). The topography in contact with water was observed in situ with the Nanowizard III (JPK Instruments, Germany) using a temperature-controlled module consisting of a flow cell with a Peltier element. Silicon nitride cantilevers DNP-S10 (Bruker) with a nominal spring constant of  $0.24 \text{ N m}^{-1}$  were utilized. Height, diameter, and lateral spacing of the nanoscale features were determined by employing Gwyddion free software.

**LSPR Transmission Measurements.** The polychromatic light beam emitted from a halogen lamp (LSH102 LOT-Oriel, Germany) was coupled to a multimode optical fiber. This beam was out-coupled from the fiber, collimated with a lens, and made normally incident at a substrate carrying arrays of gold nanoparticles. The transmitted beam was collected by a lens to another multimode optical fiber and delivered to a Shamrock SR-303I-B spectrometer from Andor Technology (Ireland). The obtained transmission spectra were normalized with that obtained without the investigated substrate. A flow cell with a Peltier element<sup>12</sup> was clamped against the substrate with the gold nanoparticles to control the temperature of the liquid flowed over its surface. Deionized water was flowed through using a peristaltic pump from Ismatec (Switzerland).

**Plasmon-Enhanced Fluorescence Instrument.** Fluorescence experiments were conducted with an in-house-developed fluorescence reader utilizing epifluorescence geometry.<sup>47</sup> The biochip carrying arrays of gold nanoparticles wrapped by the pNIPAAm-based hydrogel was placed in a microfluidic module with a flow cell and illuminated with a collimated beam at a wavelength of 785 nm and an intensity of  $1.2 \text{ mW cm}^{-2}$ . The spatial distribution of intensity of fluorescence light emitted at a wavelength of 810 nm at the biochip surface was collected and then detected with a cooled CCD camera. The optical system can be seen in Figure S2. It consisted of a diode laser (IBeam Smart 785 nm, TOptica, DE) that emitted a collimated monochromatic beam, which passed through a narrow bandwidth laser clean-up filter (LL01-785, Semrock) and a spatial filter built from a  $60\times$  microscope objective, a  $40 \mu\text{m}$  pinhole, and a collimating lens (AC-254-40-B, Thorlabs) to reduce the speckles. The excitation beam traveled through a lens (AC-254-35-B, Thorlabs) and was

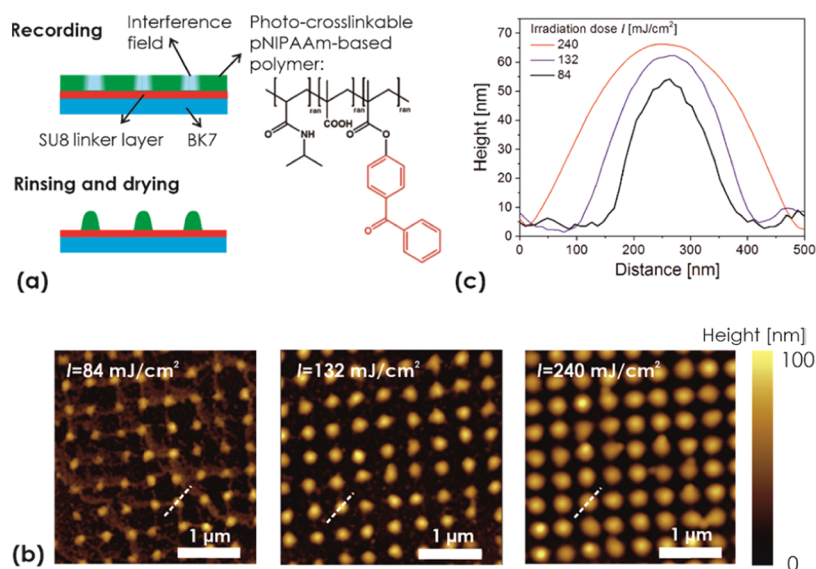


**Figure 2.** (a) Schematics of the local crosslinking of a responsive pNIPAAm-based polymer layer with arrays of interference maxima. The effect of the irradiation dose on (b) overall topography as observed with AFM and (c) the polymer feature cross-section.

reflected at a dichroic mirror (Di02-R785, Semrock) toward the biochip with arrays of gold nanoparticles. The incident excitation beam was then passed through another lens (AC-254-35-B, Thorlabs) to become recollimated before impinging on the biochip. The biochip was placed in the focal plane of the last lens in an in-house built microfluidic device. It was clamped against a flow cell that was temperature-controlled by the use of a Peltier device. Fluorescence light emitted at the biochip surface at a wavelength of 810 nm was collected by the same lens and passed through the dichroic mirror toward the detector. After passing an imaging lens (AC-254-80-B, Thorlabs), the remaining light at the excitation wavelength of 785 nm was blocked with a notch filter (NF03-785E-25, Semrock) and a fluorescence bandpass filter (FF01-810/10-25, Semrock) before hitting a scientific EM-CCD camera (Ixon 885K, Andor, UK). The camera was operated at a stable temperature of  $-70\text{ }^{\circ}\text{C}$ , and 10 images for 1 s exposure time were accumulated for an increased dynamic range. The whole device was controlled, and the data were collected by the in-house developed dedicated LabView-based software. It was used for the acquisition of fluorescence intensity from arrays of circular spots (each spot exhibited a diameter of  $220\text{ }\mu\text{m}$ ). The acquired fluorescence intensity from each spot was averaged over its area from the raw image acquired by the optical system with an optical resolution limited to about  $4\text{ }\mu\text{m}$  owing to the size of the CCD camera pixel of  $8\text{ }\mu\text{m}$  and optical magnification of 2.

**Immunoassay Experiment.** COOH groups carried by the pNIPAAm-based polymer chains on the biochip surface were activated by reacting for 15 min with EDC and TFPS dissolved in water at a concentration of 75 and 21 mg/mL, respectively. A substrate with pNIPAAm-based polymer networks forming a hydrogel nanostructure overlaid with gold nanoparticle arrays or a thin hydrogel layer on the top of a flat gold film was then rinsed with deionized water, dried, and reacted with mIgG dissolved at a concentration of  $50\text{ }\mu\text{g/mL}$  in acetate buffer (pH 4) for 90 min under shaking. Afterward, the surface was washed two times for 15 min with PBS working buffer, which contained 0.05% Tween 20 and 1 mg/mL BSA. Then, the substrate was rinsed, dried, and clamped into a flow cell to

perform plasmon-enhanced fluorescence observation of affinity binding inside the pNIPAAm-based hydrogel matrix. The flow cell was connected to a peristaltic pump through a microfluidic tubing system with a total volume of  $\approx 1\text{ mL}$ . After establishing a stable baseline in the fluorescence signal upon a flow of working buffer (PBS with Tween and BSA), changes in the fluorescence signal emitted from different spots on the biochip due to the affinity binding were measured using dedicated LabView-based software. A dilution series of a-mIgG (conjugated with Alexa Fluor 790) at concentrations of 1, 5, 10, 50, and 100 pM and a volume of 1 mL were flowed over the biochip surface for 15 min, followed by a 5 min rinsing with the working buffer in between.

## RESULTS AND DISCUSSION

At first, the patterning of pNIPAAm-based nanostructures by UV-laser interference lithography (UV-LIL) with a phase mask configuration is described. This approach allows for generating a high-contrast UV interference field pattern that is used for nanoscale control of the attachment and crosslinking of a responsive pNIPAAm-based polymer. This strategy is then employed to overlay at the nanoscale pNIPAAm structure with periodic arrays of gold nanoparticles supporting LSPs. The LSPs supported by these nanoparticles are employed to observe swelling and collapsing of the pNIPAAm hydrogel, which caps the gold nanoparticle surface, by means of detuning the resonant wavelength at which the LSPs are optically excited. In addition, this wavelength is closely tuned to the absorption and emission wavelengths of a fluorophore that serves as a label in fluorescence immunoassays. Consequently, the pNIPAAm-based hydrogel is employed as a binding matrix that is postmodified with a protein ligand and utilized for surface plasmon-amplified fluorescence readout of the assay. Additional signal enhancement by the collapse of the gel is demonstrated using the developed hybrid plasmonic material.

**UV-Laser Interference Lithography with a Phase Mask.** As illustrated in Figure 1a, laser interference lithography relies on the recording of an interference pattern formed by overlapping coherent optical beams to a photosensitive polymer layer. In the UV-LIL configuration with Lloyd's

mirror shown in Figure 1b, a periodic sinusoidal pattern is recorded by two plane waves impinging on a layer of the photosensitive polymer at an angle  $\theta$ . The recorded structure typically exhibits smoothly varying features<sup>48</sup> arranged in an array with a period equal to  $\Lambda = \lambda/2 \sin(\theta)$ , where  $\lambda$  is the wavelength of the recording interference beam. To record a periodic pattern with higher contrast, we employed four interfering waves with a setup shown in Figure 1a, featuring a phase mask. This phase mask consists of four transmission gratings a, b, c, and d on a UV-transparent glass slide, as depicted in Figure 1c. The area between the gratings is made reflective; thus, only the coherent plane wave impinging on the grating regions of the mask is transmitted. Each grating diffracts the coherent incident beam to a series of transmission orders marked as  $T_{-1}$ ,  $T_0$ , and  $T_{+1}$ , as shown in Figure 1d. These orders propagate to different directions, and the mask was designed so that four coherent diffractive beams  $T_{-1}$  and  $T_{+1}$  overlap in the central zone at a distance of 5.6 mm, forming an interference field as indicated in Figure 1c. This pattern exhibits arrays of more confined peaks in the harmonic spatial distribution of the interference field intensity when compared to that achieved by the conventional Lloyd's mirror configuration with two interfering beams, see Figure 1b. The intensity of the pattern generated by four interfering beams (phase mask configuration) drops to zero between the peaks, while that for the sequential orthogonal recording of two interfering beams (Lloyd's mirror configuration) does not. The period of the pattern generated by the four coherent interfering beams is  $\Lambda = \Lambda_{PM}/\sqrt{2}$ , where  $\Lambda_{PM}$  is the period of the transmission gratings on the phase mask. The full width of the half maximum (FWHM) of the peaks in this pattern is of  $\Lambda/2$ . To observe the interference pattern formed by the phase mask with a grating period of  $\Lambda_{PM} = 690$  nm at a wavelength of  $\lambda = 325$  nm, it was recorded to a layer of S1805 positive-tone photoresist with a thickness of 100 nm. After developing the recorded field distribution (an irradiation dose of  $27 \text{ mJ cm}^{-2}$ ), atomic force microscopy (AFM) was employed for the observation of the structured resist topography. The obtained results presented in Figure S1 show a series of circular holes in the resist layer with a periodicity of  $\Lambda = 490 \pm 4$  nm, which is in agreement with the simulated profile of the interference field distribution, as shown in Figure 1b.

**Recording of pNIPAAm-Based Hydrogel Arrays.** To prepare arrays of responsive pNIPAAm-based hydrogel features, the terpolymer shown in Figure 2a was used. This terpolymer carries pendant benzophenone groups for photocrosslinking and covalent attachment to a solid surface upon irradiation with UV light.<sup>43</sup> In addition, methacrylic acid was copolymerized, as the incorporated carboxyl groups promote swelling in water and provide a chemical postmodification site for the incorporation of biomolecules via amine coupling.<sup>49</sup>

The pNIPAAm-based polymer layer with a thickness of 70 nm was spun onto a glass substrate carrying a thin adhesion-promoting SU-8 film. After complete drying of the pNIPAAm polymer layer, the substrate was placed in the 4-beam UV-LIL optical system and exposed to the interference pattern generated by a phase mask to record a crosslinked structure with a period of  $\Lambda_H = 488$  nm. Upon irradiation, the pNIPAAm-based polymer in the area of high UV intensities is crosslinked and attached to the substrate, while the unexposed areas remain unchanged. Therefore, after subsequent rinsing of the layer with ethanol and water, the crosslinked pNIPAAm network remains in the exposed zones and only noncrosslinked

polymer is washed away in the area in between. After drying on a hot plate at temperature  $T = 100$  °C, AFM images of the pNIPAAm surface topography were acquired. In Figure 2b, a periodic pattern of nonconnected domains of crosslinked pNIPAAm with a height similar to the initial thickness of the original polymer layer can be seen. When increasing the irradiation dose of the UV light from  $I = 84$  to 132 and 240  $\text{mJ cm}^{-2}$ , the pNIPAAm domains exhibit an increasing diameter (FWHM) of  $D = 168 \pm 9$ ,  $208 \pm 8$ , and  $293 \pm 9$  nm, respectively, which were determined from the cross-sections presented in Figure 2c. These values are around FWHM of the peaks in the interference field pattern of  $\Lambda_H/2 = 244$  nm, and the changes in  $D$  reflect the nonlinear dependence of the crosslinking on the irradiation dose. In addition, the height of the structure between 50 and 65 nm determined from the cross-sections in Figure 2c are lower than the thickness of the original (noncrosslinked) pNIPAAm film, which can be ascribed to the effect of smearing of the recorded features after their swelling and drying before the AFM observation.

Interestingly, the topography of the pNIPAAm-based domains changes depending on the conditions in which they are dried prior to the AFM observation in air. As Figure 3

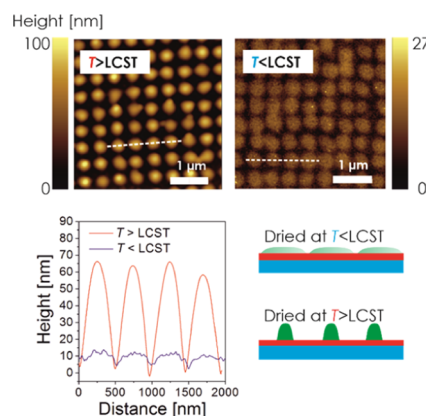


**Figure 3.** AFM observation of nanostructured pNIPAAm hydrogel topography dried at a temperature below and above the LCST. The structure was prepared with an irradiation dose of  $240 \text{ mJ/cm}^2$ .

illustrates, the height of the features strongly decreases, and the diameter increases when the surface is rinsed with water and dried at room temperature. This observation relates to what is already reported for sinusoidal corrugation of similar pNIPAAm crosslinked layers<sup>48</sup> and nanoimprinted nanopillars.<sup>27</sup> It can be attributed to the strong deformation of the elastic polymer network by the surface tension of the aqueous medium upon evaporation. The elasticity of the wet pNIPAAm network is strongly temperature-dependent due to its thermoresponsive solvation properties: below the LCST of 32 °C, the network swells in water and forms a soft structure that is planarized in the drying process (the height decreases by a factor of about 10). However, above the LCST in water, the polymer network collapses and forms more compact, rigid domains that are resistant to mechanical deformation upon drying. This swelling behavior was also investigated by acquiring AFM images of the prepared thermoresponsive nanostructures in water at varying temperatures around the LCST. As shown in Figure 4, at  $T = 30$  °C, the topography of the swollen soft pNIPAAm structure is barely captured by the AFM tip. However, when the temperature is increased above

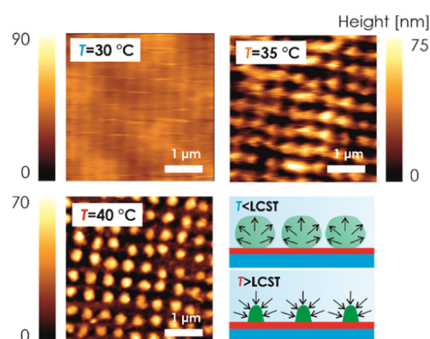


**Figure 4.** AFM observation of nanostructured pNIPAAm hydrogel topology in water for the temperature  $T = 30, 35,$  and  $40\text{ }^{\circ}\text{C}$ . The structure was prepared with an irradiation dose of  $240\text{ mJ}/\text{cm}^2$ .

the LCST to  $T = 35\text{ }^{\circ}\text{C}$ , the inscribed pattern becomes apparent for the collapsed and more rigid hydrogel network. Interestingly, upon further temperature increase to  $T = 40\text{ }^{\circ}\text{C}$ , the observed geometry in water fully resembles the morphology that was recorded in air, as presented in Figure 2b.

**Hybrid Au-pNIPAAm Nanostructures.** The developed approach for the preparation of arrays with thermoresponsive pNIPAAm-based features was further applied to gold nanoparticle arrays to yield a hybrid plasmonic nanomaterial. First, gold nanoparticle arrays were prepared on a glass surface using UV-LIL with Lloyd's mirror configuration and a dry etching protocol, as previously reported.<sup>46</sup> The obtained cylindrical gold nanoparticle exhibited a diameter of  $D = 132 \pm 5\text{ nm}$ , a height of about  $50\text{ nm}$ , and an array periodicity of  $\Lambda_G = 463 \pm 2\text{ nm}$ , as revealed by the AFM image in Figure 5a. Afterward, the gold surface of the nanoparticles was modified with a self-assembled monolayer (SAM) of benzophenone disulfide, on top of which a pNIPAAm polymer film was deposited (the benzophenone disulfide serves here as a linker for the covalent photoattachment of the polymer chains to gold<sup>44</sup>).

Then, the same phase mask-based procedure (for recording the four-beam UV interference field with the period of  $\Lambda_H = 488 \pm 2\text{ nm}$ ) was applied to generate arrays of pNIPAAm-based polymer structures, followed by rinsing with water and drying.

To circumvent the difficulty to precisely align both arrays of the hydrogel features and the gold nanoparticles, a slight mismatch of the array periodicities by 5% was intentionally

applied to yield a Moiré effect between both features. As a result, it is expected that the topography will vary periodically across the surface, resulting in a repeating pattern of areas with aligned and with misaligned geometry. The characteristic size of these domains can be estimated as  $\Lambda_H \cdot \Lambda_G / (\Lambda_H - \Lambda_G)$  in the range of about  $8\text{ }\mu\text{m}$ . Figure 5b shows an AFM image for the topography of a  $2 \times 2\text{ }\mu\text{m}$  subarea of the structure that exhibits hydrogel features aligned with the gold nanoparticle arrays after drying below the LCST. Apparently, the gold nanoparticles are visible as areas with an increased height of about  $85\text{ nm}$  surrounded by partially planarized pNIPAAm zones of lower height that spread to a diameter of about  $400\text{ nm}$  (see also the representative cross-section in Figure S3). When the structure is exposed to water and dried again above the LCST, the morphology changes, as shown in Figure 5c. The metallic nanoparticle topography is not protruding through the pNIPAAm hydrogel, which appears more compacted and spreading to a smaller diameter of about  $300\text{ nm}$ . The maximum height of the pNIPAAm features (with metallic nanoparticle inside) of  $90\text{ nm}$  is slightly higher than for the structure dried below LCST. The morphology variations due to drying in the swollen and collapsed state of pNIPAAm networks attached to gold nanoparticles are less pronounced than on the flat SU-8 film. It can be attributed to different means of the attachment (swelling and collapsing on the curved surface of Au nanoparticle walls) and to the potential difference in the interaction of pNIPAAm chains with SU-8 and BK7 glass (surrounding the hydrogel structure). For comparison, an area where the gold nanoparticles and hydrogel features are misaligned is presented in Figure 5d. The patterned hydrogel features around the metallic structures exhibit more irregular morphology compared to those measured without the gold nanoparticles in Figures 2–4. This observation can be attributed to gradually changing alignment between the center of the hydrogel feature and the gold nanoparticle along the surface and the fact that the collapse tends to pull pNIPAAm-based polymer toward gold where the attachment is utilized via the benzophenone disulfide linker.

**Actuating of LSP.** The collapse of the pNIPAAm hydrogel is associated with an increase of the polymer volume fraction and the refractive index on the surface of gold nanoparticles. Therefore, the pNIPAAm collapse around these metallic objects detunes the localized surface plasmon resonance

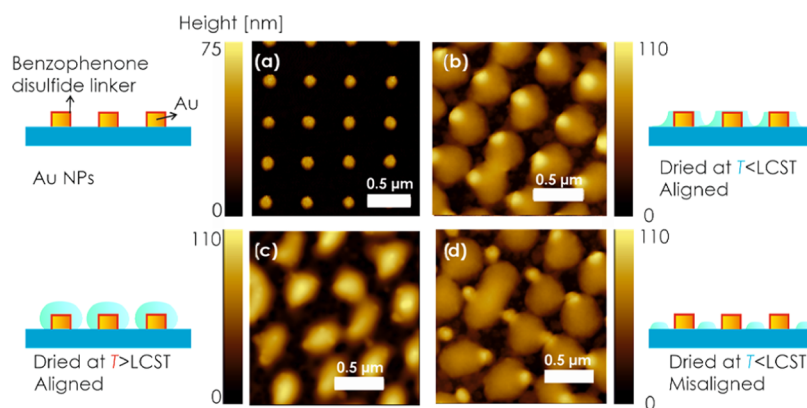


**Figure 5.** AFM topography of (a) gold nanoparticle arrays subsequently covered with covalently attached pNIPAAm-based nanostructures that are aligned with the gold nanoparticles and dried (b) below and (c) above the LCST. (d) Example of misaligned arrays of gold nanoparticles with pNIPAAm-based nanostructures dried below the LCST.



(LSPR) and manifests itself as a redshift of the resonant wavelength. Figure 6a shows the transmission spectra

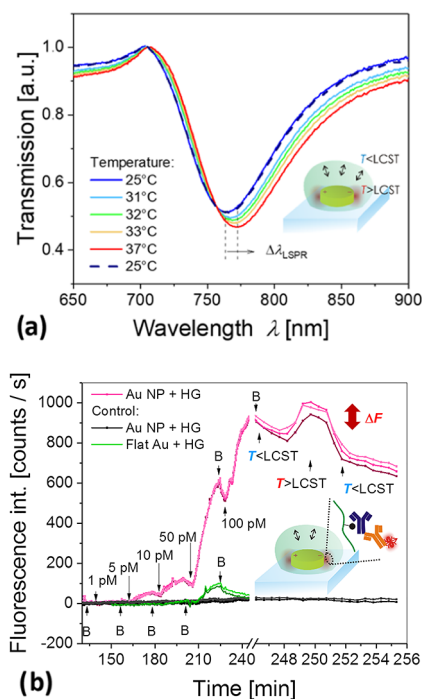


**Figure 6.** (a) Measured reversible shift in LSPR spectra upon temperature-induced swelling and collapse of the pNIPAAm-based hydrogel wrapped over metallic nanoparticles. (b) Employment of the hybrid material for plasmonic amplification of a fluorescence immunoassay with the pNIPAAm-based hydrogel serving as an affinity binding matrix that can be swollen and collapsed by an external temperature stimulus. The red-colored lines show the fluorescence signal acquired from spots with a diameter of 220  $\mu\text{m}$  at different locations on the same biochip carrying the pNIPAAm-based hydrogel that was functionalized with ligands. The black curves correspond to control spots on the same biochip that were not functionalized with the ligand molecules, and the green curves show the control experiment on a planar-functionalized hydrogel binding matrix attached to the flat gold film. The analyte concentration is clearly indicated in the graph, and B corresponds to the rinsing step with working buffer.

measured over the area of about 1  $\text{mm}^2$ , which averages the variations in the alignment between gold nanoparticles and hydrogel features with a domain size  $<10 \mu\text{m}$ . LSPR for the structure at the temperature  $T = 25 \text{ }^\circ\text{C}$  manifests itself as a dip in the transmission spectrum centered at a wavelength of  $\lambda_{\text{LSPR}} = 763.9 \text{ nm}$ . The gradual collapse of the hydrogel induces a red-shift of the LSPR wavelength upon an increase in the temperature. At a temperature of  $T = 37 \text{ }^\circ\text{C}$ , far above the LCST, the LSPR wavelength shifts to 771.9 nm. These changes are fully reversible, as after cooling to  $T = 25 \text{ }^\circ\text{C}$ , the LSPR spectrum shifts back to the original shape. It is worth noting that the observed shift of about 6 nm is half of that measured for a structure covered with a compact pNIPAAm hydrogel film (data not shown), which can be ascribed to the fact that about half of the nanoparticles is not in contact with the polymer due to the periodic regions of misalignment in the Moiré pattern.

**LSP-Enhanced Fluorescence Assay.** Finally, the developed structure was tested to serve as a biochip interface for the fluorescence readout of an immunoassay. First, the responsive

pNIPAAm-based hydrogel features wrapping (about half) of the gold nanoparticles that were postmodified with mouse IgG antibodies (mIgG). The polymer carboxylic groups were employed for establishing covalent bonds between the lysine groups of the protein and the polymer chain based on the established amine coupling scheme.<sup>49</sup> Then, the substrate was clamped against a flow cell, and a series of liquid samples with an increasing concentration of goat antibodies specific to mIgG (a-mIgG) were pumped over its surface. To detect the affinity binding, the goat antibody a-mIgG was labeled with an organic dye (Alexa Fluor 790). This label exhibits its absorption and emission wavelengths ( $\lambda_{\text{ex}} = 785 \text{ nm}$ ,  $\lambda_{\text{em}} = 810 \text{ nm}$ ) in the vicinity of the LSPR wavelength ( $\lambda_{\text{LSPR}} = 764 \text{ nm}$ ). Therefore, the kinetics of the affinity binding of a-mIgG from the liquid sample was measured using plasmon-enhanced fluorescence.<sup>50</sup>

The surface of the sample was irradiated by a laser beam at a wavelength of 785 nm that resonantly couples to LSPs and locally excites the bound fluorophores with its enhanced field intensity. The emitted light at a wavelength of 810 nm was collected with a home built instrument<sup>47</sup> separated from the excitation beam using a dichroic mirror, bandpass filter, and notch filter and detected with a cooled CCD camera. The fluorescence signal was acquired with dedicated software from a series of spots carrying the gold nanoparticle arrays in reference to an area without nanoparticles, and the data were tracked in time upon sequential flow of analyte samples. The fluorescence intensity was averaged over the surface of each circular spot with a diameter of 220  $\mu\text{m}$  that was much larger than the size of domains with aligned and misaligned arrays of gold nanoparticles and hydrogel features. The liquid samples were prepared from phosphate-buffered saline that was spiked with a-mIgG at concentrations of 1, 5, 10, 50, and 100 pM. Each sample was flushed over the surface for 15 min, followed by 5 min rinsing. As Figure 6b shows, the binding of a-mIgG manifests itself as a gradual increase in the fluorescence signal, and upon rinsing, a fluorescence intensity decrease occurs due to bleaching of the emitters. The fluorescence signal on gold nanoparticle arrays capped with the pNIPAAm hydrogel matrix (red curves in Figure 6a) is about 6 times higher compared to a control experiment (green curves in 6a). The control experiment was carried out on the hydrogel biointerface prepared in the form of a layer attached to a flat nonstructured gold film. It is worth noting that the plasmonic enhancement on the structured surface is probably higher than the factor of 6 due to the fact that the control flat architecture exhibits a larger area for the capture of the target analyte and that at least half of the metallic nanoparticles are not capped with the hydrogel binding matrix due to the miss-alignment. The measured data for a structured hydrogel biointerface overlaid with gold nanoparticles indicate that the limit of detection for the prepared biochip is 0.7 pM (determined for the standard deviation fluorescence signal baseline of 2 counts/s and the slope of the fluorescence signal of 9 counts/s/pM). After this titration experiment, the temperature of the biochip surface was increased from 25 to 40  $^\circ\text{C}$ , above the LCST of the hydrogel. As seen in Figure 6b, the induced collapse of the responsive hydrogel with the affinity-captured and fluorophore-labeled a-mIgG leads to an increase of the fluorescence signal by about 20%. This is due to the collapse and compacting of the hydrogel, which increases the polymer volume fraction and affinity-bound analyte molecules closer to the gold surface, where the plasmonic hotspot is located. This observation corroborates that affinity binding occurs in the

vicinity of the metallic nanoparticles within the matrix of the responsive pNIPAAm-based polymer network and indicates that the triggered collapse can provide an additional enhancement mechanism for high sensitivity fluorescence assays.

## CONCLUSIONS

A technique based on four-beam laser interference lithography utilizing a phase mask-based configuration allows for the preparation of well-defined responsive hydrogel nanostructures with the tailored spacing and diameter. Periodic arrays of pNIPAAm-based hydrogel nanostructures exhibiting a disk shape with a tunable diameter, as low as 170 nm, were prepared with a submicron period. The temperature-induced swelling and collapse of the inscribed polymer features were investigated, and their local attachment on top of the periodic gold nanoparticle arrays was achieved based on the Moiré effect. The fully reversible actuation by temperature changes was demonstrated by measuring the variations in LSPR of the gold nanoparticle arrays. In addition, the pNIPAAm-based hydrogel was postmodified with biorecognition elements to serve as a 3D high binding capacity matrix, and a model bioassay based on fluorescence readout was conducted. The limit of detection was proven to be in the sub-picomolar range owing to the plasmonic amplification of the fluorescence signal by the plasmonic nanoparticles. Finally, the capability of the pNIPAAm network to compact the affinity-captured analyte at the plasmonic hotspots by a temperature-induced polymer collapse was tested. The presented hybrid architecture provides a novel approach for the local attachment of chemical and biological species in the vicinity of metallic nanostructures to fully exploit the probing with the LSP field at the so-called plasmonic hotspots, where the optical field intensity is the strongest.

## ASSOCIATED CONTENT

### Supporting Information

The Supporting Information is available free of charge at <https://pubs.acs.org/doi/10.1021/acs.jpcc.9b11059>.

Schematic and atomic force spectroscopy images of the phase mask and recorded interference pattern employing a positive photoresist; schematic of the optical setup used for the plasmon-enhanced spectroscopy assay; cross-sections of AFM topography of hydrogel nanostructures (PDF)

## AUTHOR INFORMATION

### Authors

**Nestor Gisbert Quilis** – BioSensor Technologies, AIT-Austrian Institute of Technology GmbH, 3430 Tulln, Austria

**Simone Hageneder** – BioSensor Technologies, AIT-Austrian Institute of Technology GmbH, 3430 Tulln, Austria

**Stefan Fossati** – BioSensor Technologies, AIT-Austrian Institute of Technology GmbH, 3430 Tulln, Austria

**Simone K. Auer** – BioSensor Technologies, AIT-Austrian Institute of Technology GmbH, 3430 Tulln, Austria

**Priyamvada Venugopalan** – BioSensor Technologies, AIT-Austrian Institute of Technology GmbH, 3430 Tulln, Austria; CEST Kompetenzzentrum für elektrochemische Oberflächentechnologie GmbH, TFZ, Wiener Neustadt, 2700 Wiener Neustadt, Austria

**Anil Bozdogan** – CEST Kompetenzzentrum für elektrochemische Oberflächentechnologie GmbH, TFZ, Wiener Neustadt, 2700 Wiener Neustadt, Austria

**Christian Petri** – Macromolecular Chemistry, Department Chemistry-Biology, University of Siegen, Siegen 57076, Germany

**Alberto Moreno-Cencerrado** – Institute for Biophysics, Department of Nanobiotechnology, University of Natural Resources and Life Sciences Vienna (BOKU), Vienna 1190, Austria

**Jose Luis Toca-Herrera** – Institute for Biophysics, Department of Nanobiotechnology, University of Natural Resources and Life Sciences Vienna (BOKU), Vienna 1190, Austria

**Ulrich Jonas** – Macromolecular Chemistry, Department Chemistry-Biology, University of Siegen, Siegen 57076, Germany; [orcid.org/0000-0002-2161-4541](https://orcid.org/0000-0002-2161-4541)

**Jakub Dostalek** – BioSensor Technologies, AIT-Austrian Institute of Technology GmbH, 3430 Tulln, Austria; [orcid.org/0000-0002-0431-2170](https://orcid.org/0000-0002-0431-2170)

Complete contact information is available at: <https://pubs.acs.org/doi/10.1021/acs.jpcc.9b11059>

## Notes

The authors declare no competing financial interest.

## ACKNOWLEDGMENTS

N.G.Q. acknowledges funding from the European Union's Horizon 2020 research and innovation program under Grant agreement no. 642787, Marie Skłodowska-Curie Innovative Training Network BIOGEL. P.V. was supported by the project jointly funded by Agence Nationale de la Recherche (ANR) and the Austrian Science Fund (FWF) under the grant agreements ANR-15-CE29-0026 and I 2647, respectively. S.H., S.F., C.P., and J.D. received support from the European Union's Horizon 2020 research and the innovation program under Grant Agreement no. 633937, project ULTRAPLACAD. S.A. is grateful for the support from FEMTEC and S.H., S.F., and J.D. were supported by the Austrian Research Promotion Agency (FFG) with Grant agreement no. 861578 (ERANET project PLABAN).

## REFERENCES

- (1) Green, J. J.; Elisseff, J. H. Mimicking Biological Functionality with Polymers for Biomedical Applications. *Nature* **2016**, *540*, 386.
- (2) Mateescu, A.; Wang, Y.; Dostalek, J.; Jonas, U. Thin Hydrogel Films for Optical Biosensor Applications. *Membranes* **2012**, *2*, 40–69.
- (3) Liu, F.; Urban, M. W. Recent Advances and Challenges in Designing Stimuli-Responsive Polymers. *Prog. Polym. Sci.* **2010**, *35*, 3–23.
- (4) Wei, M.; Gao, Y.; Li, X.; Serpe, M. J. Stimuli-Responsive Polymers and Their Applications. *Polym. Chem.* **2017**, *8*, 127–143.
- (5) De las Heras Alarcón, C.; Pennadam, S.; Alexander, C. Stimuli Responsive Polymers for Biomedical Applications. *Chem. Soc. Rev.* **2005**, *34*, 276–285.
- (6) Jiang, N.; Zhuo, X.; Wang, J. Active Plasmonics: Principles, Structures, and Applications. *Chem. Rev.* **2017**, *118*, 3054–3099.
- (7) Huck, W. T. Responsive Polymers for Nanoscale Actuation. *Mater. Today* **2008**, *11*, 24–32.
- (8) Sidorenko, A.; Krupenkin, T.; Taylor, A.; Fratzl, P.; Aizenberg, J. Reversible Switching of Hydrogel-Actuated Nanostructures into Complex Micropatterns. *Science* **2007**, *315*, 487–490.
- (9) Haq, M. A.; Su, Y.; Wang, D. Mechanical Properties of Pnipam Based Hydrogels: A Review. *Mater. Sci. Eng., C* **2017**, *70*, 842–855.

- (10) Guan, Y.; Zhang, Y. Pnipam Microgels for Biomedical Applications: From Dispersed Particles to 3d Assemblies. *Soft Matter* **2011**, *7*, 6375–6384.
- (11) Nash, M. E.; Healy, D.; Carroll, W. M.; Elvira, C.; Rochev, Y. A. Cell and Cell Sheet Recovery from Pnipam Coatings; Motivation and History to Present Day Approaches. *J. Mater. Chem.* **2012**, *22*, 19376–19389.
- (12) Toma, M.; Jonas, U.; Mateescu, A.; Knoll, W.; Dostalek, J. Active Control of Spr by Thermoresponsive Hydrogels for Biosensor Applications. *J. Phys. Chem. C* **2013**, *117*, 11705–11712.
- (13) Kawano, T.; Niidome, Y.; Mori, T.; Katayama, Y.; Niidome, T. Pnipam Gel-Coated Gold Nanorods for Targeted Delivery Responding to a near-Infrared Laser. *Bioconjugate Chem.* **2009**, *20*, 209–212.
- (14) Erickson, D.; Mandal, S.; Yang, A. H.; Cordovez, B. Nanobiosensors: Optofluidic, Electrical and Mechanical Approaches to Biomolecular Detection at the Nanoscale. *Microfluid. Nanofluid.* **2008**, *4*, 33–52.
- (15) Paquet, C.; Kumacheva, E. Nanostructured Polymers for Photonics. *Mater. Today* **2008**, *11*, 48–56.
- (16) Ghosh, S.; Kouamé, N. A.; Ramos, L.; Remita, S.; Dazzi, A.; Deniset-Besseau, A.; Beaudier, P.; Goubard, F.; Aubert, P.-H.; Remita, H. Conducting Polymer Nanostructures for Photocatalysis under Visible Light. *Nat. Mater.* **2015**, *14*, 505.
- (17) Slepicka, P.; Kasalkova, N. S.; Siegel, J.; Kolska, Z.; Bacakova, L.; Svorcik, V. Nano-Structured and Functionalized Surfaces for Cytocompatibility Improvement and Bactericidal Action. *Biotechnol. Adv.* **2015**, *33*, 1120–1129.
- (18) Nie, Z.; Kumacheva, E. Patterning Surfaces with Functional Polymers. *Nat. Mater.* **2008**, *7*, 277.
- (19) Cheng, J. Y.; Mayes, A. M.; Ross, C. A. Nanostructure Engineering by Templated Self-Assembly of Block Copolymers. *Nat. Mater.* **2004**, *3*, 823.
- (20) Hu, H.; Gopinadhan, M.; Osuji, C. O. Directed Self-Assembly of Block Copolymers: A Tutorial Review of Strategies for Enabling Nanotechnology with Soft Matter. *Soft Matter* **2014**, *10*, 3867–3889.
- (21) Zhang, H.; Mourran, A.; Möller, M. Dynamic Switching of Helical Microgel Ribbons. *Nano Lett.* **2017**, *17*, 2010–2014.
- (22) Chen, J.-K.; Chang, C.-J. Fabrications and Applications of Stimulus-Responsive Polymer Films and Patterns on Surfaces: A Review. *Materials* **2014**, *7*, 805–875.
- (23) Yu, Q.; Ista, L. K.; Gu, R.; Zauscher, S.; López, G. P. Nanopatterned Polymer Brushes: Conformation, Fabrication and Applications. *Nanoscale* **2016**, *8*, 680–700.
- (24) Idota, N.; Tsukahara, T.; Sato, K.; Okano, T.; Kitamori, T. The Use of Electron Beam Lithographic Graft-Polymerization on Thermoresponsive Polymers for Regulating the Directionality of Cell Attachment and Detachment. *Biomaterials* **2009**, *30*, 2095–2101.
- (25) Traub, M. C.; Longsine, W.; Truskett, V. N. Advances in Nanoimprint Lithography. *Annu. Rev. Chem. Biomol. Eng.* **2016**, *7*, 583–604.
- (26) Guo, L. J. Nanoimprint Lithography: Methods and Material Requirements. *Adv. Mater.* **2007**, *19*, 495–513.
- (27) Pirani, F.; Sharma, N.; Moreno-Cencerrado, A.; Fossati, S.; Petri, C.; Descrovi, E.; Toca-Herrera, J. L.; Jonas, U.; Dostalek, J. Optical Waveguide-Enhanced Diffraction for Observation of Responsive Hydrogel Nanostructures. *Macromol. Chem. Phys.* **2017**, *218*, No. 1600400.
- (28) Mourran, A.; Zhang, H.; Vinokur, R.; Möller, M. Soft Microrobots Employing Nonequilibrium Actuation Via Plasmonic Heating. *Adv. Mater.* **2017**, *29*, No. 1604825.
- (29) Volk, K.; Fitzgerald, J. P. S.; Retsch, M.; Karg, M. Time-Controlled Colloidal Superstructures: Long-Range Plasmon Resonance Coupling in Particle Monolayers. *Adv. Mater.* **2015**, *27*, 7332.
- (30) Valsecchi, C.; Brolo, A. G. Periodic Metallic Nanostructures as Plasmonic Chemical Sensors. *Langmuir* **2013**, *29*, 5638–5649.
- (31) Halas, N. J.; Lal, S.; Chang, W.-S.; Link, S.; Nordlander, P. Plasmons in Strongly Coupled Metallic Nanostructures. *Chem. Rev.* **2011**, *111*, 3913–3961.
- (32) Baffou, G.; Quidant, R. Thermo-Plasmonics: Using Metallic Nanostructures as Nano-Sources of Heat. *Laser Photonics Rev.* **2013**, *7*, 171–187.
- (33) Brongersma, M. L.; Halas, N. J.; Nordlander, P. Plasmon-Induced Hot Carrier Science and Technology. *Nat. Nanotechnol.* **2015**, *10*, 25.
- (34) Mayer, K. M.; Hafner, J. H. Localized Surface Plasmon Resonance Sensors. *Chem. Rev.* **2011**, *111*, 3828–3857.
- (35) Goerlitzer, E. S. A.; Speichermann, L. E.; Mirzaa, T. A.; Mohammadia, R.; Vogel, N. Addressing the Plasmonic Hotspot Region by Site-Specific Functionalization of Nanostructures. *Nanoscale Adv.* **2020**, *2*, 136.
- (36) Piliarik, M.; Kvasnicka, P.; Galler, N.; Krenn, J. R.; Homola, J. Local Refractive Index Sensitivity of Plasmonic Nanoparticles. *Opt. Express* **2011**, *19*, 9213–9220.
- (37) Jonsson, M. P.; Dahlin, A. B.; Feuz, L.; Petronis, S.; Hook, F. Locally Functionalized Short-Range Ordered Nanoplasmonic Pores for Bioanalytical Sensing. *Anal. Chem.* **2010**, *82*, 2087–2094.
- (38) Herzog, N.; Kind, J.; Hess, C.; Andrieu-Brunsen, A. Surface Plasmon & Visible Light for Polymer Functionalization of Mesopores and Manipulation of Ionic Permeability. *Chem. Commun.* **2015**, *51*, 11697–11700.
- (39) Dostert, K.-H.; Álvarez, M.; Koynov, K.; del Campo, A.; Butt, H.-J. r.; Kreiter, M. Near Field Guided Chemical Nanopatterning. *Langmuir* **2012**, *28*, 3699–3703.
- (40) Mazzotta, F.; Johnson, T. W.; Dahlin, A. B.; Shaver, J.; Oh, S. H.; Hook, F. Influence of the Evanescent Field Decay Length on the Sensitivity of Plasmonic Nanodisks and Nanoholes. *ACS Photonics* **2015**, *2*, 256–262.
- (41) Wang, Y.; Brunsen, A.; Jonas, U.; Dostalek, J.; Knoll, W. Prostate Specific Antigen Biosensor Based on Long Range Surface Plasmon-Enhanced Fluorescence Spectroscopy and Dextran Hydrogel Binding Matrix. *Anal. Chem.* **2009**, *81*, 9625–9632.
- (42) Huang, C. J.; Dostalek, J.; Knoll, W. Long Range Surface Plasmon and Hydrogel Optical Waveguide Field-Enhanced Fluorescence Biosensor with 3d Hydrogel Binding Matrix: On the Role of Diffusion Mass Transfer. *Biosens. Bioelectron.* **2010**, *26*, 1425–1431.
- (43) Beines, P. W.; Klosterkamp, I.; Menges, B.; Jonas, U.; Knoll, W. Responsive Thin Hydrogel Layers from Photo-Cross-Linkable Poly (N-Isopropylacrylamide) Terpolymers. *Langmuir* **2007**, *23*, 2231–2238.
- (44) Sergelen, K.; Petri, C.; Jonas, U.; Dostalek, J. Free-Standing Hydrogel-Particle Composite Membrane with Dynamically Controlled Permeability. *Biointerphases* **2017**, *12*, No. 051002.
- (45) Gee, K. R.; Archer, E. A.; Kang, H. C. 4-Sulfotetrafluorophenyl (Stp) Esters: New Water-Soluble Amine-Reactive Reagents for Labeling Biomolecules. *Tetrahedron Lett.* **1999**, *40*, 1471–1474.
- (46) Quilis, N. G.; Lequeux, M.; Venugopalan, P.; Khan, I.; Knoll, W.; Boujday, S.; de la Chapelle, M. L.; Dostalek, J. Tunable Laser Interference Lithography Preparation of Plasmonic Nanoparticle Arrays Tailored for Sens. *Nanoscale* **2018**, *10*, 10268.
- (47) Dostalek, J.; Knoll, W.; Fossati, S.; Hageneder, S.; Jungbluth, V. Plasmon-Enhanced Fluorescence Spectroscopy Imaging by Multi-Resonant Nanostructures. European Patent Application No. 19164960.72019.
- (48) Sharma, N.; Petri, C.; Jonas, U.; Dostalek, J. Reversibly Tunable Plasmonic Bandgap by Responsive Hydrogel Grating. *Opt. Express* **2016**, *24*, 2457–2465.
- (49) Aulasevich, A.; Roskamp, R. F.; Jonas, U.; Menges, B.; Dostalek, J.; Knoll, W. Optical Waveguide Spectroscopy for the Investigation of Protein-Functionalized Hydrogel Films. *Macromol. Rapid Commun.* **2009**, *30*, 872–877.
- (50) Bauch, M.; Toma, K.; Toma, M.; Zhang, Q.; Dostalek, J. Plasmon-Enhanced Fluorescence Biosensors: A Review. *Plasmonics* **2014**, *9*, 781–799.

## Supporting Information

# UV-Laser Interference Lithography for Local Functionalization of Plasmonic Nanostructures with Responsive Hydrogel

*Nestor Gisbert Quilis<sup>a</sup>, Simone Hageneder<sup>a</sup>, Stefan Fossati<sup>a</sup>, Simone K. Auer<sup>a</sup>, Priyamvada Venugopalan<sup>a,b†</sup>, Anil Bozdogan<sup>b</sup>, Christian Petri<sup>c</sup>, Alberto Moreno-Cencerrado<sup>d</sup>, Jose Luis Toca-Herrera<sup>d</sup>, Ulrich Jonas<sup>c</sup> and Jakub Dostalek<sup>a\*</sup>*

<sup>a</sup>BioSensor Technologies, AIT-Austrian Institute of Technology GmbH, Konrad-Lorenz-Strasse 24, 3430 Tulln, Austria

<sup>b</sup>CEST Kompetenzzentrum für elektrochemische Oberflächentechnologie GmbH, TFZ, Wiener Neustadt, Viktor-Kaplan-Strasse 2, 2700 Wiener Neustadt, Austria

<sup>c</sup>Macromolecular Chemistry, Department Chemistry-Biology, University of Siegen, Adolf Reichwein-Strasse 2, Siegen 57076, Germany

<sup>d</sup>Institute for Biophysics, Department of Nanobiotechnology, University of Natural Resources and Life Sciences Vienna (BOKU), Muthgasse 11, Vienna 1190, Austria

**Observation of the interference field profile formed by the phase mask.** A thin layer of the S1805 positive photoresist (diluted 1:2 with propylene glycol monomethyl ether acetate) with a thickness of 120 nm was deposited by spin-coating (4500 rpm, 45 s) on top of a BK7 substrate. Afterward, the sample was mounted in a home-built set-up together with the phase mask to verify the recording pattern. The distance of the photoresist-coated substrate in respect with the phase mask (recording plane) was kept to 5.6 mm. At this distance the first order diffraction gratings overlap at the center of the mask for a  $\Lambda=690$  nm. Thus, the samples were irradiated once to  $27 \text{ mJ cm}^{-2}$  and developed for 35 sec.

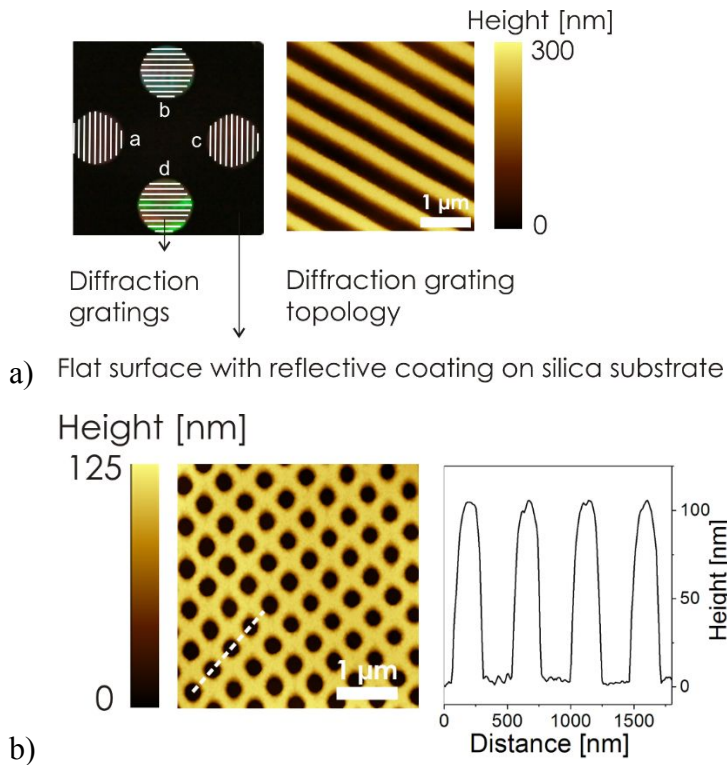


**Figure S1.** (a) Schematics of the prepared phase mask with orientation of the transmission gratings (left) and their topography obtained by AFM (right). (b) Recorded interference pattern into the S1805 positive photoresist using the prepared phase mask.

## Plasmon-enhanced fluorescence readout of model assay

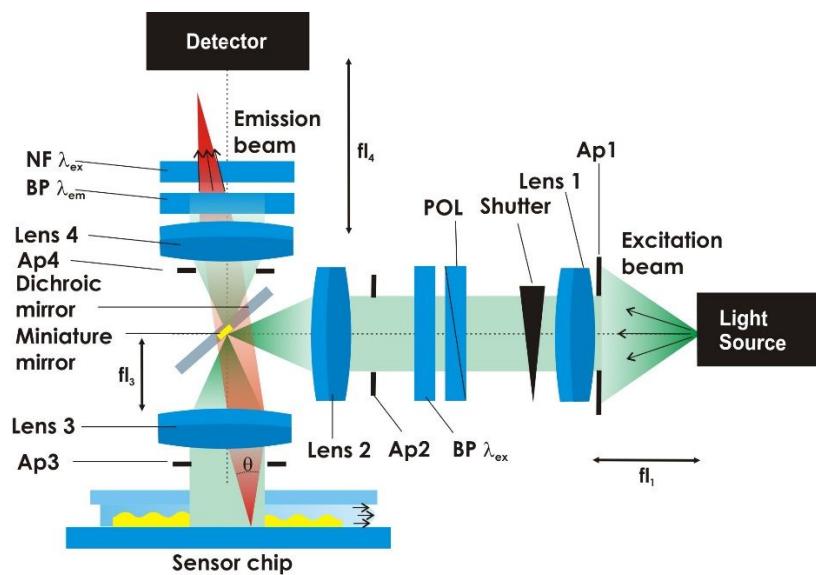


**Figure S2.** Schematics of the optical setup configuration of the reader that enables in situ readout of fluorescence signal kinetics from the sensing spots on a sensor chip: NF – notch filter, BP – bandpass filter, Ap – aperture, POL – polarizer, fl – focal length.

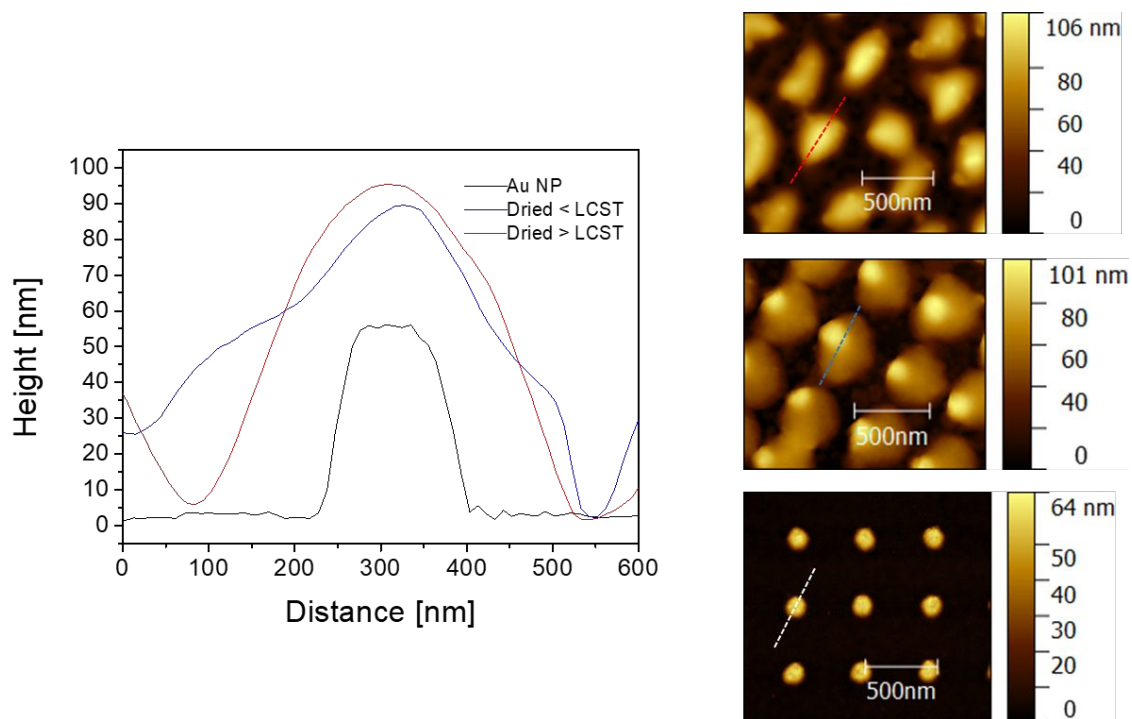


**Figure S3.** Cross-sections of representative areas of AFM topography showed in Figure 5 for bare gold nanoparticles (black curve), gold nanoparticles capped with pNIPAAm-based hydrogel dried below its LCST (blue curve) and above its LCST (red curve) and associated AFM images.

# 3.4

Plasmon-enhanced two-photon crosslinking  
for local functionalization of metallic  
nanostructures



# Plasmon-enhanced two-photon crosslinking for local functionalization of metallic nanostructures

Nestor Gisbert Quilis<sup>a</sup>, Sitara Vedaraman<sup>b</sup>, Marcel van Dongen<sup>b</sup>, Sven Klees<sup>c</sup>, Andreas Weber<sup>d</sup>, Akihiro Nishiguchi<sup>b</sup>, Jose Luis Toca-Herrera<sup>d</sup>, Laura de Laporte<sup>b</sup>, Martin Möller<sup>b</sup>, Ahmed Murrans<sup>b</sup>, Ulrich Jonas<sup>c</sup>, Jakub Dostalek<sup>a\*</sup>

<sup>a</sup>BioSensor Technologies, AIT-Austrian Institute of Technology GmbH, Konrad-Lorenz-Strasse 24, 3430 Tulln, Austria

<sup>b</sup>DWI – Leibniz Institute for Interactive Materials, Forckenbeckstrasse 50, 52056 Aachen, Germany

<sup>c</sup>Macromolecular Chemistry, Department Chemistry-Biology, University of Siegen, Adolf Reichwein-Strasse 2, Siegen 57076, Germany

<sup>d</sup>Institute for Biophysics, Department of Nanobiotechnology, University of Natural Resources and Life Sciences Vienna (BOKU), Muthgasse 11, Vienna 1190, Austria

**KEYWORDS:** *plasmonics, two-photon crosslinking, metallic nanostructures, anthraquinone crosslinker, plasmonic hotspot*

---

**ABSTRACT:** We report on a new approach to local attachment of functional materials at sub-areas of metallic nanoparticles that are referred as to plasmonic hotspots, where they can be exposed to strong electromagnetic field intensity associated with the resonant excitation of localized surface plasmons (LSPs). It is based on plasmonically enhanced two-photon crosslinking (PTPC) of polymers that are conjugated with photo-active anthraquinone groups. We show that on metallic nanostructures that are tuned to support LSPs at a wavelength coincident with the recording pulsed near-infrared laser beam, simultaneous crosslinking and attachment of the poly(N,N-dimethylacrylamide-co-acylamido-3-hydroxyanthraquinone) hydrogel occurs in spatial zones resembling the plasmonic hotspot. Their mechanical properties and swelling behavior of the PTPC hydrogel features is investigated with atomic force microscopy and compared to those observed with UV-crosslinked and two photon crosslinked structures prepared from the same polymer. This approach represents the first step towards the development of new class of plasmonic materials that take advantage of the precise spatial control of the coupling with intense LSP electromagnetic field.

---

## INTRODUCTION

Multi-photon absorption has opened the door for a variety of mask-less lithography tools enabling the preparation of microstructures<sup>1</sup> with sub-diffraction spatial resolution that reaches as low as 200 nm.<sup>2</sup> Up to now, this method has been utilized for the fabrication of 3D architectures serving in diverse areas including micro-optics<sup>3-5</sup>, micro-robotics<sup>6,7</sup>, and tissue engineering<sup>8,9</sup> to mention few examples. The vast majority of materials that are structured by the use of multi-photon absorption lithography rely on the two-photon polymerization (TPP) process.<sup>10</sup> Typically, a femtosecond pulsed laser beam with a near infrared wavelength is focused and scanned through a monomer solution in order to trigger polymerization in its small focal volume, where the threshold of the TPP process is exceeded.<sup>11</sup> A free radical polymerization reaction is employed with the use of a photo initiator molecule, which is excited via the two-photon absorption process. After the recording step, the structure is revealed by washing away the unreacted regions with a solvent.

Metallic nanostructures offer means for much tighter confinement of light than far field optics conventionally utilized in multi-photon absorption lithography. The resonant excitation of localized plasmons (LSPs) on metallic nanoparticles allows for

deep subwavelength confinement of light energy, which originate from collective oscillations of electron density and the associated electromagnetic field.<sup>12, 13</sup> The optical excitation of LSPs is accompanied with strong enhancement of the incident light intensity at a narrow spatial volume with a characteristic size below several tens of nanometers. The spatial distribution of increased enhanced electromagnetic field intensity is not homogeneous around metallic nanostructures and it is particularly intense at specific regions (e.g. edges/tips or gaps between closely arranged metallic objects) that are commonly referred as “plasmonic hotspots”.<sup>14</sup> Therefore, various strategies to spatially control the attachment of functional chemical moieties at these regions have been pursued in order to precisely control the strength of their interaction with LSPs.<sup>15-18</sup> These include the use of a photoresist mask with windows overlaying with plasmonic hotspots made by electron beam lithography<sup>19</sup>, development of orthogonal surface chemistries<sup>15</sup>, and the employment of a static electric field gradient for attracting the species at sharp parts of metallic nanostructures<sup>20</sup>. In addition, the use of chemical reactions that are locally triggered by LSPs has been explored based on the LSP-generation of hot electrons<sup>21</sup>, LSP-enhanced two-photon absorption in a negative tone resist

material<sup>22</sup> and multiphoton absorption – activated linkers for docking of proteins.<sup>23-25</sup>

Besides multi-photon lithography with TPP chemistries, there was recently reported an alternative approach based on two-photon cross-linking (TPC) of polymers composed of chains carrying anthraquinone photosensitive moieties. This approach was demonstrated for the preparation of microstructures by scanning a focused near infrared beam at a wavelength of about 780 nm across a polymer layer that were afterwards washed in order to remove non-crosslinked polymer chains.<sup>26</sup> We present an extension of this approach and investigate the recording of nanoscale structures based on surface plasmon-enhanced two photon crosslinking (PTPC). We employ plasmonic nanoparticle arrays with their localized surface plasmon resonance (LSPR) tuned to that of the NIR beam for the crosslinking. After coated by a polymer layer with polymer chains carrying anthraquinone pendant groups, the resonantly excited LSPs triggered the crosslinking and attachment of the polymer chains to certain sub-areas around the metallic nanoparticle. When exposed to water, the attached polymer network forms a hydrogel that swells and it features a size of about 75 nm, which corresponds to the distance probed by LSPs away from the metal nanoparticle surface.

## METHODS

**Materials.** Poly(N,N-Dimethylacrylamide-co-Acrylamido-3-hydroxyanthraquinone) P(DMAA-co-AAHAQ) was synthesized as previously reported<sup>26</sup>. S1805 and SU-8 resist and AZ303 developer were purchased from Micro resist (Germany). Benzophenone disulfide was synthesized as reported elsewhere<sup>27</sup>.

**Synthesis of p(DMAA-co-AAHAQ)** For the synthesis of the Acrylamido-3-hydroxyanthraquinone, 2-Amino-3-hydroxyanthraquinone (0.5 g, 2.1 mmol, 1 eq) was dissolved in 30 ml of dry dioxane. A mixture of acryloyl chloride (0.15 g, 1.7 mmol, 0.8 eq) dissolved in 10 ml of dry dioxane was then dropped into the solution under cooling and stirring. When finished, the mixture was heated to reflux for 3h and was stirred for additional 36 h. The precipitate of a yellow product was filtered and recrystallized from ethanol to obtain a yellow powder (0.16 g, 33%). Poly(N,N-dimethylacrylamide) was polymerized by free radical polymerization. For the reaction, DMAA (0.5 g, 5.04 mmol) was dissolved in dry and distilled DMF. The reaction was degassed by three freeze and thaw cycles and have been initiated by AIBN (4.3 mg, 0.5 mol %). The reaction was carried out at 56°C for 24 h. The reaction was aborted by precipitation of the reaction mixture in ice-cold diethyl ether. The resulting polymer was purified by repeated dissolving in methanol and precipitation in diethyl ether to obtain a white powder (210 mg, 45%). The copolymerization of DMAA and AAHAQ was carried out at 75°C by free radical polymerization in dry and distilled DMF under an inert gas atmosphere. For the polymerization AAHAQ (60 mg, 0.2 mmol) and DMAA (385 mg, 3.8 mmol) were dissolved in DMF (4 ml). The reaction mixture was degassed by three freeze and thaw cycles and initiated by AIBN (3.5 mg, 0.5 mol %). The polymerization then was stopped by precipitating the reaction mixture in ice-cold diethyl ether. The polymer was purified by repeatedly dissolving in MeOH and precipitating in diethyl ether to obtain a yellowish powder (290 mg, 64%). The amount of AAHAQ in the produced polymer was determined by integration of the <sup>1</sup>H-NMR spectra and was found to be approximately 4 mol %.

**Preparation of hydrogel-coated gold particle arrays.** Periodic arrays of gold nanoparticles with a diameter  $D=165\pm 10$  nm and  $\Lambda=400$  nm were employed as plasmonic substrate. Briefly, a BK7 glass substrate coated by thermal evaporation with 2 nm of Chromium and 50 nm of gold was spun coated with the S1805 positive photoresist (1:2 ratio diluted with propylene glycol monomethyl ether acetate), yielding a thickness of 120 nm. A periodic interference pattern was recorded employing a He-Cd laser ( $\lambda=325$  nm) with the Lloyd's mirror setup as previously reported by our group<sup>28</sup>. The well-defined resist particles with sub-wavelength dimensions were revealed by using the AZ-303 developer (1:15 ratio with deionized water). Finally, the inscribed pattern was transferred by etching the gold from the non-protected areas using an Argon milling system. The remaining photoresist was removed by applying an oxygen plasma treatment. The prepared plasmonic substrate was immersed overnight in a 1 mM solution made of benzophenone-disulfide dissolved in DMSO in order to form a self-assembled monolayer on the pristine gold surface. The hydrogel thin film was subsequently spun coated (3% w/w in ethanol) on top of the particle arrays at a rate of 2000 rpm for 60 s and dried overnight in a vacuum oven at 50°C.

**Observation of UV-crosslinked p(DMAA-co-AAHAQ) thin films.** Surface plasmon resonance (SPR) and optical waveguide spectroscopy (OWS) measurements were conducted using an optical setup based on the attenuated total reflection with the Kretschmann configuration<sup>29</sup>. Briefly, the hydrogel-coated substrate was mounted into an in-house developed flow cell and clamped into a high refractive index prism, previously matched with immersion oil. A polarized beam of light at  $\lambda=633$  nm emitted from a He-Ne laser (2 mW) was passed through the prism ( $n_p = 1.845$ ) containing the matched substrate with the hydrogel film. The construct with the prism, the coated sensor chip and the flow-cell was placed on a motor-controlled rotation stage (Huber AG, Germany). A photodiode connected to a lock-in amplifier (Princeton Applied Research, USA) was employed to collect and measure the intensity of the reflected laser beam at the surface. The acquired angular reflectivity spectra were fitted in order to determine the bulk refractive index ( $n_b$ ) and the thickness of the layer ( $d_b$ ). The Winspall software (Max Planck Institute for polymer research, Germany) based on a transfer matrix-based model was employed for the fitting<sup>30,31</sup>. As a sub-sensor, glass substrates were coated by thin gold film with a thickness of 50 nm (and 2 nm of chromium as adhesion layer) by vacuum thermal evaporation. The gold surface was reacted overnight in a 1 mM benzophenone disulphide solution in DMSO. A 3% (w/w) solution of the p(DMAA-co-AAHAQ) polymer (using ethanol as a solvent) was spun in the top of the gold at 2000 rpm for 60 sec and dried in a vacuum oven overnight at 50°C. The UV-curable polymer film was cross-linked with  $2\text{ J cm}^{-2}$  employing a UV-lamp with a wavelength of  $\lambda=264$  nm. Subsequently, the films were rinsed with ethanol to remove the loosely bound polymer.

**Two-photon cross-linking of p(DMAA-co-AAHAQ) thin films.** Firstly, a  $\mu\text{m}$ -thick film was deposited by drop-casting a 3% solution of the P(DMAA-co-AAHAQ) polymer on a coverslip slide and it was subsequently dried overnight at 50 °C inside an oven. The adhesion to the cover slip was promoted by the pre-coating of an epoxy-based film (SU-8 photoresist) that was spun coated at 5000 rpm for 2 min and cured in the oven at 50°C for 2 h. Afterward, the hydrogel-coated substrate was mounted into the Photonic Professional (GT) system (Na-

noscribe GmbH, Germany), equipped with a Er-doped femto-second laser source ( $\lambda=780$  nm, pulse duration of  $\sim 100$  fs and a repetition rate of 80 MHz) and connected to a 3D-piezo scanning stage. The  $63\times$  oil-immersion objective (NA: 1.4) was selected for the inscribing of the pattern via the two-photon cross-linking process. The laser power for this specific objective configuration was tuned and determined as follows: Laser power (mW) = laser power (0-100%)  $\times$  power scaling (1)  $\times$  50 mW. Series of square-shaped structures with dimensions consisting of  $100\times 100\times 15$   $\mu\text{m}$  with varying laser power ( $5-3.75\times 10^3$  mW) and writing speed (1000- 2500 l/s) were recorded to clarify the conditions to form 3D defect-free hydrogel structures. Additionally, a geometry consisting of another square-shaped structure ( $25\times 40\times 10$   $\mu\text{m}$ ;  $3.5\times 10^3$  mW laser power; 2500 l/s writing speed) connected by its base to a bigger rectangular-shaped structure was inscribed ( $250 \times 125 \times 10$   $\mu\text{m}$ ;  $4.5\times 10^3$  mW laser power; 5000 l/s writing speed) using the Nanoscribe software to clearly visualize the swelling ratio of the material. After the recording step, the unbound material was rinsed away by immersing the structure in ethanol. Afterwards, the remaining structure was observed in dry and swollen state (deionized water) with a help of an optical microscope.

**Plasmon-enhanced two-photon cross-linking of p(DMAA-co-AAHAQ).** In a similar manner, p(DMAA-co-AAHAQ) was deposited in the top of gold nanoparticle arrays carried by a glass substrate as described above. The substrate was mounted into the Photonic Professional (GT) system for the recording step, with the side carrying the plasmonic architectures facing a clean cover slip. The interface was selected by focusing on the surface with the gold nanoparticle arrays and the correct z plane was selected by recording square features with the highest writing speed and laser power and visually observing the recording of the  $\mu\text{m}$  size features with the equipped microscope camera. Once the proper interface was founded, a recording script was loaded and squares ( $100\times 100\times 1$   $\mu\text{m}$ ) with different parameters were inscribed. The scan speed was varied between  $10000-2500$   $\mu\text{m s}^{-1}$  and the laser power between  $2-5\times 10^3$  mW. After the recording step, the unbound polymer was removed with ethanol.

**Morphological characterization.** Atomic force microscopy (AFM) images of the patterned samples in air were acquired with the PicoPlus (Molecular Imaging, Agilent Technologies, USA) in tapping mode. The AFM measurements in water were carried out with the Nanowizard (JPK III, Germany) instrument equipped with the inverse microscope and a liquid chamber. Imaging of the samples in water was performed in contact mode and quantitative imaging (QI) mode (0.3 N/m cantilevers with 10 nm tip radius). The mapping to determine the mechanical properties was conducted in force volume mode both in water and in air (force curve at each pixel with 10  $\mu\text{m/s}$ , maximum force of 5 nN, up to  $200 \times 200$  resolution for  $2 \times 2$   $\mu\text{m}$  image). The Young's Modulus was determined by fitting the approach part with elastic model (Hertz model with Sneddon extension for geometry). Cantilever properties:  $k = 9$  N/m ( $\pm 2$ ), resonance frequency 150 kHz, beam shaped, 175  $\mu\text{m}$ , Al coating on backside, OPUS shape (tetrahedral), radius below 7 nm,  $35^\circ$  back angle.

## RESULTS AND DISCUSSION

In the presented experiment, we used a terpolymer poly(N,N-Dimethylacrylamide-co-Acrylamido-3-hydroxyanthraquinone)

p(DMAA-co-AAHAQ, ratio 96:4) that was copolymerized of DMAA and AAHAQ by free radical polymerization. At first, the conditions to effectively form networks from p(DMAA-co-AAHAQ) polymer layers by UV light (wavelengths of  $\lambda=264$  and 360 nm) and by two-photon crosslinking (TPC wavelength of  $\lambda=780$  nm) were investigated and their reversible swelling was characterized. Afterwards, this polymer was deposited on top of gold nanoparticle arrays that were prepared by UV-laser interference lithography with a geometry that tuned its associated LSPR wavelength close to 780 nm. Such substrates were finally tested for the plasmon-enhanced two-photon crosslinking (PTPC wavelength of 780 nm) in order to locally attach and crosslink the p(DMAA-co-AAHAQ) polymer network at the plasmonic hotspots as observed by AFM topography and Young modulus measurements.

**Figure 1**

**UV-crosslinking and polymer network swelling.** For the testing of the crosslinking with UV light, thin polymer layers were prepared and their thickness and polymer volume density were measured by a combination of surface plasmon resonance (SPR) and optical waveguide spectroscopy (OWS)<sup>32</sup>. The polymer films were prepared on the top of a flat 50 nm thick gold film that was modified with a self-assembled monolayer formed from benzophenone-disulfide. The polymer p(DMAA-co-AAHAQ) layer was deposited with a thickness of 154 nm. Afterwards, we observed that the polymer layer was not cross-linked for the irradiation with UV light emitted at  $\lambda=365$  nm (data not shown) with a dose as high as  $20$   $\text{J/cm}^2$  as all the polymer was washed away in the rinsing step. Interestingly, the irradiation at shorter wavelength of  $\lambda=264$  nm with a dose of  $2$   $\text{J/cm}^2$  generated stable polymer networks. As illustrated in Figure 2, the angular reflectivity spectra measured for such film shows a series of resonant dips due to the excitation of guided waves travelling along the surface. These spectra were fitted with a Fresnel reflectivity-based model. For a dry layer in contact with air, a thickness of  $d_h=154$  nm was determined for the assumed refractive index of  $n_h=1.45$ <sup>31</sup>. Subsequently, the reflectivity spectrum was recorded for the same polymer film that was swollen in water and a thickness of  $d_h=357$  nm and a refractive index of  $n_h=1.35$  was determined under the assumption that the polymer surface mass density does not change. These results translates to a swelling ratio of 2.3 was determined between the dry and swollen layers in the perpendicular direction to the surface (1D swelling).

**Figure 2**

**Two-photon crosslinking.** In the second step, the p(DMAA-co-AAHAQ) polymer layer was cross-linked via the scanning of a NIR laser, in order to test the TPC mechanism. For this purpose, a layer with a thickness of 10  $\mu\text{m}$  was used and a structure was recorded by scanning a pulsed laser beam over the photosensitive material with the commercial lithography tool, Photonic Professional (GT) system (Nanoscribe GmbH, Germany) followed by rinsing in ethanol to remove the non-cross-linked polymer chains. The films were prepared by drop-casting a 3% ethanol solution of the p(DMAA-co-AAHAQ) on the top of a glass substrate that carried a SU8 thin film that promotes adhesion to the p(DMAA-co-AAHAQ). In order to control the

irradiation dose, the laser power (LP) and writing speed (WS) were varied between  $2\text{-}5 \times 10^3$  mW and 1000-10000 lines/s respectively. In order to determine the patterning conditions, for which the p(DMAA-co-AAHAQ) polymer layer is sufficiently crosslinked, square shaped structures with lateral dimension of  $100\ \mu\text{m}$  were inscribed and after rinsing with ethanol, observed with an optical microscope. Figure 3a shows that for slow WS and high LP, irregular structures with defects are formed, which can be attributed to possible burning of the layer. For the WS=1000 l/s a flat surface free of defects is achieved for LP below  $3.75 \times 10^3$  mW and for the WS=2500 l/s the laser power can be increased up to  $4.25 \times 10^3$  mW without introducing defects. In order to confirm that the polymer networks form a hydrogel that swells in water, another structure was recorded consisting in two blocks. As a support a rectangular shaped blocked measuring  $250\ \mu\text{m}$  in length and  $125\ \mu\text{m}$  in width was inscribed (LP= $4.5 \times 10^3$  mW and WS=5000 l/s). To one of the shorter sides a smaller rectangular-shaped structure ( $50 \times 25\ \mu\text{m}$ ) was also patterned connected to the larger structure by its base with a LP=  $3.5 \times 10^3$  mW and a WS=2500 lines/s. As depicted in Figure 3b, the square-shaped hydrogel architecture ( $50 \times 25\ \mu\text{m}$ ) was still increasing its volume by a factor of two. The length of the shorter side that was not connected to the structure increased from  $25\ \mu\text{m}$  to  $44\ \mu\text{m}$ , which indicates that the crosslinking TPC mechanism occurs and preserves the hydrogel properties.

**Figure 3**

**Plasmon-enhanced two-photon crosslinking.** Gold nanoparticle arrays exhibiting a LSPR in the vicinity of  $780\ \text{nm}$  were engineered aiming to enhance and support the 2PC process around the plasmonic structures. As seen in Figure 4a, the pristine arrays of metallic nanoparticles were characterized via atomic force microscopy, displaying a period of  $\Lambda = 400\ \text{nm}$  and a diameter of  $D = 165 \pm 10\ \text{nm}$ . The surface of the particles was modified with a linker carrying photoactive benzophenone moieties immersing the substrate in a benzophenone disulphide solution. In a similar manner as for the thin hydrogel films, a thin layer of the P(DMAA-co-AAHAQ) was coated on the top of the metallic particles by spin-coating using a 3% (w/w) solution of the polymer yielding a thickness around  $150\ \text{nm}$ . Additionally, transmission spectroscopy was carried out to determine the resonance position of the arrays as displayed in Figure 4b. Prior the coating with the polymer film carrying anthraquinone moieties, the resonance position was located at  $706\ \text{nm}$ . After the coating with the polymer film, the resonance was red shifted to  $774\ \text{nm}$  due to the higher refractive index of the hydrogel in the dry state ( $n_h = 1.45$ ). The unexposed samples were mounted on the Nanoscribe holder for irradiation with the femtosecond laser. After the recording and washing step with ethanol, the patterned structures were investigated with atomic force microscopy. As can be seen in Figure 4c, the attachment of the polymer along the longitudinal axes of the particle arrays is clearly attained, employing a LP of  $4\ \text{mW}$   $10^3$  mW and a WS of 2500 l/s for the recording. In Figure 4d, the cross-section of a gold nanoparticle with the locally attached hydrogel is shown with its corresponding height profile. As a reference, the height profile of the same nanoparticle in the direction orthogonal to that of the patterned hydrogel is also included. The attached hydrogel can be distinguished with two peaks with lower height as for the gold nanoparticle. The patterned hydrogel spreads to a

distance of  $75 \pm 9\ \text{nm}$  with a height of  $44 \pm 3\ \text{nm}$  averaged over 22 patterned hydrogel features at 11 Au NPs.

**Figure 4**

It is worth noticing that the selective crosslinking only occurs for samples with a LSPR matching the wavelength of the laser source. This was demonstrated employing particles slightly bigger in size ( $D \sim 210\ \text{nm}$ , Figure 5a) with the corresponding red-shift of the LSPR and detuning of the resonance respect to the laser source<sup>28</sup>. In this case, a continuous layer of hydrogel is formed around the particles as seen in Figure 5b for a LP of  $3.75 \times 10^3$  mW and a WS of 2500 l/s. This manifests the importance of the LSPR position in order to plasmonically-enhanced the 2PC process and attach the hydrogel only at the regions where the electromagnetic field profile is more strongly confined. Interestingly, the areas irradiated with a LP below  $3 \times 10^3$  mW do not display crosslinking of the anthraquinone hydrogel around the the gold nanoparticles (data not shown).

**Figure 5**

**Mechanical properties and swelling degree.** The mechanical properties of the locally attached hydrogel were evaluated by determining the Young's Modulus in air (Figure 4a) and in water (Figure 4b) and calculated using the elastic contact model according to Hertz with the Sneddon extension for the tip geometry. It is clearly visible, that the Young's Modulus of the hydrogel in air is around 10x stiffer than for the hydrogel immersed in water (0 to 25 GPa for air and 0 to 2 GPa for water). The stiffness values for both the Young's Modulus in air and in water were derived by making histograms of the hydrogels YMs at random orientations (around 30 Au-NPs). The maximum of the fitting, representing the most probable value, was then determined as  $1.542 \pm 0.162\ \text{GPa}$  in air and  $0.119 \pm 0.008\ \text{GPa}$  in water. In addition, the swelling of the polymer was determined by comparing the size of the hydrogel (distance between upper and lower) in either air or water ( $N = 50$ ) from AFM images in contact or QI-mode (data not shown). The size of the hybrid features in air was of  $320.3 \pm 2.6\ \text{nm}$  while in water was slightly larger with  $349.2 \pm 2.2\ \text{nm}$  displaying a swelling of around 10%.

**Figure 6**

## CONCLUSIONS

Selective attachment of an anthraquinone-based hydrogel to the plasmonic hotspots regions of metallic nanostructures with sub-wavelength resolution is achieved. The hybrid architectures are attained by using well-ordered gold nanoparticle arrays with a LSPR in the vicinity of the laser source, which results on the local attachment of the hydrogel at the areas where the electromagnetic field is strongly confined via the plasmon-enhanced 2PC process. This strategy endows a future possibility to probe a larger distance from the hotspot regions of the metallic nanoparticles compared to most standard configurations based on self-assembled monolayers where only a limited area of the

probing field of the LSPR is employed in biosensing applications. In addition, hydrogels can serve as high capacity 3D binding matrices with high-loading capacity when modified with biorecognition elements, facilitating the diffusion and capture of target analytes inside the polymeric network<sup>33</sup>. This is but a first step proving the capability of the approach to selectively deposit the hydrogel at the plasmonic hotspots and further experiments with a novel material allowing for the post-modification of the hydrogel with biorecognition elements will be pursued.

## ASSOCIATED CONTENT

## AUTHOR INFORMATION

### Corresponding Author

\* E-mail address: jakub.dostalek@ait.ac.at (J.D.).

### Notes

The authors declare no competing financial interest.

## ACKNOWLEDGMENT

N.G.Q., S.V. and M. v. D., acknowledge funding from the European Union's Horizon 2020 research and innovation programme under grant agreement No 642787, Marie Skłodowska-Curie Innovative Training Network BIOGEL.

## REFERENCES

1. Sun, H.-B.; Kawata, S., Two-photon laser precision microfabrication and its applications to micro-nano devices and systems. *Journal of lightwave technology* 2003, 21 (3), 624.
2. Anscombe, N., *Direct laser writing*. Nature Publishing Group: 2010.
3. Gissibl, T.; Thiele, S.; Herkommer, A.; Giessen, H., Two-photon direct laser writing of ultracompact multi-lens objectives. *Nature Photonics* 2016, 10 (8), 554.
4. Florian, C.; Piazza, S.; Diaspro, A.; Serra, P.; Duocastella, M., Direct laser printing of tailored polymeric microlenses. *ACS applied materials & interfaces* 2016, 8 (27), 17028-17032.
5. Gissibl, T.; Thiele, S.; Herkommer, A.; Giessen, H., Sub-micrometre accurate free-form optics by three-dimensional printing on single-mode fibres. *Nature communications* 2016, 7, 11763.
6. Avci, E.; Grammatikopoulou, M.; Yang, G. Z., Laser-Printing and 3D Optical-Control of Untethered Microrobots. *Advanced Optical Materials* 2017, 5 (19), 1700031.
7. Zeng, H.; Martella, D.; Wasylczyk, P.; Cerretti, G.; Lavocat, J. C. G.; Ho, C. H.; Parmeggiani, C.; Wiersma, D. S., High-resolution 3D direct laser writing for liquid-crystalline elastomer microstructures. *Advanced materials* 2014, 26 (15), 2319-2322.
8. Selimis, A.; Mironov, V.; Farsari, M., Direct laser writing: Principles and materials for scaffold 3D printing. *Microelectronic Engineering* 2015, 132, 83-89.
9. Accardo, A.; Blatché, M. C.; Courson, R.; Loubinoux, I.; Thibault, C.; Malaquin, L.; Vieu, C., Multiphoton direct laser writing and 3D imaging of polymeric freestanding architectures for cell colonization. *Small* 2017, 13 (27), 1700621.

10. Zhou, X.; Hou, Y.; Lin, J., A review on the processing accuracy of two-photon polymerization. *AIP Advances* 2015, 5 (3), 030701.
11. Niesler, F.; Hermatschweiler, M., Two-Photon Polymerization—A Versatile Microfabrication Tool: From maskless lithography to 3D printing. *Laser Technik Journal* 2015, 12 (3), 44-47.
12. Hutter, E.; Fendler, J. H., Exploitation of localized surface plasmon resonance. *Advanced materials* 2004, 16 (19), 1685-1706.
13. Xia, Y.; Halas, N. J., Shape-controlled synthesis and surface plasmonic properties of metallic nanostructures. *MRS bulletin* 2005, 30 (5), 338-348.
14. Moskovits, M., Spot the hotspot: plasmonic hotspots--nanometre-sized crevices that permit the detection of single molecules--are too small to be imaged with conventional microscopes. They can now be probed using super-resolution fluorescence microscopy. *Nature* 2011, 469 (7330), 307-309.
15. Feuz, L.; Jönsson, P.; Jonsson, M. P.; Höök, F., Improving the limit of detection of nanoscale sensors by directed binding to high-sensitivity areas. *ACS Nano* 2010, 4 (4), 2167-2177.
16. Feuz, L.; Jonsson, M. P.; Höök, F., Material-selective surface chemistry for nanoplasmonic sensors: optimizing sensitivity and controlling binding to local hot spots. *Nano letters* 2012, 12 (2), 873-879.
17. Beeram, S. R.; Zamborini, F. P., Selective attachment of antibodies to the edges of gold nanostructures for enhanced localized surface plasmon resonance biosensing. *Journal of the American Chemical Society* 2009, 131 (33), 11689-11691.
18. Zhang, N.; Liu, Y. J.; Yang, J.; Su, X.; Deng, J.; Chum, C. C.; Hong, M.; Teng, J., High sensitivity molecule detection by plasmonic nanoantennas with selective binding at electromagnetic hotspots. *Nanoscale* 2014, 6 (3), 1416-1422.
19. Piliarik, M.; Kvasnička, P.; Galler, N.; Krenn, J. R.; Homola, J., Local refractive index sensitivity of plasmonic nanoparticles. *Optics express* 2011, 19 (10), 9213-9220.
20. Barik, A.; Otto, L. M.; Yoo, D.; Jose, J.; Johnson, T. W.; Oh, S.-H., Dielectrophoresis-enhanced plasmonic sensing with gold nanohole arrays. *Nano letters* 2014, 14 (4), 2006-2012.
21. Gargiulo, J.; Berté, R.; Li, Y.; Maier, S. A.; Cortés, E., From Optical to Chemical Hot Spots in Plasmonics. *Accounts of chemical research* 2019, 52 (9), 2525-2535.
22. Ueno, K.; Juodkazis, S.; Shibuya, T.; Mizeikis, V.; Yokota, Y.; Misawa, H., Nanoparticle-enhanced photopolymerization. *The Journal of Physical Chemistry C* 2009, 113 (27), 11720-11724.
23. Galloway, C. M.; Kreuzer, M. P.; Aćimović, S. S.; Volpe, G.; Correia, M.; Petersen, S. B.; Neves-Petersen, M. T.; Quidant, R., Plasmon-assisted delivery of single nano-objects in an optical hot spot. *Nano letters* 2013, 13 (9), 4299-4304.
24. Magill, B. A.; Guo, X.; Peck, C. L.; Reyes, R. L.; See, E. M.; Santos, W. L.; Robinson, H. D., Multi-photon patterning of photoactive o-nitrobenzyl ligands bound to

gold surfaces. *Photochemical & Photobiological Sciences* 2019, 18 (1), 30-44.

25. Pin, C.; Ishida, S.; Takahashi, G.; Sudo, K.; Fukaminato, T.; Sasaki, K., Trapping and Deposition of Dye-Molecule Nanoparticles in the Nanogap of a Plasmonic Antenna. *ACS Omega* 2018, 3 (5), 4878-4883.

26. Schwärzle, D.; Hou, X.; Prucker, O.; Rühle, J., Polymer Microstructures through Two-Photon Crosslinking. *Advanced Materials* 2017, 29 (39), 1703469.

27. Sergelen, K.; Petri, C.; Jonas, U.; Dostalek, J., Free-standing hydrogel-particle composite membrane with dynamically controlled permeability. *Biointerphases* 2017, 12 (5), 051002.

28. Quilis, N. G.; Lequeux, M.; Venugopalan, P.; Khan, I.; Knoll, W.; Boujday, S.; de la Chapelle, M. L.; Dostalek, J., Tunable laser interference lithography preparation of plasmonic nanoparticle arrays tailored for SERS. *Nanoscale* 2018.

29. Junk, M. J.; Jonas, U.; Hinderberger, D., EPR spectroscopy reveals nanoinhomogeneities in the structure and reactivity of thermoresponsive hydrogels. *Small* 2008, 4 (9), 1485-1493.

30. Sharma, N.; Petri, C.; Jonas, U.; Bach, M.; Tovar, G.; Mrkvová, K.; Vala, M.; Homola, J.; Knoll, W.; Dostálek, J., Molecularly Imprinted Polymer Waveguides for Direct Optical Detection of Low-Molecular-Weight Analytes. *Macromolecular Chemistry and Physics* 2014, 215 (23), 2295-2304.

31. Toma, M.; Jonas, U.; Mateescu, A.; Knoll, W.; Dostalek, J., Active control of SPR by thermoresponsive hydrogels for biosensor applications. *The Journal of Physical Chemistry C* 2013, 117 (22), 11705-11712.

32. Beines, P. W.; Klosterkamp, I.; Menges, B.; Jonas, U.; Knoll, W., Responsive thin hydrogel layers from photo-cross-linkable poly (N-isopropylacrylamide) terpolymers. *Langmuir* 2007, 23 (4), 2231-2238.

33. Mateescu, A.; Wang, Y.; Dostalek, J.; Jonas, U., Thin hydrogel films for optical biosensor applications. *Membranes* 2012, 2 (1), 40-69.

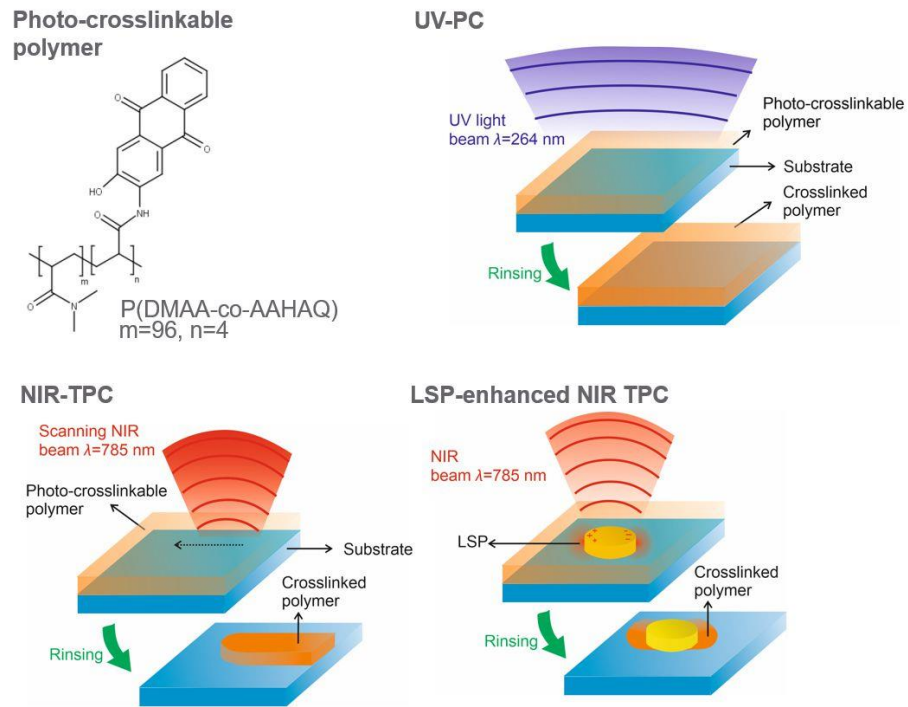


**Figure 1.** Drawing of the P(DMAA-co-AAHAQ) chemical structure (left) and schematic of the recording of the hydrogel structures via the three described mechanisms: UV-crosslinking (UV-PC), two photon crosslinking (NIR-TPC) and surface plasmon-enhanced two photon crosslinking (LSP-enhanced NIR TPC).

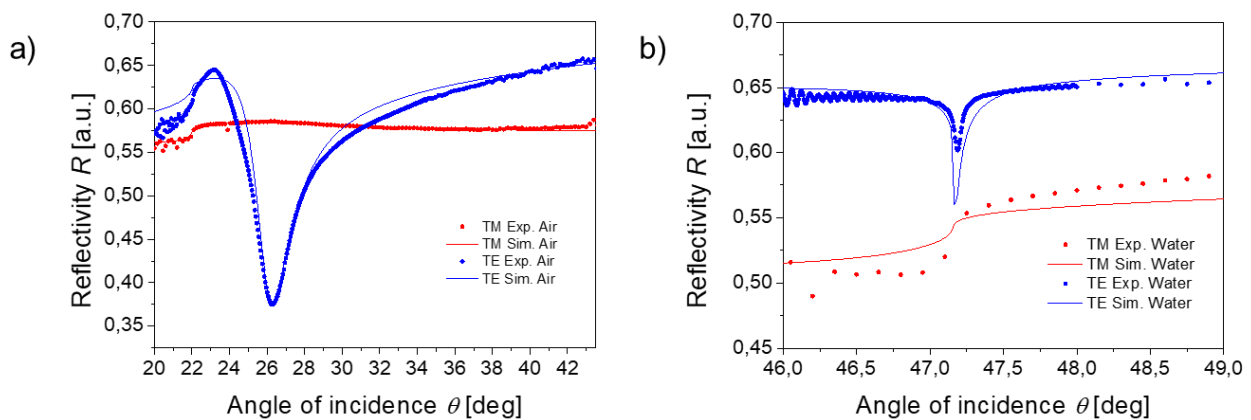


**Figure 2.** Measured and simulated reflectivity spectra in a) air and in b) water by SPR and OWS.

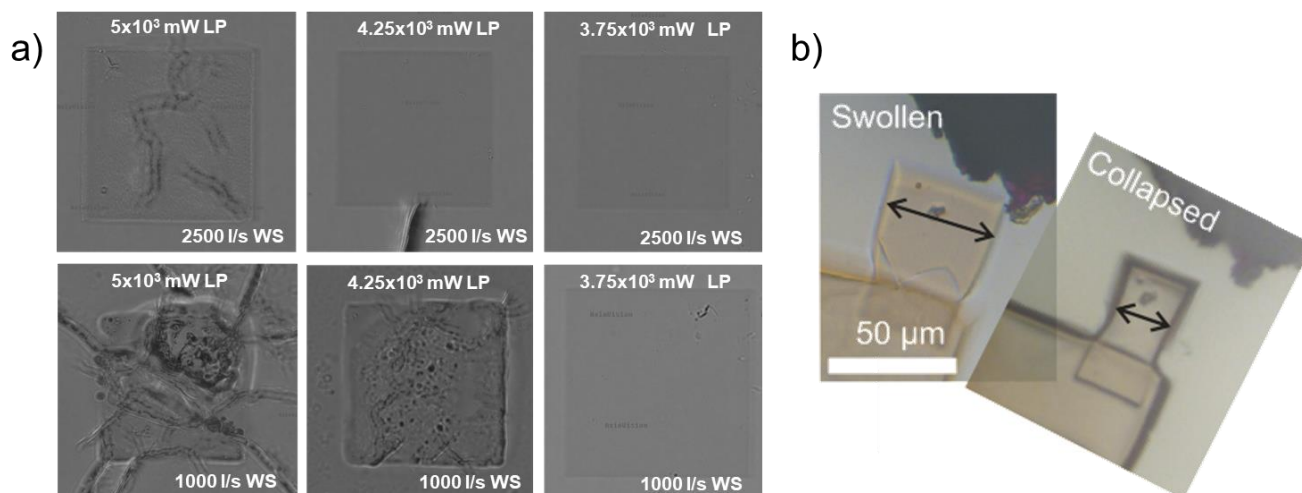


**Figure 3.** (a) Optical microscope images of the inscribed square-shaped structures with varying LP and WS. (b) Optical microscope images depicting the swelling of the hydrogel feature recorded with a LP of  $3.5 \times 10^3$  mW and a WS of 2500  $\mu\text{s}$ .

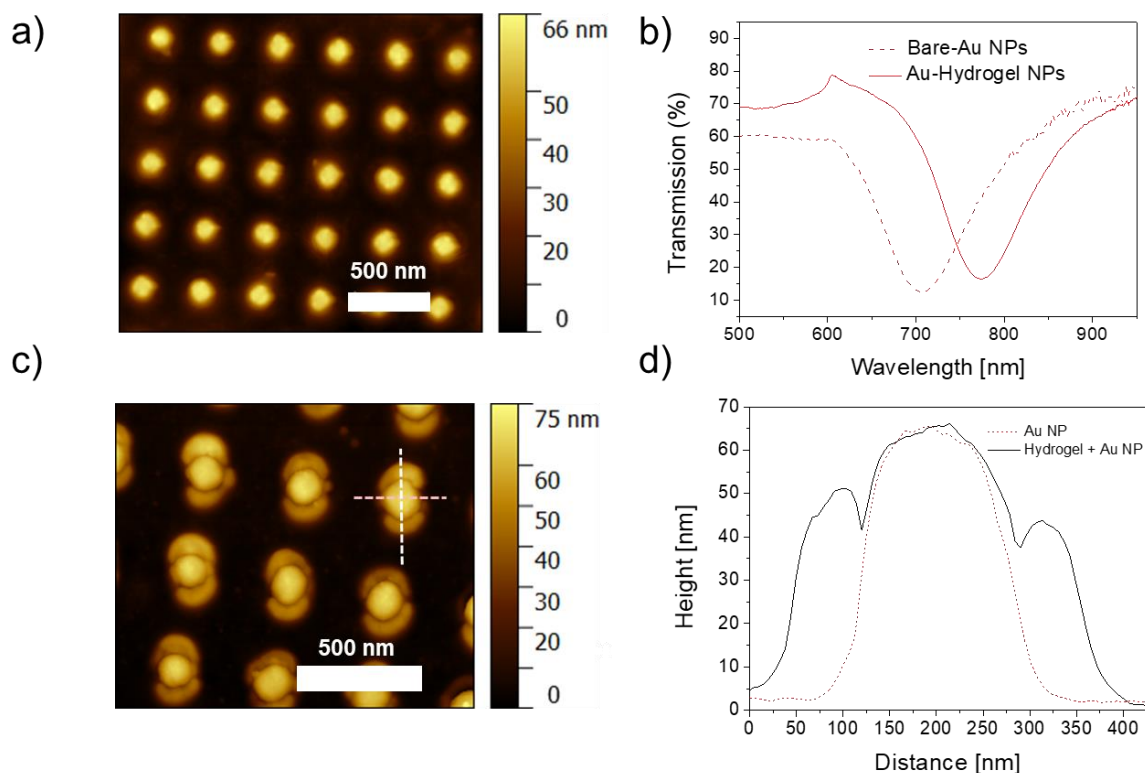


**Figure 4.** (a) AFM image of the bare Au NPs arrays prepared by laser interference lithography and (b) associated transmission spectra with and without coating with a nanometer-thick P(DMAA-co-AAHAQ) film. (c) AFM image of the attachment of the P(DMAA-co-AAHAQ) features at the plasmonic hotspots via the plasmon-enhanced 2PC mechanism. (d) Cross-section profile from the AFM image corresponding to a metallic nanoparticle with locally attached anthraquinone-based hydrogel and a the one from the side of gold nanoparticle without attached hydrogel.



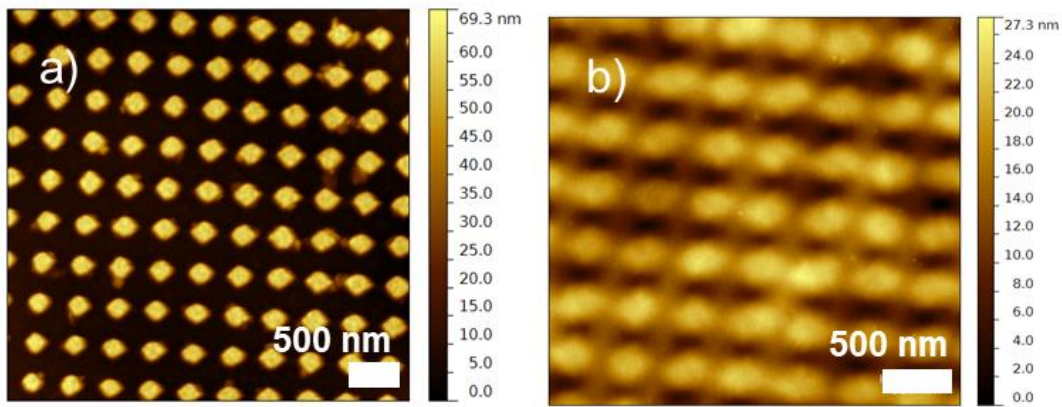


**Figure 5.** AFM images of the (a) reference area with particles displaying a spacing of  $\Lambda = 400$  nm and a diameter of  $D = 210$  nm and (b) AFM image of the patterned structure with irradiation with a LP of  $3.75 \cdot 10^3$  mW and a WS of 2500l/s.

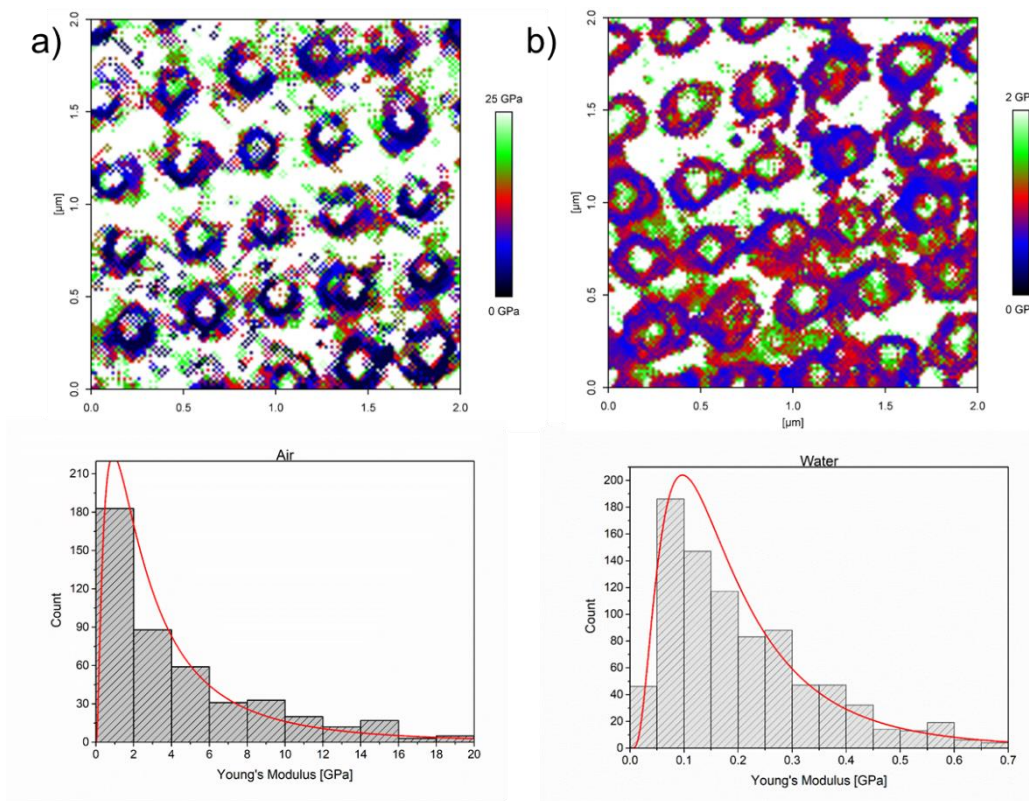


**Figure 6.** Comparison of Young's Modulus for the system in (a) air and in (b) water with a histogram below displaying the young's modulus of 30 nanoparticles at random orientations and its corresponding logarithmic fitting.

# 3.5

Actuated plasmonic nanohole arrays for sensing and optical spectroscopy applications



Cite this: *Nanoscale*, 2020, **12**, 9756

## Actuated plasmonic nanohole arrays for sensing and optical spectroscopy applications†

Daria Kotlarek,<sup>‡a</sup> Stefan Fossati,<sup>a</sup> Priyamvada Venugopalan,<sup>§a,b</sup>  
 Nestor Gisbert Quilis,<sup>a</sup> Jiří Slabý,<sup>c</sup> Jiří Homola,<sup>id c</sup> Médéric Lequeux,<sup>d</sup>  
 Frédéric Amiard,<sup>e</sup> Marc Lamy de la Chapelle,<sup>e</sup> Ulrich Jonas<sup>f</sup> and Jakub Dostálek <sup>id \*a</sup>

Herein, we report a new approach to rapidly actuate the plasmonic characteristics of thin gold films perforated with nanohole arrays that are coupled with arrays of gold nanoparticles. The near-field interaction between the localized and propagating surface plasmon modes supported by the structure was actively modulated by changing the distance between the nanoholes and nanoparticles and varying the refractive index symmetry of the structure. This approach was applied by using a thin responsive hydrogel cushion, which swelled and collapsed by a temperature stimulus. The detailed experimental study of the changes and interplay of localized and propagating surface plasmons was complemented by numerical simulations. We demonstrate that the interrogation and excitation of the optical resonance to these modes allow the label-free SPR observation of the binding of biomolecules, and is applicable for *in situ* SERS studies of low molecular weight molecules attached in the gap between the nanoholes and nanoparticles.

Received 28th January 2020,

Accepted 30th March 2020

DOI: 10.1039/d0nr00761g

rsc.li/nanoscale

Metallic nanohole arrays (NHAs) have attracted increasing attention after Ebbesen's observation of the extraordinary optical transmission<sup>1</sup> assigned to surface plasmon-mediated light tunneling through periodically arranged subwavelength pores. Subsequently, NHA structures have been employed in diverse application areas including optical filters,<sup>2,3</sup> amplification of weak spectroscopy signals such as fluorescence<sup>4,5</sup> and Raman scattering,<sup>6–9</sup> second-harmonic generation,<sup>10</sup> and particularly sensing. To date, NHA-based sensors have been utilized for the direct optical probing of proteins,<sup>11,12–14</sup> exosomes,<sup>15</sup> viruses,<sup>16,17</sup> bacteria,<sup>18</sup> and even cancer cells<sup>19,20</sup> and

organelles.<sup>21</sup> Moreover, NHA have enabled studies on lipid membranes that span over the holes<sup>22</sup> and allowed the facile incorporation of membrane proteins for interaction studies with drug candidates.<sup>16,23</sup>

NHA structures enable the electromagnetic field to be strongly confined inside subwavelength nanoholes<sup>24</sup> due to the excitation of two types of surface plasmon modes, propagating surface plasmons (PSPs, also referred to as surface plasmon polaritons) traveling along the metal surface and localized surface plasmons (LSPs), which occur at the sharp edges of the holes. The coupling to these modes can be tailored for specific purposes by controlling the structure geometry, including hole shape, diameter, and lateral periodic or quasi-periodic spacing.<sup>25</sup> In addition, a more complex spectrum of supported plasmonic modes can be utilized by combining complementary geometries that support LSP modes at similar wavelengths based on Babinet's principle.<sup>26</sup> When the NHA geometry approaches that of complementary metallic nanoparticle (NP) arrays, additional LSP resonance is introduced, which can near-field couple with the NHA.<sup>27</sup> Moreover, NHA structures that comprise stacks of periodically perforated metallic films<sup>28</sup> and NHA + NP structure with a defined lateral offset of NPs with respect to the nanohole center<sup>29</sup> have been investigated. Herein, we report a new approach to rapidly actuate the plasmonic characteristics of thin gold films perforated with nanohole arrays by thermo-responsive hydrogel and demonstrate its utilization to sensing with flow-through format SPR and SERS readout.<sup>30</sup> It is worth noting that arran-

<sup>a</sup>Biosensor Technologies, AIT-Austrian Institute of Technology GmbH, Konrad-Lorenz-Straße 24, 3430 Tulln an der Donau, Austria. E-mail: jakub.dostalek@ait.ac.at

<sup>b</sup>CEST Kompetenzzentrum für elektrochemische Oberflächentechnologie GmbH, TFZ, Wiener Neustadt, Viktor-Kaplan-Strasse 2, 2700 Wiener Neustadt, Austria

<sup>c</sup>Institute of Photonics and Electronics of the Czech Academy of Sciences, Chaberská 57, 18251 Praha 8, Czech Republic

<sup>d</sup>Université Paris 13, Sorbonne Paris Cité, Laboratoire CSPBAT, CNRS, (UMR 7244), 74 rue Marcel Cachin, 93017 Bobigny, France

<sup>e</sup>Institut des Molécules et Matériaux du Mans (IMMM – UMR CNRS 6283), Avenue Olivier Messiaen, 72085 Le Mans cedex 9, France

<sup>f</sup>Macromolecular Chemistry, Department Chemistry-Biology, University of Siegen, Adolf-Reichwein-Strasse 2, Siegen 57076, Germany

†Electronic supplementary information (ESI) available. See DOI: 10.1039/d0nr00761g

‡Current address: Captor Therapeutics Inc., ul. Duńska 11, 54-427 Wrocław, Poland.

§Current address: NYU Abu Dhabi, Saadiyat Campus, P.O. Box 129188, Abu Dhabi, United Arab Emirates.



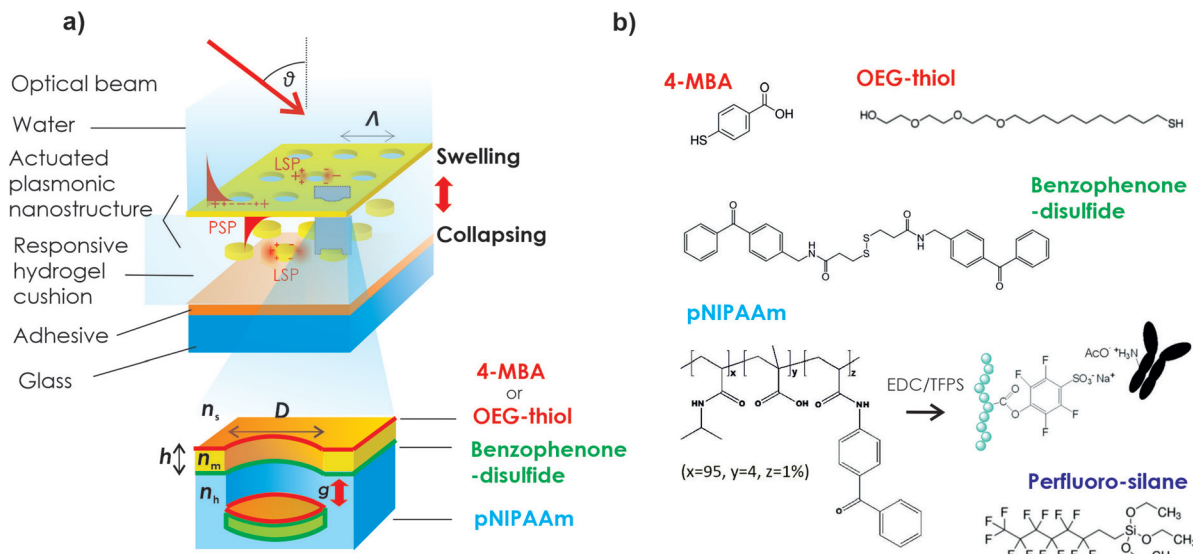


**Fig. 1** (a) Schematics of plasmonic nanostructure composed of periodic nanohole arrays (NHA) coupled with arrays of nanoparticles (NP) by the use of responsive hydrogel cushion implemented by materials with the chemical structure shown in (b).

ging the metallic nanoholes and nanoparticles in periodic arrays also decreases the damping of plasmonic modes by their diffraction coupling through the formation of the so-called surface lattice resonances.<sup>31</sup>

Perforated metal layer structures with NHA have been recently prepared using a range of lithography processes. In top-down approaches, a variety of geometries become accessible using focused ion beam milling (FIB) and electron beam lithography (EBL).<sup>32,33</sup> Nanoimprint lithography and template stripping<sup>34</sup> are used to partially alleviate the limited throughput of EBL and FIB by the replication of the NHA structure from pre-fabricated templates. Alternatively, NHAs were also prepared using bottom-up approaches, mostly relying on the self-organization of colloid particles.<sup>35</sup> Using sub-monolayer surface coverage of colloids, the colloid particles are used as a mask for the preparation of sparse and disordered nanoholes, while dense monolayers of colloids are employed to create well-ordered nanohole geometries.<sup>28,29,36</sup> This approach allows the pattern period,  $\Lambda$ , to be controlled by the size of the colloid particles and the hole diameter,  $D$ , can be independently adjusted *via* isotropic etching of the assembled particles before metal deposition. This technique was further extended for the preparation of nanoholes on cavities,<sup>37</sup> and a lift-off approach of the NHA membrane was also adopted for its subsequent transfer to more complex structures with multiple stacked patterned metallic layers.<sup>28</sup>

Typically, NHAs used for sensing applications are prepared *via* stripping-based techniques or lithographic methods directly on a non-permeable solid support, which is loaded to a microfluidic device.<sup>38,39</sup> However, the liquid sample to be analyzed is flowed over the perforated NHA surface with closed-ended pores, where the liquid flow velocity is equal to zero, and consequently, the transport of molecules to and inside the pores is dominantly driven by slow diffusion.<sup>40,41</sup>

Thus, to overcome this limitation, there a flow-through assay format has been developed, in which the analyte solution is transported internally across the nanoporous film.<sup>8,16,41,42</sup> However, these experiments typically rely on the structure of the NHA prepared on thin nitride membranes, which requires multiple lithography steps and complicates their application in sensing experiments.

The present study demonstrates a new type of NHA + NP structure, which is supported by a thermo-responsive hydrogel cushion. It is made from an *N*-isopropylacrylamide hydrogel material that can expand and contract in an aqueous environment, thereby actuating the plasmonic properties of metallic nanostructures.<sup>43–45</sup> In this architecture, the hydrogel cushion accommodates arrays of gold NPs, which are located below the NHA and their mutual distance,  $g$ , can be on demand actuated (Fig. 1). Herein, we investigate the spectra of supported PSP and LSP modes and their spectral detuning by temperature-induced reversible swelling and collapsing of a hydrogel cushion. In addition, the hydrogel can serve as a three-dimensional binding matrix for the immobilization of bio-functional molecules and the applicability of the structure for SPR (surface plasmon resonance) and SERS (surface-enhanced Raman scattering) detection is demonstrated with the use of plasmonic modes that probe the open pores, through which aqueous samples can be actively flowed.

## Results and discussion

We developed a method to prepare a nanostructure geometry that combines thin gold films perforated with NHA and arrays of gold NP, which are suspended in a thin layer of a poly(*N*-isopropyl acrylamide) (pNIPAAm)-based hydrogel. It serves as a responsive cushion, which responds to temperature changes



since pNIPAAm exhibits a lower critical solution temperature (LCST) of 32 °C. Below its LCST, it is hydrophilic, and it contains large amounts of water in its polymer network structure. When the temperature increases above its LCST, it abruptly collapses by expelling water. In the nanostructure geometry (Fig. 1a), the pNIPAAm-based hydrogel cushion was allowed to swell and collapse *via* the diffusion of water through the NHA pores and its volume changes were utilized for active control of the distance,  $g$ , between NHA and NP. In addition, the hydrogel was made from a terpolymer that carries pendant groups attached to its backbone, enabling its post-modification with bio-functional molecules (Fig. 1b) for application in optical spectroscopy and biosensors.<sup>46</sup> It is worth noting that this thermo-responsive hydrogel cushion allowed the controlled opening and closing of the nanohole arrays of pores, and switching to the open state was accompanied by the rapid diffusion of water, which drags contained biomolecules through the pores, where a plasmonic hotspot occurs. The spectrum of plasmonic modes probing the pores of the structure and their near field coupling was investigated in detail, as follows.

### Preparation of NHA + NP structure with hydrogel cushion

The NHA + NP structure featuring actively tunable plasmonic properties was prepared by a combination of UV nanoimprint lithography (UV-NIL) and template-stripping (Fig. 2a). Arrays of nanopillars cast to the transparent OrmoStamp material were used as a template. AFM observation of the structure topography showed that the arrays of nanopillars exhibited a diameter of  $D = 100$  nm, height of 100 nm, and they were arranged in rectangular arrays with a set period of  $\Lambda = 460$  nm (Fig. 2b). The arrays of OrmoStamp nanopillars were then activated by UV-ozone treatment and modified with perfluoro-silane using vapor deposition to reduce their surface energy. Subsequently, the nanopillars with a perfluoro-silane anti-adhesive layer were coated by a gold layer with a thickness of  $h = 50$  nm. SEM observation (Fig. 2c) revealed that the gold deposition led to the formation of a continuous layer, which is protruded by the nanopillars and their top is capped by gold that is not connected to the bottom continuous gold layer. Afterward, the outer gold surface was modified by a self-assembled monolayer of photo-active benzophenone-disulfide, and subsequently coated with a pNIPAAm-based terpolymer layer. This terpolymer contains the same photo-reactive benzophenone groups in its backbone (see Fig. 1b) and upon irradiation with UV light these chains were simultaneously covalently crosslinked and attached to the gold *via* the benzophenone-disulfide linker. Then, the outer surface of the crosslinked pNIPAAm-based polymer was pressed against a glass substrate with a soft adhesive layer (Ostemer resin pre-cured with UV light), which was subsequently thermally cured overnight at a temperature of 50 °C. Finally, the assembly was stripped at the OrmoStamp–gold interface (treated with anti-adhesive layer) to yield a structure with a thin gold film perforated by NHA, which were attached to the pNIPAAm-based crosslinked polymer networks and underneath comprised of embedded

gold NPs spatially separated from the perforated continuous gold film. The AFM topography image in Fig. 2d shows that the pores exhibit the same diameter,  $D$ , as the nanopillars and the SEM image of an edge of the structure in Fig. 2e confirms that under the NHA, arrays of gold NPs are present (which were stripped from the top of the OrmoStamp pillars). It is worth noting that the distortions of the surface that are visible in Fig. 2e are a result of breaking the sample to obtain the cross-section image.

### Optical observation of plasmonic modes

The spectra of the LSP and PSP modes supported by the prepared nanostructure were investigated *via* optical transmission measurements. To distinguish between the diffraction coupling to the dispersive PSP modes (traveling along the gold film) and non-dispersive LSP resonances (supported by the pores in the NHA + NP nanostructure), transmission spectra were measured *via* collimated beam impinging on the NHA + NP structure at angles in the range of  $\theta = 0^\circ$  to  $25^\circ$ . The transmitted beam emitted from a halogen light bulb was then analyzed with a spectrometer in the wavelength range of  $\lambda = 500$ – $850$  nm. Firstly, the wavelength-angular dependence of the transmission was measured for a structure that was dry and in contact with air (with a refractive index of  $n_s = 1$ ). As presented in Fig. 3a, the acquired spectrum shows that the excitation of non-dispersive resonance is manifested as a dip centered at a wavelength of  $\lambda_A = 600$  nm. Moreover, an additional dispersive mode occurs, and its excitation is associated with the dip in the transmission spectrum at  $\lambda_C^d = 750$  nm, which splits when the angle of incidence,  $\theta$ , deviates from zero. Secondly, the structure was clamped to a flow-cell and water (with a refractive index of  $n_s = 1.33$ ) was flowed over its surface, which was kept at a temperature of  $T = 40$  °C. This temperature is above the LCST of pNIPAAm, and thus this material exhibits hydrophobic properties, preventing the diffusion of water into the polymer networks through the NHA pores. Since the refractive index of the dielectric above the structure  $n_s$  increased, a new dispersive dip resonance centered at a wavelength of  $\lambda_B^d = 650$  nm appeared, while the resonance features  $\lambda_A$  and  $\lambda_C^d$  changed negligibly (Fig. 3b). Thirdly, the structure in contact with water was cooled to  $T = 22$  °C, which is below the LCST of pNIPAAm. Then, a strong blueshift in the  $\lambda_A$  and  $\lambda_C^d$  resonances occurred in the transmission spectrum, and also much weaker spectral shift of  $\lambda_B^d$  accompanied by a decrease in coupling efficiency at this wavelength (Fig. 3c). These observations indicate that the resonances at  $\lambda_A$  and  $\lambda_C^d$  are associated with the coupling to the surface plasmon modes that confine the electromagnetic field in the inner side of the structure in contact with the pNIPAAm-based hydrogel (with a refractive index of  $n_h = 1.47$  at  $T = 22$  °C and  $n_h = 1.37$  at  $T = 40$  °C, see ESI, Fig. S1†). The resonance  $\lambda_B^d$  probes the upper part of the structure in contact with water ( $n_s = 1.33$ ), which changes its refractive index with temperature much less than pNIPAAm. Since the resonances at  $\lambda_B^d$  and  $\lambda_C^d$  are dispersive, they can be attributed to the PSP modes traveling at the upper or bottom interface of the gold film, respect-



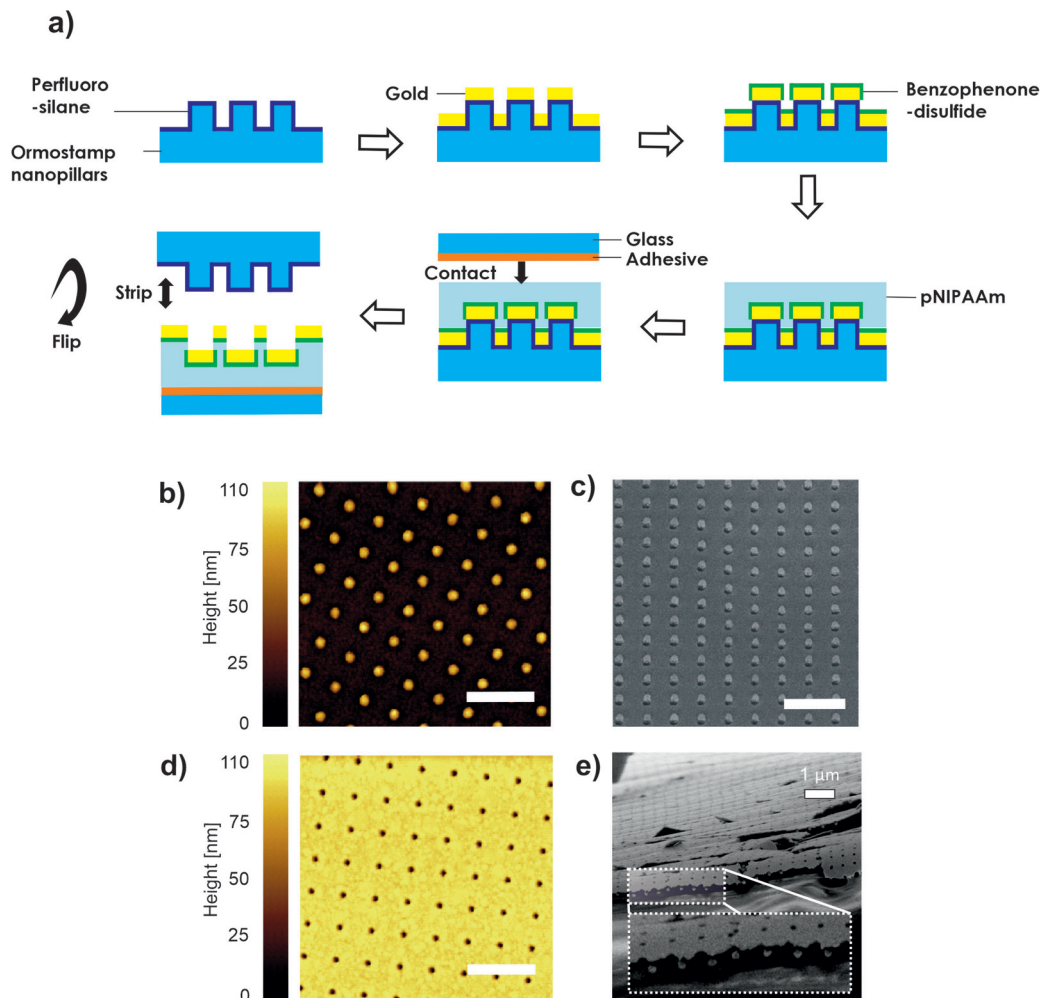


**Fig. 2** (a) Schematic of the preparation steps of the investigated NHA + NP nanostructure, (b) AFM image of the template with arrays of nanopillars cast to OrmoStamp, (c) SEM image after coating of the template with a 50 nm thick gold layer, (d) AFM image of the topography of the stripped surface with gold NHA, and (e) SEM image of a broken edge of the NHA + NP structure tethered to a solid surface via the responsive pNIPAAm-based polymer. All scale bars are 1  $\mu\text{m}$  in length.

ively. The non-dispersive nature of the  $\lambda_A$  resonance indicates it can be ascribed to the LSP mode.

A more detailed dependence of the transmission spectra on temperature  $T$  was investigated for the normal angle of incidence  $\theta = 0$  (Fig. 3d). The spectra were measured using a different light source (supercontinuum laser) in order to extend the wavelength range to 900 nm, which allowed us to observe an additional feature manifested as a transmission peak at  $\lambda_C^p = 810$  nm. Moreover, this showed more clearly that close to  $\lambda_B^d$ , a peak appeared at a wavelength  $\lambda_B^p$ . It is worth noting that the measured transmission spectra were normalized with that obtained for a flat 50 nm thick gold film, which exhibited a rapidly decreasing transmission with wavelength in the red and near infrared region of the spectrum. Therefore, the measurement of absolute transmission values was not possible, and thus only relative values are presented. In addition, the spectral positions of the resonances in Fig. 3a, b and d slightly differ since they were measured with different

(although fabricated under identical conditions) NHA + NP nanostructures.

#### Identification of plasmonic modes aided by simulations

The five observed resonant features in the measured transmission spectra were identified using numerical finite difference time domain (FDTD) simulations. This model was employed to calculate the absorption wavelength spectra and near-field distribution of the electromagnetic field occurring in the structure upon a plane wave normally impinging at its surface. The simulations of the absorption spectra allowed us to distinguish the resonant excitation of the LSP and PSP modes (which is accompanied with damping) from other features occurring in the transmission spectrum, which are related to the interference between multiple specular and non-specular diffracted beams and their falling after the horizon in the superstrate or substrate. As shown in Fig. 4a (blue curve), we initially analyzed a structure composed of only arrays of



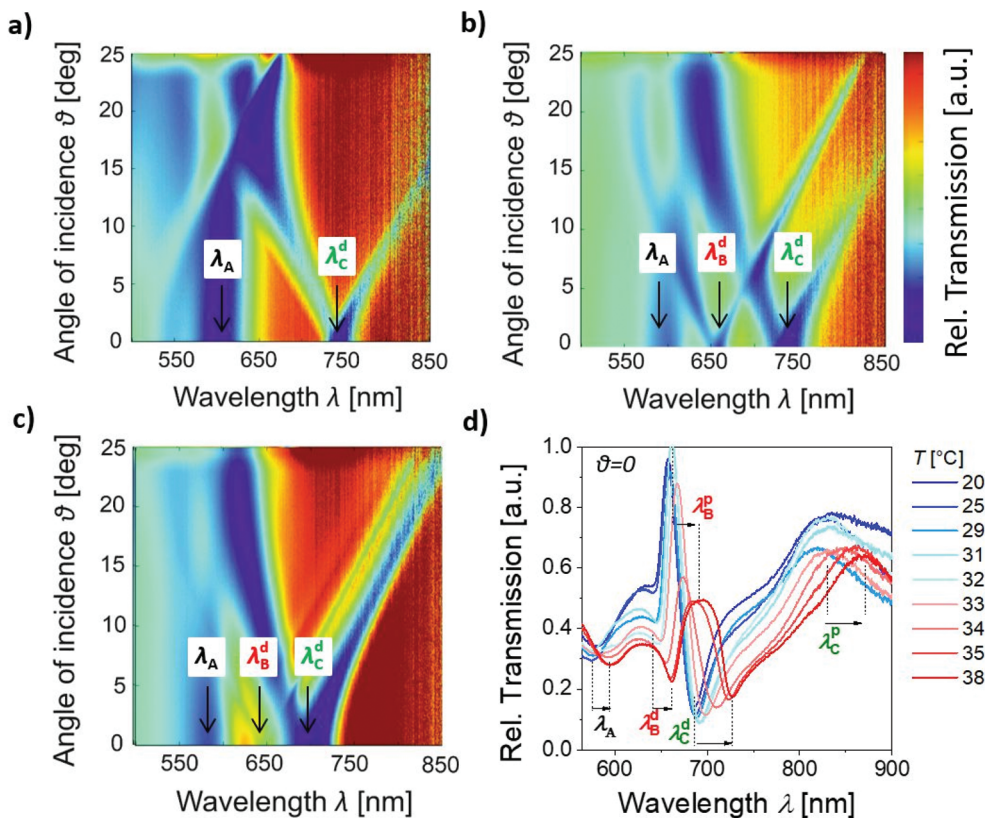


**Fig. 3** Measured dependence of wavelength transmission spectra on angle of incidence,  $\theta$ , for the NHA + NP structure in contact with (a) air ( $n_s = 1$  and  $n_h = 1.48$ ), (b) for the collapsed state of the pNIPAAm-based cushion that is in contact with water at  $T = 40$  °C ( $n_s = 1.33$  and  $n_h = 1.48$ ), and (c) for the swollen state of pNIPAAm cushion in water at  $T = 22$  °C ( $n_s = 1.33$  and  $n_h = 1.37$ ). (d) Comparison of the wavelength transmission spectra for  $\theta$  and NHA + NP structure in contact with water at varying temperature,  $T$ . The transmission spectra were normalized with that measured for the flat structure without the perforated Au film.

cylindrically shaped nanoparticles (NPs with a height of  $h = 50$  nm, average diameter of  $D = 100$ – $120$  nm, and period of  $\Lambda = 460$  nm) embedded between dielectrics with the refractive indices of  $n_h = 1.47$  and  $n_s = 1.33$ . The simulated spectrum reveals that the resonance associated with the coupling to LSP on the arrays of NPs is manifested as a strong absorption peak at a wavelength of about 707 nm. The complementary NHA structure was composed of a 50 nm thick gold film that was perforated with arrays of cylindrical nanoholes exhibiting the same diameter  $D$  and sandwiched between the same dielectrics with refractive indices of  $n_h = 1.47$  and  $n_s = 1.33$ . The absorption spectrum in Fig. 4a (red curve) shows three resonances located at the wavelengths of  $\lambda_A = 630$  nm,  $\lambda_B = 676$  nm, and  $\lambda_C = 774$  nm. At these wavelengths, the near-field distribution of the electric field amplitude  $|E|$  (normalized with that of the incidence plane wave  $|E_0|$ ) was simulated, as can be observed in the right part of Fig. 4a. These plots reveal that the resonance at wavelength  $\lambda_A$  exhibits the characteristics of the dipolar LSP mode, which confines the field inside the nanohole. The resonance at the longer wavelength  $\lambda_B$  shows a more delocalized field profile on the top interface of the gold film with the superstrate  $n_s = 1.33$ , which confirms it is due to first-order diffraction coupling to the traveling PSP mode at this

surface. The resonance at the NIR wavelength  $\lambda_C$  is accompanied with the confinement of the electric field at the bottom gold layer interface with the dielectric  $n_h = 1.47$ , which peaks at the mouth of the pore and its distribution suggests the main origin corresponds to the first-order diffraction coupling to the PSPs traveling along the bottom gold film surface. It should be noted that these simulations were carried out for the mouth of the nanopores filled by a dielectric with a refractive index  $n_s$  since the fabrication procedure involving stripping from arrays of nanopillars suggests this geometry (see Fig. 2a).

The simulations in Fig. 4b (brown curve) reveal that the short wavelength resonance was blue-shifted to  $\lambda_A = 621$  nm, the middle resonance blue-shifted to  $\lambda_A = 672$  nm, and the long-wavelength resonance red-shifted to  $\lambda_C = 813$  nm after the coupling of the nanohole arrays with the cylindrical nanoparticle arrays (NHA + NP). In these simulations, the gap distance between the bottom edge of the nanopore and the upper surface of the cylindrically shaped nanoparticle was set to  $g = 50$  nm, which corresponds to the difference between the nanopillar height of 100 nm and the thickness of the gold layer of  $h = 50$  nm (see Fig. 1 and 2). When the refractive index of the superstrate decreased from  $n_s = 1.33$  (representing



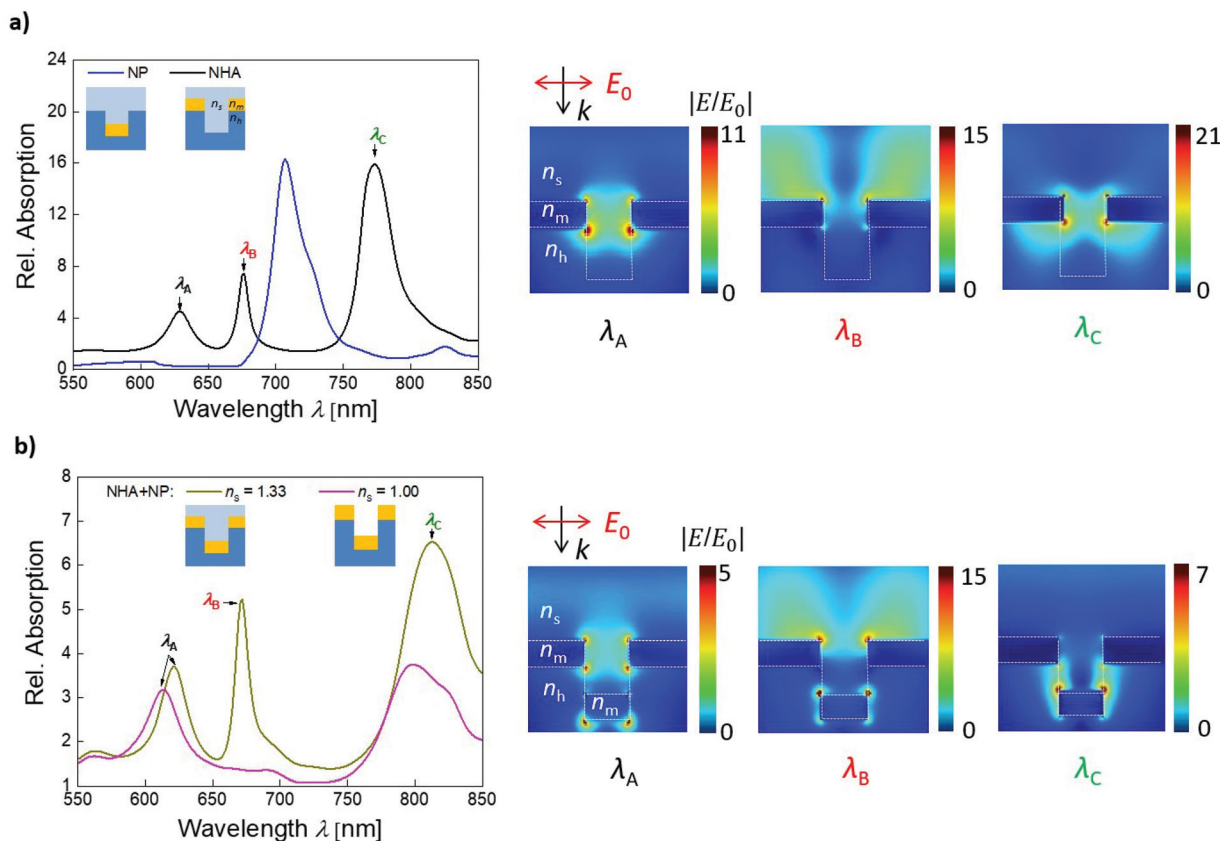


**Fig. 4** Simulation-based investigation of the spectrum of supported plasmonic modes: absorption spectra obtained for normally incident beam at (a) structure with a thin gold film perforated with arrays of nanoholes (NHA), with arrays of cylindrical nanoparticles (NP), and for the combined geometry (NHA + NP) with superstrate refractive indices  $n_s = 1$  and 1.33 and substrate refractive index  $n_h = 1.47$ . (b) Absorption spectrum simulated for the NHA + NP geometry for superstrate refractive indices  $n_s = 1$  and 1.33. The substrate refractive index was of  $n_h = 1.47$ , gap distance between NP and NHA was of  $g = 50$  nm, period of  $\Lambda = 460$  nm, diameter averaged between  $D = 100$ –120 nm, and height of  $h = 50$  nm. The cross-section of spatial distribution of the electric field amplitude was simulated for the plasmonic modes as indicated in the inset.

water) to  $n_s = 1$  (representing air), the middle-wavelength resonance disappeared, as shown in Fig. 4b (green curve). This observation agrees with the measurements presented in Fig. 3 and confirms that the middle resonance occurs due to the first-order diffractive coupling to the PSP mode at the outer gold layer surface, which is the most sensitive to variations in refractive index on the upper interface (superstrate  $n_s$ ). In addition, this refractive index decrease led to a slight blue shift in  $\lambda_A$  and  $\lambda_C$  since the field distribution corresponding to these resonances also partially probe the dielectric  $n_s$ . The spatial profile of the near field-enhanced electric field amplitude in the right part of Fig. 4b shows that the presence of gold disk nanoparticles slightly perturbed the nanohole LSP resonance at  $\lambda_A$  as the field is dragged to the bottom part of the disk nanoparticle. The resonance at  $\lambda_B$  due to the PSPs traveling on the top interface only weakly couples with the disk nanoparticles, contrary to the bottom PSP mode  $\lambda_C$ , which exhibits a field distribution with a more pronounced confinement in the gap.

Interestingly, the simulations predicted that only three plasmonic modes are supported in the investigated wavelength

range (Fig. 4b, brown curve) when the geometry of NHA (with three plasmonic modes, black curve Fig. 4a) and NP arrays (with one mode, blue curve in Fig. 4a) are combined to yield the experimentally investigated structure NHA + NP. However, five features were identified in the experimental transmission data presented Fig. 3, which is greater than the number of predicted plasmonic modes. The discrepancy between the simulated absorption spectra and experimentally measured specular transmission can be explained by the Fano shape of the two measured transmission resonances. The middle wavelength peak at  $\lambda_B^p$  and dip at  $\lambda_B^d$  can be attributed to the excitation of a single PSP mode at the interface of the structure with superstrate  $n_s$  and its asymmetric shape can be ascribed to the interference with additional waves generated by the structure in a broader wavelength range (previously observed for related plasmonic nanostructure by simulations<sup>3</sup>). Similarly, the long wavelength peak at  $\lambda_C^p$  and dip at  $\lambda_C^d$  can be attributed to the excitation of the PSP mode at the opposite interface of the structure with superstrate  $n_h$ .

In the next step, we performed more detailed simulations to reveal the spectral detuning of the resonances by the refrac-





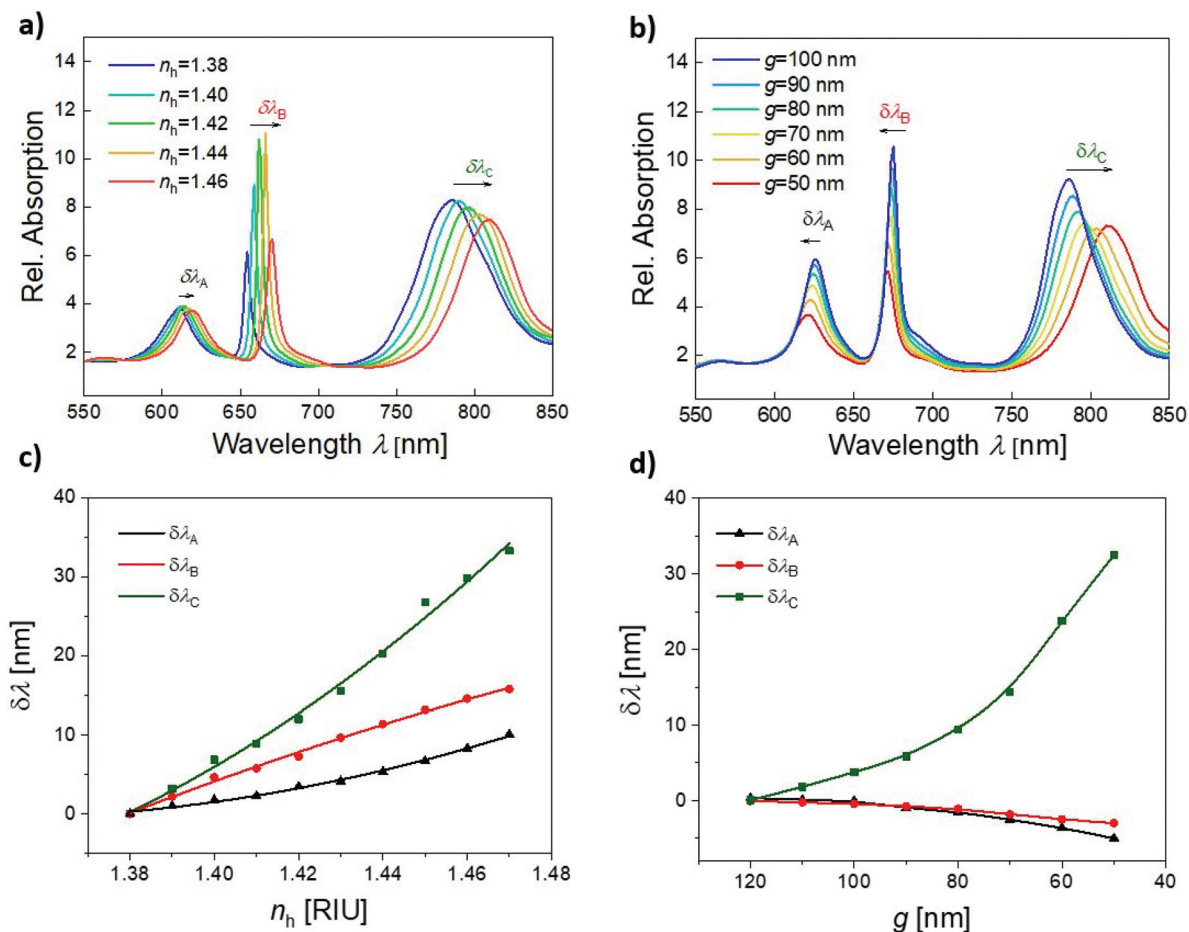


**Fig. 5** Simulated absorption spectra for the structure NHA + NP for varying: (a) refractive index of substrate  $n_h$  and (b) distance  $g$  between NHA and NP. From these spectra, the spectral shift of three resonant features were determined for changes in (c)  $n_h$  and (d)  $g$ . The superstrate refractive index was set to  $n_s = 1.33$ , the substrate refractive index for (b) and (d) was  $n_h = 1.47$ , gap distance between NP and NHA for (a) and (c) was set as  $g = 50$  nm, period was  $\Lambda = 460$  nm, average diameter between  $D = 100$ – $120$  nm, and height  $h = 50$  nm.

tive index changes of the bottom dielectric  $n_h$  and distance  $g$  between the gold NPs and NHA. These simulations represent the expected effect of the swelling and collapsing of the pNIPAAm-based hydrogel cushion. In general, an increase in swelling is assumed to be accompanied with a prolongation of distance  $g$ , a decrease in polymer volume content, and consequently a decrease in the refractive index  $n_h$ . Fig. 5a and b show that the refractive index  $n_h$  gradually increased from 1.38 to 1.46 and distance  $g$  varied between 50 and 100 nm, respectively. The increase in the substrate refractive index  $n_h$  led to a redshift for all three resonances (Fig. 5a), which is consistent with the experimental data presented in Fig. 3d. For small changes in the refractive index, the variations in the resonant wavelengths can be assumed to be linear, and accordingly, the determined refractive index sensitivity of  $\delta\lambda_B/\delta n_h = 190$  nm RIU<sup>-1</sup> and  $\delta\lambda_C/\delta n_h = 390$  nm RIU<sup>-1</sup> were obtained from the simulated data. These values are in the range reported for another SPR sensor configuration, which utilizes grating coupling to PSP modes.<sup>47</sup> The lower sensitivity of  $\delta\lambda_A/\delta n_h = 90$  nm RIU<sup>-1</sup> for the LSP mode is also in accordance with the previous

observations on LSPR.<sup>44</sup> Similarly, the refractive index sensitivity of the three plasmon modes to a change in the refractive index of the superstrate  $n_s$  was determined to be  $\delta\lambda_A/\delta n_s = 137$  nm RIU<sup>-1</sup>,  $\delta\lambda_B/\delta n_s = 260$  nm RIU<sup>-1</sup> and  $\delta\lambda_C/\delta n_s = 83$  nm RIU<sup>-1</sup> according to the data presented in Fig. S2.† Apparently, the highest sensitivity is observed for the mode at  $\lambda_B$ , which is ascribed to the PSP at the outer interface, where the field is dominantly confined.

The simulated spectra for varying gap distances  $g$  are presented in Fig. 5b. They show more complex behavior and the resonances  $\lambda_A$  and  $\lambda_B$  are weakly blue-shifted with a decrease in distance  $g$ , while  $\lambda_C$  is strongly red-shifted. These changes exhibit non-linear behavior, and for the shorter distances of  $g$ , they are more pronounced than for the longer distances of  $g$ . Therefore, this observation can be attributed to the near-field coupling between the gold NPs and NHA, which is particularly pronounced for the resonance  $\lambda_C$  with its field tightly confined in the gap (see right part of Fig. 4b). Interestingly, for the long distance  $g$ , an increase in the absorption close to the wavelength of 700 nm occurred, which may be due to the re-occur-



rence of the LSP resonance supported by gold NP arrays not coupled with NHA, as presented in Fig. 4a.

### Actuating of plasmonic modes

The swelling and collapsing of the pNIPAAm-based hydrogel cushion by varying the temperature around its LCST were further exploited for actuating the plasmonic modes supported by the prepared structure NHA + NP. In this experiment, we varied temperature in the range of  $T = 20\text{--}38\text{ }^\circ\text{C}$  and tracked the resonant positions of all the identified spectral features, including the transmission dip at  $\lambda_A = 577\text{ nm}$  due to the LSP in the nanoholes, spectral dip at  $\lambda_B^d = 641\text{ nm}$  and peak at  $\lambda_B^p = 658\text{ nm}$ , which are ascribed to the Fano resonance of the PSPs on the top NHA surface, and spectral dip at  $\lambda_C^d = 684\text{ nm}$  and peak at a wavelength of  $\lambda_C^p = 825\text{ nm}$  attributed to the Fano resonance of PSP at the bottom NHA surface coupled with arrays of NPs (measured at temperature  $T = 20\text{ }^\circ\text{C}$ ). The obtained response was measured with time upon a step-wise increase and decrease in temperature  $T$  according to the analysis of the spectra presented in Fig. 3d. The obtained time kinetics in Fig. 6 show that the changes are reversible. The features presented in Fig. 6a show a gradual increase in spectral position with an increase in temperature  $T$ . The Fano resonance features  $\lambda_B^d$  and  $\lambda_B^p$  exhibit similar shifts and the maximum change of about 20 nm occurred when the temperature increased from  $T = 22\text{ }^\circ\text{C}$  to  $38\text{ }^\circ\text{C}$ . The highest slope in the shift occurred close to the LCST of pNIPAAm of  $32\text{ }^\circ\text{C}$ . At a higher temperature, it was not possible to track the spectral shift in the peak due to the fact that it became weakly pronounced. The spectral dip  $\lambda_C^d$  showed the same trend and exhibited a stronger maximum shift of 40 nm for the temperature increase from  $T = 22\text{ }^\circ\text{C}$  to  $38\text{ }^\circ\text{C}$ .

Interestingly, the dependence of  $\lambda_A$  and  $\lambda_C^p$  shows different behavior. When the temperature increased above  $T = 22\text{ }^\circ\text{C}$ , an initial decrease in the resonance  $\lambda_A$  occurred followed by an increase with a local maximum at  $T = 29\text{ }^\circ\text{C}$ , then it decreased again, and above the LCST of pNIPAAm, it rapidly increased and shifted by about 20 nm. The peak position  $\lambda_C^p$  showed a complementary trend and it strongly decreased by 15 nm when the temperature increased from  $22\text{ }^\circ\text{C}$  to  $27\text{ }^\circ\text{C}$ , and then it increased with the local maximum at  $30\text{ }^\circ\text{C}$ , and when passing the LCST it rapidly red-shifted by 38 nm. These anomalous dependencies can be explained by the competing effect of the near-field coupling (which is dominantly controlled by distance  $g$  and exhibit non-linear dependence, as shown in Fig. 5d) and refractive index change, which shifts the resonance linearly (see Fig. 5c). The anomalous changes occurred below the LCST of pNIPAAm, which indicates that distance  $g$  is not directly proportional to the swelling degree of the hydrogel cushion layer, and other effects such as filling the pores with the swelling polymer networks can occur.

### Local probing of molecular binding events

To explore the potential of the developed hybrid nanostructure for applications in sensing, we employed the plasmonic resonances for local probing of molecular binding events at specific parts. In the first experiment, we directly monitored the binding of biomolecules in the pNIPAAm-based hydrogel cushion from the associated refractive index changes. These changes detuned the SPR wavelengths, where the excitation of the modes probing different the sub-parts of the structure occurred. After the stripping of the structure, the outer gold surface and the mouth of the pores were passivated by the thiol SAM with oligoethylene glycol (OEG) groups. Then, the pNIPAAm-based hydrogel cushion was post-modified *in situ* by covalent coupling of mouse immunoglobulin G, mIgG. The

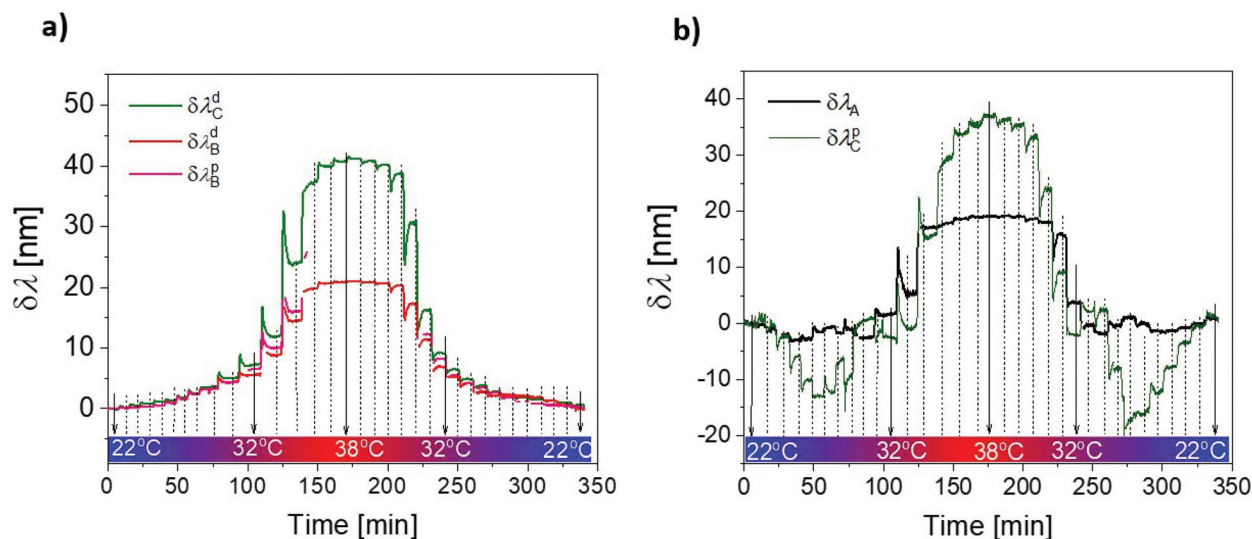


**Fig. 6** Dependence of spectral position of plasmonic features plotted as function of time for different temperatures in the range of  $T = 22\text{ }^\circ\text{C}$  to  $T = 38\text{ }^\circ\text{C}$ : (a) gradual variation in the spectral positions of dips  $\lambda_B^d$  and  $\lambda_C^d$  and peak at  $\lambda_B^p$  and (b) anomalous variations in the spectral positions of dip  $\lambda_A$  and peak  $\lambda_C^p$ .



spectral positions of the resonances at  $\lambda_A$  and  $\lambda_C^d$  were monitored by tracking their spectral detuning upon the surface reactions, as can be seen in Fig. 7a. These two resonances were

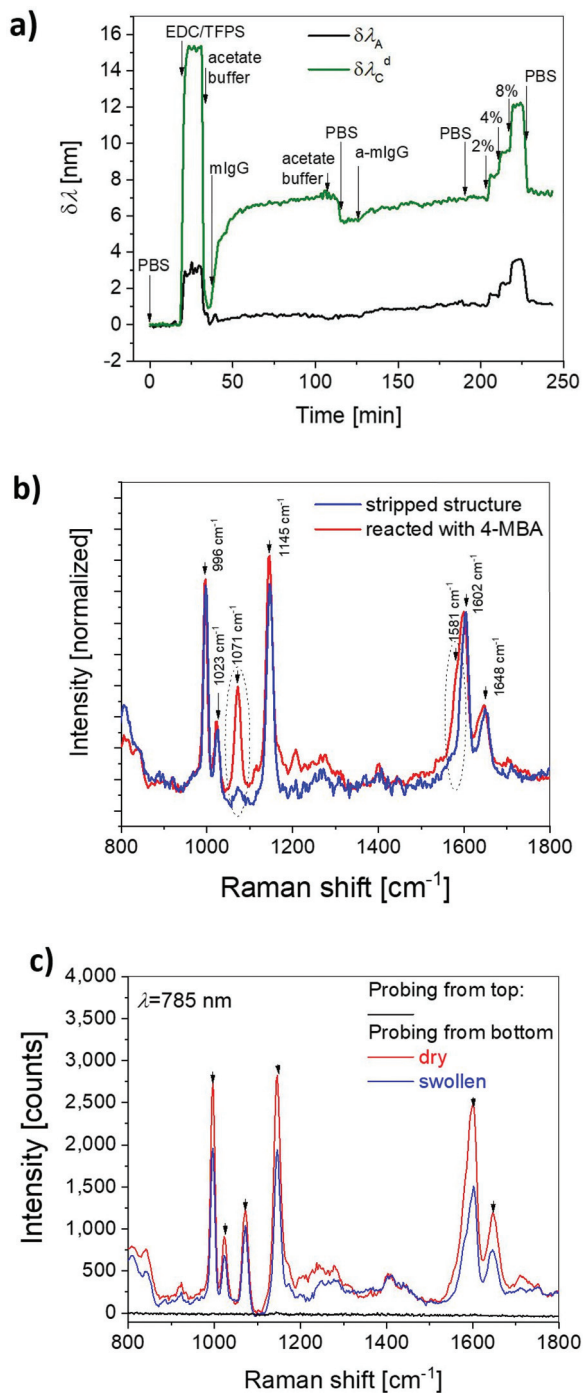


**Fig. 7** (a) Probing of covalent coupling of immunoglobulin G molecules (IgG) to pNIPAAm hydrogel polymer networks with the plasmonic modes centred at  $\lambda_A$  and  $\lambda_C^d$ . (b) SERS spectra measured before and after post-modification of the stripped area of gold with 4-MBA, as measured with a laser wavelength of 785 nm. The structure NHA + NP was swollen in water. (c) Comparison of the acquired Raman spectra from the top (dry NHA + NP structure) and bottom (swollen and dry NHA + NP structure).

selected since they probe different parts of the structure and are well pronounced in the transmission spectrum. To activate the carboxylic groups within the hydrogel cushion, they were reacted with EDC/TFPS and then a solution with mIgG was flowed over the surface in the time range of 45 to 120 min. After rinsing with a buffer at time 120 min, resonance  $\lambda_C^d$  shifted by 6 nm due to the covalent coupling of mIgG, while resonance  $\lambda_A$  showed a much weaker shift of about 0.5 nm. This observation proves that the mIgG molecules could diffuse through the pores and bind to the bottom swollen hydrogel (probed at  $\lambda_C^d$ ), while they do not attach to the pores (probed at  $\lambda_A$ ). Then, a series of PBS solutions with sucrose dissolved at a concentration of 2%, 4% and 8% was flowed over the surface to change the bulk refractive index by  $2.8$ ,  $5.6$  and  $11.2 \times 10^{-3}$  RIU, respectively. These low molecular weight molecules did not interact with the structure but freely diffused into the pNIPAAm-based hydrogel, and thus changed the refractive index on both sides of superstrate  $n_s$  and substrate hydrogel cushion  $n_h$ . From the measured shifts in  $\lambda_A$  and  $\lambda_C^d$ , the sensitivity of these resonances was determined to be  $d\lambda_A/dn = 218$  nm RIU $^{-1}$  and  $d\lambda_C^d/dn = 454$  nm RIU $^{-1}$ , respectively. These values are close to the predicted sum of the sensitivities  $d\lambda/dn_s$  and  $d\lambda/dn_h$  and support the fact that the refractive index changes at both interfaces of the permeable thin gold film.

In the second experiment, we tested the structure as a substrate for SERS detection. Accordingly, we probed the upper and bottom interfaces by a laser beam focused from the superstrate or substrate side by a lens with a numerical aperture of 0.5. The laser beam had a wavelength of  $\lambda = 785$  nm, which is close to the resonance observed at  $\lambda_C^p$  associated with the confinement of the incident field in the gap between the NHA and NP (see Fig. 4b). In this experiment, we directly used a structure that was stripped and compared the acquired Raman (Stokes shifted) spectra with that acquired for the same structure in which the upper gold surface and the pore mouth were modified with a Raman-active 4-MBA monolayer (see schematic in Fig. 1b). The results presented in Fig. 7b show a series of Raman peaks in the spectral range of 800–1800  $\text{cm}^{-1}$  for the pristine stripped structure that was probed from the bottom substrate through the pNIPAAm-based cushion. These peaks can be ascribed to the benzophenone molecules at the inner gold interface since their spectral positions are close to that reported in previous works.<sup>48</sup> After modifying the pore mouth and the upper gold interface with 4-MBA, two additional peaks appeared at 1071  $\text{cm}^{-1}$  (aromatic ring breathing, symmetric C–H in-plane bending, and C–S stretching) and 1581  $\text{cm}^{-1}$  (aromatic ring C–C stretching, asymmetric C–H in-plane bending). These spectral positions are close to that observed previously for this molecule.<sup>48,49</sup>

Finally, a comparison of the Raman peak intensity was carried out for probing from the top (through the superstrate) and from the bottom (through the pNIPAAm cushion substrate). As can be seen in Fig. 7c, the Raman peaks were observed only for the probing from the bottom, where the mode at  $\lambda_C^p$  could be efficiently excited with the laser beam at the wavelength of 785 nm. In addition, the spectral tuning of



this mode by collapsing and swelling the structure led to variations in the Raman peak intensity. An increase in the Raman peak intensity by about 45% occurred by collapsing the structure (by drying) with respect to the geometry when the hydrogel cushion was swollen in water. This can be attributed to the potentially stronger field intensity enhancement in the gap between the nanopores in the NHA and the bottom metallic nanoparticles as well as the shift in the resonance at  $\lambda_C^P$  to its optimized spectral position with respect to the excitation wavelength and Raman scattered peaks, which was observed to provide most efficient SERS.<sup>50–55</sup>

## Conclusions

We developed a new approach for the preparation of a hybrid plasmonic nanostructure that can be actuated and consists of arrays of nanoholes in a thin gold film, which is connected to arrays of gold nanoparticles by a responsive hydrogel cushion attached to a solid substrate. We explored the spectrum of the plasmonic modes supported by the structure and identified their origin due to the resonant excitation of three localized surface plasmons (confined in the nanopores and at the surface of the nanoparticles) and diffractive coupling to propagating surface plasmons (traveling along the top and bottom interfaces of the thin gold film). By swelling and collapsing the hydrogel cushion, the characteristics of these modes could be changed on-demand and the field confinement as well as resonant wavelength (up to 50 nm shifts) could be actively actuated. Among the modes, the near-field coupling between the nanoparticles and nanoholes was observed, and the simulations predicted that it leads to strong confinement of the electromagnetic field in the respective gap in the near-infrared part of the spectrum. This is particularly attractive for biosensing applications, as demonstrated by SPR observation of the attachment of 160 kDa IgG molecules inside the structure and SERS measurement of low molecular weight Raman active 4-MBA molecules immobilized in the pore mouth. In addition, this structure offers a unique opportunity to open and close the pores by swelling and collapsing the hydrogel cushion. Accordingly, the pores can be switched between the dead-end geometry and open state when water molecules are actively driven through the pores, dragging dissolved biomolecules across the plasmonic hotspot by diffusion.

## Experimental

### Materials

OrmoStamp® resin was purchased from Micro Resist Technology GmbH (Germany). Ostemer 322 Crystal Clear was purchased from Mercene Labs AB (Sweden). Polydimethylsiloxane Sylgard 184 (PDMS) was obtained from Dow Corning (USA). Trichloro (1*H*,1*H*,2*H*,2*H*-perfluorooctyl)silane (perfluoro-silane), dimethyl sulfoxide (DMSO) and 1-ethyl-3-(3-dimethylaminopropyl)carbodiimide (EDC) were obtained from Sigma Aldrich (Germany).

(11-Mercaptoundecyl)triethylene glycol (PEG-thiol, SPT-0011) was purchased from SensoPath Technologies Inc. (USA). The pNIPAAm-based terpolymer composed of *N*-isopropylacrylamide, methacrylic acid, and 4-methacryloyloxybenzophenone (in a ratio of 94 : 5 : 1), benzophenone-disulfide and 4-sulfotetrafluorophenol (TFPS) were synthesized in our laboratory, as previously reported.<sup>56,57</sup> IgG from mouse serum (mIgG, I 5381) and Tween 20 (P9416) were purchased from Sigma Aldrich (Austria), and phosphate-buffered saline (PBS) and sodium acetate were obtained from VWR Chemicals (Austria). Goat anti-mouse IgG (a-mIgG, A11375) was acquired from Life Technologies, (Eugene OR, US).

### UV-nanoimprint lithography

A template structure bearing arrays of nanopillars was fabricated from a silicon master that carried 1 cm<sup>2</sup> rectangular arrays of nanoholes with a diameter of  $D = 90$  nm, depth 260 nm, and period  $\Lambda = 460$  nm, fabricated by Temicon GmbH (Germany). 200  $\mu$ L of OrmoPrime was spun on a clean BK7 glass substrate at 4000 rpm for 60 s and hard-baked at 150 °C for 5 min. The BK7 substrate coated with OrmoPrime was contacted with the silicon master using a drop of OrmoStamp and kept still for 10 min to spread over the structure and fill the pores. The OrmoStamp was cured using UV light at  $\lambda = 365$  nm with the irradiation dose of 1 J cm<sup>-2</sup> (UV lamp Bio-Link 365, Vilber Lourmat). Then, the silicon master was carefully detached, leaving the BK7 substrate with an imprinted pattern of nanopillars in the OrmoStamp resin. The fabricated arrays of nanopillars were treated with UV-ozone for 5 min to remove the excess OrmoStamp and activate the surface for silanization. An anti-adhesive layer was deposited on the OrmoStamp structure under an argon atmosphere using 13  $\mu$ L of trichloro(1*H*,1*H*,2*H*,2*H*-perfluorooctyl)silane in a desiccator (volume 5.8 L) heated to  $T = 250$  °C for 20 min. A 50 nm thin layer of gold was deposited on the arrays of nanopillars, serving as a template, by vacuum thermal evaporation (HHVAUTO 306 from HHV Ltd) at a deposition rate of 2 Å s<sup>-1</sup> in a vacuum greater than 10<sup>-6</sup> mbar. Each sample consisted of a nanostructured region and a flat region for reference in the optical measurements.

### Deposition of the responsive polymer

The OrmoStamp arrays of nanopillars coated with 50 nm of gold were incubated overnight in a 1 mM solution of benzophenone-disulfide in DMSO to form a self-assembled monolayer serving as a linker. Then, this structure was coated with a uniform layer of pNIPAAm-based terpolymer by spin-coating 3 wt% ethanolic solution of the polymer at a spin rate of 2000 rpm for 1 min. The layer of the pNIPAAm-based terpolymer was dried overnight under vacuum at 50 °C yielding, a thickness of 230 nm. The resulting polymer film was crosslinked *via* the benzophenone moieties by UV light at  $\lambda = 365$  nm with an irradiation dose of 10 J cm<sup>-2</sup>.

### Template stripping

A drop of Ostemer epoxy was spread on clean BK7 glass by contacting it with a flat piece of PDMS and irradiating it with UV-



light at  $\lambda = 365 \text{ nm}$  ( $2 \text{ J cm}^{-2}$ ). The PDMS block was peeled-off leaving a glass substrate with a flat layer of pre-cured Ostemer epoxy on its top. Then, the Ostemer surface was pressed against the template coated with the crosslinked pNIPAAm-based film and incubated overnight at  $50 \text{ }^\circ\text{C}$  to allow its attachment to the pNIPAAm-based surface *via* its epoxy groups. Due to the pre-curing step, the Ostemer did not penetrate the pNIPAAm polymer network layer. Finally, the BK7 substrate with a layer of Ostemer was used to strip off the pNIPAAm-based film with the layer of gold from the template modified with the thin anti-adhesive layer.

### Morphological characterization

Atomic force microscopy (AFM) measurements of the patterned structures in air were performed in tapping mode using PPP-NCHR-50 tips (Nanosensors, Switzerland) and a PicoPlus instrument (Molecular Imaging, Agilent Technologies, USA). In addition, a scanning electron microscope (Zeiss Supra 40 VP (Carl Zeiss Microscopy GmbH, Germany) was used for imaging of the longitudinal and cross-section interfaces of the nanostructures at an electron high tension of  $\text{EHT} = 5 \text{ kV}$ . The height, diameter and lateral spacing of the nanoscale features were determined using the Gwyddion free software (version 2.47 from gwyddion.net).

### Optical configuration for angular-wavelength transmission measurement

Transmission optical spectra were acquired using a polychromatic light beam emitted from a halogen lamp (LSH102 LOT-Oriel, Germany), which was coupled to a multimode optical fiber and collimated with a lens. It was made incident at the structure and the transmitted beam was collected by a lens to another multimode optical fiber and delivered to a spectrometer (HR4000, Ocean Optics, USA). The obtained transmission spectra were normalized with that obtained on a reference flat  $50 \text{ nm}$  thick gold film. A flow-cell with a Peltier element<sup>58</sup> connected to a controller from Wavelength Electronics Inc. (USA) was clamped against the investigated structure to control the temperature of the liquid flowed over its surface. Deionized water was flowed by employing a peristaltic pump from Ismatec (Switzerland). The investigated structure with a flow cell was mounted on a rotation stage driven by a stepper motor from Huber GmbH (Germany) to control the angle of incident light,  $\theta$ . Transmission spectra were recorded using the in-house developed Labview software and processed using a dedicated Python script.

### Tracking of resonant wavelengths

Polychromatic light emitted from a supercontinuum laser source (WhiteLaser Micro, Fianium, UK) was collimated and the beam was expanded and spectrally filtered by a long-pass filter. The beam was made incident at a normal angle on the structure mounted in the temperature-stabilized flow cell. The transmitted beam was collected by a GRIN lens to a multimode fiber and delivered to the input of a spectrometer (S2000, Ocean Optics, USA). The acquired transmission spectra were

normalized to that measured for a reference flat gold film (thickness of  $50 \text{ nm}$ ) and analyzed using the SPR UP software developed at the Institute of Photonics and Electronics, Czech Academy of Sciences.

### Finite-difference time-domain simulations

FDTD simulations were performed using the Lumerical FDTD Solutions software. The geometry of the nanoparticle arrays was described using Cartesian coordinates with the  $x$ - and  $y$ -axis in the plane and the  $z$ -axis perpendicular to the plane of the arrays. Infinite arrays were considered in the simulations by choosing periodic boundary conditions (symmetric or anti-symmetric) along the  $x$ - and  $y$ -axis and using perfectly matched layers (PML) above and below the structure. For the field profile simulations, the simulation mesh was set to  $2 \text{ nm}$  over the volume of the unit cell. A transmission monitor was placed  $0.4 \text{ }\mu\text{m}$  below the nanoparticle arrays and a 2D monitor in the  $xz$ -plane was employed for simulating the near field distribution of the electric field intensity. The structure was illuminated by a normally incident plane wave with its polarization set along the  $x$ -direction. The optical constants for Au were taken from the CRC Optical Data Tables ( $450\text{--}950 \text{ nm}$ ). To consider the deviations in the experimental geometry from the (idealized) simulated geometry, the diameter  $D$  was varied in the range of  $100\text{--}120 \text{ nm}$  and the respective optical response was averaged.

### Immunoassay experiment

The substrate carrying the NHA + NP structure was clamped against a transparent flow-cell and loaded in an optical system for tracking of the SPR dips or peaks in the transmission spectrum. A polychromatic optical beam was made incident at a normal angle of incidence of  $\theta = 0^\circ$  at the structure, and by analysis of the transmitted light spectrum, the variations in the resonant wavelengths were monitored with time. These variations were determined by fitting the acquired spectrum with a polynomial function, as reported previously,<sup>47</sup> and which allowed the spectral shifts of the dip or peak features to be measured with the accuracy of  $0.1\text{--}0.01 \text{ nm}$ , depending on the coupling strength and noise in the transmission spectrum. Firstly, the baseline in the resonant wavelength kinetics was established upon a flow of PBS for  $20 \text{ min}$ . Then, a mixture of EDC/TFPS dissolved in water at concentrations  $75$  and  $21 \text{ mg mL}^{-1}$ , respectively, was flowed over the structure for  $10 \text{ min}$  to activate the carboxylic moieties of the pNIPAAm hydrogel. The surface was quickly rinsed with  $\text{pH } 5$  acetate buffer and reacted with a solution of  $50 \text{ }\mu\text{g mL}^{-1}$  mouse IgG in the same buffer for  $60 \text{ min}$  to covalently attach the mIgG molecules to the polymer chains. Finally, the structure was rinsed with PBS, followed by the flow of PBS spiked with  $2\%$ ,  $4\%$  and  $8\%$  sucrose ( $\Delta n = 2.8 \times 10^{-3}$ ,  $5.6 \times 10^{-3}$  and  $11.2 \times 10^{-3} \text{ RIU}$ , respectively).

### SERS experiments

The NHA + NP structure was incubated overnight in  $1 \text{ mM}$  ethanolic solution of 4-mercaptobenzoic acid to form a self-



assembled monolayer of SERS-active molecules. Prior to the experiment, the structure was rinsed with ethanol and dried. The SERS experiments were performed using an Xplora Raman microspectrometer (Horiba Scientific, France) with a  $\times 50$  long working distance objective (numerical aperture of 0.5). The laser beam at  $\lambda = 785$  nm was focused at the investigated NHA + NP structure. The spectrum was accumulated for 20 s.

## Conflicts of interest

There are no conflicts to declare.

## Acknowledgements

DK acknowledges funding from the European Union's Horizon 2020 research and innovation programme under grant agreement no. 642787, Marie Skłodowska-Curie Innovative Training Network BIOGEL. SF, JS, JD, JH and UJ were supported by European Union's Horizon 2020 research and innovation programme under grant agreement no. 633937, project ULTRAPLACAD. PV, ML, and MDLC are grateful for the financing from the project jointly funded by Agence Nationale de la Recherche (ANR) and Austrian Science Fund (FWF) under the grant agreements ANR-15-CE29-0026 and I 2647, respectively. SF and JD received support by the Austrian Research Promotion Agency (FFG) with grant agreement no. 861578 (ERANET project PLABAN). JS and JH acknowledge financial support from the Czech Science Foundation, grant agreement #19-02739S. The Raman analysis was performed at the Vibrational Spectroscopy platform of the IMMM, Université du le Mans.

## Notes and references

- 1 T. W. Ebbesen, H. J. Lezec, H. F. Ghaemi, T. Thio and P. A. Wolff, *Nature*, 1998, **391**, 667–669.
- 2 M. Najiminaini, F. Vasefi, B. Kaminska and J. J. L. Carson, *Sci. Rep.*, 2013, **3**, 1–7.
- 3 M. S. Ahn, T. Chung and K. H. Jeong, *Nanoscale*, 2018, **10**, 6313–6317.
- 4 A. G. Brolo, S. C. Kwok, M. G. Moffitt, R. Gordon, J. Riordon and K. L. Kavanagh, *J. Am. Chem. Soc.*, 2005, **127**, 14936–14941.
- 5 Q. Zhang, L. Wu, T. I. Wong, J. Zhang, X. Liu, X. Zhou, P. Bai, B. Liedberg and Y. Wang, *Int. J. Nanomed.*, 2017, **12**, 2307–2314.
- 6 A. G. Brolo, E. Arctander, R. Gordon, B. Leathem and K. L. Kavanagh, *Nano Lett.*, 2004, **4**, 2015–2018.
- 7 P. Zheng, S. K. Cushing, S. Suri and N. Wu, *Phys. Chem. Chem. Phys.*, 2015, **17**, 21211–21219.
- 8 S. Kumar, S. Cherukulappurath, T. W. Johnson and S. Oh, *Chem. Mater.*, 2014, **26**, 6523–6530.
- 9 T. Wu and Y. W. Lin, *Appl. Surf. Sci.*, 2018, **435**, 1143–1149.
- 10 S. P. Sahu, A. Mahigir, B. Chidester, G. Veronis and M. R. Gartia, *Nano Lett.*, 2019, **19**, 6192–6202.
- 11 M. E. Stewart, N. H. Mack, V. Malyarchuk, J. A. N. T. Soares, T.-W. Lee, S. K. Gray, R. G. Nuzzo and J. A. Rogers, *Proc. Natl. Acad. Sci. U. S. A.*, 2006, **103**, 17143–17148.
- 12 A. A. Yanik, A. E. Cetin, M. Huang, A. Artar, S. H. Mousavi and A. Khanikaev, *Proc. Natl. Acad. Sci. U. S. A.*, 2011, **108**, 11784–11789.
- 13 K. Nakamoto, R. Kurita, O. Niwa, T. Fujii and M. Nishida, *Nanoscale*, 2011, **3**, 5067–5075.
- 14 X. Li, M. Soler, C. I. Özdemir, A. Belushkin, F. Yesilköy and H. Altug, *Lab Chip*, 2017, **17**, 2208–2217.
- 15 H. Im, H. Shao, Y. I. Park, V. M. Peterson, C. M. Castro, R. Weissleder and H. Lee, *Nat. Biotechnol.*, 2014, **32**, 490–495.
- 16 A. A. Yanik, M. Huang, O. Kamohara, A. Artar, T. W. Geisbert, J. H. Connor and H. Altug, *Nano Lett.*, 2010, **10**, 4962–4969.
- 17 J. A. Jackman, E. Linardy, D. Yoo, J. Seo, W. B. Ng, D. J. Klemme, N. J. Wittenberg, S. H. Oh and N. J. Cho, *Small*, 2016, **12**, 1159–1166.
- 18 J. Gomez-Cruz, S. Nair, A. Manjarrez-Hernandez, S. Gavilanes-Parra, G. Ascanio and C. Escobedo, *Biosens. Bioelectron.*, 2018, **106**, 105–110.
- 19 L. Tu, X. Li, S. Bian, Y. Yu, J. Li, L. Huang, P. Liu, Q. Wu and W. Wang, *Sci. Rep.*, 2017, **7**, 11020.
- 20 J. T. Lim, Y. S. Yoon, W. Y. Lee, J. T. Jeong, G. S. Kim, T. G. Kim and S. K. Lee, *Nanoscale*, 2017, **9**, 17224–17232.
- 21 S. Kumar, G. G. Wolken, N. J. Wittenberg, E. A. Arriaga and S. H. Oh, *Anal. Chem.*, 2015, **87**, 1973–11977.
- 22 M. P. Jonsson, P. Jönsson, A. B. Dahlin and F. Höök, *Nano Lett.*, 2007, **7**, 3462–3468.
- 23 L. Plucinski, M. Ranjan, W. R. Arnold, A. Ameen, T. Chang, A. Hsiao, G. Logan and A. Das, *Biosens. Bioelectron.*, 2016, **75**, 337–346.
- 24 W.-C. Liu and T. D. Ping, *Phys. Rev. B: Condens. Matter Mater. Phys.*, 2002, **65**, 155423.
- 25 F. J. Garcia-Vidal, L. Martin-Moreno, T. W. Ebbesen and L. Kuipers, *Rev. Mod. Phys.*, 2010, **82**, 729–787.
- 26 M. Horak, V. Krapek, M. Hrton, A. Konecna, F. Ligmajer, M. Stoeger-Pollach, T. Samoril, A. Patak, Z. Edes, O. Metelka, J. Babocky and T. Sikola, *Sci. Rep.*, 2019, **9**, 4004.
- 27 L. Wang, B. Xu, W. Bai, J. Zhang, L. Cai, H. Hu and G. Song, *Plasmonics*, 2012, **7**, 659–663.
- 28 C. Stelling and M. Retsch, *Adv. Mater. Interfaces*, 2018, **5**, 1–7.
- 29 R. Mohammadi, M. Ochs, A. Andrieu-Brunsen and N. Vogel, *J. Phys. Chem. C*, 2020, **124**, 2609–2618.
- 30 M. Hentschel, T. Weiss, S. Bagheri and H. Giessen, *Nano Lett.*, 2013, **13**, 4428–4433.
- 31 V. G. Kravets, A. V. Kabashin, W. L. Barnes and A. N. Grigorenko, *Chem. Rev.*, 2018, **118**, 5912–5951.
- 32 J. F. Masson, M. P. Murray-Méthot and L. S. Live, *Analyst*, 2010, **135**, 1483–1489.



- 33 C. Escobedo, *Lab Chip*, 2013, **13**, 2445–2463.
- 34 H. Im, S. H. Lee, N. J. Wittenberg, T. W. Johnson, N. C. Lindquist, P. Nagpal, D. J. Norris and S. H. Oh, *ACS Nano*, 2011, **5**, 6244–6253.
- 35 S. H. Lee, K. C. Bantz, N. C. Lindquist, S.-H. Oh and C. L. Haynes, *Langmuir*, 2009, **25**, 13685–13693.
- 36 B. Ai, Y. Yu, H. Möhwald, G. Zhang and B. Yang, *Adv. Colloid Interface Sci.*, 2014, **206**, 5–16.
- 37 J. Junesch, T. Sannomiya and A. B. Dahlin, *ACS Nano*, 2012, **6**, 10405–10415.
- 38 H. Im, J. N. Sutherland, J. A. Maynard and S.-H. Oh, *Anal. Chem.*, 2012, **84**, 1941–1947.
- 39 A. Barik, L. M. Otto, D. Yoo, J. Jose, T. W. Johnson and S. H. Oh, *Nano Lett.*, 2014, **14**, 2006–2012.
- 40 J. Dostálek and W. Knoll, *Plasmonics*, 2012, vol. 2.
- 41 Y. Zhao, G. Gaur, S. T. Retterer, P. E. Laibinis and S. M. Weiss, *Anal. Chem.*, 2016, **88**, 10940–10948.
- 42 C. Escobedo, A. G. Brolo, R. Gordon and D. Sinton, *Anal. Chem.*, 2010, **82**, 10015–10020.
- 43 N. Sharma, C. Petri, U. Jonas and J. Dostalek, *Opt. Express*, 2016, **24**, 2457.
- 44 N. Gisbert Quilis, M. van Dongen, P. Venugopalan, D. Kotlarek, C. Petri, A. Moreno Cencerrado, S. Stanesco, J. L. Toca Herrera, U. Jonas, M. Möller, A. Mourran and J. Dostalek, *Adv. Opt. Mater.*, 2019, **7**, 1–11.
- 45 N. Sharma, H. Keshmiri, X. Zhou, T. I. Wong, C. Petri, U. Jonas, B. Liedberg and J. Dostalek, *J. Phys. Chem. C*, 2016, **120**, 561–568.
- 46 A. Aulasevich, R. F. Roskamp, U. Jonas, B. Menges, J. Dostálek and W. Knoll, *Macromol. Rapid Commun.*, 2009, **30**, 872–877.
- 47 A. T. Reiner, N. G. Ferrer, P. Venugopalan, R. C. Lai, S. K. Lim and J. Dostálek, *Analyst*, 2017, **142**, 3913–3921.
- 48 Y. Flegler, Y. Mastai, M. Rosenbluh and D. H. Dressler, *Surf. Sci.*, 2009, **603**, 788–793.
- 49 N. G. Quilis, M. Lequeux, P. Venugopalan, I. Khan, W. Knoll, S. Boujday, M. L. de la Chapelle and J. Dostalek, *Nanoscale*, 2018, **10**, 10268–10276.
- 50 S. J. Lee, Z. Guan, H. Xu and M. Moskovits, *J. Phys. Chem. C*, 2007, **111**, 17985–17988.
- 51 M. Chirumamilla, A. Gopalakrishnan, A. Toma, R. P. Zaccaria and R. Krahn, *Nanotechnology*, 2014, **25**, 235303.
- 52 N. Guillot and M. L. de la Chapelle, *J. Quant. Spectrosc. Radiat. Transfer*, 2012, **113**, 2321–2333.
- 53 N. Guillot, B. Fremaux, H. Shen, O. Péron, E. Rinnert, T. Toury and M. Lamy De La Chapelle, *Appl. Phys. Lett.*, 2010, **97**, 023113.
- 54 S. Kessentini, D. Barchiesi, C. D'Andrea, A. Toma, N. Guillot, E. Di Fabrizio, B. Fazio, O. M. Maragó, P. G. Gucciardi and M. Lamy De La Chapelle, *J. Phys. Chem. C*, 2014, **118**, 3209–3219.
- 55 F. J. Colas, M. Cottat, R. Gillibert, N. Guillot, N. Djaker, N. Lidgi-Guigui, T. Toury, D. Barchiesi, A. Toma, E. Di Fabrizio, P. G. Gucciardi and M. L. De La Chapelle, *J. Phys. Chem. C*, 2016, **120**, 13675–13683.
- 56 P. W. Beines, I. Klosterkamp, B. Menges, U. Jonas and W. Knoll, *Langmuir*, 2007, **23**, 2231–2238.
- 57 K. Sergelen, C. Petri, U. Jonas and J. Dostalek, *Biointerphases*, 2017, **12**, 051002.
- 58 M. Toma, U. Jonas, A. Mateescu, W. Knoll and J. Dostalek, *J. Phys. Chem. C*, 2013, **117**, 11705–11712.



## Supporting information

### Actuated Plasmonic Nanohole Arrays for Sensing and Optical Spectroscopy Applications

Daria Kotlarek<sup>a</sup>, Stefan Fossati<sup>a</sup>, Priyamvada Venugopalan<sup>a,b,c</sup>, Nestor Gisbert Quilis<sup>a</sup>, Jiří Slabý<sup>d</sup>, Jiří Homola<sup>d</sup>, Médéric Lequeux<sup>e</sup>, Frédéric Amiard<sup>f</sup>, Marc Lamy de la Chapelle<sup>f</sup>, Ulrich Jonas<sup>g</sup>, Jakub Dostálek<sup>a</sup>

<sup>a</sup> Biosensor Technologies, AIT-Austrian Institute of Technology GmbH, Konrad-Lorenz-Straße 24, 3430 Tulln an der Donau, Austria. E-mail: Jakub.dostalek@ait.ac.at.

<sup>b</sup> CEST Kompetenzzentrum für elektrochemische Oberflächentechnologie GmbH, TFZ, Wiener Neustadt, Viktor-Kaplan-Strasse 2, 2700 Wiener Neustadt, Austria

<sup>c</sup> Current address: NYU Abu Dhabi, Saadiyat Campus, P.O. Box 129188, Abu Dhabi, United Arab Emirates

<sup>d</sup> Institute of Photonics and Electronics, Academy of Sciences of the Czech Republic, Chaberská 57, 18251, Praha 8, Czech Republic

<sup>e</sup> Université Paris 13, Sorbonne Paris Cité, Laboratoire CSPBAT, CNRS, (UMR 7244), 74 rue Marcel Cachin, 93017 Bobigny, France

<sup>f</sup> Institut des Molécules et Matériaux du Mans (IMMM - UMR CNRS 6283), Avenue Olivier Messiaen, 72085 Le Mans cedex 9, France

<sup>g</sup> Macromolecular Chemistry, Department Chemistry-Biology, University of Siegen, Adolf Reichwein-Strasse 2, Siegen 57076, Germany

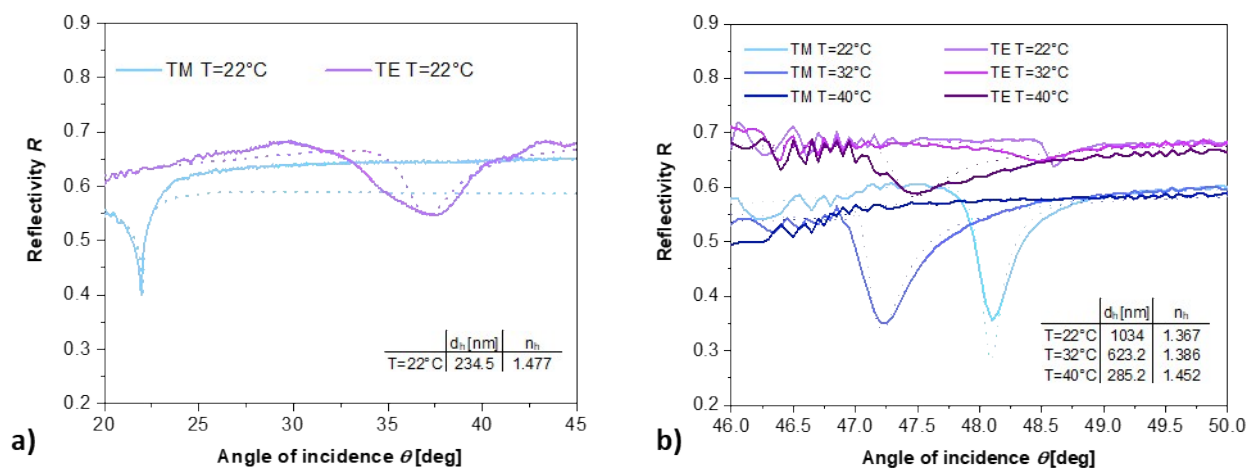


**Figure S1.** Measurement of thickness and the refractive index of a flat pNIPAAm-based polymer layer on a gold surface a) in a dry state and b) in water by using optical waveguide spectroscopy. Solid lines represent the measured angular scans and dashed curves are the fitted data.



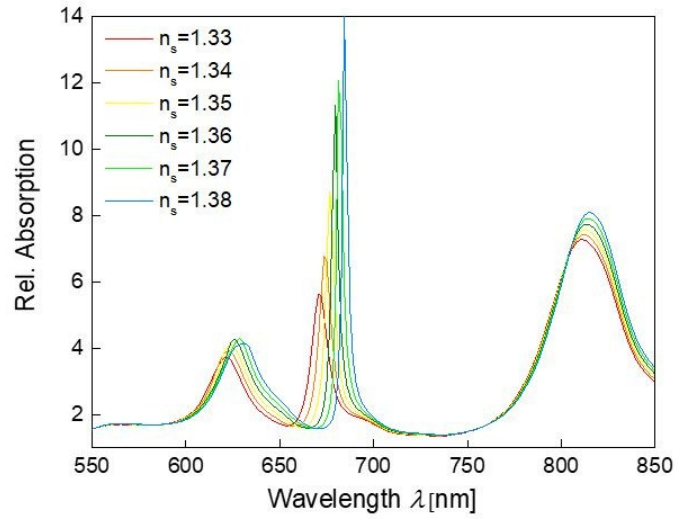


**Figure S2.** Simulated absorption spectra for the structure NHA+NP for the varied refractive index of superstrate  $n_s$  the substrate refractive index was of  $n_h=1.47$ , the gap distance between NP and NHA was set as  $g=50$  nm, the period was  $\Lambda=460$  nm, diameter averaged between  $D=100-120$  nm, height  $h=50$  nm.

# 3.6

Study of Integrin-selective bicyclic RGD-peptides

# Bicyclic RGD Peptides with Exquisite Selectivity for the Integrin $\alpha_v\beta_3$ Receptor Using a “Random Design” Approach

Dominik Bernhagen,<sup>†</sup> Vanessa Jungbluth,<sup>‡</sup> Nestor Gisbert Quilis,<sup>‡</sup> Jakob Dostalek,<sup>‡</sup> Paul B. White,<sup>§</sup> Kees Jalink,<sup>||</sup> and Peter Timmerman<sup>\*,†,⊥</sup>

<sup>†</sup>Pepscan Therapeutics, Zuidersluisweg 2, 8243 RC Lelystad, The Netherlands

<sup>‡</sup>Biosensor Technologies, AIT Austrian Institute of Technology GmbH, Konrad-Lorenz-Straße 24, 3430 Tulln, Austria

<sup>§</sup>Institute for Molecules and Materials, Radboud University, Heyendaalseweg 135, 6525 AJ Nijmegen, The Netherlands

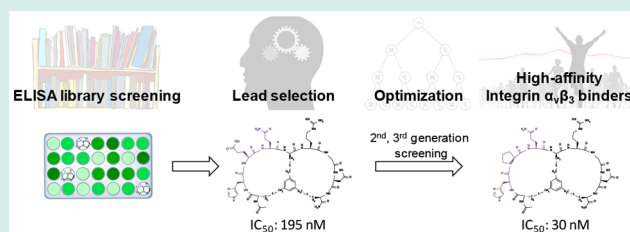
<sup>||</sup>The Netherlands Cancer Institute, Plesmanlaan 21, 1066 CX Amsterdam, The Netherlands

<sup>⊥</sup>Van't Hoff Institute for Molecular Sciences, University of Amsterdam, Science Park 904, 1098 XH Amsterdam, The Netherlands

## Supporting Information

**ABSTRACT:** We describe the identification of bicyclic RGD peptides with high affinity and selectivity for integrin  $\alpha_v\beta_3$  via high-throughput screening of partially randomized libraries. Peptide libraries (672 different compounds) comprising the universal integrin-binding sequence Arg-Gly-Asp (RGD) in the first loop and a randomized sequence XXX (X being one of 18 canonical L-amino acids) in the second loop, both enclosed by either an L- or D-Cys residue, were converted to bicyclic peptides via reaction with 1,3,5-tris(bromomethyl)benzene (T3). Screening of first-generation libraries yielded lead bicyclic inhibitors displaying submicromolar affinities for integrin  $\alpha_v\beta_3$  (e.g., C<sub>T3</sub>HEQC<sub>T3</sub>RGDC<sub>T3</sub>, IC<sub>50</sub> = 195 nM). Next generation (second and third) libraries were obtained by partially varying the structure of the strongest lead inhibitors and screening for improved affinities and selectivities. In this way, we identified the highly selective bicyclic  $\alpha_v\beta_3$ -binders C<sub>T3</sub>HPQC<sub>T3</sub>RGDC<sub>T3</sub> (IC<sub>50</sub> = 30 nM), C<sub>T3</sub>HPQC<sub>T3</sub>RGDC<sub>T3</sub> (IC<sub>50</sub> = 31 nM), and C<sub>T3</sub>HSQC<sub>T3</sub>RGDC<sub>T3</sub> (IC<sub>50</sub> = 42 nM) with affinities comparable to that of a knottin-RGD-type peptide (32 amino acids, IC<sub>50</sub> = 38 nM) and outstanding selectivities over integrins  $\alpha_v\beta_3$  (IC<sub>50</sub> > 10000 nM) and  $\alpha_5\beta_1$  (IC<sub>50</sub> > 10000 nM). Affinity measurements using surface plasmon-enhanced fluorescence spectroscopy (SPFS) yielded K<sub>d</sub> values of 0.4 and 0.6 nM for the Cy5-labeled bicycle C<sub>T3</sub>HPQC<sub>T3</sub>RGDC<sub>T3</sub> and RGD “knottin” peptide, respectively. In vitro staining of HT29 cells with Cy5-labeled bicycles using confocal microscopy revealed strong binding to integrins in their natural environment, which highlights the high potential of these peptides as markers of integrin expression.

**KEYWORDS:** RGD, integrin, peptide–protein interaction, ELISA, bicyclic peptide, library screening, SPFS



## INTRODUCTION

(Multi)cyclic peptides represent an important platform in drug development owing to their unique properties, such as conformational restriction and low toxicity. Peptides produced by nature, for example, romidepsin, vancomycin, and ciclosporin, and semisynthetic peptides such as dalbavancin are established peptide-based drugs.<sup>1</sup> Over the past years, the bicyclic CLIPS-peptide platform, first described by our group,<sup>2</sup> has attracted considerable interest by combining high target affinities and selectivities with appreciable proteolytic stabilities.<sup>3</sup> It has been actively explored to provide a variety of (enzyme) inhibitors. For example, Heinis et al. used the technology in combination with phage-display library screening to identify a bicyclic peptide inhibitor (AC<sub>T3</sub>SDRFRNC<sub>T3</sub>PADEALC<sub>T3</sub>G, T3 = 1,3,5-trimesitylanyl scaffold), displaying nanomolar affinity to plasma kallikrein (K<sub>i</sub> = 1.5 nM).<sup>4</sup> Here, the consensus motif SDRFRN was identified in the first round of selection, followed by sequential optimization of the second loop. Notably, the activities of

the linear peptides were at least 250-fold lower in comparison to the corresponding T3-bicycles. The same group also reported a bicyclic peptide inhibitor (AC<sub>T3</sub>SRYEVDCT<sub>3</sub>RGRGSACT<sub>3</sub>G) of urokinase-type plasminogen activator (uPA) with a K<sub>i</sub> of 53 nM<sup>5</sup> and, most recently, an active bicyclic inhibitor (AC<sub>T3</sub>HSRC<sub>T3</sub>PQLPPCT<sub>3</sub>G) of sortase A (K<sub>i</sub> = 1.1 μM).<sup>6</sup> Luzi et al. also explored the high-throughput potential of CLIPS phage-display libraries to identify a potent bicyclic inhibitor (AC<sub>T3</sub>PPCT<sub>3</sub>LWQVLC<sub>T3</sub>, K<sub>d</sub> = 10 nM) to TNFα, one of the key mediators of several inflammatory disorders.<sup>7</sup> As an alternative to this, Lian et al. developed a one-bead two-compound screening technology to identify double-digit nanomolar bicyclic peptide inhibitors for protein tyrosine phosphatase 1B (PTP1B), a type II diabetes target,<sup>8</sup> with the target-binding sequence in the first loop and

Received: September 20, 2018

Revised: December 4, 2018

Published: January 9, 2019

the cell-penetrating peptide F $\Phi$ RRRQ ( $\Phi$ : L-naphthylalanine) in the second loop. Recently, the same group reported a submicromolar bicyclic inhibitor for K-Ras, combining a cell-permeable peptide sequence in the first loop with the K-Ras binding motif AJFRn $\Psi$ ID (J, D-Leu;  $\Psi$ , L-propargylglycine) in the second loop.<sup>9</sup>

In this paper we describe a novel approach to identify potent bicyclic binders to integrin  $\alpha_v\beta_3$  by combining rational design<sup>10</sup> with medium diversity (total of 672 peptides). These bicycles combine a “fixed” RGD loop (“Design”) with a second loop (XXX, “Random”) that further supports the RGD-integrin affinity and also brings selectivity into the peptide. Integrins represent a family of cell adhesion receptors<sup>11</sup> that are potential targets for novel therapeutic agents resulting from their significant role in pathological processes. A major contribution to the investigation of integrin-binding peptides was made by Kessler and co-workers, who developed the potent  $\alpha_v\beta_3$  antagonist cilengitide,<sup>12</sup> and other cyclopeptides with decent affinities for integrins, such as  $\alpha_v\beta_3$ ,  $\alpha_5\beta_1$ , and  $\alpha_6\beta_1$ .<sup>13a–g</sup> In addition, integrin affinity tuning via conformational confinement on of the RGD peptide on surfaces has been reported.<sup>13h–j</sup> Recently, Cochran and co-workers described a family of high-affinity integrin-binding “cystine-knot” (knottin) RGD peptides, which are considered great candidates for drug development.<sup>14</sup> However, these disulfide-rich peptides basically do not express any selectivity in binding to the integrins  $\alpha_v\beta_3$ ,  $\alpha_5\beta_1$ , and  $\alpha_6\beta_5$ . Here we describe a set of bicyclic RGD peptides that display both high affinities and outstanding selectivities for  $\alpha_v\beta_3$ . Moreover, we also developed a similar set of binders with selectivities for the integrin  $\alpha_5\beta_1$ , the results of which will be disclosed elsewhere. We consider this combined “random-design” approach also highly suited for identifying high-affinity and -selectivity binders to different ECM target proteins based on e.g. the laminin-binding YIGSR- or IKVAV-peptide motifs.

## RESULTS AND DISCUSSION

**General Procedure for Library Screening.** Our approach involves the design of partially randomized libraries of small, RGD-containing bicyclic CLIPS (chemical linkage of peptides onto scaffolds)<sup>15</sup> peptides to be used in an iterative affinity and selectivity optimization process for the integrin receptor  $\alpha_v\beta_3$ . We used libraries of “label-free” peptides comprising acetylated N-termini and C-terminal amides, the individual  $\alpha_v\beta_3$ -binding activities of which were evaluated by measuring the extent of inhibition of biotinylated knottin-RGD binding to integrin  $\alpha_v\beta_3$  using a recently published competition ELISA setup (see Table S-1 in the Supporting Information).<sup>16</sup> A schematic representation of this setup is given in the Supporting Information of ref 16. At first, all 672 bicyclic RGD peptides were screened for inhibition at the highest concentration (1 mM). For the top 30 hits from the first screening (top 30 for second and third generations), which showed at least 90% inhibition at 1 mM, a second screening was performed at lower concentration (2.5–10  $\mu$ M) to determine their affinities more accurately. Finally, the best binders were resynthesized and HPLC-purified, followed by determination of the  $IC_{50}$  values.

**Design and Synthesis of RGD Peptide Libraries.** We designed linear peptide libraries consisting of two separate binding motifs surrounded by three cysteines. The first motif contains the well-known RGD sequence that should provide the basal integrin affinity, while the second motif contains a

randomized sequence “XXX”, which is intended to support binding of the RGD loop and also to provide integrin selectivity. The motifs are enclosed by cysteines, which ensure the double CLIPS cyclization (T3, Figure 1) and hence the formation of a bicyclic peptide comprising two different loops.

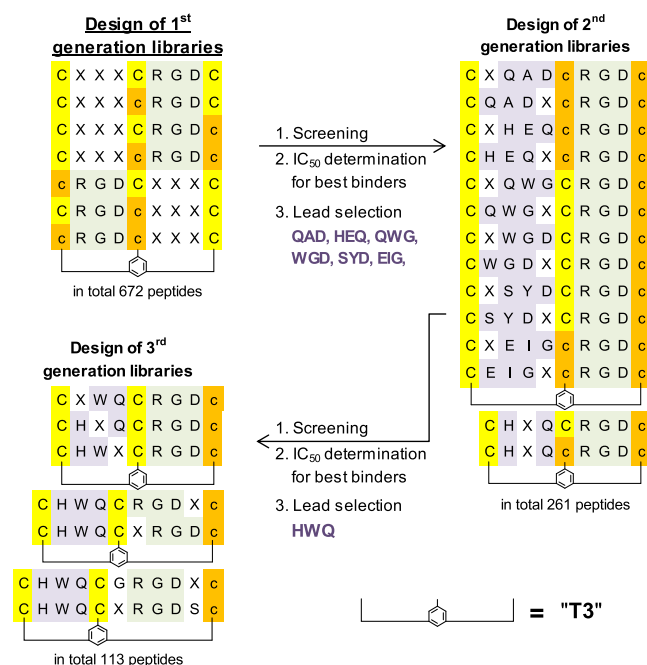


**Figure 1.** Methodology for the design of high-affinity bicyclic peptides to integrin  $\alpha_v\beta_3$ . X represents any canonical L-amino acid. L-cysteines are indicated in yellow, D-cysteines in orange, and RGD motifs in green. Lead motifs are shown in purple.

The primary challenge was to determine the proper size of both the RGD and the random X(X)<sub>n</sub>X loop. The well-known integrin binder cilengitide (*cyclo*-[V(N-Me)RGDf])<sup>12</sup> consists of five amino acids. In a bicyclic peptide, a similar 5-mer loop is generated by enclosing the 3-mer RGD sequence with two cysteines; hence, the minimal integrin-binding motif CRGDC was selected. We kept the RGD loop size constant in the first-generation library and checked for further optimization at a later stage. For the second, randomized loop, we considered a trimer XXX motif suitable to provide the required level of structural and conformational diversity. When all natural amino acids (except cysteine and methionine) are included, there are 324 (18<sup>2</sup>) possible variants of the dimer motif XX, 5832 possible trimer sequences XXX, and 104976 variants for the tetramer motif XXXX. Therefore, 96 different XXX motifs would cover 1.8% of the total viable natural L-tripeptide space, which is reasonable when one considers the chance to overlook a high-affinity integrin binder after several rounds of optimization, in particular in comparison to the 0.09% coverage of structural space when a tetrameric XXXX motif is used.

The RGD motif was located either in the C-terminal/right loop and the XXX sequence in the N-terminal/left loop or vice versa. A total of 96 random XXX sequences were generated for each loop by using the software program R. In view of the apparent effect of D-amino acids on integrin binding affinity,<sup>12,17</sup> additional sublibraries comprising different combinations of L- and D-cysteines were also designed. Hence, the entire first-generation library consisted of four sublibraries with

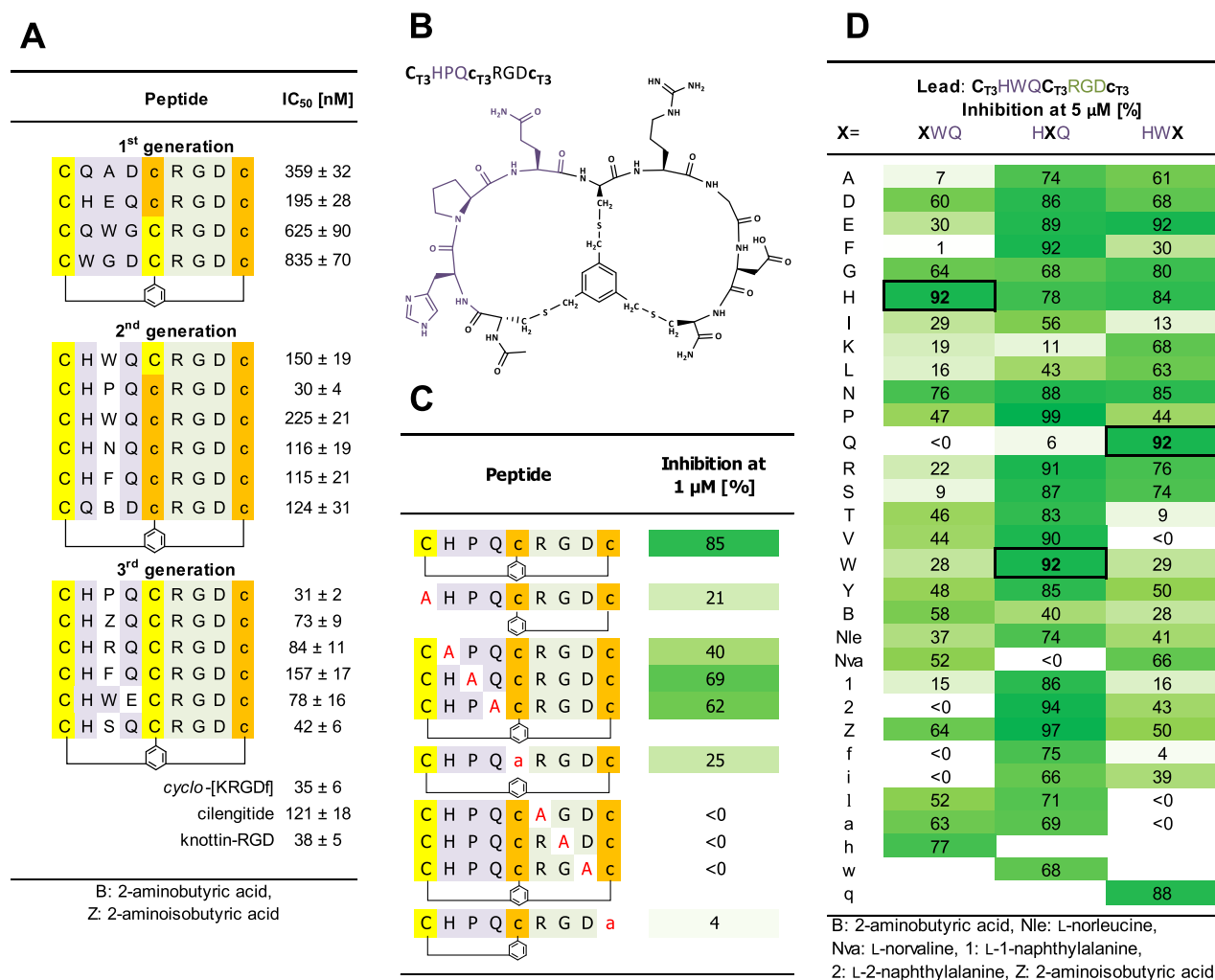


**Figure 2.** (A) IC<sub>50</sub> values for first-, second-, and third-generation bicyclic integrin  $\alpha_v\beta_3$  binders. Each concentration was tested in triplicate. IC<sub>50</sub> values were calculated via nonlinear regression analysis. Inhibition values were calculated on the basis of absorbance when the bicyclic competitor was not present (0%, OD<sub>405</sub> ≈ 1.8), or when nonbiotinylated knottin-RGD was added at 30 μM (100%, OD<sub>405</sub> ≈ 0.2). (B) Molecular structure of the second-generation bicycle with the highest integrin  $\alpha_v\beta_3$  affinity. (C) Alanine replacement analysis for the bicycle C<sub>T3</sub>HPQC<sub>T3</sub>RGDC<sub>T3</sub>. (D) Full amino acid replacement analysis (HWQ motif) of the bicycle C<sub>T3</sub>HWQC<sub>T3</sub>RGDC<sub>T3</sub> using nonpurified peptides. If absorbances were not lower but higher in the presence of nonlabeled peptide, inhibition values were reported as <0. Boldface, framed values refer to the lead peptide. D-Amino acids are represented as small letters.

96 random sequences in the left loop and three sublibraries with random sequences in the right loop, giving a total number of 672 different T3 bicycles (C<sub>T3</sub>XXXC<sub>T3</sub>RGDC<sub>T3</sub>/C<sub>T3</sub>XXXc<sub>T3</sub>RGDC<sub>T3</sub>/C<sub>T3</sub>XXXC<sub>T3</sub>RGDc<sub>T3</sub>/C<sub>T3</sub>XXXc<sub>T3</sub>RGDc<sub>T3</sub>/C<sub>T3</sub>RGDC<sub>T3</sub>XXXC<sub>T3</sub>/C<sub>T3</sub>RGDc<sub>T3</sub>XXXc<sub>T3</sub>, Figure 1). After these libraries were screened for binding to integrin  $\alpha_v\beta_3$  (method described below), various lead motifs for next-generation libraries were derived from the sequences of the best binders. The second loop in the second-generation libraries comprised (i) all first-generation lead sequences (e.g., QAD), extended by one amino acid (XQAD or QADX), and (ii) a full replacement set of the second amino acid (X in the HXQ motif, in view of multiple positive hits: HEQ/2xHLQ). After the best second-generation  $\alpha_v\beta_3$ -binders were identified, a set of third-generation libraries was designed on the basis of (i) a full set of replacement variants (86 peptides) based on the HWQ motif and (ii) extension of the RGD loops on either or both ends with one amino acid (e.g., RGDx/XRGD or

GRGDx/XRGDS) while the second loop HWQ was kept constant.

#### Screening Bicyclic Peptide Libraries for $\alpha_v\beta_3$ -Bindin.

About 4% of the 672 first-generation bicyclic RGD peptides showed OD<sub>405</sub> values below 0.4, corresponding to more than 80% inhibition of knottin-RGD binding to  $\alpha_v\beta_3$  (OD<sub>405</sub> = 0.2, 100% inhibition; OD<sub>405</sub> = 1.2, 0% inhibition). For the strongest  $\alpha_v\beta_3$ -binding bicycles, we observed an overrepresentation of peptides comprising the RGD motif in the C-terminal/right loop. Moreover, the best binders all had at least one D-Cys attached to the RGD sequence, either C-terminal or both N- and C-terminal, which is consistent with the results of Kessler et al., who reported enhanced integrin binding for (mono)cyclic peptides with a D-amino acid next to the RGD motif.<sup>17</sup> Furthermore, we also found that peptides comprising the motif HXQ (X = any L-amino acid) in the left loop mostly showed significant inhibition. Surprisingly, approximately 50% of the bicyclic RGD peptides showed OD<sub>405</sub> values of higher than 2.0, even though the OD<sub>405</sub> of pure biotinylated knottin-RGD peptide was only ~1.2. Apparently, those bicycles

somehow activate either the  $\alpha_v\beta_3$  for knottin-RGD binding or vice versa. Another possibility might be that these bicycles promiscuously bind to the integrin and streptavidin. In any event, at this point we did not further investigate those bicycles or considered them of interest as potent and selective  $\alpha_v\beta_3$  binders.

We then retested the best 96 hits from the first screening using only a 100-fold excess (10  $\mu\text{M}$ ) over the knottin-RGD peptide, and from these only 28% (27 peptides) showed >50% inhibition. The four strongest binders from both screenings ( $\text{C}_{\text{T}3}\text{QADc}_{\text{T}3}\text{RGDc}_{\text{T}3}$ ,  $\text{C}_{\text{T}3}\text{HEQc}_{\text{T}3}\text{RGDc}_{\text{T}3}$ ,  $\text{C}_{\text{T}3}\text{QWGC}_{\text{T}3}\text{RGDc}_{\text{T}3}$ , and  $\text{C}_{\text{T}3}\text{WGDC}_{\text{T}3}\text{RGDc}_{\text{T}3}$ ) were then resynthesized on a larger scale (20  $\mu\text{mol}$ ) and purified and their activities determined (195 nM <  $\text{IC}_{50}$  < 835 nM, Figure 2A). These values are still significantly higher than those determined for the knottin-RGD peptide itself (38 nM) and the *cyclo*-[KRGDf] peptide (35 nM). To further improve affinities, second-generation libraries were designed using the six best binders from first screenings as a lead, having (i) extended (4-mer) second loops, e.g. XQAD or QADX (total of 216 peptides, see Figure 1), (ii) a full set of replacements for the glutamate (E) of the motif HEQ (25 peptides), (iii) a set of 12 non-natural variants of various potent lead sequences (see the Supporting Information), and (iv) the best 8 hits from first-generation screenings. From the total set of 261 RGD bicycles 31% (82 peptides) showed >50% inhibition at 5  $\mu\text{M}$ , while only 7% (18) showed even >70% inhibition. To further narrow down the selection, we performed a rescreening of the best 30 hits at 2.5  $\mu\text{M}$ , in which only 6% of the peptides (15) showed >50% inhibition and only 2% (6 peptides) showed >70% inhibition. None of the six best binders comprised an extended 4-mer sequence (such as XQAD or WGDx), indicating the choice for a trimer sequence in the left loop was correct. Instead, five peptides comprised the HXQ motif (with X = W(2x)/P/N/F) and one the non-natural sequence Q[Abu]D (Abu = L-2-aminobutyric acid), with  $\text{IC}_{50}$  values (measured with HPLC-purified peptides) ranging from 30 nM ( $\text{C}_{\text{T}3}\text{HPQC}_{\text{T}3}\text{RGDc}_{\text{T}3}$ ) to 225 nM ( $\text{C}_{\text{T}3}\text{HWQC}_{\text{T}3}\text{RGDc}_{\text{T}3}$ , Figure 2A). Molecular structures of the best  $\alpha_v\beta_3$  inhibitors are shown in Figure 2B. Five of the six second-generation binders showed lower  $\text{IC}_{50}$  values in comparison to the best first-generation binder ( $\text{C}_{\text{T}3}\text{HEQc}_{\text{T}3}\text{RGDc}_{\text{T}3}$ ,  $\text{IC}_{50}$  = 195 nM). The strongest binder,  $\text{C}_{\text{T}3}\text{HPQC}_{\text{T}3}\text{RGDc}_{\text{T}3}$ , displayed an  $\text{IC}_{50}$  value of 30 nM, which is comparable to that of knottin-RGD (38 nM) as reported by Kimura et al.<sup>14a</sup>

We then designed third-generation libraries comprising (i) a complete set of single-replacement variants for the second-generation lead HWQ (86 peptides) and (ii) 4-mer and 5-mer RGD loops extended by an additional amino acid (X) at either one or both ends, while the HWQ loop was kept constant (57 tetramer and 56 pentamer peptides, in total 113 peptides; Figure 1). From the total of ~200 bicycles that were screened at 5  $\mu\text{M}$ , 35% (79 peptides) showed >50% inhibition, 18% (35 peptides) showed >70% inhibition, and only 4% (8 peptides) displayed >90% inhibition. In the rescreening of the best 20 hits (at 2.5  $\mu\text{M}$ ), 95% (19) of the peptides showed >80% inhibition, while only four peptides (20%) showed even >90% inhibition. The best six binders (i.e.,  $\text{C}_{\text{T}3}\text{HPQC}_{\text{T}3}\text{RGDc}_{\text{T}3}$ ,  $\text{C}_{\text{T}3}\text{H[Aib]QC}_{\text{T}3}\text{RGDc}_{\text{T}3}$  (with Aib = 2-aminoisobutyric acid),  $\text{C}_{\text{T}3}\text{HRQC}_{\text{T}3}\text{RGDc}_{\text{T}3}$ ,  $\text{C}_{\text{T}3}\text{HFQC}_{\text{T}3}\text{RGDc}_{\text{T}3}$ ,  $\text{C}_{\text{T}3}\text{HWEC}_{\text{T}3}\text{RGDc}_{\text{T}3}$ , and  $\text{C}_{\text{T}3}\text{HSQC}_{\text{T}3}\text{RGDc}_{\text{T}3}$ ) were resynthesized and purified for activity testing in a concentration-dependent manner. The most active binder

( $\text{C}_{\text{T}3}\text{HPQC}_{\text{T}3}\text{RGDc}_{\text{T}3}$ ,  $\text{IC}_{50}$  = 31 nM) differed only from the best second-generation binder, i.e.  $\text{C}_{\text{T}3}\text{HPQC}_{\text{T}3}\text{RGDc}_{\text{T}3}$  (Figure 2A), in the configuration of the second cysteine. The other third-generation binders showed  $\text{IC}_{50}$  values ranging from 42 to 157 nM.

An alanine replacement study, in which each amino acid of the best  $\alpha_v\beta_3$  binder  $\text{C}_{\text{T}3}\text{HPQC}_{\text{T}3}\text{RGDc}_{\text{T}3}$  (85% inhibition at 1  $\mu\text{M}$ ) was sequentially replaced by L- or D-alanine, revealed significantly decreased affinities when R/G/D (<0%), H/P/Q (40–69%), or either one of the L-/D-cysteine residues formed monocyclic peptides (4–25%, Figure 2C). Furthermore, a full replacement study on the HWQ loop of the second-generation binder  $\text{C}_{\text{T}3}\text{HWQC}_{\text{T}3}\text{RGDc}_{\text{T}3}$  (Figure 2D) clearly revealed the much higher importance of H (histidine) and Q (glutamine) in comparison to W (tryptophan). This obviously is the reason why so many W variants showed up as potentially improved binders.

**Essence of Cysteine Residues.** We also tested variants of the second-generation lead  $\text{C}_{\text{T}3}\text{HWQC}_{\text{T}3}\text{RGDc}_{\text{T}3}$  (27 peptides in total) in which one, two, or all three cysteines were replaced by the non-natural variants L-/D-homocysteine (hC/hc), or L-/D-penicillamine (Pen/pen) (Figure S2 in the Supporting Information). All mutations showed a clear decrease in  $\alpha_v\beta_3$  binding, but the decrease was much stronger for the Pen variants in comparison to the hC variants. For example,  $\text{C}_{\text{T}3}\text{HWQ(hC)}_{\text{T}3}\text{RGDc}_{\text{T}3}$  and  $\text{C}_{\text{T}3}\text{HWQC}_{\text{T}3}\text{RGD(hc)}_{\text{T}3}$  showed 85/53% and 80/37% inhibition at 10 or 1  $\mu\text{M}$  (88/55% for the lead), whereas the corresponding Pen variants  $\text{C}_{\text{T}3}\text{HWQ(Pen)}_{\text{T}3}\text{RGDc}_{\text{T}3}$  and  $\text{C}_{\text{T}3}\text{HWQC}_{\text{T}3}\text{RGD(pen)}_{\text{T}3}$  basically showed no measurable inhibition (i.e., 0%) at 10  $\mu\text{M}$ . Occasionally the Pen variants did show activities comparable to those of the corresponding hC variants, as for (Pen)<sub>T3</sub>HWQC<sub>T3</sub>RGDc<sub>T3</sub> (31%/8% at 10/1  $\mu\text{M}$ ) and (hC)<sub>T3</sub>HWQC<sub>T3</sub>RGD(hc)<sub>T3</sub> (20%/12% at 10/1  $\mu\text{M}$ ), but an improved affinity was never observed, suggesting that the additional methyl groups in penicillamine largely abolish the integrin–bicycle interaction.

**Single-Loop Controls.** To illustrate the essence of the bicyclic peptide format for binding activity, we synthesized and tested the single-loop variants of some of the first-generation binders in which one of the three D-/L-cysteines was replaced by alanines. The single-loop variants (C/A-1, AQAD<sub>c<sub>mT2</sub></sub>RGD<sub>c<sub>mT2</sub></sub>; c/a-2, C<sub>mT2</sub>QADaRGD<sub>c<sub>mT2</sub></sub>; c/a-3, C<sub>mT2</sub>QAD<sub>c<sub>mT2</sub></sub>RGDa) were synthesized using 1,3-bis-(bromomethyl) benzene (mT2), which is the bivalent half of the trivalent T3 scaffold (for more detailed information on peptides constrained via CLIPS scaffolds T3 and mT2, see refs 2, 3b, 4, 5, and 10). For  $\text{C}_{\text{T}3}\text{QADc}_{\text{T}3}\text{RGDc}_{\text{T}3}$ ,  $\alpha_v\beta_3$  binding strongly decreased on opening the QAD loop (79% to 7% for C/A-1), the RGD loop (79% to 0% for c/a-3), or both (79% to 32% for c/a-2) (see Table S-2 in the Supporting Information). Likewise, a vast decrease in affinity was observed for single-loop variants of bicyclic peptides  $\text{C}_{\text{T}3}\text{HEQc}_{\text{T}3}\text{RGDc}_{\text{T}3}$  (from 92% to 22% (C/A-1), 28% (c/a-3), and 22% (c/a-2)) and  $\text{C}_{\text{T}3}\text{WGDC}_{\text{T}3}\text{RGDc}_{\text{T}3}$  (from 75% to 52% (C/A-1), 8% (c/a-3), and 23% (C/A-2)), which exemplifies the essence of constraining both loops for optimal  $\alpha_v\beta_3$  inhibition. Moreover, the corresponding single-loop RGD peptides also showed much lower binding values at 10  $\mu\text{M}$  in comparison to the best bicyclic binders (C<sub>mT2</sub>RGD<sub>c<sub>mT2</sub></sub>, 23%; C<sub>mT2</sub>RGD<sub>c<sub>mT2</sub></sub>, 57%; c<sub>mT2</sub>RGD<sub>c<sub>mT2</sub></sub>, 41% (Table S-2 in the Supporting Information), which underscores the importance of the second loop for integrin  $\alpha_v\beta_3$  binding.

**Binding of HPQ Bicycles to Streptavidin.** The fact that we identified high-affinity  $\alpha_v\beta_3$  binders comprising the HPQ motif via a competition ELISA may complicate the assay interpretation, as this motif is known to bind to streptavidin under certain conditions.<sup>18</sup> In order to exclude the possibility that bicycles containing HPQ or similar motifs directly interact with streptavidin, and so would falsely indicate a strong  $\alpha_v\beta_3$  interaction, we directly measured the ability of a series of bicyclic and monocyclic peptides comprising the HPQ motif to bind to streptavidin-HRP in a simple binding ELISA (Table S-3 in the Supporting Information). As expected, none of the bi- and monocyclic peptides showed detectable binding to Strep-HRP in the 0.005–30  $\mu\text{M}$  concentration range as used in the competition ELISA. Only the bicyclic peptide  $\text{C}_{\text{T}3}\text{HPQC}_{\text{T}3}\text{RGDC}_{\text{T}3}$  (OD  $\approx$  0.2) and monocyclic control  $\text{C}_{\text{mT}2}\text{HPQC}_{\text{mT}2}$  showed very weak binding to Strep-HRP at 100  $\mu\text{M}$  (OD  $\approx$  0.4), but this can by no means be held responsible for the fact that bicycles  $\text{C}_{\text{T}3}\text{HPQC}_{\text{T}3}\text{RGDC}_{\text{T}3}$  and  $\text{C}_{\text{T}3}\text{HPQC}_{\text{T}3}\text{RGDC}_{\text{T}3}$  were identified as the most potent RGD bicycle binders to integrin  $\alpha_v\beta_3$ .

**Determination of Affinity Binding Constants ( $K_d$ ).** We also studied the bicycle–integrin interaction in a direct manner using surface plasmon-enhanced fluorescence spectroscopy (SPFS),<sup>19</sup> an optical technique that combines surface plasmon resonance (SPR) with fluorescence spectroscopy. For that purpose, (i) the bicycle-peptide  $\text{C}_{\text{T}3}\text{HPQC}_{\text{T}3}\text{RGDC}_{\text{T}3}$  (best third-generation binder), (ii) linear GRGDS, (iii) *cyclo*-[KRGDf] and (iv) knottin-RGD were resynthesized including an N-terminal linker (K-PPPSG[Abz]SG, Abz = 4-amino-benzoic acid) following earlier studies of Pallarola et al. showing this linker to be minimally invasive with integrin affinity.<sup>20</sup> The N-terminal lysine was acetylated, while the lysine side-chain amine was deprotected. Since the use of conventional SPR lacked sensitivity (data not shown), probably due to the low molecular weight ( $\sim$ 2 kDa) of the bicycles, the peptides were labeled with the fluorescent Cy5 tag via coupling of a Cy5-NHS activated ester to the lysine side-chain amine, and the surface plasmon field intensity was applied at the wavelength coincident with the absorption band of Cy5 to locally excite a fluorescence signal in close proximity to the gold surface. This approach increases the fluorescence signal originating from the peptide binding at the surface with an immobilized integrin receptor, which allows kinetic measurements.<sup>19</sup> Concentration-dependent fluorescence curves  $F(c)$  were normalized to  $\Delta F_{\text{max}}$  (value measured at saturation concentration) and fitted via Langmuir isotherm (Figure 3A). The dissociation equilibrium constant ( $K_d$ ) was determined for Cy5-labeled  $\text{C}_{\text{T}3}\text{HPQC}_{\text{T}3}\text{RGDC}_{\text{T}3}$ , which turned out to be comparable to that of Cy5-labeled knottin-RGD (0.6 nM, Figure 3B). These results perfectly align with the competition ELISA data (Figure 2A). For Cy5-labeled *cyclo*-[KRGDf], a slightly weaker affinity ( $K_d = 4.1$  nM) was determined, indicating that Cy5 labeling affects  $\alpha_v\beta_3$  binding of *cyclo*-[KRGDf] more significantly than for knottin-RGD or the bicyclic peptide (see  $\text{IC}_{50}$  values, Figure 2A). The linear peptide Cy5-GRGDS did not show measurable binding to  $\alpha_v\beta_3$  in SPFS.

**Selectivity of Bicycle Binding to  $\alpha_v\beta_3$ .** Finally, we compared the  $\alpha_v\beta_3$  binding abilities of  $\text{C}_{\text{T}3}\text{HPQC}_{\text{T}3}\text{RGDC}_{\text{T}3}$ ,  $\text{C}_{\text{T}3}\text{HPQC}_{\text{T}3}\text{RGDC}_{\text{T}3}$ , and  $\text{C}_{\text{T}3}\text{HSQC}_{\text{T}3}\text{RGDC}_{\text{T}3}$ , the three highest-affinity bicycle peptides, and control peptides (knottin-RGD and *cyclo*-[KRGDf]) with the corresponding binding values for integrins  $\alpha_5\beta_1$  and  $\alpha_5\beta_5$  by measuring  $\text{IC}_{50}$  values in

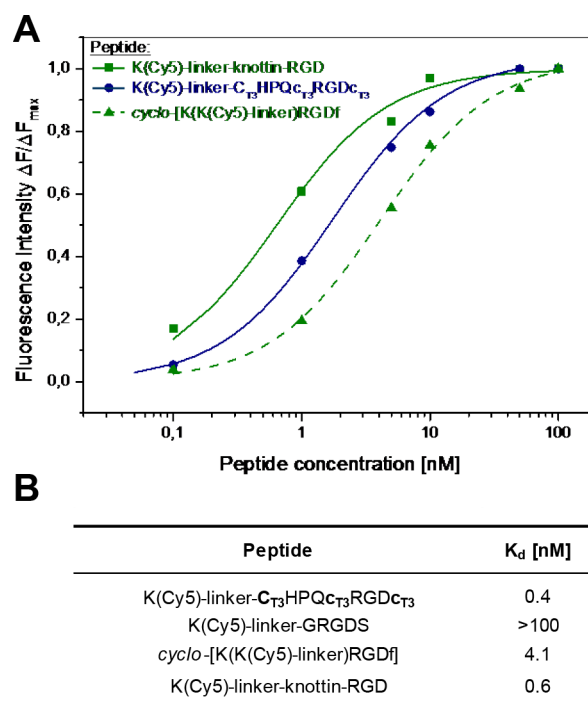


**Figure 3.** (A) Concentration-dependent, normalized fluorescence signals for selected Cy5-labeled peptide binding to integrin  $\alpha_v\beta_3$ ; (B) Overview of measured equilibrium dissociation constants ( $K_d$ ). Linker: PPPSG[4-Abz]SG.

competition ELISA. We found that none of the three bicycle peptides showed any measurable interaction with either  $\alpha_5\beta_5$  nor  $\alpha_5\beta_1$  ( $\text{IC}_{50} > 10000$  nM), which highlights their outstanding selectivities for  $\alpha_v\beta_3$  (Table 1). In sharp contrast

**Table 1.**  $\text{IC}_{50}$  Values Determined Using Competition ELISA for Three Best-Binding RGD Bicycle Peptides, *cyclo*-[KRGDf], Cilengitide, and Knottin-RGD for Different Integrins<sup>a</sup>

peptide	$\text{IC}_{50}$ (nM)		
	$\alpha_v\beta_3$	$\alpha_5\beta_5$	$\alpha_5\beta_1$
$\text{C}_{\text{T}3}\text{HPQC}_{\text{T}3}\text{RGDC}_{\text{T}3}$	30 $\pm$ 4	>10000	>10000
$\text{C}_{\text{T}3}\text{HPQC}_{\text{T}3}\text{RGDC}_{\text{T}3}$	31 $\pm$ 2	>10000	>10000
$\text{C}_{\text{T}3}\text{HSQC}_{\text{T}3}\text{RGDC}_{\text{T}3}$	42 $\pm$ 6	>10000	>10000
<i>cyclo</i> -[KRGDf]	35 $\pm$ 6	182 $\pm$ 29	>10000
cilengitide	121 $\pm$ 18	26 $\pm$ 5	>10000
knottin-RGD	38 $\pm$ 5	76 $\pm$ 7	114 $\pm$ 8

<sup>a</sup>Each concentration was tested in triplicate.  $\text{IC}_{50}$  values were calculated via nonlinear regression analysis using GraphPad.

to this, *cyclo*-[KRGDf] did show strong binding to  $\alpha_5\beta_5$  ( $\text{IC}_{50} = 182$  nM) while not to  $\alpha_5\beta_1$ , whereas knottin-RGD bound to all integrins with equally strong affinity ( $\alpha_5\beta_5$ ,  $\text{IC}_{50} = 76$  nM;  $\alpha_5\beta_1$ ,  $\text{IC}_{50} = 114$  nM). These data reveal that bicyclic RGD peptides display  $\alpha_v\beta_3$  selectivities superior to benchmark RGD peptides, such as knottin-RGD, *cyclo*-[KRGDf] and cilengitide.<sup>12</sup> Recently, Neubauer et al. described peptidomimetics with  $\alpha_v\beta_3/\alpha_5\beta_1$  selectivity ratios of  $\sim$ 0.006 and  $\sim$ 0.007 (ratio of corresponding  $\text{IC}_{50}$  values),<sup>13f</sup> which is still at least 2-fold less selective in comparison to the highest-affinity bicyclic  $\alpha_v\beta_3$  binder  $\text{C}_{\text{T}3}\text{HPQC}_{\text{T}3}\text{RGDC}_{\text{T}3}$ , for which this ratio is  $\leq$ 0.003.

**Structural Analysis via 2D-NMR Spectroscopy.** Bicycle peptide  $C_{T_3}HPQC_{T_3}RGDC_{T_3}$  was studied in detail by NMR using different techniques (COSY/ROESY/TOCSY/HSQC). Individual residues were identified through their  $^1H$  and  $^{13}C$  (in particular  $H_\alpha/C_\alpha$ ) chemical shifts (from edited HSQC) as well as chemical shifts of the side-chain resonances (2D TOCSY). From these data it can be concluded that the peptide largely adopts a random coil structure rather than an ordered secondary structure (Figure 4). This is fully in line with data

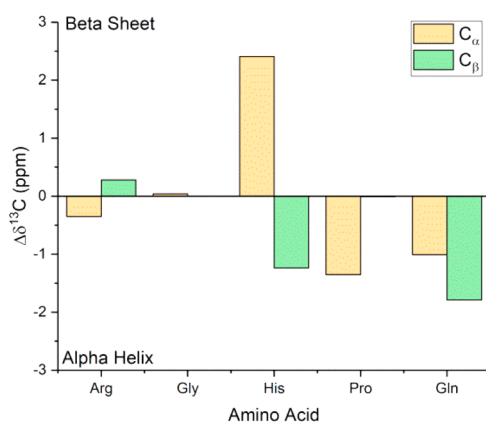


**Figure 4.** Chemical shift difference plots for  $C_\alpha$  and  $C_\beta$  calculated by  $\Delta\delta(^{13}C_\alpha) = \delta(^{13}C_{\alpha,rc}) - \delta(^{13}C_{\alpha,i})$  and  $\Delta\delta(^{13}C_\beta) = \delta(^{13}C_{\beta,i}) - \delta(^{13}C_{\beta,rc})$  ( $i$  = measured amino acid in bicycle,  $rc$  = random coil chemical shift). Positive values reflect more  $\beta$ -sheet character, while negative values represent more  $\alpha$ -helical character. Amino acids that are close to the baseline are indicative of a random coil structure or show both  $\alpha$ -helical and  $\beta$ -sheet character or alternatively structured sequences.

from circular dichroism spectroscopy (data not shown) that were also representative of mainly random-coil structures in solution. Another possibility is that the peptide adopts a different folded structure—apart from  $\alpha$ -helix or  $\beta$ -sheet—that cannot be detected with 2D NMR techniques. Interestingly, the histidine residue shows a double set of aromatic proton resonances at 8.66/8.60 and 7.33/7.29 ppm, which according to 1D/2D-ROESY experiments are belonging to different conformers in chemical exchange. Given the slight differences

in  $^1H$  and  $^{13}C$  chemical shifts of the exchanging histidines, it is unlikely the effect arises from  $\pi/\tau$  tautomerism. Rather, a more likely explanation is that two different proline conformations coexist ( $\sim 3:1$  ratio), which influences the chemical shifts of neighboring residues, such as histidine and the  $N$ -acetyl methyl resonance (1.91/2.03 ppm). This is supported by the significant differences in the proline diastereotopic  $H_\delta$  resonances (3.92 vs 3.66 ppm and 3.75 vs 3.50 ppm), and the effect diminishes as one moves farther away from the proline. Considering the sharpness of the resonances, relaxation measurements were not pursued, as the structure is most likely monomeric.

**Membrane Binding on Integrin-Expressing Cells (HT29).** In order to prove that RGD bicycles also bind to integrins in their natural environment of the cell membrane, we labeled human colon cancer cells (HT29, express integrin  $\alpha_v$  subunit) with the Cy5-functionalized bicycle peptide  $C_{T_3}HPQC_{T_3}RGDC_{T_3}$ , knottin-RGD, and *cyclo*-[KRGDf] and detected fluorescence emission via confocal microscopy. Surprisingly, the bicycle shows very high staining levels, much higher than that of the Cy5-labeled benchmark knottin-RGD (Figure 5), while the Cy5-labeled *cyclo*-[KRGDf] peptide is virtually silent under these conditions. Thereby, the peptide is clearly located on the cell membrane and is hardly internalized. Control studies with scrambled RGD bicycles showed did not show any traces of cell staining (data not shown), which proves that binding is clearly sequence specific. These data illustrate the potential of RGD bicycles as powerful markers of integrin expression on live cells.

## CONCLUSION

In this study, we presented bicyclic RGD “CLIPS” peptides as a novel platform for high-affinity and -selectivity integrin  $\alpha_v\beta_3$  binders. These peptides offer a straightforward, cost-effective, and versatile alternative for established binders, such as knottin-RGD and *cyclo*-[KRGDf]. The observed high selectivity for integrin  $\alpha_v\beta_3$  suggests applications in integrin-mediated in vivo tumor staining, cancer diagnostics, and/or cancer therapeutics.”

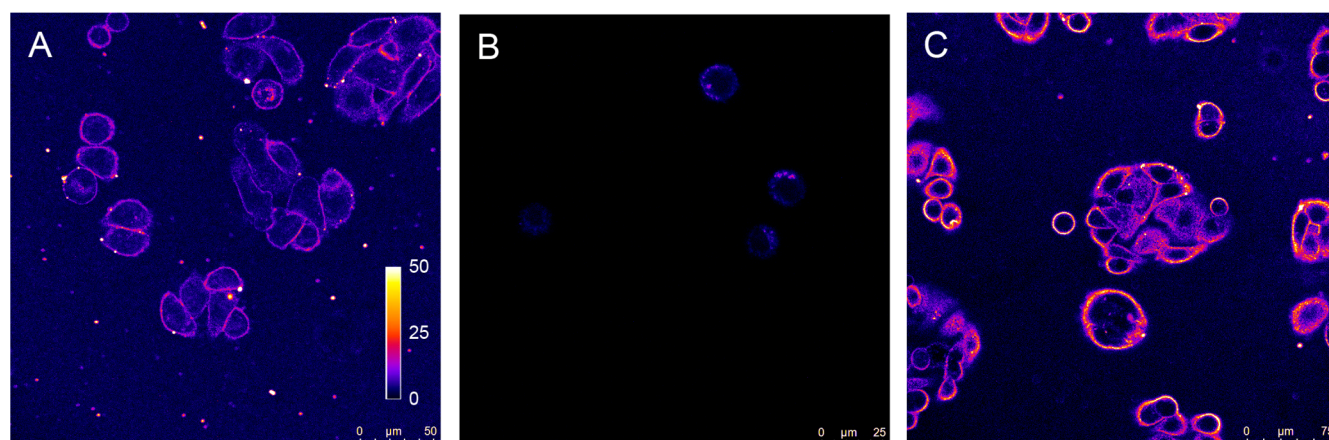


**Figure 5.** Confocal microscopy images of HT29 cells incubated with benchmarks Cy5-linker-knottin-RGD (A), *cyclo*-[K(Cy5-linker)RGDf] (B), and bicycle Cy5-linker- $C_{T_3}HPQC_{T_3}RGDC_{T_3}$  (C). Cells were incubated on glass coverslips for at least 24 h, followed by addition of Cy5-labeled peptides for 30 min at 4 °C, washing, fixation with 4% PFA, and finally confocal analysis. All images were acquired under identical imaging conditions and processed via ImageJ (LUT: Fire). The contrast is shown in arbitrary units (au): 0, no fluorescence; 50, maximum fluorescence.



## MATERIALS AND METHODS

**Reagents and Chemicals.** Incubation and washing buffers were prepared using standard protocols. Recombinant human integrins were purchased from R&D Systems (Minneapolis, USA). Strep-HRP (Streptavidin-Horseradish Peroxidase conjugate, Southern-Biotech, Birmingham, USA), was diluted 1:1000 for ELISA experiments. Amino acids were purchased from Iris Biotech (Marktredwitz, Germany) and Matrix Innovation (Quebec, Canada). Resins were purchased from Rapp Polymere (Tübingen, Germany) and Merck (Darmstadt, Germany).  $\text{MnCl}_2 \cdot 4\text{H}_2\text{O}$ , 1,3,5-tris(bromomethyl)benzene (T3), 1,3-bis(bromomethyl)-benzene (mT2), 2,2-dithiobis(5-nitropyridine) (DTNP), ethyl(dimethylaminopropyl)-carbodiimide (EDC), *N*-hydroxysuccinimide (NHS), ethanolamine, Tween20, ethylene glycol, and acetic acid and sodium acetate for the preparation of acetate buffer were purchased from Sigma-Aldrich (Steinheim, Germany).  $\text{CaCl}_2 \cdot 2\text{H}_2\text{O}$ ,  $\text{MgCl}_2 \cdot 6\text{H}_2\text{O}$ , and phosphate-buffered saline (PBS) were purchased from Merck (Darmstadt, Germany). Tween80 was purchased from Faryon (Capelle, The Netherlands), and I-Block was purchased from Tropix (Bedford, USA). Disulfo-Cy5-NHS ester was purchased from Cyandye (Sunny Isles Beach, USA). Dithiolaromatic PEG6-carboxylate (thiol-COOH; SPT0014A6) and dithiolaromatic PEG3 (thiolPEG; SPT-0013) were purchased from SensoPath Technologies (Bozeman, USA). Sodium *p*-tetrafluorophenol-sulfonate (TFPS) and *S*-3-(benzoylphenoxy)propyl ethanethioate (thiol-benzophenone) were synthesized at the Max Planck Institute for Polymer Research (Mainz, Germany) according to the literature.<sup>21,22</sup> Poly(*N*-isopropylacrylamide)-based terpolymer with a 94:5:1 molar ratio of *N*-isopropylacrylamide, methacrylic acid, and 4-methacryloyloxy benzophenone (pNIPAAm) were synthesized as previously described.<sup>23,24</sup>

**Peptide Synthesis.** Synthesis of crude bicyclic peptide libraries, purified bicyclic and monocyclic peptides, and Cy5-labeled peptides was performed using standard Fmoc-based peptide synthesis. All 672 peptides were synthesized and collected separately (synthesis on 2  $\mu\text{mol}$  scale on solid phase, collection in 96-well polypropylene storage plates (each 2 mL). For more detailed information, see the Supporting Information

**ELISA.** For buffer compositions and concentrations, see Table S-1 in the Supporting Information.

**Integrin Coating and Blocking.** Plates were coated with 100  $\mu\text{L}$  of a 0.25–0.5  $\mu\text{g}/\text{mL}$  integrin solution in coating buffer onto 96-well NUNC Polysorp plates (overnight, 4 °C) followed by blocking with 150  $\mu\text{L}$  of 1% I-Block in blocking buffer (60 min, room temperature) and 3 $\times$  washing with 400  $\mu\text{L}$  of washing buffer.

**Library Screening.** In each screening experiment, 96 or 192 different peptides were tested. Bicyclic peptide libraries (2  $\mu\text{mol}$ ) were dissolved in DMSO (10 mM stock solutions) and further diluted to working concentrations (1 mM to 2.5  $\mu\text{M}$ ) with incubation buffer. After incubation with a fixed concentration of biotinylated knottin-RGD peptide in incubation buffer (minimum 15 min, room temperature), the individual bicycle solutions were added to the integrin-coated plates (90 min, room temperature), followed by 3 $\times$  washing with washing buffer. Then the plates were incubated with 100  $\mu\text{L}$  of 1:1000 Strep-HRP in Strep-HRP buffer (60 min, room temperature). After 4 $\times$  washing they were incubated with 150  $\mu\text{L}$  of substrate buffer containing 0.91 mM ABTS (2,2'-azino-bis(3-ethylbenzothiazoline-6-sulfonic acid) and 0.006%  $\text{H}_2\text{O}_2$

in substrate buffer (0.2 M  $\text{Na}_2\text{HPO}_4$  adjusted to pH 4 using 0.2 M citric acid). Absorbance (405 nm) was measured after 4 min using a Molecular Devices Spectramax M2 plate reader.

**$IC_{50}$  Determination.** Peptides were mixed in eight different concentrations (each 3-fold dilutions) with a fixed concentration of biotinylated knottin-RGD (both in incubation buffer, 15 min, room temperature), followed by incubation of the plates with peptide/biotinylated knottin-RGD solutions for 90 min at room temperature. Strep-HRP and ABTS incubation steps were performed as described for library screening. All concentrations were tested in triplicate.  $IC_{50}$  values were calculated via nonlinear regression analysis using GraphPad Prism software and represent the peptide concentration at which 50% inhibition of biotinylated knottin binding is observed.

**Surface Plasmon-Enhanced Fluorescence Spectroscopy (SPFS).** For the description of the optical system, sensor chip preparation, and the immobilization of the ligand, see the Supporting Information.

**Measurement of Equilibrium Dissociation Constant  $K_d$ .** For measurement of the binding affinity of Cy5-labeled peptides to immobilized integrin ligands, PBS with 1 mM  $\text{CaCl}_2$ , 0.5 mM  $\text{MnCl}_2$ , 1 mg/mL BSA, and 0.05% Tween20 was used as the running buffer. Different concentrations of the peptide (0.1, 1, 5, 10, 50, 100, and 1000 nM) were sequentially flushed over the sensor surface. The sample at each concentration was allowed to react with the integrin for 30 min followed by rinsing the surface with running buffer solution for 10 min. The binding of the target analyte was monitored in real time by measuring the fluorescence intensity  $F(t)$  originating from the close proximity to the sensor surface that was probed by resonantly excited surface plasmons (Figure S-4B in the Supporting Information). The fluorescence signal  $F$  gradually increased upon binding of target analyte, and for each concentration, the equilibrium fluorescence signal  $\Delta F$  was determined as a difference to the fluorescence baseline after 10 min of rinsing with running buffer. The titration curve was established on the basis of these values, and it was fitted with a Langmuir isotherm model (function  $\Delta F = \Delta F_{\text{max}} c / (K_d + c)$ ) in order to determine the equilibrium dissociation constant  $K_d$ .

**NMR.** A detailed description of the acquisition of the NMR spectra, devices, methods, and spectrum editing, as well as the  $^1\text{H}$  NMR spectrum of the bicycle  $\text{C}_{\text{T}3}\text{HPQC}_{\text{T}3}\text{RGDC}_{\text{T}3}$  (Figure S-5) is depicted in the Supporting Information.  $T_1$  measurements were performed by properly calibrating the 90° pulse length and then performing estimates using the 1D inversion recovery sequence with excitation sculpting water suppression. After the longest  $T_1$  was determined to be approximately 2 s, a pseudo-2D inversion recovery experiment was performed with 10 separate delays of 8 scans each with a total longitudinal relaxation time of 10.3 s.  $T_2$  measurements were acquired by first performing estimates using the 1D PROJECT-CMPG sequence<sup>25</sup> with presaturation water suppression. After the longest  $T_2$  was determined to be approximately 1 s, a pseudo-2D PROJECT-CMPG sequence experiment with presaturation was performed with 12 separate delays of 8 scans each and a cycle time of 4 ms with a total longitudinal relaxation time of 10.3 s.

**Cell Integrin Staining and Confocal Microscopy.** Human colorectal adenocarcinoma cells (HT29) were obtained from The Netherlands Cancer Institute (NKI) and grown using standard procedures and conditions. For the

experiment, the cells were allowed to adhere on clean glass coverslips for at least 24 h until they reached approximately 40–50% confluency. Then, the glass coverslips were washed two times with cold HCG buffer (carbonate-buffered saline, pH 7.2, containing 140 mM NaCl, 5 mM KCl, 23 mM NaHCO<sub>3</sub>, 10 mM HEPES, 10 mM glucose, 1 mM CaCl<sub>2</sub>, 0.5 mM MgCl<sub>2</sub>, and 0.5 mM MnCl<sub>2</sub>) to remove nonadhered cells, followed by adding cold HCG buffer and cooling of the glass coverslips to 4 °C. Afterward, the Cy5-labeled peptides were added and allowed to incubate at 1 μM for 30 min at 4 °C, followed by at least five washing steps with HCG buffer, fixation with 4% paraformaldehyde solution in PBS pH 7.4 (20 min), and another four washing steps with HCG buffer. Subsequently, the cells were analyzed via confocal microscopy using a Leica TCS SP8 confocal microscope equipped with a supercontinuum white light laser (NKT Photonics) and water immersion objectives (63x W PL APO CS2, NA 1.2/40x W PL APO CS2, NA 1.1). The excitation wavelength was set to 633 nm while fluorescence was detected from 646 to 778 nm. All images were acquired under identical imaging conditions and processed via ImageJ (LUT: Fire).

## ■ ASSOCIATED CONTENT

### ● Supporting Information

The Supporting Information is available free of charge on the ACS Publications website at DOI: 10.1021/acscombsci.8b00144.

Structures of (biotinylated) knottin-RGD and cyclo-[KRGDf], detailed information about peptide synthesis, analysis, and purification and amino acids used in peptide libraries, additional peptides screened, and structure of biotinylated knottin-RGD peptide, parameters varied in the competition ELISA setup, inhibition values for selected bicyclic peptides and monocyclic analogues, position-replacement analysis for cysteines, ELISA protocol for testing HPQ<sub>2</sub>-streptavidin binding and results, description and schematic of optical instrument used for SPFS and ligand immobilization, SPR sensorgrams and SPFS measurement for Cy5-functionalized bicycle C<sub>T3</sub>HPQC<sub>T3</sub>RGDC<sub>T3</sub>, additional NMR information, and <sup>1</sup>H NMR spectrum of bicycle C<sub>T3</sub>HPQC<sub>T3</sub>RGDC<sub>T3</sub> (PDF)

## ■ AUTHOR INFORMATION

### Corresponding Author

\*P.T.: tel, +31-320-225300; fax, +31-320-225301; e-mail, p.timmerman@pepscan.com.

### ORCID

Jakub Dostalek: 0000-0002-0431-2170

Peter Timmerman: 0000-0001-6687-5297

### Author Contributions

The manuscript was written through contributions of all authors. D.B. and P.T. conceived the concept and analyzed the data. D.B. performed peptide syntheses, competition and binding ELISA experiments, and in vitro integrin staining experiments. V.J., N.G.Q., and J.D. designed, performed, and analyzed the SPR experiments. P.B.W. performed and analyzed the NMR experiments. D.B., K.J. and P.T. evaluated the confocal images. D.B., P.B.W., and P.T. wrote the manuscript. All authors have given approval to the final version of the manuscript.

## Notes

The authors declare the following competing financial interest(s): Pepsan is the inventor of the CLIPS technology and holds a patent on the synthesis of bicyclic peptides using 2-CLIPS technology.

## ■ ACKNOWLEDGMENTS

This project received funding from Horizon-2020 research and innovation program BIOGEL under the Marie Skłodowska-Curie grant agreement No. 64268.

## ■ REFERENCES

- (1) (a) Driggers, E. M.; Hale, S. P.; Lee, J.; Terrett, N. K. The exploration of macrocycles for drug discovery — an underexploited structural class. *Nat. Rev. Drug Discovery* **2008**, *7*, 608–624. (b) Craik, D. J.; Fairlie, D. P.; Liras, S.; Price, D. The Future of Peptide-based Drugs. *Chem. Biol. Drug Des.* **2013**, *81*, 136–147. (c) Wang, C. K.; Craik, D. J. Cyclic peptide oral bioavailability: Lessons from the past. *Biopolymers* **2016**, *106*, 901–909.
- (2) Timmerman, P.; Beld, J.; Puijk, W. C.; Meloen, R. H. Rapid and quantitative cyclization of multiple peptide loops onto synthetic scaffolds for structural mimicry of protein surfaces. *ChemBioChem* **2005**, *6*, 821–824.
- (3) (a) Li, P.; Roller, P. P. Cyclization strategies in peptide derived drug design. *Curr. Top. Med. Chem.* **2002**, *2*, 325–341. (b) Baeriswyl, V.; Heinis, C. Polycyclic Peptide Therapeutics. *ChemMedChem* **2013**, *8*, 377–384.
- (4) Heinis, C.; Rutherford, T.; Freund, S.; Winter, G. Phage-encoded combinatorial chemical libraries based on bicyclic peptides. *Nat. Chem. Biol.* **2009**, *5*, 502–507.
- (5) Angelini, A.; Cendron, L.; Chen, S.; Touati, J.; Winter, G.; Zanotti, G.; Heinis, C. Bicyclic peptide inhibitor reveals large contact interface with a protease target. *ACS Chem. Biol.* **2012**, *7*, 817–821.
- (6) Rentero Rebollo, I.; McCallin, S.; Bertoldo, D.; Entenza, J. M.; Moreillon, P.; Heinis, C. Development of Potent and Selective *S. aureus* Sortase A Inhibitors Based on Peptide Macrocycles. *ACS Med. Chem. Lett.* **2016**, *7*, 606–611.
- (7) Luzi, S.; Kondo, Y.; Bernard, E.; Stadler, L. K. J.; Vaysburd, M.; Winter, G.; Holliger, P. Subunit disassembly and inhibition of TNF $\alpha$  by a semi-synthetic bicyclic peptide. *Protein Eng., Des. Sel.* **2015**, *28*, 45–52.
- (8) Lian, W.; Jiang, B.; Qian, Z.; Pei, D. Cell-permeable bicyclic peptide inhibitors against intracellular proteins. *J. Am. Chem. Soc.* **2014**, *136*, 9830–9833.
- (9) Trinh, T. B.; Upadhyaya, P.; Qian, Z.; Pei, D. Discovery of a Direct Ras Inhibitor by Screening a Combinatorial Library of Cell-Permeable Bicyclic Peptides. *ACS Comb. Sci.* **2016**, *18*, 75–85.
- (10) Timmerman, P.; Barderas, R.; Desmet, J.; Shochat, S.; Monasterio, A.; Casal, J. I.; Meloen, R. H. A combinatorial approach for the design of complementarity-determining region-derived peptidomimetics with in vitro anti-tumoral activity. *J. Biol. Chem.* **2009**, *284*, 34126–34134.
- (11) (a) Barczyk, M.; Carracedo, S.; Gullberg, D. Integrins. *Cell Tissue Res.* **2010**, *339*, 269–280. (b) Takada, Y.; Ye, X.; Simon, S. The Integrins. *Genome Biol.* **2007**, *8*, 215.
- (12) Dechantsreiter, M. A.; Planker, E.; Matha, B.; Lohof, E.; Jonczyk, A.; Goodman, S. L.; Kessler, H. N-Methylated Cyclic RGD Peptides as Highly Active and selective  $\alpha_v\beta_3$  integrin antagonists. *J. Med. Chem.* **1999**, *42*, 3033–3040.
- (13) (a) Marinelli, L.; Lavecchia, A.; Gottschalk, K.-E.; Novellino, E.; Kessler, H. for example, see: Docking studies on alphavbeta3 integrin ligands: pharmacophore refinement and implications for drug design. *J. Med. Chem.* **2003**, *46*, 4393–4404. (b) Heckmann, D.; Meyer, A.; Marinelli, L.; Zahn, G.; Stragies, R.; Kessler, H. Probing integrin selectivity: rational design of highly active and selective ligands for the  $\alpha_5\beta_1$  and  $\alpha_v\beta_3$  integrin receptor. *Angew. Chem., Int. Ed.* **2007**, *46*, 3571–3574. (c) Bochen, A.; Marelli, U. K.; Otto, E.; Pallarola, D.; Mas-Moruno, C.; Saverio, F.; Leva, D.; Boehm, H.;

- Spatz, J. P.; Novellino, E.; Kessler, H.; Marinelli, L. Biselectivity of iso DGR Peptides for Fibronectin Binding Integrin Subtypes  $\alpha_5\beta_1$  and  $\alpha_5\beta_3$ : Conformational Control through Flanking Amino Acids. *J. Med. Chem.* **2013**, *56*, 1509–1519. (d) Rechenmacher, F.; Neubauer, S.; Polleux, J.; Mas-Moruno, C.; De Simone, M.; Cavalcanti-Adam, E. A.; Spatz, J. P.; Fässler, R.; Kessler, H. Functionalizing  $\alpha_v\beta_3$ - or  $\alpha_5\beta_1$ -selective integrin antagonists for surface coating: A method to discriminate integrin subtypes in vitro. *Angew. Chem., Int. Ed.* **2013**, *52*, 1572–1575. (e) Hegemann, J. D.; De Simone, M.; Zimmermann, M.; Knappe, T. A.; Xie, X.; Di Leva, F. S.; Marinelli, L.; Novellino, E.; Zahler, S.; Kessler, H.; Marahiel, M. A. Rational improvement of the affinity and selectivity of integrin binding of grafted lasso peptides. *J. Med. Chem.* **2014**, *57*, 5829–5834. (f) Neubauer, S.; Rechenmacher, F.; Brimioulle, R.; Saverio, F.; Leva, D.; Bochen, A.; Sobahi, T. R.; Schottelius, M.; Novellino, E.; Mas-Moruno, C.; Marinelli, L.; Kessler, H. Pharmacophoric Modifications Lead to Superpotent  $\alpha_v\beta_3$  Integrin Ligands with Suppressed  $\alpha_5\beta_1$  Activity. *J. Med. Chem.* **2014**, *57*, 3410–3417. (g) Maltsev, O. V.; Marelli, U. K.; Kapp, T. G.; Di Leva, F. S.; Di Maro, S.; Nieberler, M.; Reuning, U.; Schwaiger, M.; Novellino, E.; Marinelli, L.; Kessler, H. Stable Peptides Instead of Stapled Peptides: Highly Potent  $\alpha_5\beta_3$ -Selective Integrin Ligands. *Angew. Chem., Int. Ed.* **2016**, *55*, 1535–1539. (h) Kruss, S.; Wolfram, T.; Martin, R.; Neubauer, S.; Kessler, H.; Spatz, J. P. Stimulation of Cell Adhesion at Nanostructured Teflon Interfaces. *Adv. Mater.* **2010**, *22*, 5499–5506. (i) Kruss, S.; Erpenbeck, L.; Amschler, K.; Munding, T. A.; Boehm, H.; Helms, H.-J.; Friede, T.; Andrews, R. K.; Schön, M. P.; Spatz, J. P. Adhesion Maturation of Neutrophils on Nanoscopically Presented Platelet Glycoprotein Iba. *ACS Nano* **2013**, *7*, 9984–9996. (j) Polo, E.; Nitka, T. T.; Neubert, E.; Erpenbeck, L.; Vukovic, L.; Kruss, S. Control of integrin affinity by confining peptides on fluorescent carbon nanotubes. *ACS Appl. Mater. Interfaces* **2018**, *10*, 17693–17703.
- (14) (a) Kimura, R. H.; Levin, A. M.; Cochran, F. V.; Cochran, J. R. Engineered cystine knot peptides that bind  $\alpha_v\beta_3$ ,  $\alpha_5\beta_3$ , and  $\alpha_5\beta_1$  integrins with low-nanomolar affinity. *Proteins: Struct., Funct., Genet.* **2009**, *77*, 359–369. (b) Kimura, R. H.; Teed, R.; Hackel, B. J.; Pysz, M. A.; Chuang, C. Z.; Sathirachinda, A.; Willmann, J. K.; Gambhir, S. S. Pharmacokinetically Stabilized Cystine Knot Peptides that bind Alpha-v-Beta-6 Integrin with Single-Digit Nanomolar Affinities for Detection of Pancreatic Cancer. *Clin. Cancer Res.* **2012**, *18*, 839–849. (c) Kim, J. W.; Cochran, F. V.; Cochran, J. R. A Chemically Cross-Linked Knottin Dimer Binds Integrins with Picomolar Affinity and Inhibits Tumor Cell Migration and Proliferation. *J. Am. Chem. Soc.* **2015**, *137*, 6–9.
- (15) Timmerman, P.; Beld, J.; Meloen, R. H.; Puijk, W. C. Method for Selecting a Candidate Drug Compound. WO/2004/077062, 2004.
- (16) Bernhagen, D.; De Laporte, L.; Timmerman, P. High-Affinity RGD-Knottin Peptide as a New Tool for Rapid Evaluation of the Binding Strength of Unlabeled RGD-Peptides to  $\alpha_v\beta_3$ ,  $\alpha_5\beta_3$ , and  $\alpha_5\beta_1$  Integrin Receptors. *Anal. Chem.* **2017**, *89*, 5991–5997.
- (17) Aumailley, M.; Gurrath, M.; Calvete, J.; Timpl, R.; Kessler, H. Arg-Gly-Asp constrained within cyclic pentapeptides - Strong and selective inhibitors of cell adhesion to vitronectin and laminin fragment P1. *FEBS Lett.* **1991**, *291*, 50–54.
- (18) Giebel, L. B.; Cass, R. T.; Milligan, D. L.; Young, D. C.; Arze, R.; Johnson, C. R. Screening of cyclic peptide phage libraries identifies ligands that bind streptavidin with high affinities. *Biochemistry* **1995**, *34*, 15430–15435.
- (19) Bauch, M.; Toma, K.; Toma, M.; Zhang, Q.; Dostalek, J. Surface plasmon-enhanced fluorescence biosensors: a review. *Plasmonics* **2014**, *9*, 781–799.
- (20) Pallarola, D.; Bochen, A.; Boehm, H.; Rechenmacher, F.; Sobahi, T. R.; Spatz, J. P.; Kessler, H. Interface immobilization chemistry of cRGD-based peptides regulates integrin mediated cell adhesion. *Adv. Funct. Mater.* **2014**, *24*, 943–956.
- (21) Beines, P. W.; Klosterkamp, I.; Menges, B.; Jonas, U.; Knoll, W. Responsive Thin Hydrogel Layers from Photo-Cross-Linkable Poly(*N*-isopropylacrylamide) Terpolymers. *Langmuir* **2007**, *23*, 2231–2238.
- (22) Gee, K. R.; Archer, E. A.; Kang, H. C. 4-Sulfotetrafluorophenyl (STP) esters: New water-soluble amine-reactive reagents for labeling biomolecules. *Tetrahedron Lett.* **1999**, *40*, 1471–1474.
- (23) Junk, M. J. N.; Jonas, U.; Hinderberger, D. EPR spectroscopy reveals nanoinhomogeneities in the structure and reactivity of thermoresponsive hydrogels. *Small* **2008**, *4*, 1485–1493.
- (24) Anac, I.; Aulasevich, A.; Junk, M. J. N.; Jakubowicz, P.; Roskamp, R. F.; Menges, B.; Jonas, U.; Knoll, W. Optical Characterization of Co-Nonsolvency Effects in Thin Responsive PNIPAAm-Based Gel Layers Exposed to Ethanol/Water Mixtures. *Macromol. Chem. Phys.* **2010**, *211*, 1018–1025.
- (25) Aguilar, J. A.; Nilsson, M.; Bodenhausen, G.; Morris, G. A. Spin echo NMR spectra without J modulation. *Chem. Commun.* **2012**, *48*, 811–813.

## Supporting Information

### Bicyclic RGD-peptides with Exquisite Selectivity for the Integrin $\alpha_v\beta_3$ Receptor using a ‘Random Design’ Approach

Dominik Bernhagen<sup>a</sup>, Vanessa Jungbluth<sup>b</sup>, Nestor Gisbert Quilis<sup>b</sup>, Jakub Dostalek<sup>b</sup>, Paul B. White<sup>c</sup>, Kees Jalink<sup>d</sup> and Peter Timmerman<sup>a,e\*</sup>

**a:** Pepscan Therapeutics, Zuidersluisweg 2, 8243 RC Lelystad, the Netherlands; **b:** Biosensor Technologies, AIT Austrian Institute of Technology GmbH, Muthgasse 11, 1190 Vienna, Austria; **c:** Institute for Molecules and Materials, Radboud University, Heyendaalseweg 135, 6225 AJ Nijmegen, the Netherlands; **d:** The Netherlands Cancer Institute, Plesmanlaan 21, 1066 CX Amsterdam, the Netherlands; **e:** Van’t Hoff Institute for Molecular Sciences, University of Amsterdam, Science Park 904, 1098 XH Amsterdam, the Netherlands

#### Table of contents

- S-2:** Structures of (biotinylated) knottin-RGD and cyclo-[KRGDf] (**Figure S-1**)  
Peptide synthesis, analysis and purification
- S-3:** Amino acids used in peptide libraries  
Additional peptides 2<sup>nd</sup> generation libraries
- S-4:** Parameters varied in the competition ELISA setups (**Table S-1**)
- S-5:** Inhibition values for selected bicyclic peptides and monocyclic analogues (**Table S-2**)  
Molecular drawings of cysteine analogues, position-replacement for cysteines (by HCy/Pen) for  $\alpha_v\beta_3$ -binder C<sub>T3</sub>HWQC<sub>T3</sub>RGDC<sub>T3</sub>-**T3** (**Figure S-2**)
- S-6:** Binding ELISA protocol for testing HPQ-streptavidin binding  
Binding ELISA results (**Table S-3**)  
Description of optical instrument for SPR and SPFS measurements
- S-7:** Schematics of the optical instrument used for SPR and SPFS (**Figure S-3**)  
Description of sensor chip preparation and immobilization of ligand (SPFS)
- S-8:** Schematics of surface architecture for SPFS and SPR measurements (**Figure S-4**)  
Experimental description of the NMR experiments
- S-9:** <sup>1</sup>H NMR spectrum of bicycle C<sub>T3</sub>HPQC<sub>T3</sub>RGDC<sub>T3</sub> (**Figure S-5**)  
References

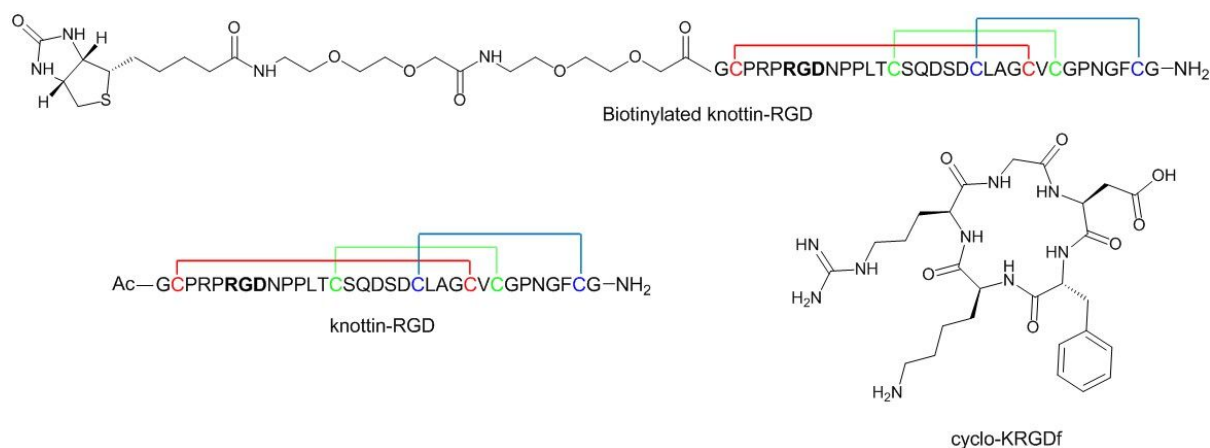


**Figure S-1.** Structures of biotinylated knottin-RGD, knottin-RGD and cyclo-[KRGDf].

## Peptide synthesis, analysis and purification

Peptide synthesis was performed on fully automated peptide synthesizers (MultisynTech, Syro, 2-4  $\mu\text{mol}$  scale for crude libraries) or Gyros Protein Technologies (Symphony, 100-200  $\mu\text{mol}$  scale, for bulk production) using Fmoc-based solid-phase peptide synthesis on TentaGel<sup>®</sup> Ram resin using standard protocols. Coupling of L- and D-cysteines was performed manually using 2,4,6-trimethylpyridine as a base to maximally suppress racemization. Knottin-RGD peptide, *cyclo*-[KRGDf] and biotinylated knottin-RGD peptide (structures shown in Supporting Information, **Figure S-1**) were synthesized according to previously published protocols.<sup>17</sup> For IC<sub>50</sub> determination and selectivity experiments, all peptides were purified by preparative HPLC on an RP-C18 column (Reposil-Pur 120 C18-AQ 150x20 mm, Dr. Maisch GmbH, Ammerbuch, Germany) using an MeCN/H<sub>2</sub>O gradient (5-65%) including 0.05% TFA followed by lyophilization (Christ Alpha 2-4 LDplus). Library screening and inhibition experiments with single-loop peptides were carried out using non-purified peptides.

**Synthesis of crude bicyclic peptide libraries.** Individual linear peptides (2  $\mu\text{mol}$ ) were dissolved in DMF (0.5 mL). Then, 1,3,5-tris(bromomethyl) benzene in DMF (4.1 mM, 0.5 mL) was added and the solution homogenized, followed by ammonium bicarbonate (150 mM, pH 8.0, 0.5 mL) again followed by homogenizing of the resulting solution and after 1 hour standing at room temperature the reaction mixtures were quenched with 0.5% ethanethiol (in 1:1 DMF/H<sub>2</sub>O, 0.1 mL/peptide). Bicyclic peptide libraries were then lyophilized using a Genevac HT-4X evaporation system.

**Synthesis of purified bicyclic and monocyclic peptides.** To a solution of linear peptide dissolved at 0.5 mM in 1:3 MeCN/H<sub>2</sub>O, was added 1.1 equiv. of the appropriate scaffolds (**T3** or **mT2**) dissolved in MeCN, where after the solution was homogenized. Then, 44 equiv. ammonium carbonate (0.2 M solution in H<sub>2</sub>O) were added and shaken for 60 min. After completion (monitoring by UPLC), the reaction was quenched with 10% TFA/H<sub>2</sub>O to pH <4, followed by lyophilization. Monocyclic peptides were further used in crude form, and bicycles were purified via preparative RP-HPLC.

For S-S-oxidation, linear peptides were dissolved at 0.5 mM in 5% MeCN/H<sub>2</sub>O and 0.5 equiv. of DTNP (5 mg/mL in MeCN) was added. 0.2 M ammonium bicarbonate solution was added until the solution was basic (color changed to yellow). After 10 min, another 0.5 equiv. of DTNP was added. After complete disappearance of the starting material, the reaction was quenched with 10% TFA/H<sub>2</sub>O until the solution was acidic (color change to green) and the S-S-oxidized peptide was subsequently purified preparative RP-HPLC.

**Peptide labeling with Cy5.** Peptides comprising an amine group were dissolved at 4 mM in DMSO, followed by adding disulfo-Cy5 NHS (1.0 equiv., 20 mg/mL in DMSO) and DIPEA (10 equiv.). After completion (30-60 min) reaction was quenched with 10% TFA/H<sub>2</sub>O, using twice the volume of DIPEA, and subsequently purified using preparative RP-HPLC.

**Peptide analysis and purification.** UPLC analysis was performed on a Waters Acquity Ultra Performance LC System, equipped with a Waters Acquity UPLC BEH130 C18 1.7  $\mu$ m column. A linear gradient of 5-55% MeCN (0.05% TFA) in H<sub>2</sub>O (0.05% TFA) was used. Peptides were purified by preparative HPLC (Waters Prep LC) on an RP-C18 column (Reprosil-Pur 120 C18-AQ 150x20 mm, Dr. Maisch GmbH, Ammerbuch, Germany) using an MeCN/H<sub>2</sub>O gradient (5-65%) including 0.05% TFA.

Freeze-drying of the peptide libraries was performed using a *GeneVac HT-4X* centrifugal vacuum evaporator.

### **Amino acids used in peptide libraries**

The following amino acids were included in the peptide library syntheses:

Ala (A), Asp (D), Glu (E), Phe (F), Gly (G), His (H), Ile (I), Lys (K), Leu (L), Asn (N), Pro (P), Gln (Q), Arg (R), Ser (S), Thr (T), Val (V), Trp (W), Tyr (Y).

Moreover, various non-natural amino acids were included for 3<sup>rd</sup> generation  $\alpha,\beta_3$ -libraries.

2-Aminobutyric acid (Z or Abu, also 2<sup>nd</sup> gen), norleucine (Nle, also 2<sup>nd</sup> gen), norvaline (Nva, also 2<sup>nd</sup> gen), 1-naphthyl alanine (1 or 1-Nal, also 2<sup>nd</sup> gen), 2-naphthyl alanine (2 or 2-Nal, also 2<sup>nd</sup> gen), 2-aminoisobutyric acid (Z or Aib), D-Ala (a), D-Phe (f), D-His (h), D-Ile (i), D-Leu (l), D-Gln (q), D-Trp (w).

### **Additional peptides 2<sup>nd</sup> generation libraries**

C<sub>T3</sub>1GDC<sub>T3</sub>RGDC<sub>T3</sub> (1: L-1-naphthylalanine)

C<sub>T3</sub>2GDC<sub>T3</sub>RGDC<sub>T3</sub> (2: L-2-naphthylalanine)

C<sub>T3</sub>Q1GC<sub>T3</sub>RGDC<sub>T3</sub>

C<sub>T3</sub>Q2GC<sub>T3</sub>RGDC<sub>T3</sub>

C<sub>T3</sub>Q(Abu)DC<sub>T3</sub>RGDC<sub>T3</sub> (Abu: 2-aminobutyric acid)

C<sub>T3</sub>Q(Aib)DC<sub>T3</sub>RGDC<sub>T3</sub> (Aib: 2-aminoisobutyric acid)

C<sub>T3</sub>H(Nle)QC<sub>T3</sub>RGDC<sub>T3</sub> (Nle: L-norleucine)

C<sub>T3</sub>H(Nva)QC<sub>T3</sub>RGDC<sub>T3</sub> (Nva: L-norvaline)

C<sub>T3</sub>E(Nle)GC<sub>T3</sub>RGDC<sub>T3</sub>

C<sub>T3</sub>E(Aib)GC<sub>T3</sub>RGDC<sub>T3</sub>

C<sub>T3</sub>S1DC<sub>T3</sub>RGDC<sub>T3</sub>

C<sub>T3</sub>S2DC<sub>T3</sub>RGDC<sub>T3</sub>

**Table S-1.** Parameters varied in the two different competition ELISA setups (**A**), and selected setups for library screening and IC<sub>50</sub> determination (**B**).<sup>1</sup>

**A**

	Setup 1	Setup 2
Coating buffer	0.1 M Na <sub>2</sub> HPO <sub>4</sub> pH 8 + 1 mM Ca <sup>2+</sup> 0.5 mM Mg <sup>2+</sup>	PBS pH 7.4 + 1 mM Ca <sup>2+</sup> 0.5 mM Mn <sup>2+</sup>
Concentration of integrin	0.5 µg/mL	0.25 µg/mL
Blocking buffer	0.05% Tween80/PBS + 1 mM Ca <sup>2+</sup> 0.5 mM Mg <sup>2+</sup>	0.05% Tween80/PBS + 1 mM Ca <sup>2+</sup> 0.5 mM Mn <sup>2+</sup>
Washing buffer	0.05% Tween80/PBS + 1 mM Ca <sup>2+</sup> 0.5 mM Mg <sup>2+</sup>	0.05% Tween80/PBS + 1 mM Ca <sup>2+</sup> 0.5 mM Mn <sup>2+</sup>
Incubation buffer	PBS pH 7.4 + 1 mM Ca <sup>2+</sup> 0.5 mM Mg <sup>2+</sup>	PBS pH 7.4 + 1 mM Ca <sup>2+</sup> 0.5 mM Mn <sup>2+</sup>
Concentration of biotinylated peptide		0.1 µM
Concentration of bicyclic peptide (1 <sup>st</sup> screening)	1 mM (1 <sup>st</sup> generation) 5 µM (2 <sup>nd</sup> generation)	5 µM
Concentration of bicyclic peptide (2 <sup>nd</sup> screening)	10 µM (1 <sup>st</sup> generation) 2.5 µM (2 <sup>nd</sup> generation)	2.5 µM
Concentration range of IC <sub>50</sub> determination	10 µM – 0.0046 µM (3 <sup>rd</sup> generation) 30 µM – 0.014 µM (1 <sup>st</sup> and 2 <sup>nd</sup> generation)	
Strep-HRP buffer	PBS pH 7.4 + 1 mM Ca <sup>2+</sup> 0.5 mM Mg <sup>2+</sup>	PBS pH 7.4 + 1 mM Ca <sup>2+</sup> 0.5 mM Mn <sup>2+</sup>

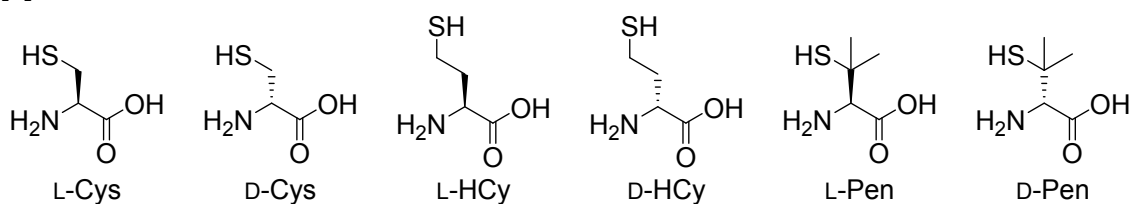
**B**

Library Generation	1 <sup>st</sup>	2 <sup>nd</sup>	3 <sup>rd</sup>
Screening	1	1	2
IC <sub>50</sub> determination	2	2	2

**Table S-2.** Inhibition values (determined using setup 1) for  $\alpha_v\beta_3$  integrin for selected bicyclic peptides (three cysteines, constrained with 1,3,5-tris[bromomethyl] benzene, T3) and their monocyclic analogues (two cysteines, constrained with 1,3-bis[bromomethyl] benzene, mT2).

				Inhibition at 10 $\mu$ M [%]		
C	Q	A	D	c	RGDc	79
C	Q	A	D	a	RGDc	32
A	Q	A	D	c	RGDc	7
C	Q	A	D	c	RGD a	0
C	H	E	Q	c	RGDc	92
C	H	E	Q	a	RGDc	16
A	H	E	Q	c	RGDc	22
C	H	E	Q	c	RGD a	28
C	W	G	D	C	RGDc	75
C	W	G	D	A	RGDc	23
A	W	G	D	C	RGDc	52
C	W	G	D	C	RGD a	8
				C	RGDc	23
				C	RGDc	57
				C	RGDc	41

**A**



**B**

$X^1$		Inhibition [%]		$X^1$		Inhibition [%]		$X^1$		Inhibition [%]	
$T_3$	$T_3$	$T_3$	$T_3$	$T_3$	$T_3$	$T_3$	$T_3$	$T_3$	$T_3$	$T_3$	$T_3$
X <sup>1</sup>	X <sup>2</sup>	10 $\mu$ M	1 $\mu$ M	X <sup>1</sup>	X <sup>2</sup>	10 $\mu$ M	1 $\mu$ M	X <sup>1</sup>	X <sup>2</sup>	10 $\mu$ M	1 $\mu$ M
Cys	Cys	88	55	Cys	Cys	80	37	Cys	Cys	<0	5
Cys	HCy	85	53	Cys	HCy	20	12	Cys	HCy	<0	<0
Cys	Pen	<0	<0	Cys	Pen	2	15	Cys	Pen	<0	<0
HCy	Cys	30	<0	HCy	Cys	62	33	HCy	Cys	<0	<0
Pen	Cys	31	8	Pen	Cys	<0	24	Pen	Cys	<0	<0
HCy	HCy	8	<0	HCy	HCy	58	31	HCy	HCy	<0	10
HCy	Pen	<0	<0	HCy	Pen	20	18	HCy	Pen	<0	<0
Pen	HCy	49	22	Pen	HCy	18	33	Pen	HCy	<0	6
Pen	Pen	<0	<0	Pen	Pen	<0	6	Pen	Pen	<0	<0

c: D-Cys

1: D-HCy

2: D-Pen

**Figure S-2.** A) Molecular drawings of L/D-cysteine (Cys) and non-natural amino acids L-homocysteine (HCy), L-penicillamine (Pen), D-homocysteine (**1**) and D-penicillamine (**2**); B) Inhibition values (using setup 2, Table S-1) for various derivatives of 2<sup>nd</sup> generation  $\alpha_v\beta_3$ -inhibitor  $C_{T_3}HWQX^2_{T_3}RGDc_{T_3}-T_3$ .



## Binding ELISA protocol for testing HPQ-streptavidin binding

Greiner cell culture plates were coated with 100  $\mu$ L 0.2% glutardialdehyde in PBS pH 7.4 coating buffer (see setup 2, **Table S-1**) at r.t. for 4 h, followed by 3x washing with 400  $\mu$ L washing buffer. Aoa-functionalized peptides were incubated overnight at 4  $^{\circ}$ C, followed by 3x washing and blocking with 150  $\mu$ L 1% I-Block<sup>TM</sup> in blocking buffer (1 h, r.t.). After another 3x washing plates were incubated with 100  $\mu$ L 1:1000 Strep-HRP in strep-HRP buffer (1 h, r.t.), followed by 4x washing and incubation with 150  $\mu$ L ABTS-substrate buffer at r.t. Absorbance was measured at 405 nm after 45 min using a Molecular Devices Spectramax M2 plate reader and corrected for background absorbance (background refers to absorbance without non-labeled peptide present). Experiments were carried out in triplicate.

**Table S-3.** Binding ELISA studies to measure streptavidin-affinity of selected 2<sup>nd</sup> generation  $\alpha_v\beta_3$ -binding bicyclic peptides and control sequences (monocyclic HPQ and RGD, and biotinylated linear GRGDS). Absorbance values shown as mean of triplicate including standard deviation.

Peptide	Absorbance (405 nm)		
	100 $\mu$ M	10 $\mu$ M	1 $\mu$ M
Aoa [PEG] C H P Q c R G D c	-0.01 $\pm$ 0.07	0.01 $\pm$ 0.03	0.02 $\pm$ 0.06
C H P Q c R G D c [PEG] K(Aoa)	0.00 $\pm$ 0.04	0.00 $\pm$ 0.04	0.02 $\pm$ 0.03
Aoa [PEG] C H N Q c R G D c	0.03 $\pm$ 0.03	0.02 $\pm$ 0.04	0.01 $\pm$ 0.04
C H N Q c R G D c [PEG] K(Aoa)	-0.02 $\pm$ 0.04	0.01 $\pm$ 0.04	0.00 $\pm$ 0.04
Aoa [PEG] C H F Q c R G D c	0.01 $\pm$ 0.04	0.01 $\pm$ 0.04	0.03 $\pm$ 0.03
C H F Q c R G D c [PEG] K(Aoa)	0.13 $\pm$ 0.08	0.00 $\pm$ 0.03	0.03 $\pm$ 0.05
Aoa [PEG] C H P Q c	0.39 $\pm$ 0.08	-0.02 $\pm$ 0.06	0.03 $\pm$ 0.04
Aoa [PEG] c R G D c	0.04 $\pm$ 0.05	-0.01 $\pm$ 0.06	0.02 $\pm$ 0.03
Biotin [PEG] G R G D S P [PEG] K(Aoa)	3.80 $\pm$ 0.03	3.14 $\pm$ 0.09	0.65 $\pm$ 0.07

## SPFS observation of affinity binding kinetics

**Optical system.** An optical system combining surface plasmon resonance (SPR) and surface plasmon enhanced fluorescence spectroscopy (SPFS) was used for direct investigation of affinity interaction of selected peptides and integrins. The Kretschmann configuration of attenuated total reflection method (**Figure S-3**) was used for the resonant excitation and interrogation of surface plasmons as described before in more detail.<sup>2</sup> Briefly, a laser beam (633 nm) was coupled to a high refractive index glass prism and glass substrate coated with SPR-active thin gold film, and optically matched to its base. The beam was made incident at the angle of incidence that was tuned close to  $\theta_{\text{SPR}}$  where surface plasmons are resonantly excited at the outer interface of gold surface. A flow cell was clamped against the gold sensor surface in order to flow liquid samples with a flow rate of 40  $\mu$ L/min. The reflected beam intensity was measured with a lockin amplifier (EG&G, USA) in order to track changes in SPR signal. The fluorescence signal excited via surface plasmons that was propagating from the sensor surface through the flow cell was collected by a lens with a numerical aperture about NA=2, and detected by a photomultiplier (H6240-01, Hamamatsu, Japan) connected to a counter (53131A, Agilent, USA). The intensity of the excitation beam irradiating area on the sensor chip of about 1 mm<sup>2</sup> was reduced to 30-60  $\mu$ W in order to reduce bleaching of Cy5 excited by the enhanced field intensity of surface plasmons. The fluorescence light emitted by Cy5 at wavelength of about 670 nm was spectrally separated from the excitation light (633 nm) by using a set of laser notch filters (XNF-632.8-25.0M, CVI Melles Griot, USA) and fluorescence band pass filters (670FS10-25, Andover Corporation Optical Filter, USA).

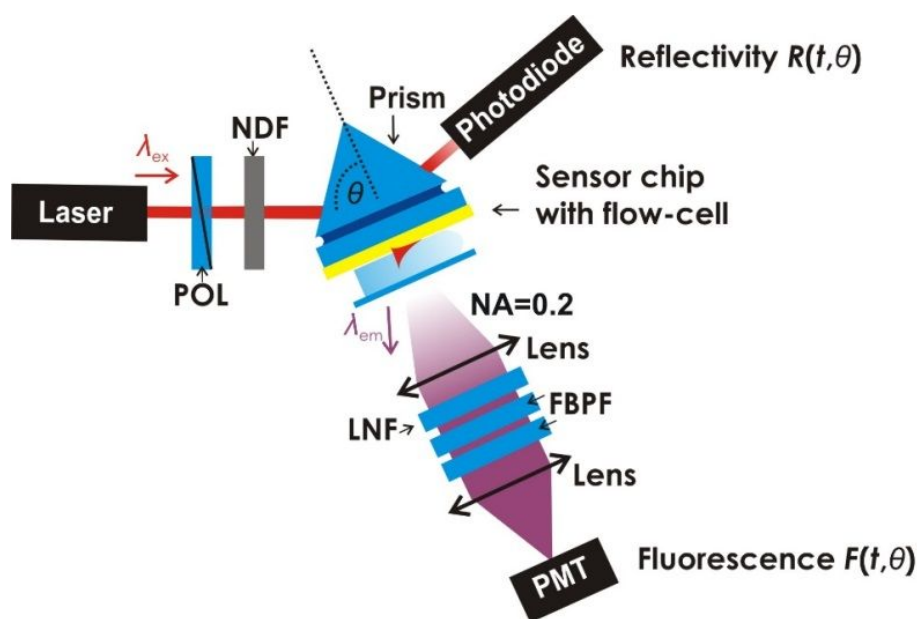


**Figure S-3.** Schematics of the optical instrument used for the surface plasmon resonance (SPR) and surface plasmon-enhanced fluorescence spectroscopy (SPFS) measurements with polarizer (POL), neutral density filter (NDF), laser notch filter (LNF), fluorescence bandpass filter (FBPF).

**Sensor chip preparation.** Sensor chips were prepared on BK7 glass substrates which were subsequently coated with 2 nm chromium and 50 nm gold films by thermal vacuum evaporation (Model HHV FL400, HHV Ltd, UK). Onto the gold surface integrin  $\alpha_v\beta_3$  was attached by using two surface architectures (**Figure S4**). The 2D architecture relied on a mixed self-assembled monolayer (SAM) that was formed by immersing the gold surface in a 1 mM ethanolic solution with a dithiol-PEG6-COOH and dithiol-PEG3, mixed at molar ratio of 1:9. After overnight incubation, the gold surface was rinsed with ethanol, dried in a stream of air, and stored under argon atmosphere.

**Immobilization of ligand.** The immobilization of integrin  $\alpha_v\beta_3$  was performed *in situ* by amine coupling according to standard protocols. The surface reactions were monitored by SPR (Supporting Information, **Figure S-4A**). First, PBS and acetate buffer (pH=4) were flowed over the gold surface to reach a stable baseline SPR signal. Then, the sensor surface carrying carboxylic acid groups on mixed thiol SAM layer was reacted with 75 mg/mL EDC and 21 mg/mL NHS dissolved in water for 15 minutes. Recombinant human integrins (c: 10  $\mu\text{g/mL}$ ), dissolved in acetate buffer (pH=4), was flowed over the activated sensor surface for 90 minutes to immobilize the integrin molecules via their amine groups to activated carboxylic groups. Finally, the remaining active ester groups were inactivated with 1M ethanolamine/ $\text{H}_2\text{O}$  for 15 minutes.

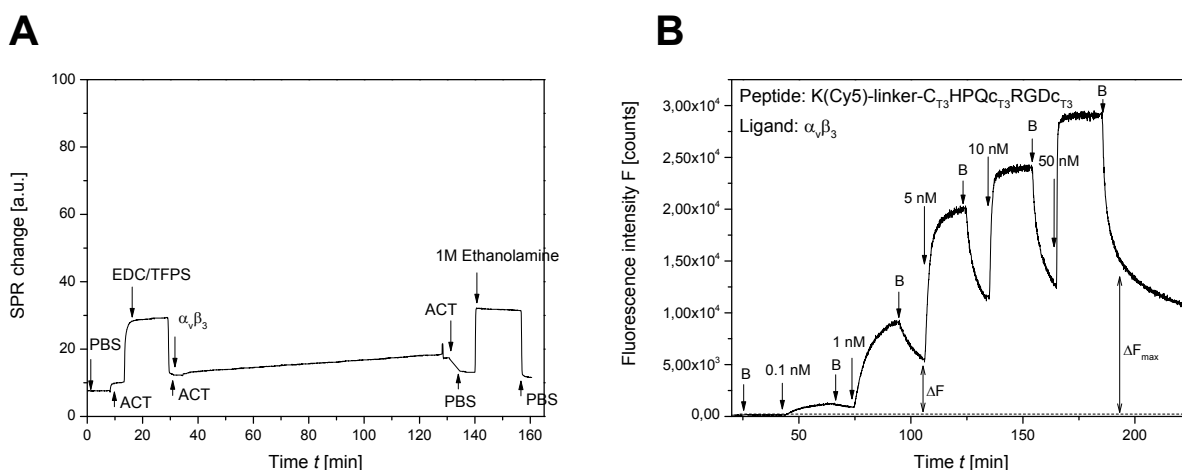


**Figure S-4.** Example of A) SPR sensorgram showing covalent immobilization of integrin  $\alpha_v\beta_3$  ligand into a 3D hydrogel binding matrix, and B) fluorescence signal kinetics acquired upon titration of peptide Cy5-functionalized  $C_{T3}HPQc_{T3}RGDc_{T3}-T3$ .

## NMR

All NMR spectra were collected on a Bruker Avance III 500 MHz spectrometer equipped with a Prodigy BB cryoprobe at 298 K. Samples were prepared by dissolving the compounds in  $D_2O$  and adding a small amount of DSS for internal referencing.  $^1H$ -NMR spectra were acquired using 32 scans and a relaxation delay of 3 s. 2D COSYDQF spectra with presaturation were acquired with a 6000 Hz spectral width in both dimensions using 2048 x 512 points and processed using 2048 x 512 points, 4 scans per increment and a relaxation delay of 1.5 seconds. 2D gradient TOCSY spectra with presaturation were acquired with a 5000 Hz spectral width in both dimensions using 1024 x 512 points and processed using 1024 x 1024 points, 8 scans per increment, a relaxation delay of 2 seconds and a TOCSY mix time of 100 ms. A TOCSY spinlock field of 8.3 kHz was applied. 2D gradient ROESY spectra were acquired with a 6000 Hz spectral width in both dimensions using 4096 x 512 points and processed using 4096 x 512 points, 24 scans per increment, a relaxation delay of 1.5 seconds and a ROESY mix time of 0.3 s. A ROESY spinlock field of 5 kHz was applied. Multiplicity-edited  $^1H$ - $^{13}C$  HSQC spectra were acquired using a 6010 Hz spectral width in F2 and 18868 Hz spectral width in F1 using 1024 x 512 points and processed to 1024 x 1024 points, 2 scans per increment, relaxation delay of 1.5 seconds and 1-bond  $J_{CH} = 145$  Hz.  $^1H$ - $^{13}C$  HMBC spectra were acquired using a 5319.1 Hz spectral width in F2 and 22321.4 Hz spectral width in F1 using 2048 x 512 points and processed to 2048 x 2048 points, 4 scans per increment, relaxation delay of 1.5 seconds and a long-range  $J_{CH} = 8$  Hz.

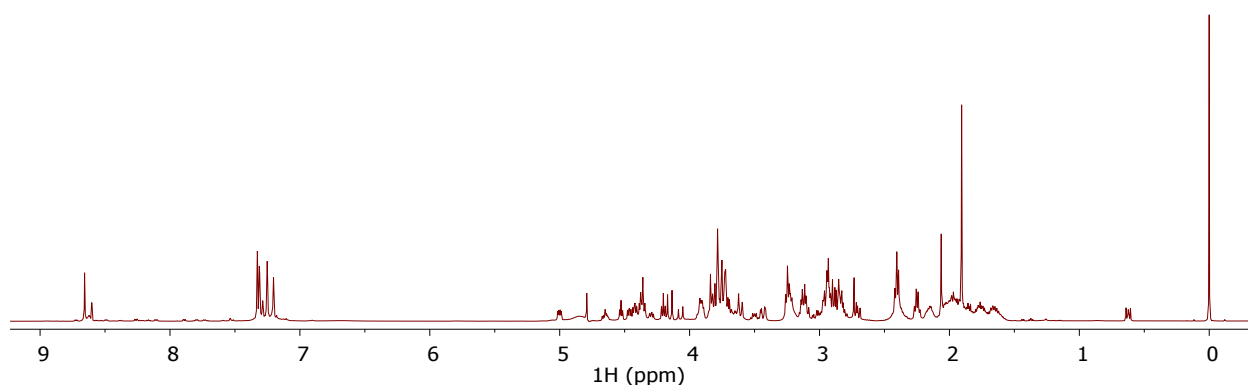


**Figure S-5.**  $^1\text{H}$  spectrum of  $\text{C}_{\text{T}3}\text{HPQC}_{\text{T}3}\text{RGDC}_{\text{T}3}$  acquired with composite pulse presaturation. The spectrum was referenced to the trimethylsilyl peaks of the internal standard of DSS at 0.0 ppm. NS = 32, D1 = 3 s, AQ = 3.3 s.

## References

- (1) Bernhagen, D.; De Laporte, L.; Timmerman, P. High-Affinity RGD-Knottin Peptide as a New Tool for Rapid Evaluation of the Binding Strength of Unlabeled RGD-Peptides to  $\alpha_v\beta_3$ ,  $\alpha_v\beta_5$ , and  $\alpha_5\beta_1$  Integrin Receptors. *Anal. Chem.* **2017**, *89*, 5991–5997.
- (2) Hageneder, S.; Bauch, M.; Dostalek, J. Plasmonically amplified bioassay – total internal reflection fluorescence vs. epifluorescence geometry. *Talanta* **2016**, *156–157*, 225–231.
- (3) Wang, Y.; Huang, C. J.; Jonas, U.; Wei, T.; Dostalek, J.; Knoll, W. Biosensor based on Hydrogel Optical Waveguide Spectroscopy. *Biosens. Bioelectron.* **2010**, *25*, 1663–1668.

# High-Affinity $\alpha_5\beta_1$ -Integrin-Selective Bicyclic RGD Peptides Identified via Screening of Designed Random Libraries

Dominik Bernhagen,<sup>†</sup> Vanessa Jungbluth,<sup>‡</sup> Nestor Gisbert Quilis,<sup>‡</sup> Jakob Dostalek,<sup>‡</sup> Paul B. White,<sup>¶</sup> Kees Jalink,<sup>⊥</sup> and Peter Timmerman<sup>\*,†,§,||</sup>

<sup>†</sup>Pepscan Therapeutics, Zuidersluisweg 2, 8243 RC Lelystad, the Netherlands

<sup>‡</sup>Biosensor Technologies, AIT Austrian Institute of Technology GmbH, Konrad-Lorenz-Straße 24, 3430 Tulln, Austria

<sup>¶</sup>Institute for Molecules and Materials, Radboud University, Heyendaalseweg 135, 6525 AJ Nijmegen, the Netherlands

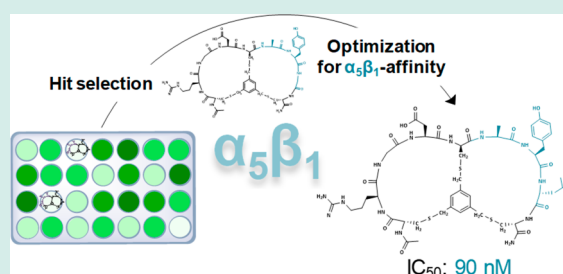
<sup>⊥</sup>The Netherlands Cancer Institute, Plesmanlaan 21, 1066 CX Amsterdam, the Netherlands

<sup>§</sup>Van't Hoff Institute for Molecular Sciences, University of Amsterdam, Science Park 904, 1098 XH Amsterdam, the Netherlands

## Supporting Information

**ABSTRACT:** We report the identification of high-affinity and selectivity integrin  $\alpha_5\beta_1$ -binding bicyclic peptides via “designed random libraries”, that is, the screening of libraries comprising the universal integrin-binding sequence Arg-Gly-Asp (RGD) in the first loop in combination with a randomized sequence (XXX) in the second loop. Screening of first-generation libraries for  $\alpha_5\beta_1$ -binding peptides yielded a triple-digit nanomolar bicyclic  $\alpha_5\beta_1$ -binder ( $C_{T_3}RGDC_{T_3}AYGC_{T_3}$ ,  $IC_{50} = 406$  nM). Next-generation libraries were designed by partially varying the structure of the strongest first-generation lead inhibitor and screened for improved affinities and selectivities for this receptor. In this way, we identified three high-affinity  $\alpha_5\beta_1$ -binders ( $C_{T_3}RGDC_{T_3}AYJC_{T_3}$ ,  $J = D\text{-Leu}$ ,  $IC_{50} = 90$  nM;  $C_{T_3}RGDC_{T_3}AYaC_{T_3}$ ,  $IC_{50} = 156$  nM;  $C_{T_3}RGDC_{T_3}AWGC_{T_3}$ ,  $IC_{50} = 173$  nM), of which one even showed a higher  $\alpha_5\beta_1$ -affinity than the 32 amino acid benchmark peptide knottin-RGD ( $IC_{50} = 114$  nM). Affinity for  $\alpha_5\beta_1$ -integrin was confirmed by SPFS analysis showing a  $K_d$  of 4.1 nM for Cy5-labeled RGD-bicycle  $C_{T_3}RGDC_{T_3}AYJC_{T_3}$  ( $J = D\text{-Leu}$ ) and a somewhat higher  $K_d$  (9.0 nM) for Cy5-labeled knottin-RGD. The  $\alpha_5\beta_1$ -bicycles, for example,  $C_{T_3}RGDC_{T_3}AYJC_{T_3}$  ( $J = D\text{-Leu}$ ), showed excellent selectivities over  $\alpha_v\beta_5$  ( $IC_{50}$  ratio  $\alpha_5\beta_1/\alpha_v\beta_5$  between <0.009 and 0.039) and acceptable selectivities over  $\alpha_v\beta_3$  ( $IC_{50}$  ratios  $\alpha_5\beta_1/\alpha_v\beta_3$  between 0.090 and 0.157). In vitro staining of adipose-derived stem cells with Cy5-labeled peptides using confocal microscopy revealed strong binding of the  $\alpha_5\beta_1$ -selective bicycle  $C_{T_3}RGDC_{T_3}AWGC_{T_3}$  to integrins in their natural environment, illustrating the high potential of these RGD bicycles as markers for  $\alpha_5\beta_1$ -integrin expression.

**KEYWORDS:** RGD, integrin, peptide–protein interaction, ELISA, bicyclic peptide, library screening, SPFS



## INTRODUCTION

Integrins, a group of 24 different heterodimeric transmembrane proteins,<sup>1,2</sup> are involved in many cellular processes, such as signaling, proliferation, migration, and differentiation.<sup>3,4</sup> Integrin expression is a dynamic process that depends on the microenvironment and developmental age of cells.<sup>1</sup> For example, epidermal and neural stem cells solely overexpress the  $\beta_1$ -subunit, while adipose-tissue-derived stem cells overexpress the heterodimeric  $\alpha_5\beta_1$  in undifferentiated state, as well as during chondrogenic differentiation.<sup>5</sup>

High levels of  $\alpha_5\beta_1$ -integrin expression increase the invasiveness of breast cancer cells into 3D collagen fiber matrices by 3-fold compared to cells with low levels of  $\alpha_5\beta_1$  expression.<sup>6</sup> Integrins also exhibit extensive crosstalk among each other.<sup>7</sup> For example, integrin  $\alpha_3\beta_1$  is a regulator of angiogenesis and was furthermore reported to control integrin  $\alpha_v\beta_3$  expression during in vitro migration and in vivo angiogenesis.<sup>8</sup> Moreover,  $\alpha_5\beta_1$  efficiently mediates fibronectin fibrillogenesis<sup>9</sup> and also binds osteopontin, fibrillin, and

thrombospondin.<sup>10</sup> Several high-affinity  $\alpha_5\beta_1$ -integrin binders not displaying any selectivity toward other integrins have been reported, such as knottin-RGD ( $\alpha_v\beta_3/\alpha_v\beta_5/\alpha_5\beta_1$ -binder)<sup>11–13</sup> or echistatin (binds  $\alpha_v\beta_3$ ,  $\alpha_v\beta_5$ ,  $\alpha_v\beta_6$ ,  $\alpha_v\beta_8$ ,  $\alpha_5\beta_1$ , and  $\alpha_{IIb}\beta_3$ ).<sup>14,15</sup> Ligands with improved  $\alpha_5\beta_1$  selectivity, such as the 5-mer PHSCN (ATN-161) that proved to inhibit  $\alpha_5\beta_1$  in immunoassays<sup>15</sup> and in vivo,<sup>16,17</sup> recently raised considerable interest as potential cancer therapeutics. Also, high-affinity peptidomimetic ligands with  $\alpha_5\beta_1$  selectivity were reported by Heckmann et al. as potential antiangiogenic cancer therapeutics.<sup>18</sup> When covalently linked to a gold surface, these ligands showed a much higher level of cell adhesion to  $\alpha_5\beta_1$ -transfected fibroblasts as compared to  $\alpha_v\beta_3$ -transfected cells.<sup>19</sup> However, these peptidomimetics require complex multistep syntheses (in particular the building blocks), which

Received: April 18, 2019

Revised: June 5, 2019

Published: July 3, 2019

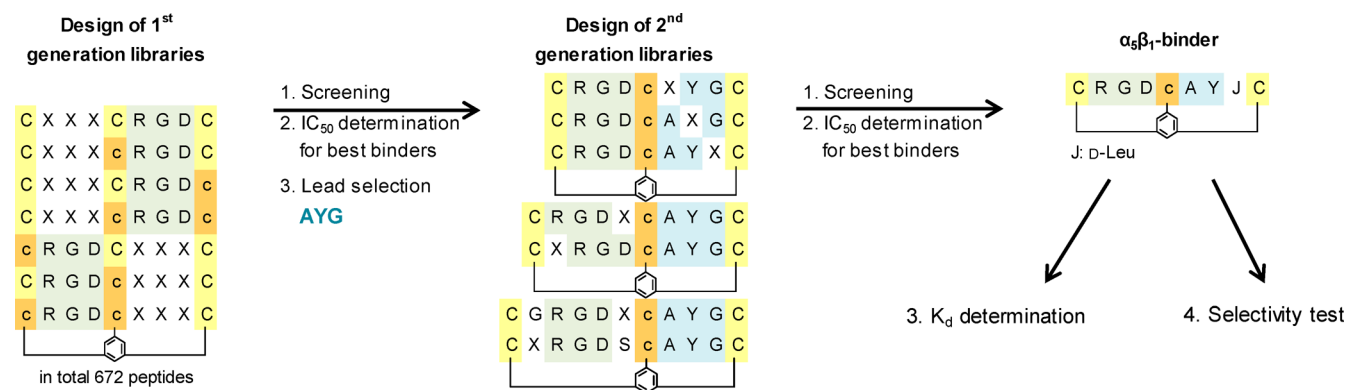


**Figure 1.** Methodology for the structural design, affinity selection, identification, and characterization of high affinity bicyclic peptides to integrin  $\alpha_5\beta_1$ .

does (not yet) allow for economically feasible bulk production. There is a strong need for novel peptidic  $\alpha_5\beta_1$ -integrin binders that could circumvent this problem. Very recently, Kapp et al. reported *N*-methylated, cyclic *iso*DGR peptides with high  $\alpha_5\beta_1$ -selectivity over integrins  $\alpha_v\beta_6$  and  $\alpha_v\beta_3$ .<sup>20</sup> Our group recently described strong and selective  $\alpha_v\beta_3$ -binders obtained via a “designed random library” based approach involving medium-throughput screening of libraries of bicyclic peptides comprising both an RGD-loop combined with a second randomized loop.<sup>21,22</sup> Bicyclic CLIPS peptides<sup>23</sup> represent a group of target-specific and proteolytically stable compounds that recently showed great potential for therapeutic drug development.<sup>24–26</sup> For example, the bicyclic peptide AC<sub>T3</sub>SDRFRNC<sub>T3</sub>PADEALC<sub>T3</sub>G (T<sub>3</sub> = scaffold derived from 1,3,5-trisubstituted benzene) was identified as a nanomolar plasma kallikrein-inhibitor ( $K_i = 1.5$  nM) consisting of a consensus binding motif (SDRFRN) in combination with an optimized supporting sequence (PADEAL).<sup>27</sup>

The excellent integrin  $\alpha_v\beta_3$ -affinities and selectivities observed with bicyclic RGD-peptides<sup>21</sup> prompted us to test the same libraries also for binding to the  $\alpha_5\beta_1$  integrin receptor. Here, we describe the results of those screenings together with the structural optimization and characterization of high-affinity bicyclic RGD-binders to integrin  $\alpha_5\beta_1$ .

## RESULTS AND DISCUSSION

**Design of RGD Peptide Libraries.** We designed linear peptide libraries consisting of two separate binding motifs, surrounded by three cysteines. The first motif is the well-known RGD sequence that should provide the basic integrin affinity, while the second motif contains a random-diversity sequence that is intended to provide integrin-selectivity. The motifs are surrounded by cysteines that allow for the double CLIPS-cyclization via 1,3,5-tris(bromomethyl) benzene (T<sub>3</sub>, see Figure S6A), and hence the formation of a bicyclic peptide comprising two different loops is achieved. According to the design of high-affinity monocyclic RGD-peptides, as reported by Dechantsreiter et al.,<sup>28</sup> we synthesized bicyclic peptide libraries containing two “5-mer” loops, that is, RGD and XXX, each enclosed by L- or D-cysteines. Seven libraries, each containing 96 peptides, were converted to bicyclic peptides via T<sub>3</sub> (C<sub>T3</sub>XXXC<sub>T3</sub>RGDC<sub>T3</sub>, C<sub>T3</sub>XXXc<sub>T3</sub>RGDC<sub>T3</sub>, C<sub>T3</sub>XXXC<sub>T3</sub>RGDc<sub>T3</sub>, and C<sub>T3</sub>XXXc<sub>T3</sub>RGDc<sub>T3</sub>, c<sub>T3</sub>RGDC<sub>T3</sub>XXXC<sub>T3</sub>, C<sub>T3</sub>RGDc<sub>T3</sub>XXXC<sub>T3</sub>, c<sub>T3</sub>RGDc<sub>T3</sub>XXXc<sub>T3</sub>, Figure 1). All 34 amino acid building blocks that were applied in this study are listed in the

Supporting Information (Table S-1). For more detailed information on the design, we kindly refer to ref 21.

**General Procedure for RGD Bicycle Library Screening.** We screened the bicyclic RGD-peptide libraries for integrin-binding using our recently developed and published protocol for a competition ELISA (for experimental conditions, see Table S-2).<sup>22</sup>

All 672 bicyclic RGD-peptides were screened for inhibition of biotinylated knottin-RGD binding to integrin  $\alpha_5\beta_1$  and sorted for the highest degree of inhibition. A second screening with the best hits from the first screening was performed at 2.5  $\mu$ M to further fine tune the differences in integrin affinities. Following screening of the various crude bicycle peptide libraries, the best binding bicycles were resynthesized and HPLC-purified, followed by determination of their IC<sub>50</sub> values.

**Screening Data for  $\alpha_5\beta_1$ -Binding Bicycles.** We screened the first-generation bicycle libraries for high-affinity binding to integrin  $\alpha_5\beta_1$ . Only nine out of 672 peptides (1.3%) showed >70% inhibition, and all of these peptides comprised the RGD-sequence in the left loop, enclosed by an N-terminal L-Cys and a central D-Cys. Still 4% of the peptides (29) showed >50% inhibition, whereas 80% (540 peptides) showed inhibition levels <30%. Two bicycles, that is, C<sub>T3</sub>RGDc<sub>T3</sub>AYGC<sub>T3</sub> (100%) and C<sub>T3</sub>RGDc<sub>T3</sub>NWGC<sub>T3</sub> (91%) showed >90% inhibition of (biotinylated) knottin-RGD binding after the second screening. For C<sub>T3</sub>RGDc<sub>T3</sub>AYGC<sub>T3</sub> an IC<sub>50</sub> value of 406 nM was determined, whereas bicycle C<sub>T3</sub>RGDc<sub>T3</sub>NWGC<sub>T3</sub> exhibited an IC<sub>50</sub> > 2  $\mu$ M (Figure 2). The IC<sub>50</sub> value for C<sub>T3</sub>RGDc<sub>T3</sub>AYGC<sub>T3</sub> was much lower than observed for *cyclo*-[KRGDf], cilengitide (each >10  $\mu$ M), and slightly higher than for knottin-RGD (114 nM). The unexpected discrepancy between inhibition values of C<sub>T3</sub>RGDc<sub>T3</sub>NWGC<sub>T3</sub> in the screening (91% at 10  $\mu$ M) and IC<sub>50</sub> (> 2  $\mu$ M) may be explained by the fact that “polymeric” impurities in the crude peptide sample create an “apparent” inhibition value that is much lower than the IC<sub>50</sub> value as determined using the purified bicycle peptide. On the basis of the sequence of C<sub>T3</sub>RGDc<sub>T3</sub>AYGC<sub>T3</sub>, we designed a set of second generation libraries, including (1) a full position-replacement analysis of the AYG-loop (i.e., C<sub>T3</sub>RGDc<sub>T3</sub>XYGC<sub>T3</sub>, C<sub>T3</sub>RGDc<sub>T3</sub>AXGC<sub>T3</sub>, C<sub>T3</sub>RGDc<sub>T3</sub>AYXC<sub>T3</sub>), (2) the RGD-loop extended by an additional amino acid “X”, while keeping the “AYG”-loop constant (i.e., C<sub>T3</sub>RGDXc<sub>T3</sub>AYGC<sub>T3</sub>, C<sub>T3</sub>XRGDc<sub>T3</sub>AYGC<sub>T3</sub>), and (3) the extended 5-mer loops “GRGDx” and “XRGDS” in combination with a constant “AYG”-loop (i.e.,

Peptide		IC <sub>50</sub> [nM]
<b>1<sup>st</sup> generation</b>		
C <sub>T3</sub>	R G D C <sub>T3</sub> A Y G C <sub>T3</sub>	406 ± 63
C <sub>T3</sub>	R G D C <sub>T3</sub> N W G C <sub>T3</sub>	2084 ± 499
<b>2<sup>nd</sup> generation</b>		
C <sub>T3</sub>	R G D C <sub>T3</sub> V Y G C <sub>T3</sub>	211 ± 33
C <sub>T3</sub>	R G D C <sub>T3</sub> A Y J C <sub>T3</sub>	90 ± 15
C <sub>T3</sub>	R G D C <sub>T3</sub> A W G C <sub>T3</sub>	173 ± 35
C <sub>T3</sub>	R G D C <sub>T3</sub> A Y a C <sub>T3</sub>	156 ± 23
C <sub>T3</sub>	R G D C <sub>T3</sub> A Y i C <sub>T3</sub>	395 ± 153
C <sub>T3</sub>	R G D C <sub>T3</sub> I Y G C <sub>T3</sub>	386 ± 82
	knottin-RGD	114 ± 8
	<i>cyclo</i> -[KRGDf]	>10,000
	cilengitide	>10,000
	GRGDS	>10,000

J: D-Leu

**Figure 2.** IC<sub>50</sub> values of 1<sup>st</sup> and 2<sup>nd</sup> generation bicyclic integrin  $\alpha_5\beta_1$ -binders.

C<sub>T3</sub>GRGDxc<sub>T3</sub>AYGC<sub>T3</sub>, C<sub>T3</sub>XRGDS<sub>cT3</sub>AYGC<sub>T3</sub>, Figure 1). We screened all 196 second generation bicycles at 5  $\mu$ M and identified 18 bicycles (9%) with inhibition rates >70%. In a second screening of the best 20 hits at 2.5  $\mu$ M 15 bicyclic peptides (75%) showed >70% inhibition and seven bicycles (35%) displayed >85% inhibition. Also, eight of the 20 bicycles exhibited higher inhibition values than C<sub>T3</sub>RGDC<sub>T3</sub>AYGC<sub>T3</sub> itself (82% inhibition), for example, C<sub>T3</sub>RGDC<sub>T3</sub>VYGC<sub>T3</sub> (90% inhibition) or C<sub>T3</sub>RGDC<sub>T3</sub>AYaC<sub>T3</sub> (87% inhibition). Remarkably, the IC<sub>50</sub> of the best inhibitor C<sub>T3</sub>RGDC<sub>T3</sub>AYJC<sub>T3</sub> (90 nM, J: D-Leu, Figure 2) was even lower than that for knottin-RGD peptide (114 nM) and showed a 4-fold increased inhibition as compared to the first-generation binder C<sub>T3</sub>RGDC<sub>T3</sub>AYGC<sub>T3</sub> (406 nM). The other five peptides all showed IC<sub>50</sub> values below 400 nM, for example, C<sub>T3</sub>RGDC<sub>T3</sub>AYaC<sub>T3</sub> (IC<sub>50</sub> 156 nM). Hence, a change from “G” to “a” (i.e., D-Ala) at position 8, which is equivalent to the

introduction of a single methyl group at the  $\alpha$ -carbon, led to ~2.5-fold improved affinity for integrin  $\alpha_5\beta_1$ . For bicycles C<sub>T3</sub>RGDC<sub>T3</sub>AWGC<sub>T3</sub> and C<sub>T3</sub>RGDC<sub>T3</sub>VYGC<sub>T3</sub> comparable values were obtained (i.e. 173 and 211 nM, respectively), whereas the IC<sub>50</sub>'s for bicycles C<sub>T3</sub>RGDC<sub>T3</sub>AYiC<sub>T3</sub> (395 nM) and C<sub>T3</sub>RGDC<sub>T3</sub>IYGC<sub>T3</sub> (386 nM) were almost identical to that of the lead.

**Ala-Replacement Study for Selected  $\alpha_5\beta_1$  Binders.** To prove the unique binding affinity of the bicycles, we synthesized peptide libraries based on the sequences of the three highest-affinity  $\alpha_5\beta_1$ -binding bicycles, in which each amino acid was replaced by alanine, followed by CLIPS cyclization with mT2 (see Figure S6A) to give the corresponding monocyclic peptides (for all Cys/Ala replacements), or with T3 to give the corresponding bicyclic peptides (for all noncysteine replacements). Subsequently, we analyzed the libraries for the inhibition of  $\alpha_5\beta_1$ -binding in competition ELISA at 1  $\mu$ M. The inhibitory values of the three best  $\alpha_5\beta_1$ -binding bicycles decreased massively when single amino acids in the loops were substituted by Ala (Figure 3). In general, Ala-replacements in the RGD loops gave the strongest effects. For example, replacing R or G in bicycle C<sub>T3</sub>RGDC<sub>T3</sub>AYJC<sub>T3</sub> (Figure 3A), R or D in bicycle C<sub>T3</sub>RGDC<sub>T3</sub>AYaC<sub>T3</sub> (Figure 3B), and R, G, or D in bicycle C<sub>T3</sub>RGDC<sub>T3</sub>AWGC<sub>T3</sub> (Figure 3C) led to a complete loss of  $\alpha_5\beta_1$ -affinity (% inhibition at 1  $\mu$ M  $\leq$ ). Similarly, Ala-replacement of the cysteines (and hence loss of the bicyclic structure) also led to a massive decrease in binding strength. For example, substitution of either the N-terminal L-cysteine or the middle D-cysteine (“opening” of RGD-loop) led to a complete loss of  $\alpha_5\beta_1$ -affinity for bicycles C<sub>T3</sub>RGDC<sub>T3</sub>AYaC<sub>T3</sub> and C<sub>T3</sub>RGDC<sub>T3</sub>AWGC<sub>T3</sub> (% inhibition each <0). Also, when replacing the C-terminal L-cysteine, the inhibition values decreased significantly (e.g., to 26% for bicycle C<sub>T3</sub>RGDC<sub>T3</sub>AYJC<sub>T3</sub> or to 45% for C<sub>T3</sub>RGDC<sub>T3</sub>AWGC<sub>T3</sub>), albeit to a much lower extent than for the Ala-replacement of the amino acids in the RGD loop.

Finally, Ala-replacement of the non-RGD loop also resulted in significant losses of  $\alpha_5\beta_1$ -affinity, albeit to a somewhat lower extent. While the Y/A-replacement in C<sub>T3</sub>RGDC<sub>T3</sub>AYJC<sub>T3</sub> showed a complete loss of inhibition (from 73% to <0%), Y/A-substitution in C<sub>T3</sub>RGDC<sub>T3</sub>AYaC<sub>T3</sub> had a much reduced effect (inhibition from 60% to only 27%). In contrast to this, the J/A or G/A-replacement at the third position of the non-

Peptide		Inhibition at 1 $\mu$ M [%]
C <sub>T3</sub>	R G D C <sub>T3</sub> A Y J C <sub>T3</sub>	73
A	R G D C <sub>mT2</sub> A Y J C <sub>mT2</sub>	8
C <sub>T3</sub>	A G D C <sub>T3</sub> A Y J C <sub>T3</sub>	<0
C <sub>T3</sub>	R A D C <sub>T3</sub> A Y J C <sub>T3</sub>	<0
C <sub>T3</sub>	R G A C <sub>T3</sub> A Y J C <sub>T3</sub>	20
C <sub>mT2</sub>	R G D a A Y J C <sub>mT2</sub>	<0
C <sub>T3</sub>	R G D C <sub>T3</sub> A A J C <sub>T3</sub>	33
C <sub>T3</sub>	R G D C <sub>T3</sub> A Y A C <sub>T3</sub>	<0
C <sub>mT2</sub>	R G D C <sub>mT2</sub> A Y J A	26

J: D-Leu

Peptide		Inhibition at 1 $\mu$ M [%]
C <sub>T3</sub>	R G D C <sub>T3</sub> A Y a C <sub>T3</sub>	60
A	R G D C <sub>mT2</sub> A Y a C <sub>mT2</sub>	<0
C <sub>T3</sub>	A G D C <sub>T3</sub> A Y a C <sub>T3</sub>	<0
C <sub>T3</sub>	R A D C <sub>T3</sub> A Y a C <sub>T3</sub>	12
C <sub>T3</sub>	R G A C <sub>T3</sub> A Y a C <sub>T3</sub>	<0
C <sub>mT2</sub>	R G D a A Y a C <sub>mT2</sub>	<0
C <sub>T3</sub>	R G D C <sub>T3</sub> A A a C <sub>T3</sub>	27
C <sub>T3</sub>	R G D C <sub>T3</sub> A Y A C <sub>T3</sub>	<0
C <sub>mT2</sub>	R G D C <sub>mT2</sub> A Y a A	15

Peptide		Inhibition at 1 $\mu$ M [%]
C <sub>T3</sub>	R G D C <sub>T3</sub> A W G C <sub>T3</sub>	82
A	R G D C <sub>mT2</sub> A W G C <sub>mT2</sub>	<0
C <sub>T3</sub>	A G D C <sub>T3</sub> A W G C <sub>T3</sub>	<0
C <sub>T3</sub>	R A D C <sub>T3</sub> A W G C <sub>T3</sub>	<0
C <sub>T3</sub>	R G A C <sub>T3</sub> A W G C <sub>T3</sub>	1
C <sub>mT2</sub>	R G D a A W G C <sub>mT2</sub>	<0
C <sub>T3</sub>	R G D C <sub>T3</sub> A A G C <sub>T3</sub>	27
C <sub>T3</sub>	R G D C <sub>T3</sub> A W A C <sub>T3</sub>	6
C <sub>mT2</sub>	R G D C <sub>mT2</sub> A W G A	45

**Figure 3.** Ala-replacement study for  $\alpha_5\beta_1$ -binding bicycles (A) C<sub>T3</sub>RGDC<sub>T3</sub>AYJC<sub>T3</sub>, (B) C<sub>T3</sub>RGDC<sub>T3</sub>AYaC<sub>T3</sub>, and (C) C<sub>T3</sub>RGDC<sub>T3</sub>AWGC<sub>T3</sub>. When cysteines were replaced by L- or D-Ala (A/a), peptides were cyclized using the bivalent scaffold mT2. For all other (noncysteine) replacements, peptides were cyclized using scaffold T3.

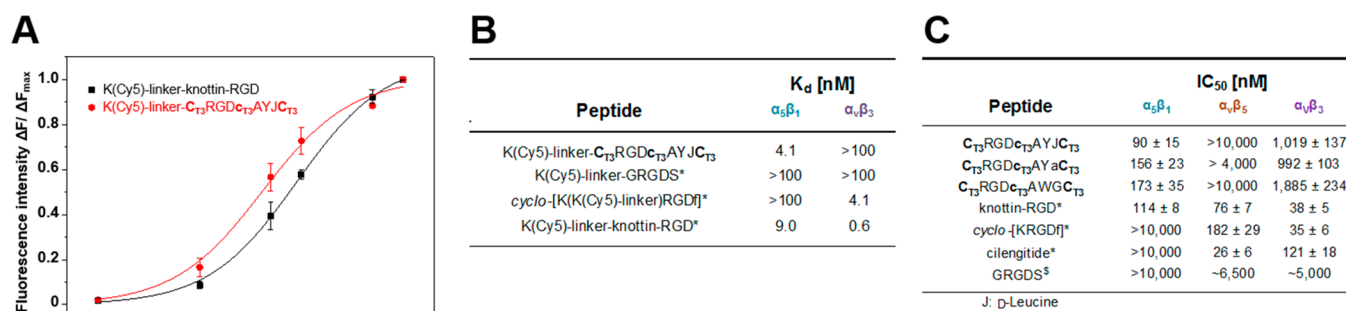


**Figure 4.** (A) Concentration-dependent, normalized fluorescence signals for K(Cy5)-linker-C<sub>T3</sub>RGDC<sub>T3</sub>AYJC<sub>T3</sub> and K(Cy5)-linker-knottin-RGD binding to integrin  $\alpha_5\beta_1$  (triplicate experiment). (B) Overview of equilibrium dissociation constants ( $K_d$ ) as determined by SPFS. Values for  $\alpha_5\beta_1$  were obtained by applying the 3D-hydrogel surface architecture. Values for  $\alpha_v\beta_3$  were obtained by applying the thiol SAM surface architecture; (C) IC<sub>50</sub> values for three structurally fully optimized bicycles, knottin-RGD and *cyclo*-[KRGDf]. Each concentration was tested in triplicate. IC<sub>50</sub> values were calculated via nonlinear regression analysis. \*<sup>§</sup>These values were determined previously (\* → ref 21, § → ref 22).

RGD loop in bicycles C<sub>T3</sub>RGDC<sub>T3</sub>AYJC<sub>T3</sub> and C<sub>T3</sub>RGDC<sub>T3</sub>AWGC<sub>T3</sub> also led to a complete loss of integrin affinity. Much to our surprise, a simple change from D- to L-alanine at the third position of the non-RGD loop in bicycle C<sub>T3</sub>RGDC<sub>T3</sub>AYaC<sub>T3</sub> also resulted in a total loss of  $\alpha_5\beta_1$ -binding activity, thus exemplifying the fact that very subtle structural changes in the bicycles can have a drastic effect on their binding activities.

#### Determination of Affinity Binding Constants ( $K_d$ ).

Determination of IC<sub>50</sub> values provides an indirect method to estimate the corresponding binding affinities. In order to be able to directly observe the bicycle-integrin interactions, we employed an optical approach by combining surface plasmon resonance (SPR) with surface plasmon-enhanced fluorescence spectroscopy (SPFS). For this, we modified  $\alpha_5\beta_1$ -selective bicycle C<sub>T3</sub>RGDC<sub>T3</sub>AYJC<sub>T3</sub>, linear GRGDS, *cyclo*-[KRGDf], and knottin-RGD with a linker (K-PPPSG(Abz)SG; Abz = 4-aminobenzoic acid; abbreviated hereafter as “K(Cy5)-linker”) based on studies by Pallarola et al.<sup>29</sup> In the first SPR experiment, the binding of RGD-bicycle to integrins attached to the gold sensor surface was monitored directly from induced changes in the refractive index (data not shown). However, this approach did not provide sufficient sensitivity, probably because of the low molecular weight of the bicycles (~2 kDa). Therefore, we labeled the peptides with a fluorescent Cy5-tag and used its absorption band to locally excite the fluorescence signal close to the gold sensor surface carrying the immobilized integrins. This approach increases the fluorescence signal originating from peptide binding at the surface, which allowed us to measure the kinetics of the peptide-integrin interaction.<sup>30</sup> Dissociation equilibrium constants ( $K_d$ ) of selected peptides were determined for both  $\alpha_5\beta_1$  and  $\alpha_v\beta_3$  integrins by real-time fluorescence signal analysis upon Cy5-labeled peptide binding to the integrin-anchored surface at various different concentrations using either a 2D-architecture with thiol SAM (data not shown),<sup>21</sup> or a 3D-hydrogel matrix of ~100 nm thick. The latter provided a significantly higher signal to noise ratio because it allowed to avoid the effect of quenching. Binding was measured at 0.1, 1.0, 10, and 100 nM, normalized to  $\Delta F_{\max}$  (value measured at saturation) and fitted via a Langmuir isotherm model (Figure 4A). For the interaction of bicycle K(Cy5)-linker-C<sub>T3</sub>RGDC<sub>T3</sub>AYJC<sub>T3</sub> with integrin  $\alpha_5\beta_1$ , a  $K_d$  of 4.1 nM was determined (Figure 4B). Interestingly, this value indicates a substantially higher affinity as compared to knottin-

RGD ( $K_d$  = 9 nM). It is worth noting that competition ELISA values revealed a much lower difference in IC<sub>50</sub> for knottin-RGD and bicycle K(Cy5)-linker-C<sub>T3</sub>RGDC<sub>T3</sub>AYJC<sub>T3</sub> (Figure 4B), which can be ascribed to the impact of attached Cy5-linker. For *cyclo*-[K(Cy5)-linker]RGDf and K(Cy5)-linker-GRGDS binding in SPFS was not observed for integrin  $\alpha_5\beta_1$ , in accordance with the IC<sub>50</sub> measurements. The additional SPFS results for the affinity interaction with integrin  $\alpha_v\beta_3$  confirmed the high selectivity of bicycle K(Cy5)-linker-C<sub>T3</sub>RGDC<sub>T3</sub>AYJC<sub>T3</sub> between both integrins  $\alpha_v\beta_3$  and  $\alpha_5\beta_1$  in accordance with ELISA IC<sub>50</sub> measurements.

**Selectivity Studies.** Finally, we investigated the integrin selectivity of the three highest affinity  $\alpha_5\beta_1$  integrin-binders via competition ELISA (Figure 4C). Bicycles C<sub>T3</sub>RGDC<sub>T3</sub>AYJC<sub>T3</sub> and C<sub>T3</sub>RGDC<sub>T3</sub>AWGC<sub>T3</sub> showed excellent selectivity over integrin  $\alpha_v\beta_5$  (IC<sub>50</sub> each >10 000 nM) with a selectivity ratio  $\alpha_5\beta_1/\alpha_v\beta_5$  of <0.009 and <0.017, respectively (ratio of corresponding IC<sub>50</sub> values). The selectivity over  $\alpha_v\beta_3$  was also quite substantial, but not as good as for  $\alpha_v\beta_5$  (IC<sub>50</sub> = 1019 nM and 1185 nM, respectively), with a selectivity ratio  $\alpha_5\beta_1/\alpha_v\beta_3$  of approximately 0.09. Bicycle C<sub>T3</sub>RGDC<sub>T3</sub>AYaC<sub>T3</sub>, however, exhibited significantly lower selectivities (ratios of only 0.034 for  $\alpha_5\beta_1/\alpha_v\beta_5$  and 0.157 for  $\alpha_5\beta_1/\alpha_v\beta_3$ ). These data nicely illustrate the fact that the bicyclic RGD-peptide platform represents an excellent alternative to the high-affinity  $\alpha_5\beta_1$  integrin-binder knottin-RGD, which shows basically no selectivity in integrin-binding.

**Structural Assignment of Individual Amino Acids in C<sub>T3</sub>RGDC<sub>T3</sub>AYJC<sub>T3</sub> via 2D NMR.** Individual amino acids were identified through their H <sub>$\alpha$</sub> /C <sub>$\alpha$</sub>  chemical shifts from the edited HSQC (Figure S-8), as well as the number and chemical shift of the side-chain resonances as revealed through 2D TOCSY (Figure S-9). The residue easiest to identify belonged to the phenol side chain of the tyrosine. The aromatic protons at 7.11 and 6.83 ppm were assigned ortho and meta to the phenol, respectively, and could be connected to the carbons at 133.3 and 118.3 ppm, respectively. Using a <sup>1</sup>H-<sup>13</sup>C HMBC long-range coupling experiment, the H <sub>$\alpha$</sub>  and H <sub>$\beta$</sub>  protons of the tyrosine residue were identified at 4.44 ppm and 3.03/2.90 ppm, while the corresponding C <sub>$\alpha$</sub>  and C <sub>$\beta$</sub>  were identified at 58.9 and 38.2 ppm, respectively, via a 1-bond <sup>1</sup>H-<sup>13</sup>C HSQC correlation experiment (Figure S-8). These shifts were consistent with a random coil conformation as opposed to a stable  $\alpha$  helix or  $\beta$  sheet structure. An identical analysis was



performed for all readily identifiable amino acid residues, which yielded an overall random coil conformation for the RGD-bicyclic peptide (Figure 5A). Ideally, the bicyclic peptide

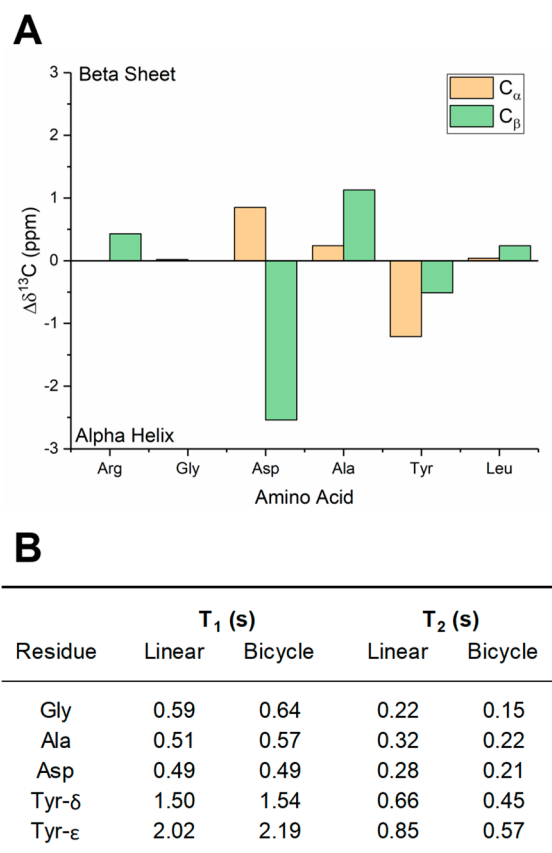


**Figure 5.** (A) Chemical shift difference plots for  $C_{\alpha}$  and  $C_{\beta}$  calculated by  $\Delta\delta^{13}C_{\alpha} = \Delta\delta^{13}C_{\alpha,rc} - \Delta\delta^{13}C_{\alpha,i}$  and  $\Delta\delta^{13}C_{\beta} = \Delta\delta^{13}C_{\beta,i} - \Delta\delta^{13}C_{\beta,rc}$  ( $i$  = measured amino acid in bicycle,  $rc$  = random coil). Positive values reflect more  $\beta$ -sheet character while negative values represent more  $\alpha$ -helical character. Amino acids that are close to the baseline are indicative of random coil structures, show both  $\alpha$ -helical and  $\beta$ -sheet character, or alternatively structured sequences; (B) NMR relaxation times  $T_1$  and  $T_2$  as a function of amino acid residue.

should not have the tendency to either polymerize or aggregate in solution. To determine the effect of structuring the peptide by linking the peptide chain to a central mesityl moiety via the cysteine residues,  $T_1$  and  $T_2$  NMR relaxation measurements were undertaken for both the free chain peptide and bicyclic compound.  $T_1$  relaxation for protons arises primarily through dipole–dipole interactions with neighboring nuclei that occur at the Larmor precession frequency, usually via molecular motion.  $T_2$  relaxation involves the loss of spin coherence in the  $XY$  plane through variations in local magnetic fields of any frequency interacting with the nuclear spin. As both of these parameters involve molecular motion, they can be sensitive probes for phenomena, such as polymerization, aggregation, and complexation, which affect the rotational correlation time of the molecule. The residues that were most readily identifiable in both the free and bicyclic peptide were  $H_{\alpha,Gly}$ ,  $H_{\beta,Ala}$ ,  $H_{\delta,Asp}$ ,  $H_{\delta,Tyr}$  and  $H_{\epsilon,Tyr}$  (Figure 5B). In all cases, the  $T_1$  values of these protons deviated less than 10% between the free and bicyclic forms, indicating that overall the molecular rotation of the molecule remains relatively unchanged. The  $T_2$  values decreased slightly more, reflecting the increase in

rigidity of the peptide, however not significantly enough to indicate dimerization or aggregation. Therefore, it can be concluded with relative certainty that these compounds exist as monomers in solution.

**Membrane Binding on Integrin-Expressing Adipose-derived Stem Cells (ASC).** To prove that RGD-bicycles also bind to integrins in their natural environment of the cell membrane, we labeled human adipose-derived stem cells (ASC, express integrin subunits  $\alpha_5$  and  $\beta_1$ ) with the Cy5-functionalized,  $\alpha_5\beta_1$ -selective bicycle peptide K(Cy5)-linker- $C_{T_3}RGDC_{T_3}AWGC_{T_3}$  together with two scrambled variants of this bicycle ( $AWG \rightarrow WGA$  and  $RGD \rightarrow GDR$ , respectively) as well as the  $\alpha_v\beta_3$ -selective bicycle peptide  $C_{T_3}HPQC_{T_3}RGDC_{T_3}$ ,<sup>21</sup> and benchmark RGD-peptides knottin-RGD, *cyclo*-[KRGDf] and GRGDS, and detected fluorescence emission via confocal microscopy. The  $\alpha_5\beta_1$ -selective bicycle showed similar staining levels (Figure 6A) as compared to Cy5-labeled benchmark knottin-RGD (Figure 6E), while the  $\alpha_v\beta_3$ -selective bicycle  $C_{T_3}HPQC_{T_3}RGDC_{T_3}$  (Figure 6D) and benchmarks *cyclo*-[KRGDf] (Figure 6F) and GRGDS (Figure 6G) were virtually silent under these conditions. Control studies with scrambled RGD-bicycle  $C_{T_3}GDRc_{T_3}AWGC_{T_3}$  (Figure 6B) showed hardly any traces of cell-staining, which proves the essential role of RGD for binding to membrane integrins. Moreover, the scrambled bicycle  $C_{T_3}RGDC_{T_3}WGAc_{T_3}$  (Figure 6C) showed mediocre staining levels, albeit much weaker than observed for the parent bicycle, which proves the fact that binding is unequivocally AWG-sequence specific. The cell-staining data further illustrate the high potential of these highly integrin-selective RGD-bicycles as powerful markers of specific integrin-expression on live cells.

**Screening for  $\alpha_v\beta_5$ -Binding Peptides.** Finally, the fact that a selective integrin  $\alpha_v\beta_5$ -binder has not yet been reported in the literature encouraged us to extend the RGD-bicycle library screening to the search for  $\alpha_v\beta_5$ -binding bicycles. Integrin  $\alpha_v\beta_5$  is an important mediator of cell adhesion and spreading,<sup>31</sup> among others, by internalizing conformationally modified vitronectin.<sup>32</sup> However, this integrin has been much less investigated as compared to integrins  $\alpha_v\beta_3$  and  $\alpha_5\beta_1$ , and its action is generally described in alignment with  $\alpha_v\beta_3$ .<sup>33–35</sup> For example, both integrins  $\alpha_v\beta_3$  and  $\alpha_v\beta_5$  individually direct human cardiac myofibroblast differentiation via activation of TGF- $\beta_1$ .<sup>36</sup> Moreover,  $\alpha_v\beta_5$  promoted angiogenesis induced by VEGF in corneal models in vivo, while  $\alpha_v\beta_3$  supported bFGF-induced angiogenesis.<sup>37</sup>

Screening of our first-generation bicycle libraries for integrin  $\alpha_v\beta_5$  revealed that only one out of 672 peptides showed more than 50% inhibition of knottin-RGD- $\alpha_v\beta_5$  binding ( $C_{T_3}RGDC_{T_3}NWGC_{T_3}$ ). It is interesting to note, though, that exactly the same peptide was also identified as a first-generation binder to  $\alpha_5\beta_1$  (vide supra). Approximately 94% of the RGD-bicycles showed <25% inhibition, revealing a clearly suboptimal positioning of the “RGD”-motif within the various bicycles tested. We determined a relatively high  $IC_{50}$  value of 1.46  $\mu M$  for this lead (Figure 7), for which the  $\alpha_v\beta_5$ -inhibiting ability was much lower than that of knottin-RGD (76 nM), *cyclo*-[KRGDf] (182 nM), and cilengitide (26 nM). We then designed and synthesized second generation libraries (in total 196 peptides) based on the lead motif “NWG” and screened these for improved  $\alpha_v\beta_5$ -inhibiting activity at 5  $\mu M$  concentration. Much to our surprise, not a single peptide exhibited an increased extent of  $\alpha_v\beta_5$ -inhibition in the

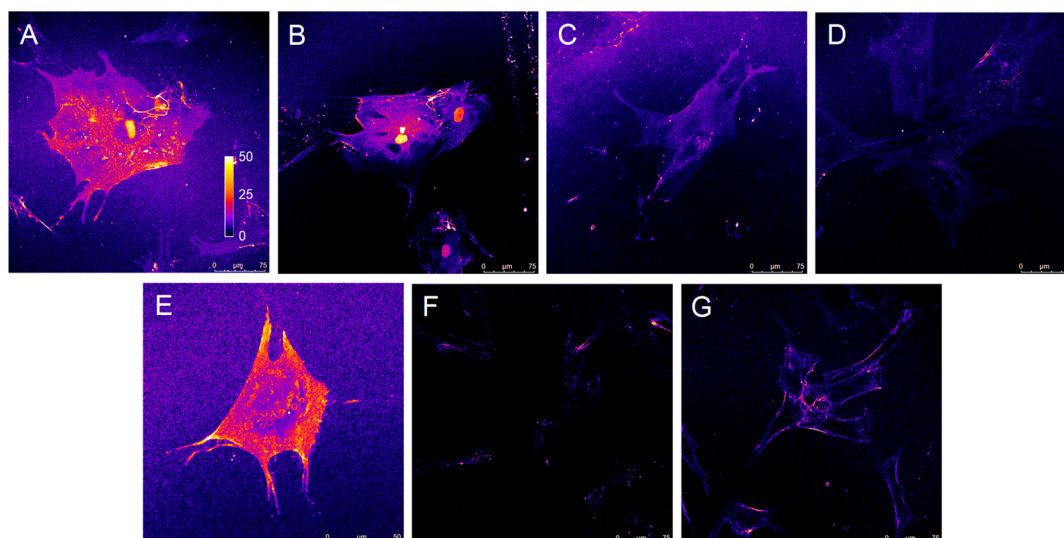


**Figure 6.** Confocal microscopy images of adipose-derived stem cells (ASC) incubated with (A) the  $\alpha_5\beta_1$ -selective bicycle  $C_{T3}RGDC_{T3}AWGC_{T3}$ , (B) the structural variant with a scrambled AWG-loop (i.e., bicycle  $Cy5$ -linker- $C_{T3}RGDC_{T3}WGAC_{T3}$ ), (C) the structural variant with a scrambled RGD-loop (i.e., bicycle  $Cy5$ -linker- $C_{T3}GDR_{C_{T3}}AWGC_{T3}$ ), (D) the  $\alpha_3\beta_3$ -selective bicycle  $Cy5$ -linker- $C_{T3}HPQC_{T3}RGDC_{T3}$ , and benchmark peptides (E)  $Cy5$ -linker-knottin-RGD, (F)  $cyclo$ -[K(K(Cy5)-linker)RGDf], and (G) K(Cy5)-linker-GRGDS. Cells were incubated on glass coverslips for at least 4 days, followed by addition of Cy5-labeled peptides for 10 min at 4 °C, washing, fixation with 4% PFA, and finally confocal analysis. All images were acquired under identical imaging conditions and processed via ImageJ (LUT: Fire). The contrast is shown in arbitrary units (au): 0, no fluorescence; 50, maximum fluorescence. Images were taken at, or very close to, the basal membrane to ensure an optimal visualization of plasma membrane labeling. We want to explicitly emphasize that cytosolic labeling was thereby not observed for these cells.

Peptide	IC <sub>50</sub> [nM]
<b>1<sup>st</sup> generation</b>	
$C_{T3}$ R G D $C_{T3}$ N W G $C_{T3}$	1457 ± 452
<b>2<sup>nd</sup> generation</b>	
$C_{T3}$ R G D $C_{T3}$ N W f $C_{T3}$	3668 ± 1407
$C_{T3}$ R G D $C_{T3}$ N W a $C_{T3}$	650 ± 104
$C_{T3}$ G R G D a $C_{T3}$ N W G $C_{T3}$	1150 ± 206
knottin-RGD	76 ± 7
$cyclo$ -[KRGDf]	182 ± 29
cilengitide	26 ± 5
GRGDS	> 10,000

**Figure 7.** IC<sub>50</sub> values of 1<sup>st</sup> and 2<sup>nd</sup> generation of RGD-bicyclic integrin  $\alpha_5\beta_5$ -binders.

screening as compared to the lead itself, while only four second generation bicycles showed more than 50% inhibition. Two of these, that is, bicycles  $C_{T3}GRGDac_{T3}NWGC_{T3}$  and  $C_{T3}RGDC_{T3}NWaC_{T3}$ , exhibited lower IC<sub>50</sub> values (i.e., 1150 and 650 nM, respectively) compared to those of the lead (crude peptides used for initial screening, IC<sub>50</sub> values determined using HPLC-purified bicycles), whereas  $C_{T3}RGDC_{T3}NWfC_{T3}$  had a much higher IC<sub>50</sub> values (>3.5  $\mu$ M, Figure 7). However, the binding affinities of these peptides were still much lower compared to that of the control RGD peptides, which reveals that the bicyclic RGD-peptide platform used seems not too well suited for identifying high-affinity  $\alpha_5\beta_5$ -binders.

## CONCLUSION

The screening of partially randomized RGD-bicycle libraries was successfully applied in the search for integrin  $\alpha_5\beta_1$ -binders,

eventually yielding three high-affinity second-generation bicyclic peptides, that is,  $C_{T3}RGDC_{T3}AYJC_{T3}$  (J = D-Leu, IC<sub>50</sub> = 90 nM),  $C_{T3}RGDC_{T3}AYaC_{T3}$  (IC<sub>50</sub> = 156 nM), and  $C_{T3}RGDC_{T3}AWGC_{T3}$  (IC<sub>50</sub> = 173 nM), with very good selectivities over integrin  $\alpha_5\beta_5$  (selectivity ratios  $\alpha_5\beta_1/\alpha_5\beta_5$  from <0.007 to <0.034) and moderate selectivities over  $\alpha_5\beta_3$  (selectivity ratios  $\alpha_5\beta_1/\alpha_5\beta_3$  of 0.09–0.157). Therefore, these bicycles represent an attractive structural platform to target  $\alpha_5\beta_1$ , be it in the context of therapeutic applications, biomaterial functionalization, or in vitro/in vivo tracers.

## MATERIALS AND METHODS

Parts of the procedures have already been described in ref 21.

**Reagents and Chemicals.** Incubation and washing buffers were prepared using standard protocols. Recombinant human integrins were purchased from R&D Systems (Minneapolis, USA). Strep-HRP (streptavidin–horseradish peroxidase conjugate, Southern-Biotech, Birmingham, USA), was diluted 1:1000 for ELISA experiments. Amino acids were purchased from Iris Biotech (Marktredwitz, Germany) and Matrix Innovation (Quebec, Canada). Resins were purchased from Rapp Polymere (Tübingen, Germany) and Merck (Darmstadt, Germany).  $MnCl_2 \cdot 4H_2O$ , 1,3,5-tris(bromomethyl)benzene (T3), 1,2-bis(bromomethyl)benzene (oT2), 1,3-bis(bromomethyl)benzene (mT2), 2,6-bis(bromomethyl)pyridine (mP2), 1,4-bis(bromomethyl)benzene (pT2), 2,2-dithiobis(5-nitropyridine) (DTNP), ethyl(dimethylaminopropyl) carbodiimide (EDC), N-hydroxysuccinimide (NHS), ethanolamine, Tween 20, ethylene glycol, acetic acid, and sodium acetate for the preparation of acetate buffer were purchased from Sigma-Aldrich (Steinheim, Germany).  $CaCl_2 \cdot 2H_2O$ ,  $MgCl_2 \cdot 6H_2O$ , and phosphate buffered saline (PBS) were purchased from Merck (Darmstadt, Germany). Tween 80 was purchased from Faryon (Capelle, The Netherlands) and I-Block was purchased from Tropix

(Bedford, USA). Disulfo-Cy5-NHS ester was purchased from Cyandye (Sunny Isles Beach, USA). Dithiolaromatic PEG6-carboxylate (thiol-COOH; SPT0014A6) and dithiolaromatic PEG3 (thiolPEG); SPT-0013) were purchased from SensoPath Technologies (Bozeman, USA). Sodium para-tetrafluorophenol-sulfonate (TFPS) and S-3-(benzoylphenoxy)propyl ethethanethioate (thiol-benzophenone) were synthesized at the Max Planck Institute for Polymer Research (Mainz, Germany) according to literature.<sup>38,39</sup> A poly(*N*-isopropylacrylamide)-based terpolymer with 94:5:1 molar ratio of *N*-isopropylacrylamide, methacrylic acid, and 4-methacryloyloxy benzophenone (pNIPAAm) were synthesized as previously described.<sup>40,41</sup>

**Peptide Synthesis. General Information.** Peptide syntheses were carried out on fully automated peptide synthesizers from MultiSyntech (Syracuse, NY, 2  $\mu$ mol scale for libraries) or Gyros Protein Technologies (Symphony) via Fmoc-based solid-phase peptide synthesis on Rink-amide resin using standard protocols. The couplings of L- and D-cysteines were performed manually using 2,4,6-trimethylpyridine as base to prevent racemization. Knottin-RGD peptide, *cyclo*-[KRGDF], and biotinylated knottin-RGD peptide were synthesized according to previous published protocols.<sup>21,22</sup> For IC<sub>50</sub> determination and selectivity experiments, all peptides were purified by preparative HPLC on an RP-C18 column (Reprosil-Pur 120 C18-AQ 150  $\times$  20 mm, Dr. Maisch GmbH, Ammerbuch, Germany) using an MeCN/H<sub>2</sub>O gradient (5–65%) including 0.05% TFA, followed by lyophilization (Christ Alpha 2–4 LDplus). Library screening and inhibition experiments with single-loop peptides were carried out using nonpurified peptides. For all amino acids used, see [Supporting Information](#).

**Synthesis of Bicyclic Peptide Libraries.** Linear peptide libraries (2  $\mu$ mol) were dissolved in 0.5 mL of DMF. 1,3,5-Tris(bromomethyl) benzene (T3) in DMF (4.1 mM, 0.5 mL) and ammonium bicarbonate (150 mM, 0.5 mL) were added and the combined solutions mixed. After 1 hour at r.t., the reaction was quenched with 0.5% ethanethiol (in 1:1 DMF/H<sub>2</sub>O, 0.1 mL). The bicyclic peptide libraries were freeze-dried using a Genevac HT-4X evaporation system. For a list of all applied amino acids, see [Table S-1](#).

**Synthesis of Bicyclic Peptides.** To linear peptides dissolved at 0.5 mM in 1:3 MeCN/H<sub>2</sub>O, 1.1 equiv of 1,3,5-tris(bromomethyl) benzene (T3) dissolved in MeCN, and 1.4 equiv ammonium bicarbonate (0.2 M solution in H<sub>2</sub>O) were added and shaken for 60 min. After completion (monitored by UPLC), the reaction was quenched with 10% TFA/H<sub>2</sub>O to pH < 4, followed by lyophilization.

**Peptide Labeling with Cy5.** Peptides with an N-terminal amine were dissolved at 4 mM in DMSO, followed by adding disulfo-Cy5 NHS (1 equiv, 20 mg/mL in DMSO) and DIPEA (10 equiv). After completion (30–60 min), the reaction was quenched with 10% TFA/H<sub>2</sub>O, using twice the volume of DIPEA, and subsequently purified via HPLC.

**ELISA.** For composition of all buffers and detailed concentrations, see [Table S-2](#).

**Integrin Coating and Blocking.** Plates were coated with 100  $\mu$ L of a 0.5  $\mu$ g/mL integrin solution in coating buffer onto 96-well NUNC Polysorp (overnight, 4 °C) followed by blocking with 150  $\mu$ L of 1% I-Block in blocking buffer (60 min, r.t.) and 3 $\times$  washing with 400  $\mu$ L of washing buffer.

**Library Screening.** Peptide libraries (2  $\mu$ mol) were dissolved at 10 mM in DMSO and further diluted with incubation buffer. After incubation with a fixed concentration

of biotinylated knottin-RGD peptide in incubation buffer (15 min, r.t.), mixed solutions were added to the integrin-coated plates (90 min, r.t.), followed by 3 $\times$  washing with washing buffer. Then, the plates were incubated with 100  $\mu$ L of 1:1000 Strep-HRP in Strep-HRP buffer (60 min, r.t.). After they were washed 4 $\times$ , they were incubated with 150  $\mu$ L of substrate buffer containing 0.91 mM ABTS (2,2'-azino-bis(3-ethylbenzothiazoline-6-sulfonic acid) and 0.006% H<sub>2</sub>O<sub>2</sub> in substrate buffer (0.2 M Na<sub>2</sub>HPO<sub>4</sub> adjusted to pH 4 using 0.2 M citric acid). Absorbance was measured after 45 min using a Molecular Devices Spectramax M2 plate reader.

**IC<sub>50</sub> Determination.** Peptides were mixed in eight different concentrations (each 3-fold dilutions) with a fixed concentration of biotinylated knottin-RGD (both in incubation buffer, 15 min, r.t.), followed by incubation of the plates with peptide/biotinylated knottin-RGD solutions for 90 min at room temperature. Strep-HRP and ABTS incubation steps were performed like described for library screening. All concentrations were tested in triplicate. IC<sub>50</sub> values were calculated via nonlinear regression analysis using GraphPad Prism software and represent the peptide concentration at which 50% inhibition of biotinylated knottin binding is observed.

**Surface Plasmon Resonance-Enhanced Fluorescence (SPFS).** For the description of the optical system and sensor chip preparation, the reader is referred to the [Supporting Information](#).

**Immobilization of Ligand.** Immobilization of integrin  $\alpha_5\beta_1$  was performed in situ by amine coupling according to standard protocols. The surface reactions were monitored by SPR ([Figure S5A](#)). First, acetate buffer (ACT, pH 4) was flowed over the gold surface until a stable baseline in SPR signal was established. Then, the sensor surface carrying carboxylic groups on mixed thiol self-assembled monolayer (SAM) was reacted with 75 mg/mL EDC and 21 mg/mL NHS dissolved in water for 15 min. For the 3D hydrogel interface carrying higher density of carboxylic moieties in its open polymer network structure, the activation was performed by TFPS dissolved in water ( $c = 21$  mg/mL). Recombinant human integrins ( $c = 10$   $\mu$ g/mL), dissolved in acetate buffer (pH = 4), was flowed over the activated sensor surface for 90 min to bind the integrin molecules via their amine groups to activated carboxylic groups. Finally, remaining active ester groups were inactivated by flowing 1 M ethanolamine solution over the gold surface for 15 min.

**Measurement of Equilibrium Dissociation Constant  $K_d$ .** For measuring the binding affinity of Cy5-labeled peptides to immobilized integrin ligands, PBS with 1 mM CaCl<sub>2</sub>, 0.5 mM MnCl<sub>2</sub>, 1 mg/mL BSA, and 0.05% Tween20 was used as running buffer. Different concentrations of the peptide (0.1, 1, 5, 10, 50, 100, and 1000 nM) were sequentially flushed over the sensor surface. Each concentration was allowed to react with the integrin for 30 min, followed by rinsing the surface with running buffer solution for 10 min. The affinity binding of target analyte was monitored in real-time by measuring the fluorescence intensity  $F(t)$  originating from the close proximity to the sensor surface that was probed by resonantly excited surface plasmons ([Figure S-5B](#)). The fluorescence signal  $F$  gradually increases upon the affinity binding of target analyte, and for each concentration, the equilibrium fluorescence signal  $\Delta F$  was determined as a difference between fluorescence baseline after 10 min rinsing with running buffer. The titration curve was established based on these values and fitted with a

Langmuir isotherm model [function  $\Delta F = \Delta F_{\max} c / (K_d + c)$ ] to determine the equilibrium dissociation constant  $K_d$ .

**NMR.** All NMR spectra were collected on a Bruker Avance III 500 MHz spectrometer equipped with a Prodigy BB cryoprobe at 298 K. Samples were prepared by dissolving the compounds in  $D_2O$  and adding a small amount of DSS for internal referencing.  $^1H$  spectra were acquired using 32 scans and a relaxation delay of 3 s. 2D COSYDQF spectra with presaturation were acquired with a 6000 Hz spectral width in both dimensions using  $2048 \times 512$  points and processed using  $2048 \times 512$  points, 4 scans per increment and a relaxation delay of 1.5 s. 2D gradient TOCSY spectra with presaturation were acquired with a 5000 Hz spectral width in both dimensions using  $1024 \times 512$  points and processed using  $1024 \times 1024$  points, 8 scans per increment, a relaxation delay of 2 s, and a TOCSY mix time of 100 ms. A TOCSY spinlock field of 8.3 kHz was applied. 2D gradient ROESY spectra were acquired with a 6000 Hz spectral width in both dimensions using  $4096 \times 512$  points and processed using  $4096 \times 512$  points, 24 scans per increment, a relaxation delay of 1.5 s and a ROESY mix time of 0.3 s. A ROESY spinlock field of 5 kHz was applied. Multiplicity-edited  $^1H$ - $^{13}C$  HSQC spectra were acquired using a 6010 Hz spectral width in F2 and 18868 Hz spectral width in F1 using  $1024 \times 512$  points and processed to  $1024 \times 1024$  points, 2 scans per increment, relaxation delay of 1.5 s and 1-bond  $J_{CH} = 145$  Hz.  $^1H$ - $^{13}C$  HMBC spectra were acquired using a 5319.1 Hz spectral width in F2 and 22321.4 Hz spectral width in F1 using  $2048 \times 512$  points and processed to  $2048 \times 2048$  points, 4 scans per increment, relaxation delay of 1.5 s and a long-range  $J_{CH} = 8$  Hz.

$T_1$  measurements were performed by properly calibrating the 90-degree pulse length and then performing estimates using the 1D inversion recovery sequence with excitation sculpting water suppression. After the longest  $T_1$  was determined to be approximately 2 s, a pseudo-2D inversion recovery experiment was performed with 10 separate delays of 8 scans each with a total longitudinal relaxation time of 10.3 s.  $T_2$  measurements were acquired by first performing estimates using the 1D PROJECT-CMPG<sup>42</sup> sequence with presaturation water suppression. After the longest  $T_2$  was determined to be approximately 1 s, a pseudo-2D PROJECT-CPMG sequence experiment with presaturation was performed with 12 separate delays of 8 scans each, a cycle time of 4 ms with a total longitudinal relaxation time of 10.3 s.

**Cell Integrin Staining and Confocal Microscopy.** Human adipose-derived stem cells (ASC) were obtained from the University Medical Center Nijmegen and grown using standard procedures and conditions. For the experiment, the cells were allowed to adhere on clean glass coverslips for at least 4 d until reaching approximately 40–50% confluency. Then, the glass coverslips were washed two times with cold HCG buffer (carbonate-buffered saline, pH 7.2, containing 140 mM NaCl, 5 mM KCl, 23 mM  $NaHCO_3$ , 10 mM HEPES, 10 mM glucose, 1 mM  $CaCl_2$ , 0.5 mM  $MgCl_2$ , and 0.5 mM  $MnCl_2$ ) to remove nonadhered cells, followed by adding cold HCG buffer, and cooling of the glass coverslips to 4 °C. Afterward, the Cy5-labeled peptides added and allowed to incubate at 1  $\mu M$  for 10 min at 4 °C, followed by at least five washing steps with HCG buffer, fixation with 4% paraformaldehyde solution in PBS pH 7.4 (20 min) and another four washing steps with HCG buffer. Subsequently, the cells were analyzed via confocal microscopy using a Leica TCS SP8 confocal microscope equipped with a supercontinuum white

light laser (NKT Photonics) and water immersion objectives (63 $\times$  W PL APO CS2, NA 1.2/40 $\times$  W PL APO CS2, NA 1.1). The excitation wavelength was set to 633 nm, while fluorescence was detected from 646 to 778 nm. All images were acquired at identical imaging conditions, and processed via ImageJ (LUT: Fire).

## ■ ASSOCIATED CONTENT

### 📄 Supporting Information

The Supporting Information is available free of charge on the ACS Publications website at DOI: 10.1021/acscombsci.9b00081.

List of amino acids applied in this study, parameters varied in the competition ELISA setups, UPLC/ESI-MS spectra of purified bicycles  $C_{T3}RGDC_{T3}AYJC_{T3}$ ,  $C_{T3}RGDC_{T3}AYaC_{T3}$ , and  $C_{T3}RGDC_{T3}AWGC_{T3}$ , description of optical instrument for SPR and SPFS measurements, optical instrument for SPFS and SPR measurements, description of sensor chip preparation and immobilization of ligand, example of an SPR sensorgram showing covalent immobilization of integrin  $\alpha_5\beta_1$  into a 3D hydrogel binding matrix and fluorescence signal kinetics acquired upon titration of K(Cy5)-linker- $C_{T3}RGDC_{T3}AYJC_{T3}$ , description of screening of single-loop CLIPS variants, overview of bi- and trivalent scaffolds for the synthesis of mono- and bicyclic peptides,  $\alpha_5\beta_1$ -inhibitory capacities of various monocyclic CLIPS-variants,  $^1H$ ,  $^1H$ - $^{13}C$  HSQCED, HMBC, and  $^1H$ - $^1H$  TOCSY spectra of  $C_{T3}RGDC_{T3}AYJC_{T3}$ , and absolute absorbances of library screening for 1<sup>st</sup> and 2<sup>nd</sup> generation of  $\alpha_5\beta_1$ -binders (PDF)

## ■ AUTHOR INFORMATION

### Corresponding Author

\*Tel.: +31-320-225300. Fax: +31-320-225301. E-mail: p.timmerman@pepscan.com.

### ORCID

Jakub Dostalek: 0000-0002-0431-2170

Peter Timmerman: 0000-0001-6687-5297

### Author Contributions

The manuscript was written through contributions of all authors. D.B. and P.T. conceived the concept and analyzed the data. D.B. performed peptide syntheses, competition and binding ELISA experiments, and in vitro integrin staining experiments. V.J., N.G.Q., and J.D. designed, performed, and analyzed the SPR/SPFS experiments. P.B.W. performed and analyzed the NMR experiments. D.B., K.J., and P.T. analyzed the confocal images. D.B., P.B.W., and P.T. wrote the manuscript. All authors have given approval to the final version of the manuscript.

### Notes

The authors declare the following competing financial interest(s): Pepsan is the inventor of the CLIPS technology and holds a patent on the synthesis of bicyclic peptides using 2-CLIPS technology.

## ■ ACKNOWLEDGMENTS

This project has received funding from the European Union's Horizon 2020 research and innovation program under the Marie Skłodowska-Curie grant agreement no. 64268. Prof.

Egbert Oosterwijk is kindly acknowledged for providing the stem cells.

## REFERENCES

- (1) Barczyk, M.; Carracedo, S.; Gullberg, D. Integrins. *Cell Tissue Res.* **2010**, *339*, 269–280.
- (2) Goodman, S. L.; Picard, M. Integrins as therapeutic targets. *Trends Pharmacol. Sci.* **2012**, *33*, 405–412.
- (3) Schwartz, M. A.; Schaller, M. D.; Ginsberg, M. H. Integrins: Emerging Paradigms of Signal Transduction. *Annu. Rev. Cell Dev. Biol.* **1995**, *11*, 549–599.
- (4) Avraamides, C. J.; Garmy-Susini, B.; Varner, J. A. Integrins in angiogenesis and lymphangiogenesis. *Nat. Rev. Cancer* **2008**, *8*, 604–617.
- (5) Goessler, U. R.; Bugert, P.; Bieback, K.; Stern-Straeter, J.; Bran, G.; Hörmann, K.; Riedel, F. Integrin expression in stem cells from bone marrow and adipose tissue during chondrogenic differentiation. *Int. J. Mol. Med.* **2008**, *21*, 271–279.
- (6) Mierke, C. T.; Frey, B.; Fellner, M.; Herrmann, M.; Fabry, M. Integrin  $\alpha_5\beta_1$  facilitates cell invasion through enhanced contractile forces. *J. Cell Sci.* **2011**, *124*, 369–383.
- (7) Schwartz, M. A.; Ginsberg, M. H. Networks and crosstalk: Integrin signalling spreads. *Nat. Cell Biol.* **2002**, *4*, E65–E68.
- (8) Kim, S.; Harris, M.; Varner, J. A. Regulation of integrin  $\alpha_5\beta_1$ -mediated endothelial cell migration and angiogenesis by integrin  $\alpha_5\beta_1$  and protein kinase A. *J. Biol. Chem.* **2000**, *275*, 33920–33928.
- (9) Danen, E. H. J.; Sonneveld, P.; Brakebusch, C.; Fässler, R.; Sonnenberg, A. The fibronectin-binding integrins  $\alpha_5\beta_1$  and  $\alpha_4\beta_3$  differentially modulate RhoA-GTP loading, organization of cell matrix adhesions, and fibronectin fibrillogenesis. *J. Cell Biol.* **2002**, *159*, 1071–1086.
- (10) Takada, Y.; Ye, X.; Simon, S. The Integrins. *Genome Biol.* **2007**, *8*, 215.
- (11) Kimura, R. H.; Levin, A. M.; Cochran, F. V.; Cochran, J. R. Engineered cystine knot peptides that bind  $\alpha_v\beta_3$ ,  $\alpha_5\beta_3$ , and  $\alpha_5\beta_1$  integrins with low-nanomolar affinity. *Proteins: Struct., Funct., Genet.* **2009**, *77*, 359–369.
- (12) Kimura, R. H.; Teed, R.; Hackel, B. J.; Pysz, M. A.; Chuang, C. Z.; Sathirachinda, A.; Willmann, J. K.; Gambhir, S. S. Pharmacokinetically Stabilized Cystine Knot Peptides that bind Alpha-v-Beta-6 Integrin with Single-Digit Nanomolar Affinities for Detection of Pancreatic Cancer. *Clin. Cancer Res.* **2012**, *18*, 839–849.
- (13) Kim, J. W.; Cochran, F. V.; Cochran, J. R. A Chemically Cross-Linked Knottin Dimer Binds Integrins with Picomolar Affinity and Inhibits Tumor Cell Migration and Proliferation. *J. Am. Chem. Soc.* **2015**, *137*, 6–9.
- (14) Gan, Z.-R.; Gould, R. J.; Jacobs, J. W.; Friedman, P. A.; Polokoff, M. A. Echistatin. A Potent Platelet Aggregation Inhibitor from the Venom of the Viper, *Echis carinatus*. *J. Biol. Chem.* **1988**, *263*, 19827–19832.
- (15) Kapp, T. G.; Rechenmacher, F.; Neubauer, S.; Maltsev, O. V.; Cavalcanti-Adam, E. A.; Zarka, R.; Reuning, U.; Notni, J.; Wester, H.-J.; Mas-Moruno, C.; Spatz, J. P.; Geiger, B.; Kessler, H. A Comprehensive Evaluation of the Activity and Selectivity Profile of Ligands for RGD-binding Integrins. *Sci. Rep.* **2017**, *7*, 39805.
- (16) Stoeltzing, O.; Liu, W.; Reinmuth, N.; Fan, F.; Parry, G. C.; Parikh, A. A.; McCarty, M. F.; Bucana, C. D.; Mazar, A. P.; Ellis, L. M. Inhibition of integrin  $\alpha_5\beta_1$  function with a small peptide (ATN-161) plus continuous 5-FU infusion reduces colorectal liver metastases and improves survival in mice. *Int. J. Cancer* **2003**, *104*, 496–503.
- (17) Khalili, P.; Arakelian, A.; Chen, G.; Plunkett, M. L.; Beck, I.; Parry, G. C.; Shaw, D. E.; Mazar, A. P.; Rabbani, S. A. A non-RGD-based integrin binding peptide (ATN-161) blocks breast cancer growth and metastasis in vivo. *Mol. Cancer Ther.* **2006**, *5*, 2271–2281.
- (18) Heckmann, D.; Meyer, A.; Laufer, B.; Zahn, G.; Stragies, R.; Kessler, H. Rational Design of Highly Active and Selective Ligands for the  $\alpha_5\beta_1$  Integrin Receptor. *ChemBioChem* **2008**, *9*, 1397–1407.
- (19) Rechenmacher, F.; Neubauer, S.; Polleux, J.; Mas-Moruno, C.; De Simone, M.; Cavalcanti-Adam, E. A.; Spatz, J. P.; Fässler, R.; Kessler, H. Functionalizing  $\alpha_v\beta_3$ - or  $\alpha_5\beta_1$ -selective integrin antagonists for surface coating: A method to discriminate integrin subtypes in vitro. *Angew. Chem., Int. Ed.* **2013**, *52*, 1572–1575.
- (20) Kapp, T. G.; Di Leva, F. S.; Notni, J.; et al. N-Methylation of iso DGR Peptides: Discovery of a Selective  $\alpha_5\beta_1$ -Integrin Ligand as a Potent Tumor Imaging Agent. *J. Med. Chem.* **2018**, *61*, 2490–2499.
- (21) Bernhagen, D.; Jungbluth, V.; Quilis, N. G.; Dostalek, J.; White, P. B.; Jalink, K.; Timmerman, P. Bicyclic RGD Peptides with Exquisite Selectivity for the Integrin  $\alpha_v\beta_3$  Receptor Using a “Random Design” Approach. *ACS Comb. Sci.* **2019**, *21*, 198–206.
- (22) Bernhagen, D.; De Laporte, L.; Timmerman, P. High-Affinity RGD-Knottin Peptide as a New Tool for Rapid Evaluation of the Binding Strength of Unlabeled RGD-Peptides to  $\alpha_v\beta_3$ ,  $\alpha_5\beta_3$ , and  $\alpha_5\beta_1$  Integrin Receptors. *Anal. Chem.* **2017**, *89*, 5991–5997.
- (23) Timmerman, P.; Beld, J.; Puijk, W. C.; Meloen, R. H. Rapid and quantitative cyclization of multiple peptide loops onto synthetic scaffolds for structural mimicry of protein surfaces. *ChemBioChem* **2005**, *6*, 821–824.
- (24) Li, P.; Roller, P. P. Cyclization strategies in peptide derived drug design. *Curr. Top. Med. Chem.* **2002**, *2*, 325–341.
- (25) Baeriswyl, V.; Heinis, C. Polycyclic Peptide Therapeutics. *ChemMedChem* **2013**, *8*, 377–384.
- (26) Timmerman, P.; Barderas, R.; Desmet, J.; Shochat, S.; Monasterio, A.; Casal, J. I.; Meloen, R. H.; et al. A combinatorial approach for the design of complementarity-determining region-derived peptidomimetics with in vitro anti-tumoral activity. *J. Biol. Chem.* **2009**, *284*, 34126–34134.
- (27) Heinis, C.; Rutherford, T.; Freund, S.; Winter, G. Phage-encoded combinatorial chemical libraries based on bicyclic peptides. *Nat. Chem. Biol.* **2009**, *5*, 502–507.
- (28) Dechantsreiter, M. A.; Planker, E.; Matha, B.; Lohof, E.; Jonczyk, A.; Goodman, S. L.; Kessler, H.; et al. N-Methylated Cyclic RGD Peptides as Highly Active and selective  $\alpha_v\beta_3$  integrin antagonists. *J. Med. Chem.* **1999**, *42*, 3033–3040.
- (29) Pallarola, D.; Bochen, A.; Boehm, H.; Rechenmacher, F.; Sobahi, T. R.; Spatz, J. P.; Kessler, H. Interface immobilization chemistry of rRGD-based peptides regulates integrin mediated cell adhesion. *Adv. Funct. Mater.* **2014**, *24*, 943–956.
- (30) Bauch, M.; Toma, K.; Toma, M.; Zhang, Q.; Dostalek, J. Surface plasmon-enhanced fluorescence biosensors: a review. *Plasmonics* **2014**, *9*, 781–799.
- (31) Asano, Y.; Ihn, H.; Yamane, K.; Kubo, M.; Tamaki, K. Increased Expression Levels of Integrin  $\alpha_v\beta_3$  on Scleroderma Fibroblasts. *Am. J. Pathol.* **2004**, *164*, 1275–1292.
- (32) Panetti, T. S.; McKeown-Longo, P. J. The  $\alpha_5\beta_5$  integrin receptor regulates receptor-mediated endocytosis of vitronectin. *J. Biol. Chem.* **1993**, *268*, 11492–11495.
- (33) Friedlander, M.; Theesfeld, C. L.; Sugita, M.; Fruttiger, M.; Thomas, M. A.; Chang, S.; Cheresch, D. A. Involvement of integrins  $\alpha_v\beta_3$  and  $\alpha_5\beta_5$  in ocular neovascular diseases. *Proc. Natl. Acad. Sci. U. S. A.* **1996**, *93*, 9764–9769.
- (34) Hynes, R. O. A re-evaluation of integrins as regulators of angiogenesis. *Nat. Med.* **2002**, *8*, 918–921.
- (35) Conroy, K. P.; Kitto, L. J.; Henderson, N. C.  $\alpha\beta$  Integrins: Key Regulators of Tissue Fibrosis. *Cell Tissue Res.* **2016**, *365*, 511–519.
- (36) Sarrazy, V.; Koehler, A.; Chow, M. L.; Zimina, E.; Li, C. X.; Kato, H.; Caldarone, C. A.; Hinz, B. Integrins  $\alpha v\beta_3$  and  $\alpha_5\beta_3$  promote latent TGF- $\beta$ 1 activation by human cardiac fibroblast contraction. *Cardiovasc. Res.* **2014**, *102*, 407–417.
- (37) Friedlander, M.; Brooks, P. C.; Shaffer, R. W.; Kincaid, C. M.; Varner, J. A.; Cheresch, D. A. Definition of Two Angiogenic Pathways by Distinct  $\alpha$ , Integrins. *Science* **1995**, *270*, 1500–1502.
- (38) Beines, P. W.; Klosterkamp, I.; Menges, B.; Jonas, U.; Knoll, W. Responsive Thin Hydrogel Layers from Photo-Cross-Linkable Poly(N-isopropylacrylamide) Terpolymers. *Langmuir* **2007**, *23*, 2231–2238.
- (39) Gee, K. R.; Archer, E. A.; Kang, H. C. 4-Sulfotetrafluorophenyl (STP) esters: New water-soluble amine-reactive reagents for labeling biomolecules. *Tetrahedron Lett.* **1999**, *40*, 1471–1474.

(40) Junk, M. J. N.; Jonas, U.; Hinderberger, D. EPR spectroscopy reveals nanoinhomogeneities in the structure and reactivity of thermoresponsive hydrogels. *Small* **2008**, *4*, 1485–1493.

(41) Anac, I.; Aulasevich, A.; Junk, M. J. N.; Jakubowicz, P.; Roskamp, R. F.; Menges, B.; Jonas, U.; Knoll, W. Optical Characterization of Co-Nonsolvency Effects in Thin Responsive PNIPAAm-Based Gel Layers Exposed to Ethanol/Water Mixtures. *Macromol. Chem. Phys.* **2010**, *211*, 1018–1025.

(42) Aguilar, J. A.; Nilsson, M.; Bodenhausen, G.; Morris, G. A. Spin echo NMR spectra without J modulation. *Chem. Commun.* **2012**, *48*, 811–813.

## Supporting Information

### High Affinity $\alpha_5\beta_1$ Integrin-Selective Bicyclic RGD-Peptides Identified via Screening of Designed Random Libraries

Dominik Bernhagen<sup>a</sup>, Vanessa Jungbluth<sup>b</sup>, Nestor Gisbert Quilis<sup>b</sup>, Jakub Dostalek<sup>b</sup>, Paul B. White<sup>c</sup>, Kees Jalink<sup>d</sup> and Peter Timmerman<sup>a,e\*</sup>

**a:** Pepscan Therapeutics, Zuidersluisweg 2, 8243 RC Lelystad, the Netherlands; **b:** Biosensor Technologies, AIT Austrian Institute of Technology GmbH, Konrad-Lorenz-Straße 24, 3430 Tulln, Austria; **c:** Institute for Molecules and Materials, Radboud University, Heyendaalseweg 135, 6225 AJ Nijmegen, the Netherlands; **d:** The Netherlands Cancer Institute, Plesmanlaan 21, 1066 CX Amsterdam, the Netherlands; **e:** Van't Hoff Institute for Molecular Sciences, University of Amsterdam, Science Park 904, 1098 XH Amsterdam, the Netherlands

#### Table of contents

- S-2:** List of amino acids applied in this study (**Table S-1**)
- S-3:** Parameters varied in the competition ELISA setups (**Table S-2**)
- S-4:** UPLC/ESI-MS spectrum of purified bicycle  $C_{T3}RGDc_{T3}AYJC_{T3}$  (**Figure S-1**)
- S-5:** UPLC/ESI-MS spectrum of purified bicycle  $C_{T3}RGDc_{T3}AYaC_{T3}$  (**Figure S-2**)
- S-6:** UPLC/ESI-MS spectrum of purified bicycle  $C_{T3}RGDc_{T3}AWGC_{T3}$  (**Figure S-3**)  
Description of optical instrument for SPR and SPFS measurements
- S-7:** Optical instrument for SPFS and SPR measurements (**Figure S-4**)  
Description of sensor chip preparation and immobilization of ligand (SPFS)
- S-8:** Example of an SPR sensorgram showing covalent immobilization of integrin  $\alpha_5\beta_1$  into a 3D hydrogel binding matrix, and fluorescence signal kinetics acquired upon titration of K(Cy5)-linker- $C_{T3}RGDc_{T3}AYJC_{T3}$  (**Figure S-5**)  
Description of screening of single-loop *CLIPS* variants  
Overview of bi- and trivalent scaffolds for the synthesis of mono- and bicyclic peptides, and  $\alpha_5\beta_1$ -inhibitory capacities of various monocyclic *CLIPS*-variants (**Figure S-6**)
- S-9:**  $^1H$  NMR spectrum of  $C_{T3}RGDc_{T3}AYJC_{T3}$  (**Figure S-7**)  
 $^1H$ - $^{13}C$  HSQCED and HMBC spectra of  $C_{T3}RGDc_{T3}AYJC_{T3}$  (**Figure S-8**)
- S-10:**  $^1H$ - $^1H$  TOCSY spectrum of  $C_{T3}RGDc_{T3}AYJC_{T3}$  (**Figure S-9**)
- S-11:** Absorbance values of library screening for 1<sup>st</sup> generation of  $\alpha_5\beta_1$ -binders (**Tables S-3–S-9**)
- S-18:** Absorbance values of library screening for 2<sup>nd</sup> generation of  $\alpha_5\beta_1$ -binders (**Tables S-10–S-12**)
- S-20:** References

**Table S-1.** List of amino acids applied in this study including short codes, 1-letter codes and protective groups.

Amino acid	Short code	1-letter code	Amino acid <sub>protected</sub>	Application
L-alanine	Ala	A	Fmoc-L-Ala	all libraries
D-alanine	–	a	Fmoc-D-Ala	2 <sup>nd</sup> gen libraries
L-cysteine	Cys	C	Fmoc-L-Cys(Trt)	all libraries
D-cysteine	–	c	Fmoc-D-Cys(Trt)	all libraries
L-aspartic acid	Asp	D	Fmoc-L-Asp(OtBu)	all libraries
			Fmoc-L-Asp(OMpe)	all libraries
L-glutamic acid	Glu	E	Fmoc-L-Glu(OtBu)	all libraries
L-phenylalanine	Phe	F	Fmoc-L-Phe	all libraries
D-phenylalanine	–	f	Fmoc-D-Phe	2 <sup>nd</sup> gen libraries
Glycine	Gly	G	Fmoc-Gly	all libraries
L-histidine	His	H	Fmoc-L-His(Trt)	all libraries
L-isoleucine	Ile	I	Fmoc-L-Ile	all libraries
D-isoleucine	–	i	Fmoc-D-Ile	2 <sup>nd</sup> gen libraries
L-lysine	Lys	K	Fmoc-L-Lys(Boc)	all libraries
			Fmoc-L-Lys(Mmt)	all libraries
L-leucine	Leu	L	Fmoc-L-Leu	all libraries
D-leucine	–	J	Fmoc-D-Leu	2 <sup>nd</sup> gen libraries
L-asparagine	Asn	N	Fmoc-L-Asn(Trt)	all libraries
D-asparagine	–	n	Fmoc-D-Asn(Trt)	2 <sup>nd</sup> gen libraries ( $\alpha\beta 5$ )
L-proline	Pro	P	Fmoc-L-Pro	all libraries
L-glutamine	Gln	Q	Fmoc-L-Gln(Trt)	all libraries
L-arginine	Arg	R	Fmoc-L-Arg(Pbf)	all libraries
L-serine	Ser	S	Fmoc-L-Ser(tBu)	all libraries
L-threonine	Thr	T	Fmoc-L-Thr(tBu)	all libraries
L-valine	Val	V	Fmoc-L-Val	all libraries
L-tryptophan	Trp	W	Fmoc-L-Trp(Boc)	all libraries
D-tryptophan	–	w	Fmoc-D-Trp(Boc)	2 <sup>nd</sup> gen libraries ( $\alpha\beta 5$ )
L-tyrosine	Tyr	Y	Fmoc-L-Tyr(tBu)	all libraries
D-tyrosine	–	y	Fmoc-D-Tyr(tBu)	2 <sup>nd</sup> gen libraries ( $\alpha\beta 1$ )
L-1-naphthylalanine	1Nal	–	Fmoc-L-1-Nal	2 <sup>nd</sup> gen libraries
L-2-naphthylalanine	2Nal	–	Fmoc-L-2-Nal	2 <sup>nd</sup> gen libraries
L-aminobutyric acid	Abu	B	Fmoc-Abu	2 <sup>nd</sup> gen libraries
L-aminoisobutyric acid	Aib	Z	Fmoc-Aib	2 <sup>nd</sup> gen libraries
L-norleucine	Nle	–	Fmoc-L-Nle	2 <sup>nd</sup> gen libraries
L-norvaline	Nva	–	Fmoc-L-Nva	2 <sup>nd</sup> gen libraries
4-aminobenzoic acid	Abz	–	Fmoc-4-Abz	linker



**Table S-2.** Parameters varied in the two different competition ELISA setups (A), and selected setups for library screening, IC<sub>50</sub> determination and selectivity experiments (B).

**A**

	Setup 1	Setup 2
Coating buffer	0.1 M Na <sub>2</sub> HPO <sub>4</sub> pH 8 + 1 mM Ca <sup>2+</sup> 0.5 mM Mg <sup>2+</sup>	PBS pH 7.4 + 1 mM Ca <sup>2+</sup> 0.5 mM Mn <sup>2+</sup>
Concentration of integrin		0.5 µg/mL
Blocking buffer	0.05% Tween80/PBS + 1 mM Ca <sup>2+</sup> 0.5 mM Mg <sup>2+</sup>	0.05% Tween80/PBS + 1 mM Ca <sup>2+</sup> 0.5 mM Mn <sup>2+</sup>
Washing buffer	0.05% Tween80/PBS + 1 mM Ca <sup>2+</sup> 0.5 mM Mg <sup>2+</sup>	0.05% Tween80/PBS + 1 mM Ca <sup>2+</sup> 0.5 mM Mn <sup>2+</sup>
Incubation buffer	PBS pH 7.4 + 1 mM Ca <sup>2+</sup> 0.5 mM Mg <sup>2+</sup>	PBS pH 7.4 + 1 mM Ca <sup>2+</sup> 0.5 mM Mn <sup>2+</sup>
Concentration of biotinylated peptide		0.2 µM
Concentration of bicyclic peptide (1 <sup>st</sup> screening)	10 µM	5 µM
Concentration of bicyclic peptide (2 <sup>nd</sup> screening)	–	2.5 µM
Concentration range of IC <sub>50</sub> determination		30 µM – 0.014 µM
Strep-HRP buffer	PBS pH 7.4 + 1 mM Ca <sup>2+</sup> 0.5 mM Mg <sup>2+</sup>	PBS pH 7.4 + 1 mM Ca <sup>2+</sup> 0.5 mM Mn <sup>2+</sup>

**B**

Library Generation	$\alpha_5\beta_1$		$\alpha_v\beta_5$	
	1 <sup>st</sup>	2 <sup>nd</sup>	1 <sup>st</sup>	2 <sup>nd</sup>
Screening	1	2	1	2
IC <sub>50</sub> determination	2	2	2	2
Selectivity tests (all integrins)		2		

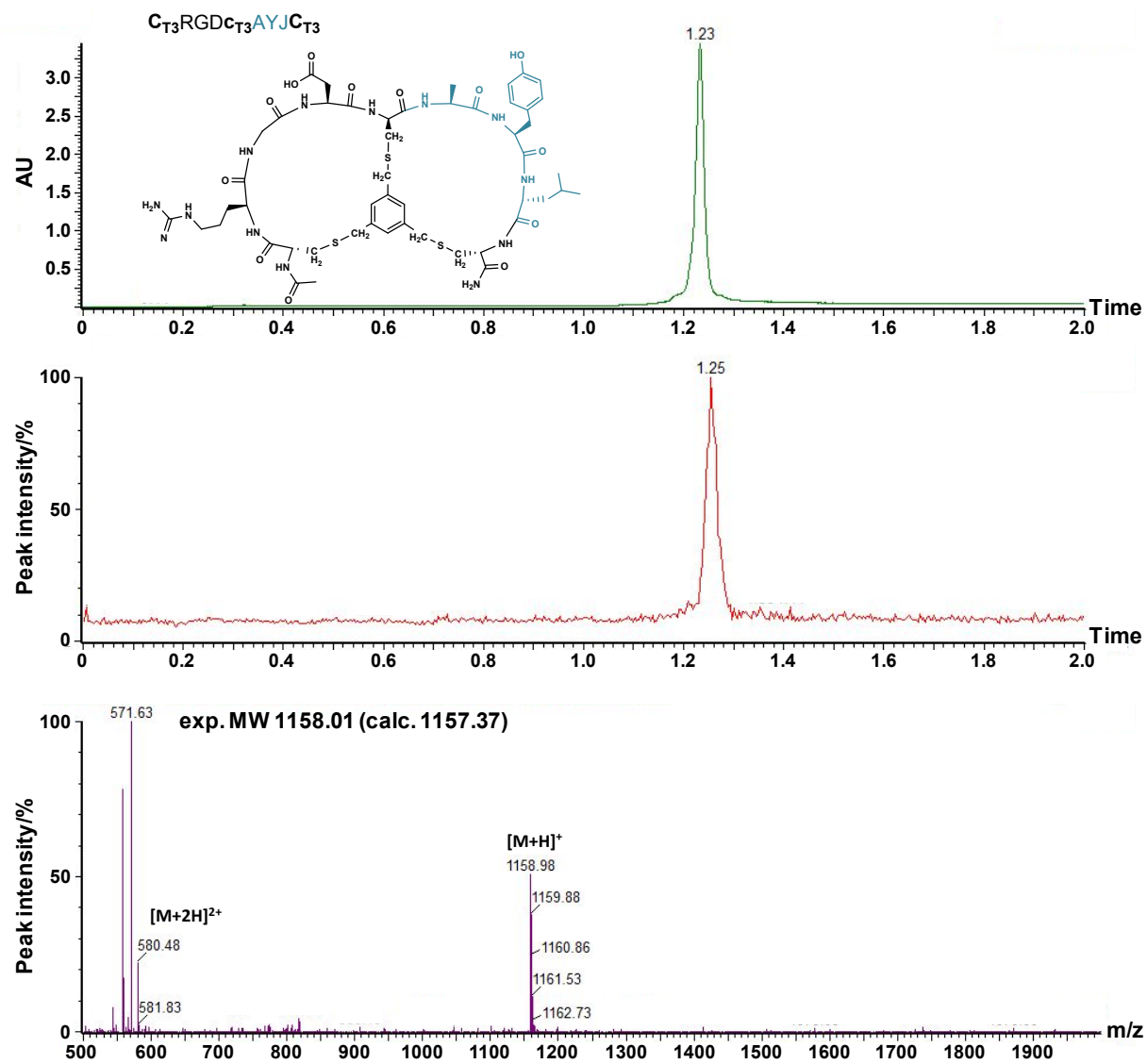


**Figure S-1:** UPLC/ESI-MS spectrum of purified bicyclic peptide  $C_{T3}RGDC_{T3}AYJC_{T3}$  (J: D-Leu, top: UV detection at 215 nm, middle/bottom: ESI-MS detection).

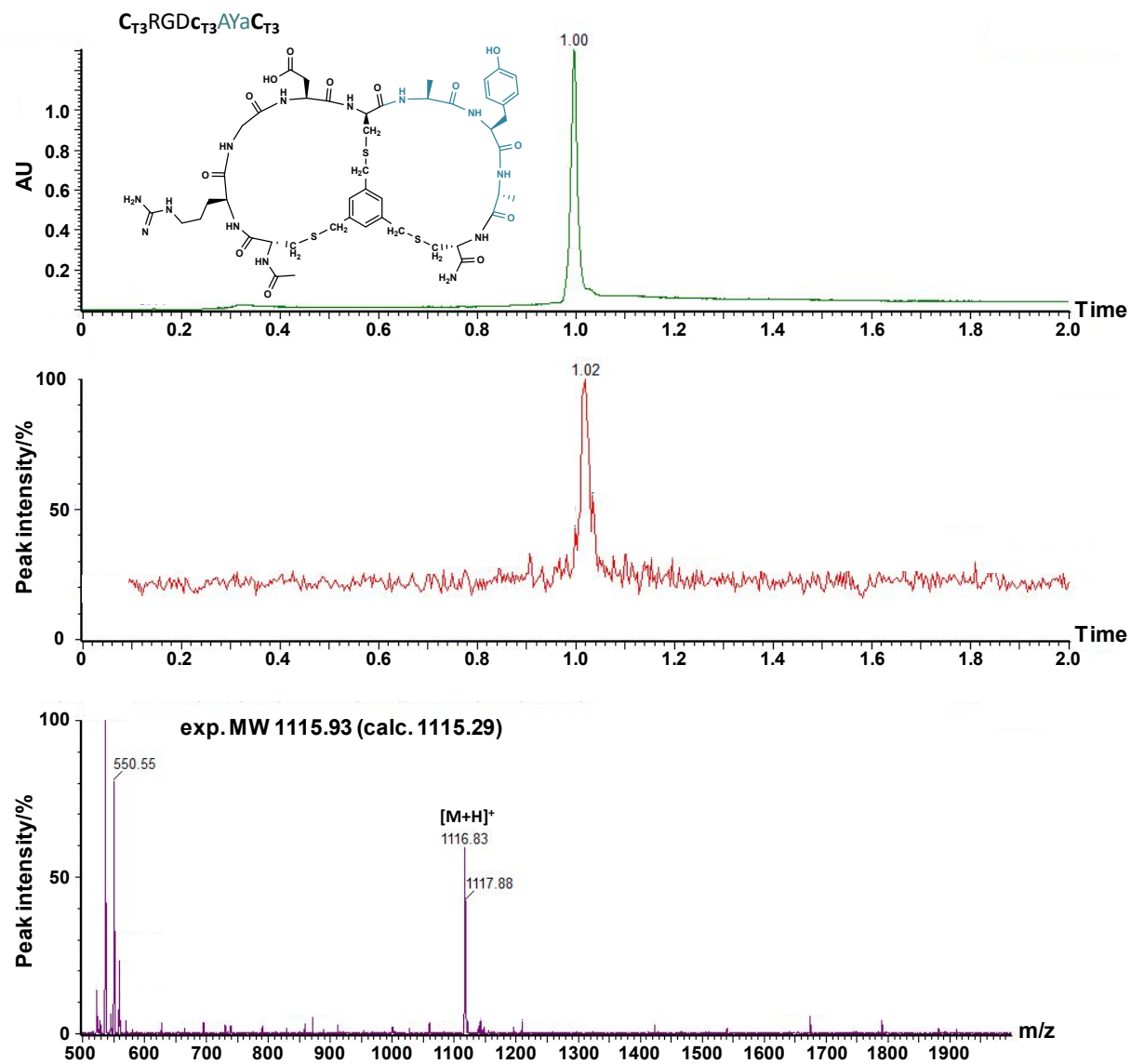


**Figure S-2:** UPLC/ESI-MS spectrum of purified bicyclic peptide **C<sub>T3</sub>RGDC<sub>T3</sub>AYaC<sub>T3</sub>** (top: UV detection at 215 nm, middle/bottom: ESI-MS detection).

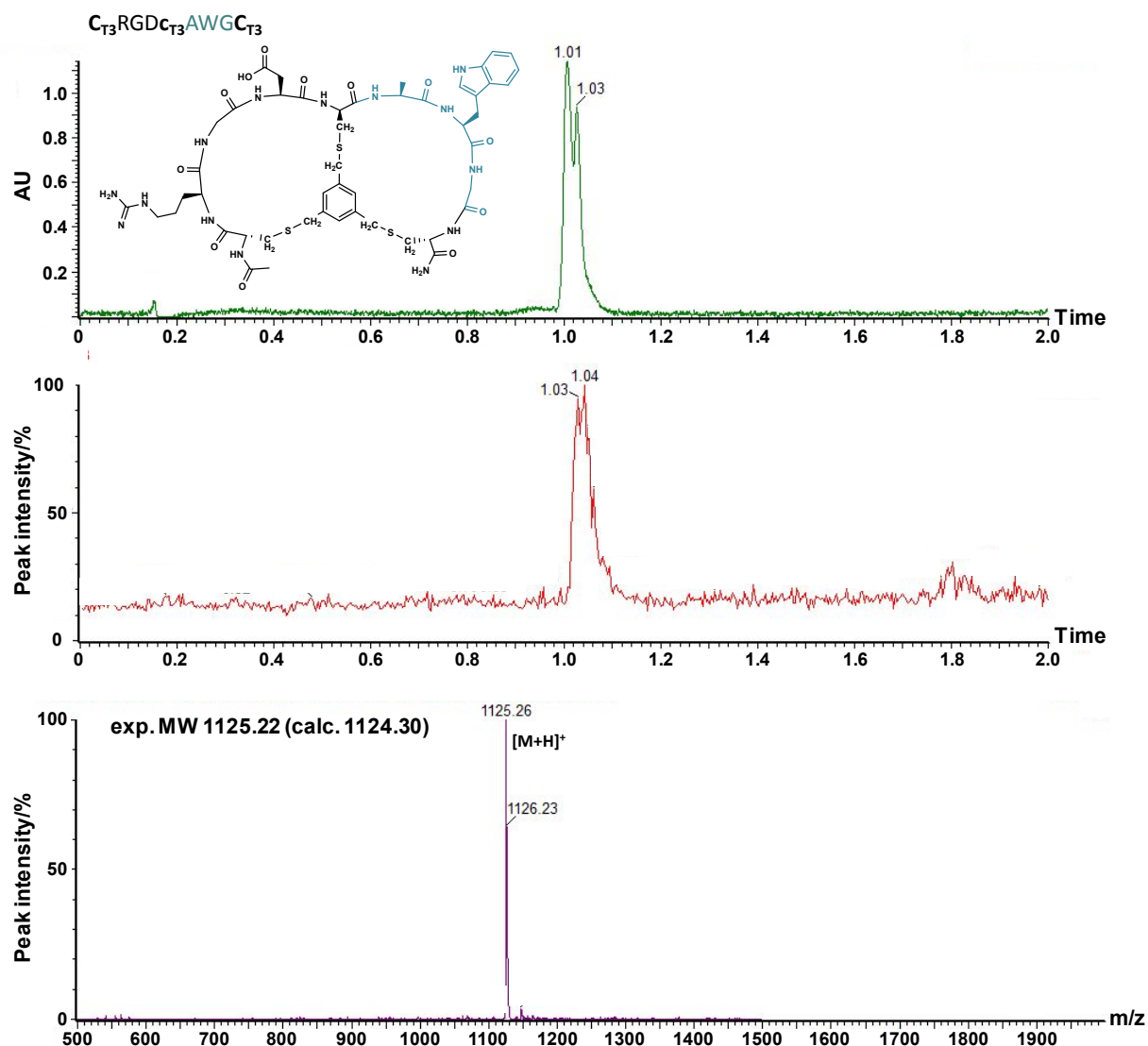


**Figure S-3:** UPLC/ESI-MS spectrum of purified bicyclic  $C_{T3}RGDC_{T3}AWGC_{T3}$  (top: UV detection at 215 nm, middle/bottom: ESI-MS detection).

### SPFS observation of affinity binding kinetics

**Optical system.** An optical system combining surface plasmon resonance (SPR) and surface plasmon enhanced fluorescence spectroscopy (SPFS) was used for direct investigation of affinity interaction of selected peptides and integrins. The Kretschmann configuration of attenuated total reflection method (**Figure S-4**) was used for the resonant excitation and interrogation of surface plasmons as described before in more detail.<sup>1</sup> Briefly, a laser beam (633 nm) was coupled to a high refractive index glass prism and glass substrate coated with SPR-active thin gold film, and optically matched to its base. The beam was made incident at the angle of incidence that was tuned close to  $\theta_{SPR}$  where surface plasmons are resonantly excited at the outer interface of gold surface. A flow cell was clamped against the gold sensor surface in order to flow liquid samples with a flow rate of 40  $\mu$ L/min. The reflected beam intensity was measured with a lockin amplifier (EG&G, USA) in order to track changes in SPR signal. The fluorescence signal excited via surface plasmons that was propagating from the sensor surface through the flow cell was collected by a lens with a numerical aperture about  $NA=2$ , and detected by a photomultiplier (H6240-01, Hamamatsu, Japan) connected

to a counter (53131A, Agilent, USA). The intensity of the excitation beam irradiating area on the sensor chip of about 1 mm<sup>2</sup> was reduced to 30-60 μW in order to reduce bleaching of Cy5 excited by the enhanced field intensity of surface plasmons. The fluorescence light emitted by Cy5 at wavelength of about 670 nm was spectrally separated from the excitation light (633 nm) by using a set of laser notch filters (XNF-632.8-25.0M, CVI Melles Griot, USA) and fluorescence band pass filters (670FS10-25, Andover Corporation Optical Filter, USA).

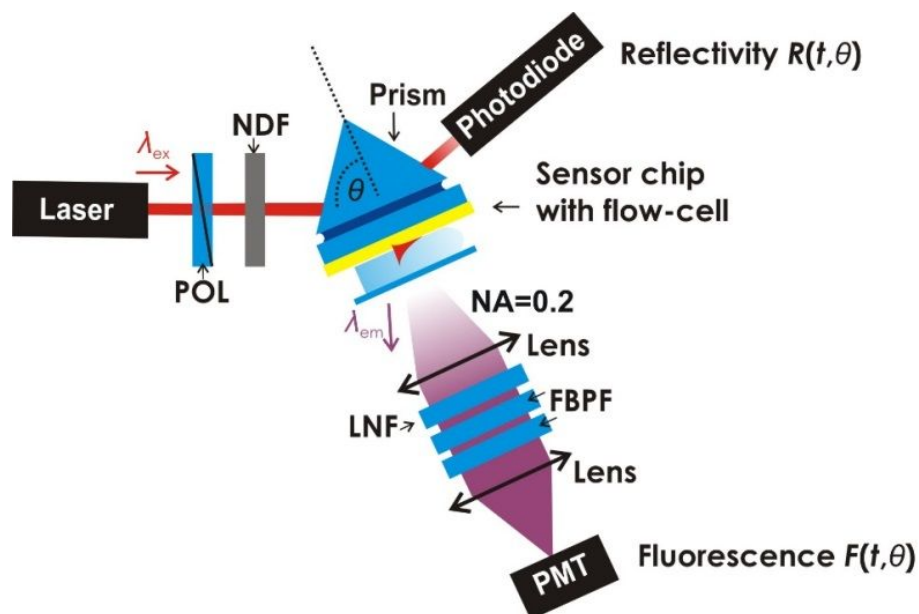


**Figure S-4.** Schematics of the optical instrument used for the surface plasmon resonance (SPR) and surface plasmon-enhanced fluorescence spectroscopy (SPFS) measurements with polarizer (POL), neutral density filter (NDF), laser notch filter (LNF), fluorescence bandpass filter (FBPF).

**Sensor chip preparation.** Sensor chips were prepared on BK7 glass substrates which were subsequently coated with 2 nm chromium and 50 nm gold films by thermal vacuum evaporation (Model HHV FL400, HHV Ltd, UK). Onto the gold surface integrin  $\alpha_5\beta_1$  was attached by using two surface architectures. The 2D architecture relied on a mixed self-assembled monolayer (SAM) that was formed by immersing the gold surface in a 1 mM ethanolic solution with a dithiol-PEG6-COOH and dithiol-PEG3, mixed at molar ratio of 1:9. After overnight incubation, the gold surface was rinsed with ethanol, dried in a stream of air, and stored under argon atmosphere. For the 3D architecture, a protocol for preparation of a thin hydrogel from poly(*N*-isopropylacrylamide)-based polymer was adopted based on our previous work.<sup>2</sup> Briefly, a thin hydrogel film was spin-coated (from an ethanol solution with polymer dissolved at a concentration of 0.5% w/w) on the gold surface, which was modified by a thiol-benzophenone SAM. The polymer film was dried overnight at 50 °C under vacuum, and the polymer chains were crosslinked to the gold surface via benzophenone units by irradiating the sample with UV light ( $\lambda=365$  nm) with an irradiation dose of 4 Jcm<sup>-2</sup> (UV lamp Bio-Link 365, Vilber Lourmat). Afterwards, the gold surface was rinsed with ethanol, dried in a stream of air, and stored under argon atmosphere.

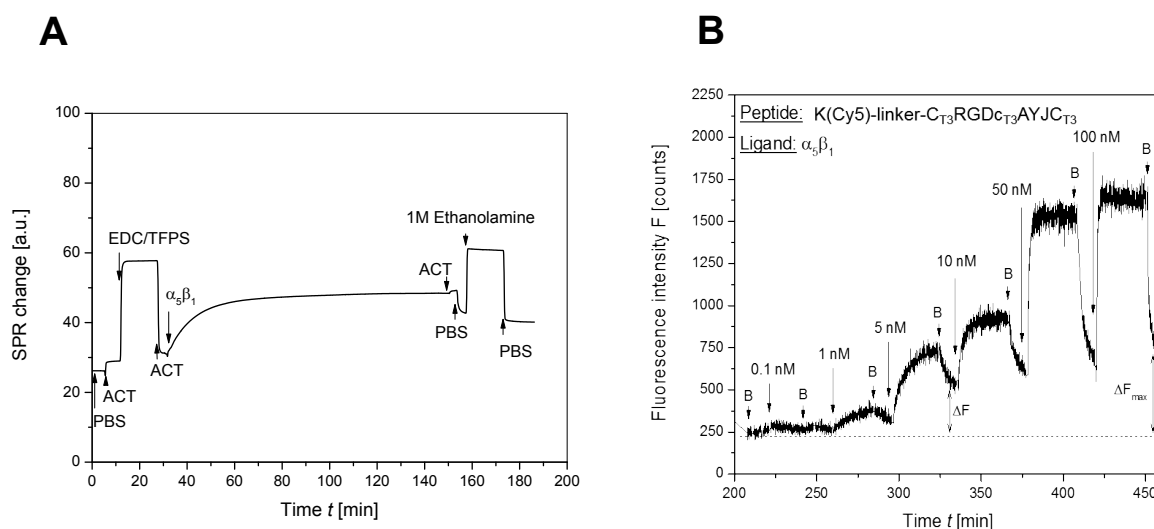


**Figure S-5.** Example of a) SPR sensorgram showing covalent immobilization of integrin  $\alpha_5\beta_1$  into a 3D hydrogel binding matrix, and b) fluorescence signal kinetics acquired upon titration of K(Cy5)-linker- $C_{T3}RGDc_{T3}AYJC_{T3}$  (J: D-Leu).

**Screening of single-loop CLIPS variants.** We also investigated if the RGD-loop size can further be optimized for higher  $\alpha_5\beta_1$ -affinity by synthesizing various monocyclic peptides comprising the sequences CRGDc, CGRGDc, CRGDSC, CVRGDfC, and CGRGDSC, followed by constraining these using various bis(bromomethyl)benzene scaffolds or via disulfide bond formation (**Figure S-6A**). Remarkably, the monocycle  $C_{mT2}RGDc_{mT2}$  entirely lost the inhibition capability (<0%) compared to the bicycle  $C_{T3}RGDc_{T3}AYJC_{T3}$  (85%), which highlights the essential role of the second loop for  $\alpha_5\beta_1$ -inhibition (**Figure S-6B**). Only monocycle  $C_{mT2}GRGDc_{mT2}$  showed a measurable (i.e. 10%) inhibition, whereas the remaining peptides containing ‘RGD’, ‘RGDS’, ‘VRGDF’ or ‘GRGDS’ did not show any binding.

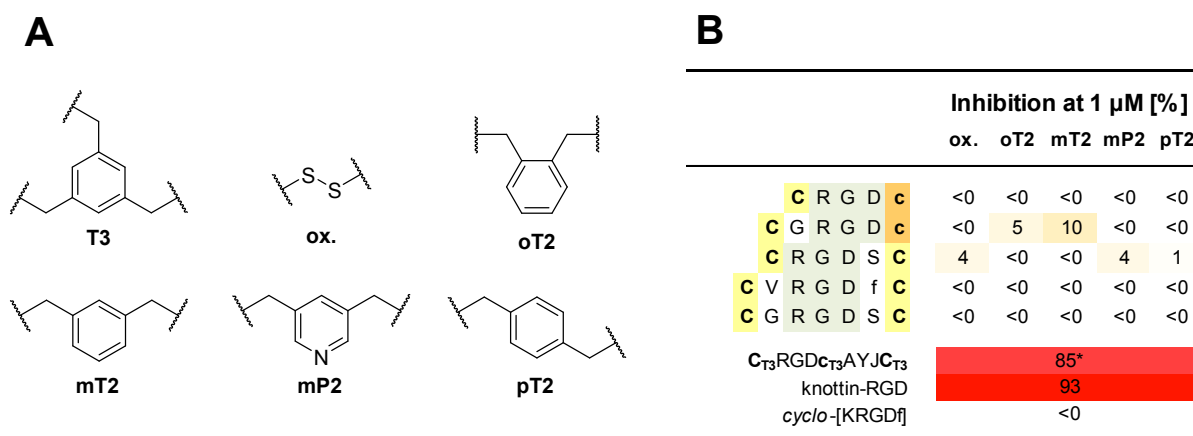


**Figure S-6.** (A) Overview of bi- and trivalent scaffolds for the synthesis of mono- and bicyclic peptides; (B)  $\alpha_5\beta_1$ -inhibitory capacities of various monocyclic CLIPS-variants. The value marked with an asterisk was taken from an IC50 inhibition curve rather than being a fixed-point measurement. Inhibition values were obtained via nonlinear regression analysis based on AU values without bicyclic competitor (0%,  $OD_{405} \sim 0.9-1.5$ ) or non-labeled knottin-RGD at 30  $\mu$ M (100 %,  $OD_{405} \sim 0.2$ ) being present.

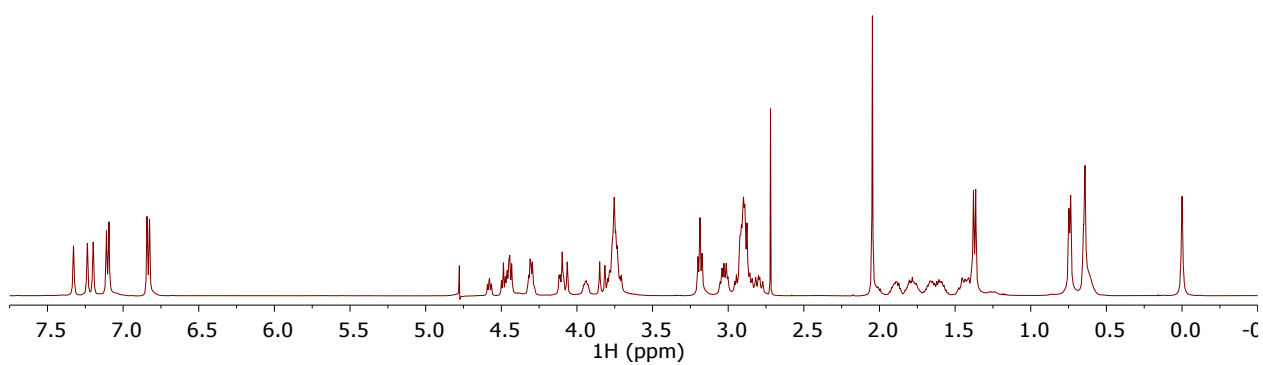


**Figure S-7.**  $^1\text{H}$  NMR spectrum of  $\text{C}_{\text{T}3}\text{RGDc}_{\text{T}3}\text{AYJC}_{\text{T}3}$  (J: D-Leu) acquired with composite pulse presaturation. The spectrum was referenced to the trimethylsilyl peak of the internal standard of DSS at 0.0 ppm. NS = 64, D1 = 3 s, AQ = 3.3 s.

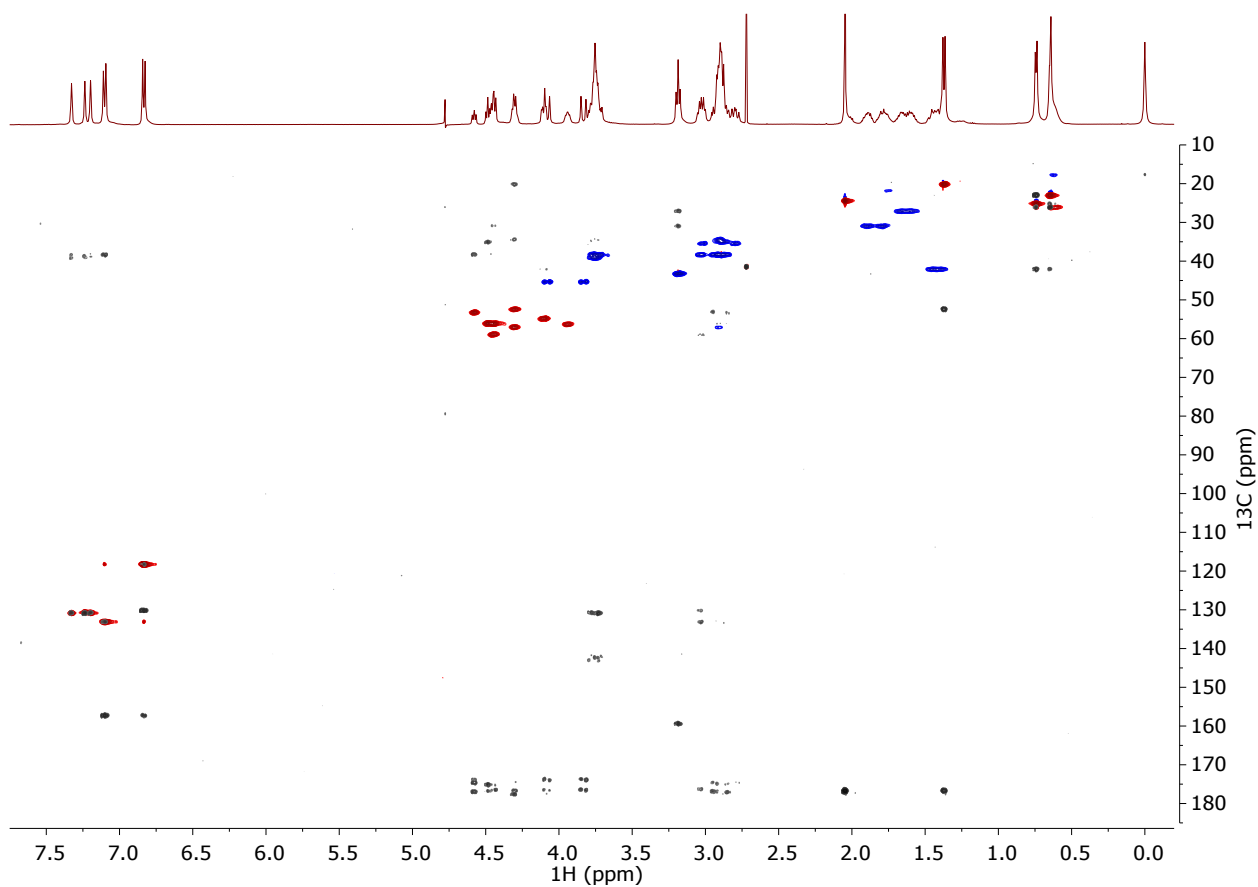


**Figure S-8.**  $^1\text{H}$ - $^{13}\text{C}$  HSQCED (red/blue) and HMBC (grey) spectrum of  $\text{C}_{\text{T}3}\text{RGDc}_{\text{T}3}\text{AYJC}_{\text{T}3}$  (J: D-Leu) acquired with HSQCED: NS = 2, D1 = 1.5 s, AQ = 0.17 s and HMBC: NS = 4, D1 = 1.5 s, AQ = 0.34 s.

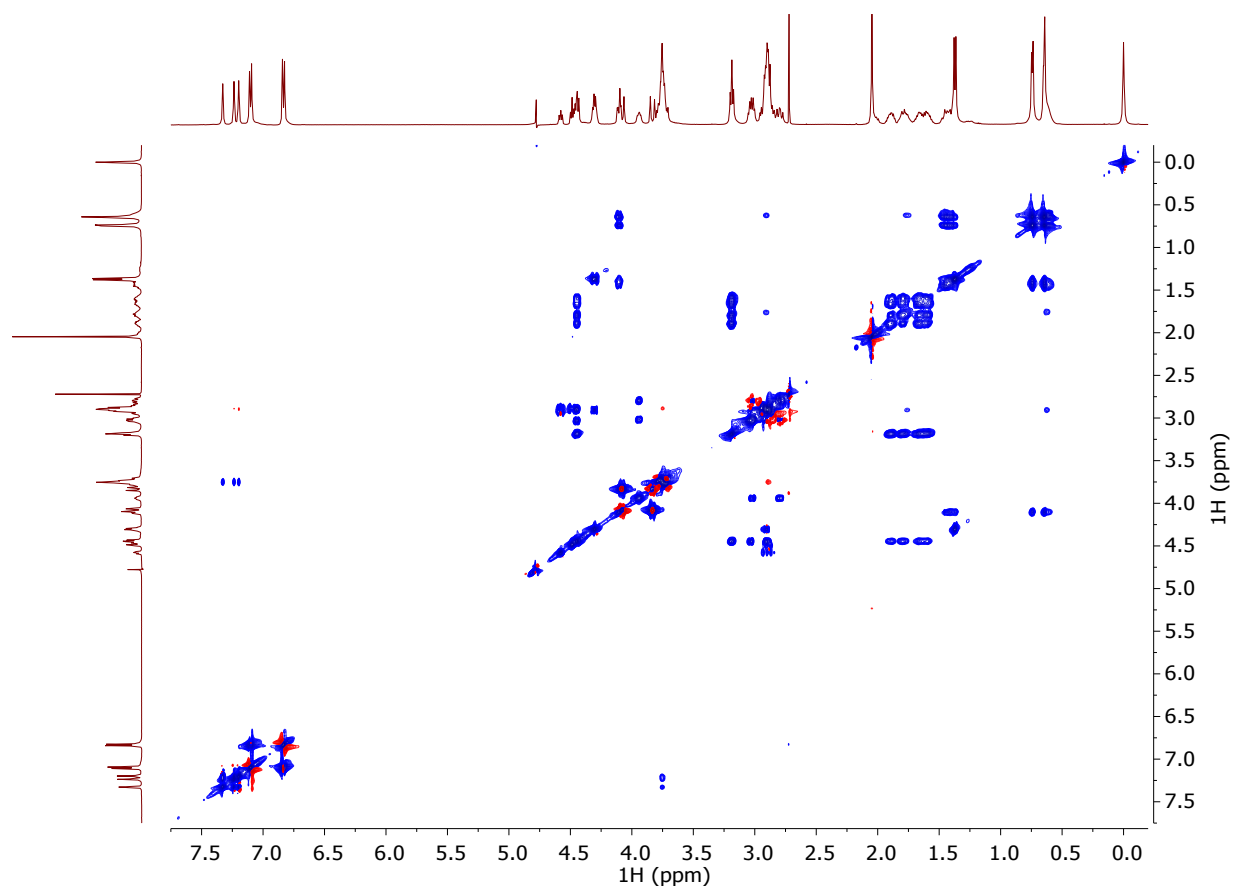


**Figure S-9.**  $^1\text{H}$ - $^1\text{H}$  TOCSY spectrum of  $\text{C}_{\text{T}3}\text{RGDC}_{\text{T}3}\text{AYJC}_{\text{T}3}$  (J: D-Leu) acquired with NS = 8, TD1 = 512, D1 = 2 s, AQ = 0.20 s, and 100 ms of mix time.



## First generation screening of 672 random-diversity peptides

**Table S-3.** Absorbance values of library screening for 1<sup>st</sup> generation of  $\alpha_5\beta_1$ -binders. Motif: C<sub>T3</sub>XXXC<sub>T3</sub>RGDC<sub>T3</sub>. c<sub>Integrin</sub>: 0.5  $\mu$ g/mL, c<sub>biotinylated knottin-RGD</sub>: 0.2  $\mu$ M, c<sub>peptides</sub>: 10  $\mu$ M. Best five hits are in bold print.

	XXX	A.U.		XXX	A.U.		XXX	A.U.		XXX	A.U.
A1	QWG	0.81	C1	PNV	0.86	E1	PHI	1.05	G1	LPD	1.01
A2	AIP	0.81	C2	PYI	0.87	E2	YPS	0.97	G2	RLG	0.81
A3	DGY	0.79	C3	TPT	0.83	E3	TRV	0.95	G3	YIY	1.04
A4	ILP	0.95	C4	NWG	0.79	E4	VVR	1.61	G4	FRA	0.88
A5	VSL	0.75	C5	FTQ	0.85	E5	NST	1.11	G5	LTI	1.06
A6	DEW	0.76	C6	QYL	0.87	E6	FLW	0.98	G6	APS	0.84
<b>A7</b>	<b>YEE</b>	<b>0.66</b>	C7	WGD	1.00	E7	NSY	0.99	G7	RDP	0.99
<b>A8</b>	<b>PLE</b>	<b>0.63</b>	C8	ISY	0.88	E8	ILK	1.89	G8	DHL	0.83
<b>A9</b>	<b>KKP</b>	<b>0.72</b>	C9	EIG	0.80	E9	SDQ	0.91	G9	NDA	0.86
A10	QGS	0.77	C10	WFH	0.84	E10	WQY	1.47	G10	DAD	0.84
A11	HVK	0.93	C11	NKP	0.78	E11	YYT	1.02	G11	NYA	0.89
A12	RNS	1.01	C12	PNE	0.79	E12	NVA	1.06	G12	EDT	0.93
B1	DTI	0.86	<b>D1</b>	<b>KTN</b>	<b>0.70</b>	F1	NWQ	0.95	H1	WYV	1.12
B2	QAK	0.90	D2	GYE	0.86	F2	TFI	1.40	H2	QSL	0.92
B3	WSL	0.85	D3	SYD	0.99	F3	QRG	0.94	H3	TIH	1.17
B4	RAA	0.88	D4	IEE	1.03	F4	LDW	0.95	H4	GLA	1.00
B5	KHI	0.88	D5	HLQ	1.09	F5	PHL	0.92	H5	LWI	1.67
B6	RGS	0.78	D6	GNS	0.89	F6	KID	0.90	H6	GLY	1.01
B7	IIV	1.04	D7	IRW	0.85	F7	RQV	0.94	H7	SSG	1.09
B8	WFT	0.78	D8	IIG	0.86	F8	KRW	3.05	H8	GWN	1.05
B9	RSK	1.11	D9	DFP	0.81	F9	QAD	0.96	H9	SWS	0.98
B10	GHF	0.77	D10	PPG	0.81	F10	ERV	0.91	H10	QIH	0.99
<b>B11</b>	<b>QDH</b>	<b>0.74</b>	D11	QGI	0.88	F11	YLT	1.07	H11	KQL	0.94
B12	HEQ	0.76	D12	FSH	1.39	F12	RWD	0.86	H12	GYG	1.06

references: knottin-RGD (5 $\mu$ M): 0.19, no peptide: 1.12.

**Table S-4.** Absorbance values of library screening for 1<sup>st</sup> generation of  $\alpha_5\beta_1$ -binders. Motif:  $C_{T3}XXXC_{T3}RGDC_{T3}$ .  $c_{Integrin}$ : 0.5  $\mu\text{g/mL}$ ,  $c_{\text{biotinylated knottin-RGD}}$ : 0.2  $\mu\text{M}$ ,  $c_{\text{peptides}}$ : 10  $\mu\text{M}$ . Best five hits are in bold print.

	<b>XXX</b>	<b>A.U.</b>		<b>XXX</b>	<b>A.U.</b>		<b>XXX</b>	<b>A.U.</b>		<b>XXX</b>	<b>A.U.</b>
A1	QWG	1.50	C1	PNV	1.56	E1	PHI	1.64	G1	LPD	1.70
A2	AIP	2.00	C2	PYI	1.76	<b>E2</b>	<b>YPS</b>	<b>1.36</b>	G2	RLG	3.81
A3	DGY	1.99	C3	TPT	1.63	E3	TRV	2.40	G3	YIY	1.95
A4	ILP	1.81	<b>C4</b>	<b>NWG</b>	<b>1.38</b>	E4	VVR	1.99	G4	FRA	1.79
<b>A5</b>	<b>VSL</b>	<b>1.46</b>	C5	FTQ	1.84	E5	NST	2.06	G5	LTI	1.99
A6	DEW	1.57	C6	QYL	2.23	E6	FLW	2.19	G6	APS	1.97
A7	YEE	2.24	C7	WGD	1.74	E7	NSY	1.73	G7	RDP	1.84
<b>A8</b>	<b>PLE</b>	<b>1.49</b>	C8	ISY	2.24	E8	ILK	3.56	G8	DHL	1.79
A9	KKP	2.31	C9	EIG	1.80	E9	SDQ	1.92	G9	NDA	1.90
<b>A10</b>	<b>QGS</b>	<b>1.33</b>	C10	WFH	1.88	E10	WQY	1.77	G10	DAD	2.11
A11	HVK	3.20	C11	NKP	1.69	E11	YYT	2.01	G11	NYA	2.06
A12	RNS	1.73	C12	PNE	1.64	E12	NVA	2.00	G12	EDT	2.00
B1	DTI	2.07	D1	KTN	2.44	F1	NWQ	1.68	H1	WYV	2.53
B2	QAK	3.18	D2	GYE	1.90	F2	TFI	2.09	H2	QSL	1.79
B3	WSL	1.61	D3	SYD	2.06	F3	QRG	1.94	H3	TIH	2.18
B4	RAA	2.33	D4	IEE	1.88	F4	LDW	2.07	H4	GLA	1.98
B5	KHI	2.13	D5	HLQ	1.64	F5	PHL	1.74	H5	LWI	2.67
B6	RGS	1.74	D6	GNS	1.85	F6	KID	1.66	H6	GLY	1.66
B7	IIV	1.74	D7	IRW	1.91	F7	RQV	3.03	H7	SSG	1.79
B8	WFT	1.89	D8	IIG	1.80	F8	KRW	3.82	H8	GWN	1.87
B9	RSK	1.96	D9	DFP	1.93	F9	QAD	2.21	H9	SWS	1.74
B10	GHF	1.78	D10	PPG	2.02	F10	ERV	1.93	H10	QIH	2.15
B11	QDH	1.65	D11	QGI	1.57	F11	YLT	2.04	H11	KQL	2.07
B12	HEQ	1.53	D12	FSH	1.84	F12	RWD	1.81	H12	GYG	1.94

references: knottin-RGD (5 $\mu\text{M}$ ): 0.25, no peptide: 2.08.

**Table S-5.** Absorbance values of library screening for 1<sup>st</sup> generation of  $\alpha_5\beta_1$ -binders. Motif: C<sub>T3</sub>XXXc<sub>T3</sub>RGDC<sub>T3</sub>. c<sub>Integrin</sub>: 0.5  $\mu$ g/mL, c<sub>biotinylated knottin-RGD</sub>: 0.2  $\mu$ M, c<sub>peptides</sub>: 10  $\mu$ M. Best five hits are in bold print.

	XXX	A.U.	XXX	A.U.	XXX	A.U.	XXX	A.U.
A1	QWG	1.60	C1	PNV	1.46	E1	PHI	1.82
A2	AIP	1.61	C2	PYI	1.72	E2	YPS	1.92
A3	DGY	1.67	C3	TPT	1.97	E3	TRV	1.51
A4	ILP	1.80	C4	NWG	1.81	E4	VVR	2.16
A5	VSL	1.60	C5	FTQ	1.74	E5	NST	1.60
A6	DEW	1.52	<b>C6</b>	<b>QYL</b>	<b>1.40</b>	E6	FLW	2.46
A7	YEE	3.45	C7	WGD	1.99	E7	NSY	1.91
A8	PLE	1.65	C8	ISY	2.23	E8	ILK	2.05
A9	KKP	2.95	C9	EIG	2.17	E9	SDQ	1.56
A10	QGS	1.57	C10	WFH	2.13	E10	WQY	2.11
A11	HVK	1.63	C11	NKP	1.55	<b>E11</b>	<b>YYT</b>	<b>1.38</b>
A12	RNS	1.86	C12	PNE	2.15	E12	NVA	1.97
B1	DTI	2.01	D1	KTN	1.84	F1	NWQ	2.18
B2	QAK	1.48	D2	GYE	1.94	F2	TFI	2.21
B3	WSL	1.77	D3	SYD	1.62	F3	QRG	1.77
B4	RAA	2.08	D4	IEE	2.14	<b>F4</b>	<b>LDW</b>	<b>1.45</b>
B5	KHI	1.68	D5	HLQ	1.82	F5	PHL	1.91
B6	RGS	1.56	<b>D6</b>	<b>GNS</b>	<b>1.43</b>	F6	KID	1.53
B7	IIV	1.82	D7	IRW	1.90	F7	RQV	1.55
B8	WFT	2.02	D8	IIG	2.22	F8	KRW	2.79
B9	RSK	2.05	D9	DFP	2.04	F9	QAD	1.77
B10	GHF	1.77	D10	PPG	1.95	F10	ERV	2.01
B11	QDH	1.50	D11	QGI	2.10	F11	YLT	2.21
B12	HEQ	1.66	D12	FSH	2.10	F12	RWD	2.08
G1	LPD	2.11						
G2	RLG	2.04						
G3	YTY	1.84						
G4	FRA	1.85						
<b>G5</b>	<b>LTI</b>	<b>1.41</b>						
G6	APS	1.75						
G7	RDP	1.66						
G8	DHL	1.99						
G9	NDA	2.11						
G10	DAD	2.03						
G11	NYA	2.50						
G12	EDT	1.88						
H1	WYV	1.83						
H2	QSL	1.89						
H3	TIH	1.61						
H4	GLA	1.69						
H5	LWI	2.29						
H6	GLY	1.48						
H7	SSG	2.09						
H8	GWN	2.05						
H9	SWS	1.83						
H10	QIH	2.05						
H11	KQL	1.88						
H12	GYG	1.72						

references: knottin-RGD (5 $\mu$ M): 0.25, no peptide: 2.08.

**Table S-6.** Absorbance values of library screening for 1<sup>st</sup> generation of  $\alpha_5\beta_1$ -binders. Motif: C<sub>T3</sub>XXXC<sub>T3</sub>RGDC<sub>T3</sub>. c<sub>Integrin</sub>: 0.5  $\mu\text{g/mL}$ , c<sub>biotinylated knottin-RGD</sub>: 0.2  $\mu\text{M}$ , c<sub>peptides</sub>: 10  $\mu\text{M}$ . Best five hits are in bold print.

	XXX	A.U.		XXX	A.U.		XXX	A.U.		XXX	A.U.
A1	QWG	0.86	C1	PNV	1.23	E1	PHI	1.21	G1	LPD	1.22
A2	AIP	0.97	C2	PYI	1.03	E2	YPS	1.04	G2	RLG	0.99
A3	DGY	0.82	C3	TPT	1.02	E3	TRV	1.97	G3	YTY	2.01
A4	ILP	1.72	C4	NWG	0.93	E4	VVR	3.68	G4	FRA	1.06
A5	VSL	2.56	C5	FTQ	1.02	E5	NST	0.77	G5	LTI	2.64
A6	DEW	0.86	<b>C6</b>	<b>QYL</b>	<b>0.74</b>	E6	FLW	1.41	G6	APS	1.05
A7	YEE	0.81	C7	WGD	0.85	E7	NSY	1.08	G7	RDP	0.97
A8	PLE	0.97	C8	ISY	0.87	E8	ILK	1.82	G8	DHL	1.35
A9	KKP	1.02	C9	EIG	0.82	E9	SDQ	0.84	G9	NDA	0.83
A10	QGS	0.77	C10	WFH	2.82	E10	WQY	0.85	G10	DAD	0.96
A11	HVK	2.57	C11	NKP	1.16	E11	YYT	0.87	G11	NYA	0.89
A12	RNS	0.89	C12	PNE	0.87	E12	NVA	1.41	G12	EDT	1.06
B1	DTI	1.27	D1	KTN	1.27	F1	NWQ	1.47	H1	WYV	1.05
B2	QAK	0.85	<b>D2</b>	<b>GYE</b>	<b>0.63</b>	F2	TFI	1.22	H2	QSL	2.26
B3	WSL	0.93	D3	SYD	0.80	F3	QRG	0.87	H3	TIH	1.41
B4	RAA	0.93	D4	IEE	0.81	F4	LDW	0.76	H4	GLA	0.99
B5	KHI	2.65	D5	HLQ	0.91	F5	PHL	0.94	H5	LWI	3.51
B6	RGS	1.09	<b>D6</b>	<b>GNS</b>	<b>0.71</b>	F6	KID	1.03	H6	GLY	1.05
B7	IIV	1.51	D7	IRW	1.41	F7	RQV	1.22	H7	SSG	1.01
B8	WFT	3.76	D8	IIG	1.20	F8	KRW	1.60	H8	GWN	0.97
B9	RSK	2.82	<b>D9</b>	<b>DFP</b>	<b>0.63</b>	F9	QAD	0.96	H9	SWS	1.16
B10	GHF	0.85	<b>D10</b>	<b>PPG</b>	<b>0.72</b>	F10	ERV	1.11	H10	QIH	2.88
B11	QDH	0.84	D11	QGI	1.90	F11	YLT	1.54	H11	KQL	0.84
B12	HEQ	0.81	D12	FSH	0.86	F12	RWD	1.85	H12	GYG	1.27

references: knottin-RGD (5 $\mu\text{M}$ ): 0.19, no peptide: 1.12

**Table S-7.** Absorbance values of library screening for 1<sup>st</sup> generation of  $\alpha_5\beta_1$ -binders. Motif: C<sub>T3</sub>RGDc<sub>T3</sub>XXXC<sub>T3</sub>. c<sub>Integrin</sub>: 0.5  $\mu$ g/mL, c<sub>biotinylated knottin-RGD</sub>: 0.2  $\mu$ M, c<sub>peptides</sub>: 10  $\mu$ M. Best five hits are in bold print.

	XXX	A.U.		XXX	A.U.		XXX	A.U.		XXX	A.U.
A1	FII	0.49	C1	SWH	0.54	E1	YPS	0.89	G1	EVN	0.25
A2	TWN	0.29	C2	RSL	0.29	E2	RVT	0.30	G2	HDA	0.26
A3	EQD	0.31	C3	RSY	0.27	E3	RQQ	0.59	G3	NYA	0.26
A4	WFH	0.35	C4	ARS	0.29	E4	FWK	1.97	G4	DTI	0.26
A5	FPF	1.38	C5	LQP	0.26	E5	RWW	1.66	G5	KPE	0.28
A6	KGR	3.65	C6	PTP	0.26	E6	SLL	0.25	G6	KPD	0.28
A7	TVD	0.25	<b>C7</b>	<b>NWG</b>	<b>0.17</b>	E7	GRI	0.30	G7	AKN	0.64
A8	HSW	0.34	C8	TQS	0.24	E8	QSY	0.22	G8	WPA	1.72
A9	ATH	0.58	C9	LSE	0.21	E9	NWQ	0.23	<b>G9</b>	<b>AYG</b>	<b>0.15</b>
A10	NVT	0.28	C10	GSA	0.25	E10	FIH	0.25	G10	VSW	0.31
A11	VKI	3.35	C11	PLI	1.62	E11	GFH	0.32	G11	QIH	0.23
A12	GVS	0.24	C12	GKF	3.41	E12	TFP	0.27	G12	QLP	0.24
B1	DEW	0.28	D1	HYI	0.27	F1	SWK	0.83	H1	GAY	0.28
B2	EEQ	0.24	D2	GIK	0.51	<b>F2</b>	<b>WQI</b>	<b>0.20</b>	H2	SHQ	0.28
B3	EDE	0.28	<b>D3</b>	<b>QGY</b>	<b>0.20</b>	F3	LGD	0.23	H3	FFR	0.61
B4	VTH	0.20	D4	SYD	0.21	F4	SVE	0.22	H4	WVY	0.33
B5	RFI	0.92	D5	EEY	0.30	F5	IHV	0.49	H5	RPY	0.30
B6	RHD	0.32	<b>D6</b>	<b>QNT</b>	<b>0.20</b>	F6	RWD	0.24	H6	SGN	0.31
B7	HWT	0.28	D7	TDQ	0.21	F7	PDI	0.22	H7	ENH	0.29
B8	IQW	0.30	D8	WIV	0.72	F8	GRN	0.27	H8	GVA	0.28
B9	GRA	0.28	D9	GTS	0.22	F9	WRT	0.22	H9	PYI	1.51
B10	KHI	0.57	D10	LAY	0.34	F10	RLR	3.56	H10	WLS	0.81
B11	GSR	1.47	D11	HIF	0.28	F11	HGP	0.21	H11	WPE	0.28
B12	VVH	0.30	D12	SPH	0.20	F12	TGV	0.22	H12	NST	0.27

references: knottin-RGD (5 $\mu$ M): 0.15, no peptide: 0.33.

**Table S-8.** Absorbance values of library screening for 1<sup>st</sup> generation of  $\alpha_5\beta_1$ -binders. Motif:  $c_{T3}RGDC_{T3}XXX_{T3}$ .  $c_{Integrin}$ : 0.5  $\mu\text{g/mL}$ ,  $c_{\text{biotinylated knottin-RGD}}$ : 0.2  $\mu\text{M}$ ,  $c_{\text{peptides}}$ : 10  $\mu\text{M}$ . Best five hits are in bold print.

	XXX	A.U.		XXX	A.U.		XXX	A.U.		XXX	A.U.
A1	FII	0.65	C1	SWH	0.38	E1	YPS	0.31	G1	EVN	0.36
A2	TWN	0.46	C2	RSL	0.29	E2	RVT	2.19	G2	HDA	0.29
A3	EQD	0.35	C3	RSY	1.14	E3	RQQ	0.38	G3	NYA	0.35
A4	WFH	0.39	C4	ARS	0.91	E4	FWK	1.21	G4	DTI	0.28
A5	FPF	0.43	C5	LQP	0.26	E5	RWW	1.68	G5	KPE	0.28
A6	KGR	0.37	C6	PTP	0.27	E6	SLL	0.64	G6	KPD	0.30
A7	TVD	0.31	C7	NWG	0.25	E7	GRI	0.32	G7	AKN	0.34
A8	HSW	0.32	C8	TQS	0.29	E8	QSY	0.32	G8	WPA	0.32
A9	ATH	0.32	C9	LSE	0.27	E9	NWQ	0.26	G9	AYG	0.30
A10	NVT	0.58	C10	GSA	0.27	E10	FIH	1.47	G10	VSU	0.48
A11	VKI	1.26	C11	PLI	0.42	E11	GFH	0.52	G11	QIH	0.27
A12	GVS	0.32	C12	GKF	1.00	E12	TFP	0.61	<b>G12</b>	<b>QLP</b>	<b>0.25</b>
B1	DEW	0.35	D1	HUI	0.33	F1	SWK	0.38	H1	GAY	0.33
B2	EEQ	0.36	D2	GIK	0.43	F2	WQI	0.30	H2	SHQ	0.30
B3	EDE	0.33	<b>D3</b>	<b>QGY</b>	<b>0.25</b>	F3	LGD	0.27	H3	FFR	0.88
B4	VTH	0.30	D4	SYD	0.27	F4	SVE	0.27	H4	WVY	1.37
B5	RFI	2.35	D5	EEY	0.44	F5	IHV	0.54	H5	RPY	0.34
B6	RHD	0.31	D6	QNT	0.29	F6	RWD	0.25	H6	SGN	0.33
B7	HWT	0.46	D7	TDQ	0.25	<b>F7</b>	<b>PDI</b>	<b>0.24</b>	H7	ENH	0.28
B8	IQW	0.37	D8	WIV	0.63	F8	GRN	0.28	H8	GVA	0.30
B9	GRA	0.36	D9	GTS	0.28	F9	WRT	3.09	H9	PYI	0.44
B10	KHI	0.44	D10	LAY	0.46	F10	RLR	3.29	H10	WLS	0.58
B11	GSR	0.28	D11	HIF	0.52	F11	HGP	0.27	<b>H11</b>	<b>WPE</b>	<b>0.24</b>
B12	VVH	2.28	D12	SPH	0.29	F12	TGV	0.29	<b>H12</b>	<b>NST</b>	<b>0.24</b>

references: knottin-RGD (5 $\mu\text{M}$ ): 0.16, no peptide: 0.33.

**Table S-9.** Absorbance values of library screening for 1<sup>st</sup> generation of  $\alpha_5\beta_1$ -binders. Motif:  $c_{T3}RGDc_{T3}XXXc_{T3}$ .  $c_{Integrin}$ : 0.5  $\mu\text{g/mL}$ ,  $c_{\text{biotinylated knottin-RGD}}$ : 0.2  $\mu\text{M}$ ,  $c_{\text{peptides}}$ : 10  $\mu\text{M}$ . Best five hits are in bold print.

	XXX	A.U.		XXX	A.U.		XXX	A.U.		XXX	A.U.
A1	FII	0.57	C1	SWH	0.43	E1	YPS	0.41	G1	EVN	0.49
A2	TWN	0.46	C2	RSL	0.50	E2	RVT	0.41	G2	HDA	0.47
A3	EQD	0.47	C3	RSY	0.48	E3	RQQ	0.46	G3	NYA	0.48
A4	WFH	0.46	C4	ARS	0.50	E4	FWK	0.42	G4	DTI	0.46
A5	FPF	0.43	C5	LQP	0.44	<b>E5</b>	<b>RWW</b>	<b>0.35</b>	G5	KPE	0.43
A6	KGR	3.87	C6	PTP	0.50	<b>E6</b>	<b>SLL</b>	<b>0.38</b>	G6	KPD	0.47
A7	TVD	0.43	C7	NWG	0.51	E7	GRI	0.44	G7	AKN	0.49
A8	HSW	0.48	C8	TQS	0.51	<b>E8</b>	<b>QSY</b>	<b>0.37</b>	G8	WPA	0.43
A9	ATH	0.57	C9	LSE	0.40	E9	NWQ	0.45	G9	AYG	0.39
A10	NVT	0.43	C10	GSA	0.49	E10	FIH	0.43	G10	VSW	0.44
A11	VKI	0.96	C11	PLI	0.50	E11	GFH	0.45	G11	QIH	0.74
A12	GVS	0.48	C12	GKF	0.54	E12	TFP	0.39	G12	QLP	0.41
B1	DEW	0.40	D1	HYI	0.39	F1	SWK	0.59	H1	GAY	0.49
B2	EEQ	0.47	D2	GIK	1.07	F2	WQI	0.43	H2	SHQ	0.49
B3	EDE	0.46	D3	QGY	0.43	F3	LGD	0.44	H3	FFR	0.49
B4	VTH	0.45	D4	SYD	0.42	F4	SVE	0.47	H4	WVY	0.42
B5	RFI	0.44	D5	EEY	1.27	F5	IHV	0.44	H5	RPY	0.42
B6	RHD	0.48	<b>D6</b>	<b>QNT</b>	<b>0.37</b>	F6	RWD	0.43	H6	SGN	0.42
B7	HWT	0.43	D7	TDQ	0.41	F7	PDI	0.44	H7	ENH	0.43
B8	IQW	0.42	D8	WIV	0.91	F8	GRN	0.48	H8	GVA	0.47
B9	GRA	1.30	D9	GTS	0.43	F9	WRT	0.56	H9	PYI	0.56
B10	KHI	0.45	<b>D10</b>	<b>LAY</b>	<b>0.34</b>	F10	RLR	2.21	H10	WLS	0.43
B11	GSR	1.60	D11	HIF	0.38	F11	HGP	0.42	H11	WPE	0.41
B12	VVH	0.49	D12	SPH	0.41	F12	TGV	0.48	H12	NST	0.45

references: knottin-RGD (5 $\mu\text{M}$ ): 0.16, no peptide: 0.51.

## Second generation screening of 197 peptides

**Table S-10.** Absorbance values of library screening for 2<sup>nd</sup> generation of  $\alpha_5\beta_1$ -binders. Motif:  $C_{T3}RGDC_{T3}XXXC_{T3}$ .  $c_{Integrin}$ : 0.49  $\mu\text{g/mL}$ ,  $c_{\text{biotinylated knottin-RGD}}$ : 0.2  $\mu\text{M}$ ,  $c_{\text{peptides}}$ : 5  $\mu\text{M}$ . Best five hits are in bold print.

	<b>XXX</b>	<b>A.U.</b>		<b>XXX</b>	<b>A.U.</b>		<b>XXX</b>	<b>A.U.</b>		<b>XXX</b>	<b>A.U.</b>
A1	DYG	1.82	C1	iYG	1.75	E1	A5G	0.81	G1	AYW	2.45
A2	EYG	1.53	C2	9YG	1.41	E2	A6G	0.74	G2	AYY	2.33
A3	FYG	1.23	C3	aYG	0.92	E3	A7G	0.64	G3	AY3	1.54
A4	GYG	1.51	C4	RGD	1.50	E4	A8G	0.98	G4	AY4	2.21
A5	HYG	1.47	C5	AAG	0.66	E5	AfG	1.33	G5	AY5	1.49
<b>A6</b>	<b>IYG</b>	<b>0.52</b>	C6	ADG	0.91	E6	AiG	1.05	G6	AY6	2.10
A7	KYG	1.54	C7	AEG	0.68	E7	A9G	1.15	G7	AY7	2.79
A8	LYG	0.89	C8	AFG	0.66	E8	AaG	1.13	G8	AY8	1.07
A9	NYG	0.91	C9	AGG	1.97	E9	AyG	1.04	G9	AYf	1.58
A10	PYG	1.35	C10	AGG	1.19	E10	AYA	0.93	G10	AYi	0.56
A11	QYG	0.61	C11	AIG	0.71	E11	AYD	0.94	G11	AY9	0.64
A12	RYG	1.95	C12	AKG	1.17	E12	AYE	0.82	G12	AYa	0.54
B1	SYG	0.97	D1	ALG	0.81	F1	AYF	1.65			
B2	TYG	0.95	D2	ANG	1.13	F2	AYH	1.61			
<b>B3</b>	<b>VYG</b>	<b>0.45</b>	D3	APG	1.29	F3	AYI	1.80			
B4	WYG	1.33	D4	AQG	1.09	F4	AYK	3.02			
B5	YYG	1.55	D5	ARG	1.11	F5	AYL	1.90			
<b>B6</b>	<b>3YG</b>	<b>0.47</b>	D6	ASG	0.92	F6	AYN	1.06			
B7	4YG	0.54	D7	ATG	0.54	F7	AYP	0.87			
B8	5YG	0.54	<b>D8</b>	<b>AVG</b>	<b>0.54</b>	F8	AYQ	1.21			
B9	6YG	1.22	<b>D9</b>	<b>AWG</b>	<b>0.52</b>	F9	AYR	3.21			
B10	7YG	2.12	D10	AYG	0.65	F10	AYS	1.32			
B11	8YG	1.14	D11	A3G	1.31	F11	AYT	1.24			
B12	fYG	2.14	D12	A4G	0.93	F12	AYV	1.62			

references: knottin-RGD (5 $\mu\text{M}$ ): 0.37, no peptide: 1.54.



**Table S-11.** Absorbance values of library screening for 2<sup>nd</sup> generation of  $\alpha_5\beta_1$ -binders. Motif: C<sub>T3</sub>XXXXc<sub>T3</sub>AYGC<sub>T3</sub>. c<sub>Integrin</sub>: 0.49  $\mu\text{g/mL}$ , c<sub>biotinylated knottin-RGD</sub>: 0.2  $\mu\text{M}$ , c<sub>peptides</sub>: 5  $\mu\text{M}$ . Best five hits are in bold print.

	XXXX	A.U.		XXXX	A.U.		XXXX	A.U.
A1	RGDA	1.14	C1	RGDf	1.92	E1	4RGD	1.46
A2	RGDD	1.53	C2	RGDi	1.47	E2	5RGD	1.31
A3	RGDE	1.50	C3	RGD9	1.41	E3	6RGD	1.82
A4	RGDF	1.50	C4	RGDa	1.13	E4	7RGD	1.94
A5	RGDG	1.11	C5	ARGD	1.16	E5	8RGD	1.12
A6	RGDH	1.45	C6	DRGD	1.14	E6	fRGD	1.32
A7	RGDI	1.36	<b>C7</b>	<b>ERGD</b>	<b>1.01</b>	E7	iRGD	1.07
A8	RGDK	2.42	C8	FRGD	1.51	E8	9RGD	1.12
A9	RGDL	1.31	<b>C9</b>	<b>GRGD</b>	<b>0.74</b>	<b>E9</b>	<b>aRGD</b>	<b>0.98</b>
<b>A10</b>	<b>RGDN</b>	<b>0.99</b>	C10	HRGD	1.04			
A11	RGDP	1.45	C11	IRGD	1.23			
A12	RDGQ	1.88	C12	KRGD	2.01			
B1	RGDR	1.93	D1	LRGD	1.70			
B2	RGDS	1.41	D2	NRGD	1.34			
B3	RGDT	1.35	D3	PRGD	1.29			
B4	RGDV	1.36	D4	QRGD	1.49			
B5	RGDW	2.33	D5	RRGD	1.36			
B6	RGDY	1.53	D6	SRGD	1.30			
B7	RGD3	1.23	D7	TRGD	1.23			
B8	RGD4	1.28	<b>D8</b>	<b>VRGD</b>	<b>0.90</b>			
B9	RGD5	1.19	D9	WRGD	1.68			
B10	RGD6	1.81	D10	YRGD	1.30			
B11	RGD7	2.12	D11	2RGD	0.48			
B12	RGD8	1.23	D12	3RGD	1.28			

references: knottin-RGD (5 $\mu\text{M}$ ): 0.37, no peptide: 1.54.

**Table S-12.** Absorbance values of library screening for 2<sup>nd</sup> generation of  $\alpha_5\beta_1$ -binders. Motif: C<sub>T3</sub>XXXXXC<sub>T3</sub>AYGC<sub>T3</sub>. c<sub>Integrin</sub>: 0.49  $\mu$ g/mL, c<sub>biotinylated knottin-RGD</sub>: 0.2  $\mu$ M, c<sub>peptides</sub>: 5  $\mu$ M. Best five hits are in bold print.

	XXXXX	A.U.		XXXXX	A.U.		XXXXX	A.U.
<b>A1</b>	<b>GRGDA</b>	<b>0.99</b>	<b>C1</b>	<b>GRGDf</b>	<b>1.09</b>	E1	5RGDS	1.34
A2	GRGDD	1.11	<b>C2</b>	<b>GRGDi</b>	<b>1.05</b>	E2	6RGDS	2.48
A3	GRGDE	1.31	C3	GRGD9	1.79	E3	7RGDS	2.08
A4	GRGDF	1.31	C4	GRGDa	2.60	E4	8RGDS	3.40
A5	GRGDG	1.12	C5	ARGDS	1.59	E5	fRGDS	2.00
A6	GRGDH	1.17	C6	DRGDS	1.33	E6	iRGDS	1.80
A7	GRGDI	1.11	C7	ERGDS	1.58	E7	9RGDS	1.67
A8	GRGDK	1.35	C8	FRGDS	1.38	E8	aRGDS	1.53
A9	GRGDL	1.54	C9	HRGDS	1.58			
A10	GRGDN	1.35	C10	IRGDS	1.45			
A11	GRGDP	1.46	C11	KRGDS	1.38			
A12	GRDGQ	1.18	C12	LRGDS	1.62			
<b>B1</b>	<b>GRGDR</b>	<b>1.04</b>	D1	NRGDS	1.29			
<b>B2</b>	<b>GRGDS</b>	<b>1.05</b>	D2	PRGDS	1.68			
B3	GRGDT	1.57	D3	QRGDS	2.54			
B4	GRGDV	1.61	D4	RRGDS	3.82			
B5	GRGDW	1.70	D5	SRGDS	3.41			
B6	GRGDY	1.32	D6	TRGDS	3.12			
B7	GRGD3	1.17	D7	VRGDS	2.48			
B8	GRGD4	1.38	D8	WRGDS	3.12			
B9	GRGD5	1.27	D9	YRGDS	1.63			
B10	GRGD6	1.94	D10	2RGDS	1.34			
B11	GRGD7	2.09	D11	3RGDS	1.38			
B12	GRGD8	1.16	D12	4RGDS	1.59			

references: knottin-RGD (5 $\mu$ M): 0.37, no peptide: 1.54.

## References

- (1) Hageneder, S.; Bauch, M.; Dostalek, J. Plasmonically amplified bioassay – total internal reflection fluorescence vs. epifluorescence geometry. *Talanta* **2016**, *156–157*, 225–231.
- (2) Wang, Y.; Huang, C. J.; Jonas, U.; Wei, T.; Dostalek, J.; Knoll, W. Biosensor based on Hydrogel Optical Waveguide Spectroscopy. *Biosens. Bioelectron.* **2010**, *25*, 1663–1668.



# 4 Summary and outlook





## 4.1 Summary

Within the framework of this thesis, we included several projects that successfully demonstrated the preparation of hybrid architectures composed of gold nanostructures interfaced with functional “smart” materials. These architectures were pursued to provide additional functionalities in biosensing applications by actively controlling their optical characteristics while taking advantage of the unique properties offered by responsive hydrogel polymeric networks. Particular effort was made to develop strategies to selectively direct the binding of target analytes to the plasmonic hotspot regions and use the polymer network as a 3D binding matrix with capability to encompass the entire probing area at the hotspots while providing a high loading capacity compare to SAMs. To this end, lithography-based approaches to prepare metallic nanostructures with controlled morphology were successfully developed and merged with hydrogel films. These techniques include laser interference lithography, template stripping and nanoimprint lithography and enabled preparation of the nanostructures over macroscopic areas. In particular, thermo-responsive pNIPAAm-based polymeric networks with a lower critical solution temperature around 32°C were incorporated to the gold nanostructures. The pNIPAAm polymer backbone contained functional groups including benzophenone moieties for the crosslinking chemistry of the polymer chains and carboxylic functional groups for post-modification with ligand molecules. Cross-linked pNIPAAm films exhibited an open 3D structure facilitating the diffusion of chemical and biological species inside the network and provided on-demand actuation by temperature triggers. Post-modification of such 3D binding matrix with antibodies for their use in immunoassays was also demonstrated and plasmon-enhanced spectroscopy techniques were employed to test the sensing performance, including SERS and PEF spectroscopy.

A special emphasis was directed towards the targeted deposition of polymer networks only at the areas in close vicinity of the walls of the metallic nanoparticles in order to fully exploit and probe the locations with the strongest EM field confinement. In particular, two approaches were carefully designed for the selective cross-linking of the polymer networks. The first one utilized a highly confined interference beam to precisely record pNIPAAm features (with remarkable resolution around 170 nm) and exploited the moiré effect to overlay the hydrogel arrays on top of well-ordered gold nanoparticles with slightly mismatched periodicity. The collapsing of the pNIPAAm network above its LCST at 32 °C was also taken advantage of for compacting the target analyte to the surface of the gold nanostructures. PEF spectroscopy was used in combination with a model assay to assess the sensing performance with a LOD in the low picomolar range with a further

six times signal increase upon collapsing of the network. The second presented approach utilized the plasmon-assisted two-photon crosslinking of an anthraquinone-based polymeric network with selective deposition of the polymer only at the edges of the gold particles covering the entire probing range of the LSPs at the plasmonic hotspots regions.

Additionally, the embedding of gold nanoparticles inside pNIPAAm hydrogel membranes resulted in the excitation of collective localized plasmon modes. Such modes displayed sharp spectral features with strong shifts of the LSPR by solvent exchange or by temperature actuation. In particular, the free-standing hydrogel membrane configuration yielded remarkable shifts of the LSPR, as large as 100 nm, due to largely changed grating constant of the array upon the swelling of the membrane. Additionally, the tethered hydrogel membrane configuration was successfully applied to monitor binding of proteins in a label-free manner. Furthermore, another plasmonic architecture supporting propagating and localized surface plasmons was developed comprising a nanohole metallic film coupled with gold nanoparticles separated by a hydrogel cushion, which was actuated by collapsing and swelling the network with temperature and refractive index variations. The structure was used to monitor the binding of molecules at specific locations in a label free manner and it was also employed as SERS substrate. Finally, SPFS was employed to monitor the binding kinetics of bicyclic RGD peptides to  $\alpha_5\beta_1$  and  $\alpha_v\beta_3$  integrins, which were directly estimated with SPFS measurements and compared with those obtained by inhibition assays. The comparison between dissociation constants obtained for integrins directly immobilized on SAM or by using a thin hydrogel layer as binding matrix were also investigated.

## 4.2 Future outlook

The developed hybrid plasmonic materials hold potential to improve performance characteristics of various analytical technologies and find applications in diverse newly developing fields of optically driven actuators and nanomachines for medical sciences. The versatile means of the preparation of gold nanostructures over macroscopic areas with tunable size and spacing can be further extended to other geometries (e.g. elliptical or rod shaped nanoparticles) and exploited to design tailored configurations resonant at multiple desired wavelengths in various applications such as heat generation sources for thermoplasmonics applications. In addition, the developed methodology to pattern hydrogel arrays with nanoscale resolution can also create possibilities for additional projects in biological studies such as directed cell growth and proliferation investigations in the context of tissue engineering employing nanopatterned surfaces. In optical



spectroscopy, the adaptive properties of the plasmonic materials offer opportunities to advance optical spectroscopy studies, where the plasmonic-based substrates providing enhancement of weak optical signals can be on demand adjusted to maximize amplification strength at certain wavelengths. For example, resonant plasmonic wavelengths can be swept through specific Raman bands of investigated molecules or implemented to provide fluorescence enhancement for fluorophores with different emission and absorption spectra. These materials would particularly benefit from the demonstrated approaches to selectively capture the analyzed molecules at sub-areas of metallic nanostructures corresponding to the plasmonic hotspot regions, which can efficiently boost optical response. In addition, the LCST transition at 32 °C of the used pNIPAAm polymer networks is very close to that of the human body temperature and it thus can be applied to create drug carriers or to harvest cells. By modification of the polymer backbone or using other polymers (such as oxazoline-based) the LCST can be shifted to other temperatures. Therefore, the reported materials can be potentially combined with other hydrogels exhibiting complementary upper critical solution temperature (UCST). Research in such polymer networks that exhibit biocompatible properties may enable translating the reported mechanisms with optical tunability for their use in entirely new types of medical sensor devices, triggering the on-demand swelling and collapsing of the polymer network via temperature cues. These include for instance implants with continuously operated biosensors actuated externally by near infrared (NIR) light in the NIR spectral window where the tissues are transparent.

## References

1. Polman, A., Plasmonics applied. *Science* **2008**, 322 (5903), 868-869.
2. Aroca, R. F., Plasmon enhanced spectroscopy. *Physical Chemistry Chemical Physics* **2013**, 15 (15), 5355-5363.
3. Homola, J.; Piliarik, M., Surface plasmon resonance (SPR) sensors. In *Surface plasmon resonance based sensors*, Springer: 2006; pp 45-67.
4. Hou, W.; Cronin, S. B., A review of surface plasmon resonance-enhanced photocatalysis. *Advanced Functional Materials* **2013**, 23 (13), 1612-1619.
5. Baffou, G.; Quidant, R.; Girard, C., Heat generation in plasmonic nanostructures: Influence of morphology. *Applied Physics Letters* **2009**, 94 (15), 153109.
6. Hoa, X. D.; Kirk, A.; Tabrizian, M., Towards integrated and sensitive surface plasmon resonance biosensors: a review of recent progress. *Biosensors and bioelectronics* **2007**, 23 (2), 151-160.
7. Fang, Y.; Sun, M., Nanoplasmonic waveguides: towards applications in integrated nanophotonic circuits. *Light: Science & Applications* **2015**, 4 (6), e294.
8. Hu, M.; Chen, J.; Li, Z.-Y.; Au, L.; Hartland, G. V.; Li, X.; Marquez, M.; Xia, Y., Gold nanostructures: engineering their plasmonic properties for biomedical applications. *Chemical Society Reviews* **2006**, 35 (11), 1084-1094.
9. Vial, S.; Reis, R. L.; Oliveira, J. M., Recent advances using gold nanoparticles as a promising multimodal tool for tissue engineering and regenerative medicine. *Current Opinion in Solid State and Materials Science* **2017**, 21 (2), 92-112.
10. Han, G.; Ghosh, P.; Rotello, V. M., Multi-functional gold nanoparticles for drug delivery. In *Bio-applications of Nanoparticles*, Springer: 2007; pp 48-56.
11. Ghosh, P.; Han, G.; De, M.; Kim, C. K.; Rotello, V. M., Gold nanoparticles in delivery applications. *Advanced drug delivery reviews* **2008**, 60 (11), 1307-1315.
12. Jagur-Grodzinski, J., Polymers for tissue engineering, medical devices, and regenerative medicine. Concise general review of recent studies. *Polymers for advanced technologies* **2006**, 17 (6), 395-418.
13. Smith, J. R.; Lamprou, D. A., Polymer coatings for biomedical applications: a review. *Transactions of the IMF* **2014**, 92 (1), 9-19.
14. Angelova, N.; Hunkeler, D., Rationalizing the design of polymeric biomaterials. *Trends in biotechnology* **1999**, 17 (10), 409-421.
15. Wei, M.; Gao, Y.; Li, X.; Serpe, M. J., Stimuli-responsive polymers and their applications. *Polymer Chemistry* **2017**, 8 (1), 127-143.
16. Barnes, W. L.; Dereux, A.; Ebbesen, T. W., Surface plasmon subwavelength optics. *nature* **2003**, 424 (6950), 824.
17. Reiner, A. T.; Toma, K.; Brisson, A. R.; Pils, D.; Knoll, W.; Dostalek, J., Plasmonic Exosome Biosensors for Medical Diagnostics. In *Frontiers in Biophotonics for Translational Medicine*, Springer: 2016; pp 249-272.
18. Knoll, W., Evanescent Wave Biosensors with a Hydrogel Binding Matrix. In *Handbook of Biofunctional Surfaces*, Jenny Stanford Publishing: 2013; pp 395-440.
19. Jiang, N.; Zhuo, X.; Wang, J., Active Plasmonics: Principles, Structures, and Applications. *Chemical reviews* **2017**.
20. Homola, J.; Yee, S. S.; Gauglitz, G., Surface plasmon resonance sensors. *Sensors and Actuators B: Chemical* **1999**, 54 (1-2), 3-15.
21. Byun, K. M.; Kim, S. J.; Kim, D., Grating-coupled transmission-type surface plasmon resonance sensors based on dielectric and metallic gratings. *Applied optics* **2007**, 46 (23), 5703-5708.
22. Quilis, N. G.; Sharma, N.; Fossati, S.; Knoll, W.; Dostalek, J., Responsive Polymer Networks and Brushes for Active Plasmonics. *Polymer and Biopolymer Brushes: for Materials Science and Biotechnology 2 Volume Set* **2017**, 687-707.

23. Van Duyne, R. P.; Haes, A. J.; McFarland, A. D. In *Nanoparticle optics: sensing with nanoparticle arrays and single nanoparticles*, Physical Chemistry of Interfaces and Nanomaterials II, International Society for Optics and Photonics: 2003; pp 197-207.
24. Cheng, Y.; Wang, M.; Borghs, G.; Chen, H., Gold nanoparticle dimers for plasmon sensing. *Langmuir* **2011**, *27* (12), 7884-7891.
25. Gómez, D.; Vernon, K.; Davis, T., Symmetry effects on the optical coupling between plasmonic nanoparticles with applications to hierarchical structures. *Physical Review B* **2010**, *81* (7), 075414.
26. Li, W.; Zhang, L.; Zhou, J.; Wu, H., Well-designed metal nanostructured arrays for label-free plasmonic biosensing. *Journal of Materials Chemistry C* **2015**, *3* (25), 6479-6492.
27. Eftekhari, F.; Escobedo, C.; Ferreira, J.; Duan, X.; Girotto, E. M.; Brolo, A. G.; Gordon, R.; Sinton, D., Nanoholes as nanochannels: flow-through plasmonic sensing. *Analytical chemistry* **2009**, *81* (11), 4308-4311.
28. Hanske, C.; Hill, E. H.; Vila-Liarte, D.; González-Rubio, G.; Matricardi, C.; Mihi, A.; Liz-Marzán, L. M., Solvent-assisted self-assembly of gold nanorods into hierarchically organized plasmonic mesostructures. *ACS applied materials & interfaces* **2019**, *11* (12), 11763-11771.
29. Zayats, A. V.; Smolyaninov, I. I., Near-field photonics: surface plasmon polaritons and localized surface plasmons. *Journal of Optics A: Pure and Applied Optics* **2003**, *5* (4), S16.
30. Mayer, K. M.; Hafner, J. H., Localized surface plasmon resonance sensors. *Chemical reviews* **2011**, *111* (6), 3828-3857.
31. Petryayeva, E.; Krull, U. J., Localized surface plasmon resonance: nanostructures, bioassays and biosensing--a review. *Analytica chimica acta* **2011**, *706* (1), 8-24.
32. Svedendahl, M.; Chen, S.; Dmitriev, A.; Kall, M., Refractometric sensing using propagating versus localized surface plasmons: a direct comparison. *Nano letters* **2009**, *9* (12), 4428-4433.
33. Huang, F.; Baumberg, J. J., Actively tuned plasmons on elastomerically driven Au nanoparticle dimers. *Nano letters* **2010**, *10* (5), 1787-1792.
34. Yue, W.; Wang, Z.; Yang, Y.; Li, J.; Wu, Y.; Chen, L.; Ooi, B.; Wang, X.; Zhang, X.-x., Enhanced extraordinary optical transmission (EOT) through arrays of bridged nanohole pairs and their sensing applications. *Nanoscale* **2014**, *6* (14), 7917-7923.
35. Santos, A.; Deen, M.; Marsal, L., Low-cost fabrication technologies for nanostructures: state-of-the-art and potential. *Nanotechnology* **2015**, *26* (4), 042001.
36. Valsecchi, C.; Brolo, A. G., Periodic metallic nanostructures as plasmonic chemical sensors. *Langmuir* **2013**, *29* (19), 5638-5649.
37. Lindquist, N. C.; Nagpal, P.; McPeak, K. M.; Norris, D. J.; Oh, S.-H., Engineering metallic nanostructures for plasmonics and nanophotonics. *Reports on Progress in Physics* **2012**, *75* (3), 036501.
38. Knight, M. W.; King, N. S.; Liu, L.; Everitt, H. O.; Nordlander, P.; Halas, N. J., Aluminum for plasmonics. *ACS nano* **2013**, *8* (1), 834-840.
39. Gérard, D.; Gray, S. K., Aluminium plasmonics. *Journal of Physics D: Applied Physics* **2014**, *48* (18), 184001.
40. Kravets, V.; Jalil, R.; Kim, Y.-J.; Ansell, D.; Aznakayeva, D.; Thackray, B.; Britnell, L.; Belle, B.; Withers, F.; Radko, I., Graphene-protected copper and silver plasmonics. *Scientific reports* **2014**, *4*, 5517.
41. Garcia, G.; Buonsanti, R.; Runnerstrom, E. L.; Mendelsberg, R. J.; Llordes, A.; Anders, A.; Richardson, T. J.; Milliron, D. J., Dynamically modulating the surface plasmon resonance of doped semiconductor nanocrystals. *Nano letters* **2011**, *11* (10), 4415-4420.
42. Chu, Y.; Schonbrun, E.; Yang, T.; Crozier, K. B., Experimental observation of narrow surface plasmon resonances in gold nanoparticle arrays. *Applied Physics Letters* **2008**, *93* (18), 181108.

43. Rodriguez, S. R. K.; Abass, A.; Maes, B.; Janssen, O. T.; Vecchi, G.; Rivas, J. G., Coupling bright and dark plasmonic lattice resonances. *Physical Review X* **2011**, *1* (2), 021019.
44. Miroshnichenko, A. E.; Flach, S.; Kivshar, Y. S., Fano resonances in nanoscale structures. *Reviews of Modern Physics* **2010**, *82* (3), 2257.
45. Limonov, M. F.; Rybin, M. V.; Poddubny, A. N.; Kivshar, Y. S., Fano resonances in photonics. *Nature Photonics* **2017**, *11* (9), 543.
46. Qazi, U. Y.; Javaid, R., A review on metal nanostructures: preparation methods and their potential applications. *Advances in Nanoparticles* **2016**, *5* (1), 27-43.
47. Wang, Y.; Zhou, J.; Li, J., Construction of Plasmonic Nano-Biosensor-Based Devices for Point-of-Care Testing. *Small Methods* **2017**, *1* (11), 1700197.
48. Grzelczak, M.; Pérez-Juste, J.; Mulvaney, P.; Liz-Marzán, L. M., Shape control in gold nanoparticle synthesis. *Chemical Society Reviews* **2008**, *37* (9), 1783-1791.
49. Sun, Y.; Xia, Y., Shape-controlled synthesis of gold and silver nanoparticles. *Science* **2002**, *298* (5601), 2176-2179.
50. Guerrero-Martínez, A.; Barbosa, S.; Pastoriza-Santos, I.; Liz-Marzán, L. M., Nanostars shine bright for you: colloidal synthesis, properties and applications of branched metallic nanoparticles. *Current Opinion in Colloid & Interface Science* **2011**, *16* (2), 118-127.
51. Grzelczak, M.; Vermant, J.; Furst, E. M.; Liz-Marzán, L. M., Directed self-assembly of nanoparticles. *ACS nano* **2010**, *4* (7), 3591-3605.
52. Vieu, C.; Carcenac, F.; Pepin, A.; Chen, Y.; Mejias, M.; Lebib, A.; Manin-Ferlazzo, L.; Couraud, L.; Launois, H., Electron beam lithography: resolution limits and applications. *Applied surface science* **2000**, *164* (1-4), 111-117.
53. Watt, F.; Bettiol, A.; Van Kan, J.; Teo, E.; Breese, M., Ion beam lithography and nanofabrication: a review. *International Journal of Nanoscience* **2005**, *4* (03), 269-286.
54. Qin, D.; Xia, Y.; Whitesides, G. M., Soft lithography for micro-and nanoscale patterning. *Nature protocols* **2010**, *5* (3), 491.
55. Guo, L. J., Nanoimprint lithography: methods and material requirements. *Advanced materials* **2007**, *19* (4), 495-513.
56. Haynes, C. L.; Van Duyne, R. P., Nanosphere lithography: a versatile nanofabrication tool for studies of size-dependent nanoparticle optics. ACS Publications: 2001.
57. Pietsch, T.; Gindy, N.; Mahltig, B.; Fahmi, A., Fabrication of functional nano-objects via self-assembly of nanostructured hybrid materials. *Journal of Polymer Science Part B: Polymer Physics* **2010**, *48* (14), 1642-1650.
58. Tseng, Y.-C.; Darling, S. B., Block copolymer nanostructures for technology. *Polymers* **2010**, *2* (4), 470-489.
59. Jang, J. H.; Ullal, C. K.; Maldovan, M.; Gorishnyy, T.; Kooi, S.; Koh, C.; Thomas, E. L., 3D micro-and nanostructures via interference lithography. *Advanced Functional Materials* **2007**, *17* (16), 3027-3041.
60. Rodriguez, A.; Echeverría, M.; Ellman, M.; Perez, N.; Verevkin, Y. K.; Peng, C. S.; Berthou, T.; Wang, Z.; Ayerdi, I.; Savall, J., Laser interference lithography for nanoscale structuring of materials: From laboratory to industry. *Microelectronic Engineering* **2009**, *86* (4-6), 937-940.
61. Hsiao, V. K.; Zheng, Y. B.; Juluri, B. K.; Huang, T. J., Light-driven plasmonic switches based on au nanodisk arrays and photoresponsive liquid crystals. *Advanced Materials* **2008**, *20* (18), 3528-3532.
62. MacDonald, K. F.; Sámson, Z. L.; Stockman, M. I.; Zheludev, N. I., Ultrafast active plasmonics. *Nature Photonics* **2009**, *3* (1), 55-58.
63. MacDonald, K. F.; Zheludev, N. I., Active plasmonics: current status. *Laser & Photonics Reviews* **2009**, *4* (4), 562-567.
64. Ellenbogen, T.; Seo, K.; Crozier, K. B., Chromatic plasmonic polarizers for active visible color filtering and polarimetry. *Nano letters* **2012**, *12* (2), 1026-1031.

65. Li, Z.; Clark, A. W.; Cooper, J. M., Dual color plasmonic pixels create a polarization controlled nano color palette. *ACS nano* **2016**, *10* (1), 492-498.
66. Hall, W. P.; Modica, J.; Anker, J.; Lin, Y.; Mrksich, M.; Van Duyne, R. P., A conformation-and ion-sensitive plasmonic biosensor. *Nano letters* **2011**, *11* (3), 1098-1105.
67. Lamberti, A.; Virga, A.; Angelini, A.; Ricci, A.; Descrovi, E.; Cocuzza, M.; Giorgis, F., Metal–elastomer nanostructures for tunable SERS and easy microfluidic integration. *RSC Advances* **2015**, *5* (6), 4404-4410.
68. Li, Z.; Yin, Y., Stimuli-Responsive Optical Nanomaterials. *Advanced Materials* **2019**, *31* (15), 1807061.
69. Vasa, P.; Pomraenke, R.; Cirimi, G.; De Re, E.; Wang, W.; Schwieger, S.; Leipold, D.; Runge, E.; Cerullo, G.; Lienau, C., Ultrafast manipulation of strong coupling in metal–molecular aggregate hybrid nanostructures. *Acs Nano* **2010**, *4* (12), 7559-7565.
70. Evans, R. A.; Hanley, T. L.; Skidmore, M. A.; Davis, T. P.; Such, G. K.; Yee, L. H.; Ball, G. E.; Lewis, D. A., The generic enhancement of photochromic dye switching speeds in a rigid polymer matrix. *Nature materials* **2005**, *4* (3), 249-253.
71. Yao, Y.; Kats, M. A.; Genevet, P.; Yu, N.; Song, Y.; Kong, J.; Capasso, F., Broad electrical tuning of graphene-loaded plasmonic antennas. *Nano letters* **2013**, *13* (3), 1257-1264.
72. Yao, Y.; Kats, M. A.; Shankar, R.; Song, Y.; Kong, J.; Loncar, M.; Capasso, F., Wide wavelength tuning of optical antennas on graphene with nanosecond response time. *Nano letters* **2013**, *14* (1), 214-219.
73. Lu, W.; Jiang, N.; Wang, J., Active electrochemical plasmonic switching on polyaniline-coated gold nanocrystals. *Advanced Materials* **2017**, *29* (8), 1604862.
74. Yavuz, M. S.; Jensen, G. C.; Penaloza, D. P.; Seery, T. A.; Pendergraph, S. A.; Rusling, J. F.; Sotzing, G. A., Gold nanoparticles with externally controlled, reversible shifts of local surface plasmon resonance bands. *Langmuir* **2009**, *25* (22), 13120-13124.
75. Jiang, N.; Shao, L.; Wang, J., (Gold nanorod core)/(polyaniline shell) plasmonic switches with large plasmon shifts and modulation depths. *Advanced Materials* **2014**, *26* (20), 3282-3289.
76. Kozlovskaya, V.; Kharlampieva, E.; Khanal, B. P.; Manna, P.; Zubarev, E. R.; Tsukruk, V. V., Ultrathin Layer-by-Layer Hydrogels with Incorporated Gold Nanorods as pH-Sensitive Optical Materials. *Chemistry of Materials* **2008**, *20* (24), 7474-7485.
77. Chen, K.; Leong, E. S. P.; Rukavina, M.; Nagao, T.; Liu, Y. J.; Zheng, Y., Active molecular plasmonics: tuning surface plasmon resonances by exploiting molecular dimensions. *Nanophotonics* **2015**, *4* (1).
78. Sun, Y.; Jiang, L.; Zhong, L.; Jiang, Y.; Chen, X., Towards active plasmonic response devices. *Nano Research* **2015**, *8* (2), 406-417.
79. Prajapati, D. G.; Kandasubramanian, B., Progress in the development of intrinsically conducting polymer composites as biosensors. *Macromolecular Chemistry and Physics* **2019**, *220* (10), 1800561.
80. Scognamiglio, V.; Pezzotti, G.; Pezzotti, I.; Cano, J.; Buonasera, K.; Giannini, D.; Giardi, M. T., Biosensors for effective environmental and agrifood protection and commercialization: from research to market. *Microchimica Acta* **2010**, *170* (3-4), 215-225.
81. Tu, J.; Torrente-Rodríguez, R. M.; Wang, M.; Gao, W., The Era of Digital Health: A Review of Portable and Wearable Affinity Biosensors. *Advanced Functional Materials* **2019**, 1906713.
82. Kassal, P.; Steinberg, M. D.; Steinberg, I. M., Wireless chemical sensors and biosensors: A review. *Sensors and Actuators B: Chemical* **2018**, *266*, 228-245.
83. Kirsch, J.; Siltanen, C.; Zhou, Q.; Revzin, A.; Simonian, A., Biosensor technology: recent advances in threat agent detection and medicine. *Chemical Society Reviews* **2013**, *42* (22), 8733-8768.
84. Luong, J. H.; Male, K. B.; Glennon, J. D., Biosensor technology: technology push versus market pull. *Biotechnology advances* **2008**, *26* (5), 492-500.

85. Rogers, K. R.; Gerlach, C. L., Peer reviewed: environmental biosensors: a status report. *Environmental science & technology* **1996**, *30* (11), 486A-491A.
86. Grieshaber, D.; MacKenzie, R.; Vörös, J.; Reimhult, E., Electrochemical biosensors-sensor principles and architectures. *Sensors* **2008**, *8* (3), 1400-1458.
87. Baggerman, J.; Smulders, M. M.; Zuilhof, H., Romantic Surfaces: A Systematic Overview of Stable, Biospecific, and Antifouling Zwitterionic Surfaces. *Langmuir* **2019**, *35* (5), 1072-1084.
88. de los Santos Pereira, A.; Riedel, T.; Brynda, E.; Rodriguez-Emmenegger, C., Hierarchical antifouling brushes for biosensing applications. *Sensors and Actuators B: Chemical* **2014**, *202*, 1313-1321.
89. Lyratzopoulos, G.; Vedsted, P.; Singh, H., Understanding missed opportunities for more timely diagnosis of cancer in symptomatic patients after presentation. *British journal of cancer* **2015**, *112* (1), S84-S91.
90. Babayan, A.; Pantel, K., Advances in liquid biopsy approaches for early detection and monitoring of cancer. *Genome medicine* **2018**, *10* (1), 21.
91. Visser, E. W.; Yan, J.; van IJendoorn, L. J.; Prins, M. W., Continuous biomarker monitoring by particle mobility sensing with single molecule resolution. *Nature communications* **2018**, *9* (1), 1-10.
92. Singh, P., SPR biosensors: Historical perspectives and current challenges. *Sensors and actuators B: Chemical* **2016**, *229*, 110-130.
93. Sandhyarani, N., Surface modification methods for electrochemical biosensors. In *Electrochemical Biosensors*, Elsevier: 2019; pp 45-75.
94. Morales, M. A.; Halpern, J. M., Guide to selecting a biorecognition element for biosensors. *Bioconjugate chemistry* **2018**, *29* (10), 3231-3239.
95. Karlsson, R., SPR for molecular interaction analysis: a review of emerging application areas. *Journal of Molecular Recognition* **2004**, *17* (3), 151-161.
96. Khansili, N.; Rattu, G.; Krishna, P. M., Label-free optical biosensors for food and biological sensor applications. *Sensors and Actuators B: Chemical* **2018**, *265*, 35-49.
97. Homola, J., Surface plasmon resonance sensors for detection of chemical and biological species. *Chemical reviews* **2008**, *108* (2), 462-493.
98. Slavík, R.; Homola, J., Ultrahigh resolution long range surface plasmon-based sensor. *Sensors and Actuators B: Chemical* **2007**, *123* (1), 10-12.
99. Sreekanth, K. V.; Alapan, Y.; Elkabbash, M.; Ilker, E.; Hinczewski, M.; Gurkan, U. A.; De Luca, A.; Strangi, G., Extreme sensitivity biosensing platform based on hyperbolic metamaterials. *Nature materials* **2016**, *15* (6), 621-627.
100. Chen, H.; Kou, X.; Yang, Z.; Ni, W.; Wang, J., Shape-and size-dependent refractive index sensitivity of gold nanoparticles. *Langmuir* **2008**, *24* (10), 5233-5237.
101. Piliarik, M.; Kvasnička, P.; Galler, N.; Krenn, J. R.; Homola, J., Local refractive index sensitivity of plasmonic nanoparticles. *Optics express* **2011**, *19* (10), 9213-9220.
102. Kvasnička, P.; Homola, J., Optical sensors based on spectroscopy of localized surface plasmons on metallic nanoparticles: sensitivity considerations. *Biointerphases* **2008**, *3* (3), FD4-FD11.
103. Elshorbagy, M. H.; Cuadrado, A.; González, G.; González, F. J.; Alda, J., Performance improvement of refractometric sensors through hybrid plasmonic-fano resonances. *Journal of Lightwave Technology* **2019**, *37* (13), 2905-2913.
104. Verellen, N.; Van Dorpe, P.; Huang, C.; Lodewijks, K.; Vandenbosch, G. A.; Lagae, L.; Moshchalkov, V. V., Plasmon line shaping using nanocrosses for high sensitivity localized surface plasmon resonance sensing. *Nano letters* **2011**, *11* (2), 391-397.
105. Shen, Y.; Zhou, J.; Liu, T.; Tao, Y.; Jiang, R.; Liu, M.; Xiao, G.; Zhu, J.; Zhou, Z.-K.; Wang, X., Plasmonic gold mushroom arrays with refractive index sensing figures of merit approaching the theoretical limit. *Nature communications* **2013**, *4* (1), 1-9.
106. Li, J.; Ye, J.; Chen, C.; Li, Y.; Verellen, N.; Moshchalkov, V. V.; Lagae, L.; Van Dorpe, P., Revisiting the surface sensitivity of nanoplasmonic biosensors. *Acs Photonics* **2015**, *2* (3), 425-431.

107. Li, J.; Chen, C.; Lagae, L.; Van Dorpe, P., Nanoplasmonic sensors with various photonic coupling effects for detecting different targets. *The Journal of Physical Chemistry C* **2015**, *119* (52), 29116-29122.
108. Wijaya, E.; Lenaerts, C.; Maricot, S.; Hastanin, J.; Habraken, S.; Vilcot, J.-P.; Boukherroub, R.; Szunerits, S., Surface plasmon resonance-based biosensors: From the development of different SPR structures to novel surface functionalization strategies. *Current Opinion in Solid State and Materials Science* **2011**, *15* (5), 208-224.
109. Law, W.-C.; Yong, K.-T.; Baev, A.; Prasad, P. N., Sensitivity improved surface plasmon resonance biosensor for cancer biomarker detection based on plasmonic enhancement. *ACS nano* **2011**, *5* (6), 4858-4864.
110. Acimovic, S. S.; Kreuzer, M. P.; González, M. U.; Quidant, R., Plasmon near-field coupling in metal dimers as a step toward single-molecule sensing. *ACS nano* **2009**, *3* (5), 1231-1237.
111. Dodson, S.; Haggui, M.; Bachelot, R.; Plain, J.; Li, S.; Xiong, Q., Optimizing electromagnetic hotspots in plasmonic bowtie nanoantennae. *The journal of physical chemistry letters* **2013**, *4* (3), 496-501.
112. Zhou, X.; Deeb, C.; Kostcheev, S.; Wiederrecht, G. P.; Adam, P.-M.; Béal, J. r. m.; Plain, J. r. m.; Gosztola, D. J.; Grand, J.; Félidj, N., Selective functionalization of the nanogap of a plasmonic dimer. *Acs Photonics* **2015**, *2* (1), 121-129.
113. Lal, S.; Grady, N. K.; Kundu, J.; Levin, C. S.; Lassiter, J. B.; Halas, N. J., Tailoring plasmonic substrates for surface enhanced spectroscopies. *Chemical Society Reviews* **2008**, *37* (5), 898-911.
114. Li, J.-F.; Li, C.-Y.; Aroca, R. F., Plasmon-enhanced fluorescence spectroscopy. *Chemical Society Reviews* **2017**, *46* (13), 3962-3979.
115. Jin, Y.; Gao, X., Plasmonic fluorescent quantum dots. *Nature nanotechnology* **2009**, *4* (9), 571.
116. Hwang, E.; Smolyaninov, I. I.; Davis, C. C., Surface plasmon polariton enhanced fluorescence from quantum dots on nanostructured metal surfaces. *Nano letters* **2010**, *10* (3), 813-820.
117. Dong, Z.-C.; Guo, X.-L.; Trifonov, A.; Dorozhkin, P.; Miki, K.; Kimura, K.; Yokoyama, S.; Mashiko, S., Vibrationally resolved fluorescence from organic molecules near metal surfaces in a scanning tunneling microscope. *Physical review letters* **2004**, *92* (8), 086801.
118. Chen, X.; Wu, Y.-W., Selective chemical labeling of proteins. *Organic & biomolecular chemistry* **2016**, *14* (24), 5417-5439.
119. Holmes, K.; Lantz, L., Protein labeling with fluorescent probes. *Essential cytometry methods* **2009**.
120. Ming, T.; Chen, H.; Jiang, R.; Li, Q.; Wang, J., Plasmon-controlled fluorescence: beyond the intensity enhancement. *The Journal of Physical Chemistry Letters* **2012**, *3* (2), 191-202.
121. Bauch, M.; Toma, K.; Toma, M.; Zhang, Q.; Dostalek, J., Plasmon-enhanced fluorescence biosensors: a review. *Plasmonics* **2014**, *9* (4), 781-799.
122. Giannini, V.; Fernández-Domínguez, A. I.; Heck, S. C.; Maier, S. A., Plasmonic nanoantennas: fundamentals and their use in controlling the radiative properties of nanoemitters. *Chemical reviews* **2011**, *111* (6), 3888-3912.
123. Ford, G. W.; Weber, W. H., Electromagnetic interactions of molecules with metal surfaces. *Physics Reports* **1984**, *113* (4), 195-287.
124. Aslan, K.; Gryczynski, I.; Malicka, J.; Matveeva, E.; Lakowicz, J. R.; Geddes, C. D., Metal-enhanced fluorescence: an emerging tool in biotechnology. *Current opinion in biotechnology* **2005**, *16* (1), 55-62.
125. Geddes, C. D., Metal-enhanced fluorescence. *Physical Chemistry Chemical Physics* **2013**, *15* (45), 19537-19537.
126. Aslan, K.; Malyn, S. N.; Geddes, C. D., Angular-dependent metal-enhanced fluorescence from silver island films. *Chemical physics letters* **2008**, *453* (4-6), 222-228.

127. Benner, R. E.; Dornhaus, R.; Chang, R. K., Angular emission profiles of dye molecules excited by surface plasmon waves at a metal surface. *Optics Communications* **1979**, *30* (2), 145-149.
128. Lakowicz, J. R., Radiative decay engineering 5: metal-enhanced fluorescence and plasmon emission. *Analytical biochemistry* **2005**, *337* (2), 171-194.
129. Tabakman, S. M.; Lau, L.; Robinson, J. T.; Price, J.; Sherlock, S. P.; Wang, H.; Zhang, B.; Chen, Z.; Tangsombatvisit, S.; Jarrell, J. A., Plasmonic substrates for multiplexed protein microarrays with femtomolar sensitivity and broad dynamic range. *Nature communications* **2011**, *2* (1), 1-9.
130. Wang, Y.; Brunsen, A.; Jonas, U.; Dostalek, J.; Knoll, W., Prostate specific antigen biosensor based on long range surface plasmon-enhanced fluorescence spectroscopy and dextran hydrogel binding matrix. *Analytical chemistry* **2009**, *81* (23), 9625-9632.
131. Kinkhabwala, A.; Yu, Z.; Fan, S.; Avlasevich, Y.; Müllen, K.; Moerner, W., Large single-molecule fluorescence enhancements produced by a bowtie nanoantenna. *Nature Photonics* **2009**, *3* (11), 654-657.
132. Yu, F.; Yao, D.; Knoll, W., Oligonucleotide hybridization studied by a surface plasmon diffraction sensor (SPDS). *Nucleic acids research* **2004**, *32* (9), e75-e75.
133. Biggs, K. B.; Camden, J. P.; Anker, J. N.; Duyne, R. P. V., Surface-enhanced Raman spectroscopy of benzenethiol adsorbed from the gas phase onto silver film over nanosphere surfaces: determination of the sticking probability and detection limit time. *The Journal of Physical Chemistry A* **2009**, *113* (16), 4581-4586.
134. Qian, X.-M.; Nie, S. M., Single-molecule and single-nanoparticle SERS: from fundamental mechanisms to biomedical applications. *Chemical Society Reviews* **2008**, *37* (5), 912-920.
135. Rodríguez-Lorenzo, L.; Alvarez-Puebla, R. A.; Pastoriza-Santos, I.; Mazzucco, S.; Stéphan, O.; Kociak, M.; Liz-Marzán, L. M.; García de Abajo, F. J., Zeptomol detection through controlled ultrasensitive surface-enhanced Raman scattering. *Journal of the American Chemical Society* **2009**, *131* (13), 4616-4618.
136. Morton, S. M.; Jensen, L., Understanding the molecule– surface chemical coupling in SERS. *Journal of the American Chemical Society* **2009**, *131* (11), 4090-4098.
137. Morla-Folch, J.; Gisbert-Quilis, P.; Masetti, M.; Garcia-Rico, E.; Alvarez-Puebla, R. A.; Guerrini, L., Conformational SERS Classification of K-Ras Point Mutations for Cancer Diagnostics. *Angewandte Chemie* **2017**, *129* (9), 2421-2425.
138. Nativo, P.; Prior, I. A.; Brust, M., Uptake and intracellular fate of surface-modified gold nanoparticles. *ACS nano* **2008**, *2* (8), 1639-1644.
139. Jimenez de Aberasturi, D.; Serrano-Montes, A. B.; Langer, J.; Henriksen-Lacey, M.; Parak, W. J.; Liz-Marzán, L. M., Surface enhanced Raman scattering encoded gold nanostars for multiplexed cell discrimination. *Chemistry of Materials* **2016**, *28* (18), 6779-6790.
140. Pucek, R.; Panacek, A.; Soukupova, J.; Novotny, R.; Kvitek, L., Reproducible synthesis of silver colloidal particles tailored for application in near-infrared surface-enhanced Raman spectroscopy. *Journal of Materials Chemistry* **2011**, *21* (17), 6416-6420.
141. Bibikova, O.; Haas, J.; López-Lorente, A. I.; Popov, A.; Kinnunen, M.; Meglinski, I.; Mizaikoff, B., Towards enhanced optical sensor performance: SEIRA and SERS with plasmonic nanostars. *Analyst* **2017**, *142* (6), 951-958.
142. Wang, Y.; Yan, B.; Chen, L., SERS tags: novel optical nanoprobe for bioanalysis. *Chemical reviews* **2013**, *113* (3), 1391-1428.
143. Chen, H.-Y.; Lin, M.-H.; Wang, C.-Y.; Chang, Y.-M.; Gwo, S., Large-scale hot spot engineering for quantitative SERS at the single-molecule scale. *Journal of the American Chemical Society* **2015**, *137* (42), 13698-13705.
144. Cialla, D.; März, A.; Böhme, R.; Theil, F.; Weber, K.; Schmitt, M.; Popp, J., Surface-enhanced Raman spectroscopy (SERS): progress and trends. *Analytical and bioanalytical chemistry* **2012**, *403* (1), 27-54.



145. Mrksich, M.; Whitesides, G. M., Using self-assembled monolayers to understand the interactions of man-made surfaces with proteins and cells. *Annual review of biophysics and biomolecular structure* **1996**, *25* (1), 55-78.
146. Gooding, J. J.; Mearns, F.; Yang, W.; Liu, J., Self-assembled monolayers into the 21st century: recent advances and applications. *Electroanalysis: An International Journal Devoted to Fundamental and Practical Aspects of Electroanalysis* **2003**, *15* (2), 81-96.
147. Wink, T.; Van Zuilen, S.; Bult, A.; Van Bennekom, W., Self-assembled monolayers for biosensors. *Analyst* **1997**, *122* (4), 43R-50R.
148. Ulman, A., Formation and structure of self-assembled monolayers. *Chemical reviews* **1996**, *96* (4), 1533-1554.
149. Nyquist, R.; Eberhardt, A.; Silks, L.; Li, Z.; Yang, X.; Swanson, B., Characterization of self-assembled monolayers for biosensor applications. *Langmuir* **2000**, *16* (4), 1793-1800.
150. Nelson, K. E.; Gamble, L.; Jung, L. S.; Boeckl, M. S.; Naeemi, E.; Golledge, S. L.; Sasaki, T.; Castner, D. G.; Campbell, C. T.; Stayton, P. S., Surface characterization of mixed self-assembled monolayers designed for streptavidin immobilization. *Langmuir* **2001**, *17* (9), 2807-2816.
151. Huang, C.-J., Advanced surface modification technologies for biosensors. In *Chemical, Gas, and Biosensors for Internet of Things and Related Applications*, Elsevier: 2019; pp 65-86.
152. Krishnamoorthy, M.; Hakobyan, S.; Ramstedt, M.; Gautrot, J. E., Surface-initiated polymer brushes in the biomedical field: applications in membrane science, biosensing, cell culture, regenerative medicine and antibacterial coatings. *Chemical reviews* **2014**, *114* (21), 10976-11026.
153. Huang, C. J.; Brault, N. D.; Li, Y.; Yu, Q.; Jiang, S., Controlled Hierarchical Architecture in Surface-initiated Zwitterionic Polymer Brushes with Structurally Regulated Functionalities. *Advanced Materials* **2012**, *24* (14), 1834-1837.
154. Ullah, F.; Othman, M. B. H.; Javed, F.; Ahmad, Z.; Akil, H. M., Classification, processing and application of hydrogels: A review. *Materials Science and Engineering: C* **2015**, *57*, 414-433.
155. Maitra, J.; Shukla, V. K., Cross-linking in hydrogels-a review. *Am. J. Polym. Sci* **2014**, *4* (2), 25-31.
156. Gerlach, G.; Arndt, K.-F., *Hydrogel sensors and actuators: engineering and technology*. Springer Science & Business Media: 2009; Vol. 6.
157. Kuckling, D.; Harmon, M. E.; Frank, C. W., Photo-cross-linkable PNIPAAm copolymers. 1. Synthesis and characterization of constrained temperature-responsive hydrogel layers. *Macromolecules* **2002**, *35* (16), 6377-6383.
158. Sood, N.; Bhardwaj, A.; Mehta, S.; Mehta, A., Stimuli-responsive hydrogels in drug delivery and tissue engineering. *Drug Delivery* **2016**, *23* (3), 748-770.
159. Li, J.; Mooney, D. J., Designing hydrogels for controlled drug delivery. *Nature Reviews Materials* **2016**, *1* (12), 1-17.
160. Jung, I. Y.; Kim, J. S.; Choi, B. R.; Lee, K.; Lee, H., Hydrogel based biosensors for in vitro diagnostics of biochemicals, proteins, and genes. *Advanced healthcare materials* **2017**, *6* (12), 1601475.
161. Cao, B.; Li, L.; Wu, H.; Tang, Q.; Sun, B.; Dong, H.; Zhe, J.; Cheng, G., Zwitteration of dextran: a facile route to integrate antifouling, switchability and optical transparency into natural polymers. *Chemical Communications* **2014**, *50* (24), 3234-3237.
162. Wang, Y.; Huang, C.-J.; Jonas, U.; Wei, T.; Dostalek, J.; Knoll, W., Biosensor based on hydrogel optical waveguide spectroscopy. *Biosensors and Bioelectronics* **2010**, *25* (7), 1663-1668.
163. Toma, M.; Jonas, U.; Mateescu, A.; Knoll, W.; Dostalek, J., Active control of SPR by thermoresponsive hydrogels for biosensor applications. *The Journal of Physical Chemistry C* **2013**, *117* (22), 11705-11712.

164. Zhang, Q.; Wang, Y.; Mateescu, A.; Sergelen, K.; Kibrom, A.; Jonas, U.; Wei, T.; Dostalek, J., Biosensor based on hydrogel optical waveguide spectroscopy for the detection of 17 $\beta$ -estradiol. *Talanta* **2013**, *104*, 149-154.
165. Feuz, L.; Jonsson, M. P.; Höök, F., Material-selective surface chemistry for nanoplasmonic sensors: optimizing sensitivity and controlling binding to local hot spots. *Nano letters* **2012**, *12* (2), 873-879.
166. Feuz, L.; Jonsson, P.; Jonsson, M. P.; Hook, F., Improving the limit of detection of nanoscale sensors by directed binding to high-sensitivity areas. *Acs Nano* **2010**, *4* (4), 2167-2177.
167. Zhang, N.; Liu, Y. J.; Yang, J.; Su, X.; Deng, J.; Chum, C. C.; Hong, M.; Teng, J., High sensitivity molecule detection by plasmonic nanoantennas with selective binding at electromagnetic hotspots. *Nanoscale* **2014**, *6* (3), 1416-1422.
168. Goerlitzer, E. S.; Speichermann, L. E.; Mirza, T. A.; Mohammadi, R.; Vogel, N., Addressing the plasmonic hotspot region by site-specific functionalization of nanostructures. *Nanoscale Advances* **2020**.
169. Beeram, S. R.; Zamborini, F. P., Selective attachment of antibodies to the edges of gold nanostructures for enhanced localized surface plasmon resonance biosensing. *Journal of the American Chemical Society* **2009**, *131* (33), 11689-11691.
170. Cortés, E.; Xie, W.; Cambiasso, J.; Jermyn, A. S.; Sundararaman, R.; Narang, P.; Schlücker, S.; Maier, S. A., Plasmonic hot electron transport drives nano-localized chemistry. *Nature communications* **2017**, *8* (1), 1-10.
171. Simoncelli, S.; Li, Y.; Cortés, E.; Maier, S. A., Nanoscale control of molecular self-assembly induced by plasmonic hot-electron dynamics. *ACS nano* **2018**, *12* (3), 2184-2192.
172. Galloway, C. M.; Kreuzer, M. P.; Aćimović, S. S.; Volpe, G.; Correia, M.; Petersen, S. B.; Neves-Petersen, M. T.; Quidant, R., Plasmon-assisted delivery of single nano-objects in an optical hot spot. *Nano letters* **2013**, *13* (9), 4299-4304.

## List of figures

<b>Figure 1.</b> Schematic of localized and propagating surface plasmons with its typical penetration depth ( $L_p$ ).....	6
<b>Figure 2.</b> Dispersion relation of photons in free space (red), after coupling with a prism (violet) and that of PSPs (black). .....	7
<b>Figure 3.</b> Schematics of the a) ATR and b) grating-coupled configuration supporting the excitation of PSPs. ....	8
<b>Figure 4.</b> Refractive index sensitivity of PSPs with a) grating-coupled scheme ( $\Lambda=440$ nm, amplitude of 12.5 nm and $\theta=0$ deg) and b) ATR configuration (50 nm thick gold layer, $n_p=1.845$ , $\theta=51.7$ deg).....	8
<b>Figure 5.</b> a) Shifts in the LSPR for individual spherical Au particles with diameter $D=30$ nm by refractive index variations ( $n_d$ ) and b) spectral position variations due to gap distance changes between a closely arranged oblate nanoparticle dimer ( $D= 40$ and 30 nm). ....	9
<b>Figure 6.</b> a) Schematic with different sorts of nanostructures classified with representative examples including scanning electron images of b) 0D systems, c) 1D systems, d) 2D architectures, e) Quasi 3D architectures and f) 3D architectures.....	11
<b>Figure 7.</b> Three approaches to attain active plasmonic systems based on dielectric variations and tunable carriers or spacing.....	13
<b>Figure 8.</b> a) LSPR shift of Au nanorods capped with PANI polymer (thickness of 39 nm) between its doped and undoped state and b) its corresponding switching kinetics. ....	14
<b>Figure 9.</b> Components of a biosensor. ....	15
<b>Figure 10.</b> Size distribution of common ligand molecules and target analytes. ....	18
<b>Figure 11.</b> Schematic of the additional radiative paths for the excitation of fluorophores via surface plasmons.....	20
<b>Figure 12.</b> Schematic of the Raman scattering process with a Jablonski diagram. ....	21

---

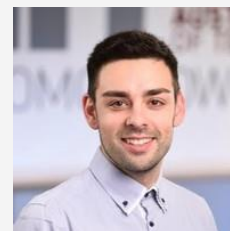
<b>Figure 13.</b> Schematic of common SAMs depicting material composition. ....	23
<b>Figure 14.</b> Schematic of PB regimes with chemical structures of typical polymer chain employed. ....	23
<b>Figure 15.</b> Schematic of the architecture combining both low and high density PB for attaining high loading capacity and nonfouling characteristics. ....	24
<b>Figure 16.</b> Schematic of SPs and higher HW modes inside a hydrogel film. ...	25
<b>Figure 17.</b> a) Reflectivity spectra obtained via SPR-HOWS measurements of a pNIPAAm thin film at different temperatures. b) Swelling ration and refractive index as function of temperature. ....	26
<b>Figure 18.</b> Schematic of the three studied surface chemistries and its associated binding kinetics for case I (Au targeted binding, blue), case II (TiO <sub>2</sub> /Au active area, red) and case III (TiO <sub>2</sub> -directed binding, green).. ....	27

## Abbreviations

2D/3D	Two dimensional/ Three dimensional
2PP	Two-photon polymerization
2PC	Two-photon crosslinking
ATR	Attenuated total internal reflection
AFM	Atomic force microscopy
BRE	Biorecognition element
cLSPs	Collective localized surface plasmons
cLSPR	Collective localized surface plasmon resonance
DNA	Deoxyribonucleic acid
EDC	1-ethyl-3-(3-dimethylaminopropyl)carbodiimide
ELISA	Enzyme-linked immunosorbent assay
EM	Electromagnetic
FDTD	Finite difference time domain
FOM	Figure of merit
FWHM	Full width at half maximum
HOWS	Hydrogel optical waveguide spectroscopy
HW	Hydrogel waveguide
IgG	Immunoglobulin G
LIL	Laser interference lithography
LOD	Limit of detection
LSPs	Localized surface plasmons
LSPR	Localized surface plasmon resonance
L <sub>p</sub>	Penetration depth
NHS	N-Hydroxysuccinimide
NIR	Near infrared
PB	Polymer brushes
PDMS	Polydimethylsiloxane
PEF	Plasmon enhanced fluorescence
PBS/PBST	Phosphate buffer saline/ tween
pNIPAAm	Poly(N-isopropylacrylamide)
PSPs	Propagating surface plasmons
PANI	Polyaniline
PEDOT	Poly (3,4-ethylenedioxythiophene)
RI	Refractive index
RIU	Refractive index unit
RNA	Ribonucleic acid
SAM	Self-assembled monolayer
SPR	Surface plasmon resonance
SPs	Surface plasmons
SERS	Surface-enhanced Raman spectroscopy
SEM	Scanning electron microscopy
TE	Transverse electric
TM	Transverse magnetic
UV	Ultraviolet



# NESTOR GISBERT QUILIS



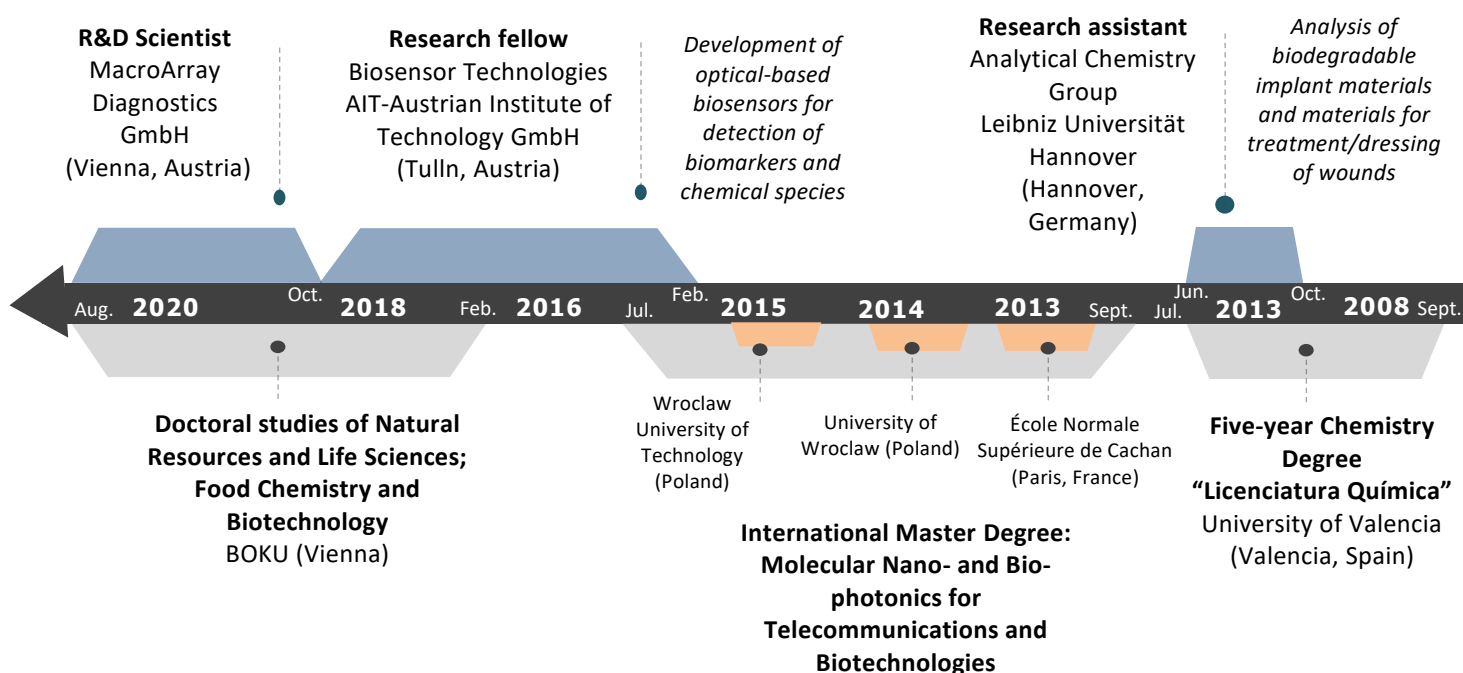
✉ nestor.gisbert.quilis@gmail.com

Date of birth: 27/08/1990  
Nationality: Spanish

Scientist with 3+ years of experience carrying out multi-disciplinary research in the field of biosensors. Skilled in bioassays, nanofabrication methods, implementation of novel materials, surface functionalization, and amplification schemes for medical diagnostics applications. Experience in collaborative development and management of projects at an international level.

- Development and implementation of **biosensors**
- Experience in **bioassays**, **surface functionalization** and **molecular interaction studies**
- Integration of **coatings** and **novel materials**
- **International** and **cross-cultural** team working experience

## EXPERIENCE ▼



## EDUCATION ▲

### RESEARCH EXPERIENCE

**MacroArray Diagnostics GmbH (Oct. 2018 till present):** Development and optimization of immunoassays. Implementation of surface chemistries for conjugation of proteins to nanoparticles.

**Austrian Institute of Technology GmbH (3 years 8 months):** Designed and fabricated biosensors based on metallic structures with nanoscale features. Planned and executed immunoassays, surface functionalization strategies and molecular interaction studies. Implemented novel materials and anti-fouling coatings to overcome limitations and add new functionalities in sensing platforms.

**Analytical chemistry group, Leibniz Universität Hannover (9 months):** Prepared and measured large numbers of liquid and solid samples for detection of trace-level compounds with several analytic techniques.

### RESEARCH METHODS

**Analytical techniques:** Surface plasmon resonance (SPR), surface plasmon-enhanced fluorescence (SPFS), surface-enhanced Raman spectroscopy (SERS), inductively coupled plasma optical emission spectrometry and mass spectrometry (ICP-OES, ICP-MS), Ultraviolet-visible spectroscopy (UV-VIS), Fourier-transform infrared spectroscopy (FTIR).

**Bioassays:** Development of Immunoassays and peptide-based assays, protein labeling, surface functionalization, and interaction studies.

**Imaging:** Atomic force microscopy (AFM), scanning electron microscopy with energy dispersive X-ray spectroscopy (SEM/EDX).

**Fabrication Micro-Nano structures:** Laser interference lithography (LIL), nanoimprint lithography (NIL), mask aligner, two-photon lithography.

## SKILLS

**Data & writing-** Data analysis (origin, excel), report and paper writing.

**Image-** Blender (3D software), Image J, Illustrator, Photoshop.

**Communication-** Presentations at conferences, project meetings and public events.

**Organization-** Workshops, project meetings and dissemination activities.

**Teaching-** Training of incoming personnel and supervision of undergraduate students.

## LANGUAGES

SPANISH		Native
CATALAN		Native
ENGLISH		Fluent
ITALIAN		Fluent
GERMAN		Learning A2-B1

## COURSES & WORKSHOPS (Selected)

- ✓ **Statistical Validation and Experimental Design**  
Biostatech, Dec. 2015
- ✓ **Time and Project Management**  
Bpmsat, Dec. 2015
- ✓ **Coatings & Sensors**  
Noviosense, Apr. 2017
- ✓ **Advanced Study Course on Optical Chemical Sensors**  
Ascoss Series, Jul. 2017

## CONFERENCES (Selected)

- ✓ **Biosensors**  
June 2018 (Miami, USA)
- ✓ **Kárman Conference-Materials for life**  
April 2018 (Bensberg, Germany)
- ✓ **Europt(r)ode**  
March 2018 (Napoli, Italy), 2016 (Graz, Austria)
- ✓ **NANOP**  
September 2017 (Barcelona, Spain)

## PUBLICATIONS

- [1] **Gisbert-Quilis N.**; Sharma, N.; Fossati, S.; Knoll, W.; Dostalek, J., Responsive Polymer Networks and Brushes for Active Plasmonics. Polymer and Biopolymer Brushes: for Materials Science and Biotechnology 2 Volume Set 2017, 687-707.
- [2] **Gisbert-Quilis N.**; Lequeux, M.; Venugopalan, P.; Khan, I.; Knoll, W.; Boujday, S.; de La Chapelle, M. L.; Dostalek, J., Tunable laser interference lithography preparation of plasmonic nanoparticle arrays tailored for SERS. Nanoscale 2018, 10 (21), 10268-10276.
- [3] **Gisbert-Quilis N.**; van Dongen, M.; Venugopalan, P.; Kotlearek, D.; Petri, C.; Moreno Cencerrado, A.; Stanescu, S.; Toca Herrera, J. L.; Jonas, U.; Möller, M.; Mourran, A.; Dostalek, J., Actively Tunable Collective Localized Surface Plasmons by Responsive Hydrogel Membrane. Advanced Optical Materials 2019, 7 (15), 1900342.
- [4] **Gisbert-Quilis N.**; Hageneder, S.; Fossati, S.; Auer, S. K.; Venugopalan, P.; Bozdogan, A.; Petri, C.; Moreno-Cencerrado, A.; Toca-Herrera, J. L.; Jonas, U., UV-Laser Interference Lithography for Local Functionalization of Plasmonic Nanostructures with Responsive Hydrogel. The Journal of Physical Chemistry C 2020, 124 (5), 3297-3305.
- [5] Bernhagen, D.; Jungbluth, V.; **Gisbert Quilis, N.**; Dostalek, J.; White, P. B.; Jalink, K.; Timmerman, P., Bicyclic RGD peptides with exquisite selectivity for the integrin  $\alpha v \beta 3$  receptor using a "random design" approach. ACS combinatorial science 2019, 21 (3), 198-206.
- [6] Bernhagen, D.; Jungbluth, V.; **Gisbert Quilis, N.**; Dostalek, J.; White, P. B.; Jalink, K.; Timmerman, P., High-Affinity  $\alpha 5 \beta 1$ -Integrin-Selective Bicyclic RGD Peptides Identified via Screening of Designed Random Libraries. ACS combinatorial science 2019, 21 (8), 598-607.

## AWARDS

- ✓ **Marie Curie Fellowship for Early Stage Research Training**  
Sept. 2015
- ✓ **Erasmus Mundus Master Scholarship**  
Sept. 2013
- ✓ **Third price ASCOS 2018 Group Project**  
Jul. 2018
- ✓ **Bancaja Scholarship**  
Sept. 2012





